

Impact of Amphiphilic Molecules on the Miscibility of (Model) Crude Oils and CO₂: Phase Behavior and Slim Tube Studies

Von der Fakultät Chemie der Universität Stuttgart
zur Erlangung der Würde eines Doktors der
Naturwissenschaften (Dr. rer. nat.) genehmigte Abhandlung

Vorgelegt von
Harun Bilgili
aus Mutlangen

Hauptberichter: Apl. Prof. Dr. Thomas Sottmann

Mitberichter: Prof. Dr. Frank Gießelmann

Tag der mündlichen Prüfung: 10.06.2021

Institut für Physikalische Chemie der Universität Stuttgart

Table of Contents

Symbols and Abbreviations	4
Abstract	6
Kurzzusammenfassung.....	8
1 Introduction	11
1.1 Objectives.....	13
2 Fundamentals	15
2.1 Conventional Oil Recovery	15
2.2 Immiscible and Miscible Displacement.....	16
2.3 Principles of Phase Behavior and Miscibility.....	17
2.4 The Miscible Processes.....	22
2.5 The CO ₂ Miscible Process	25
2.6 CO ₂ -EOR with Additives.....	32
2.7 Methods for Determining Miscibility Conditions.....	33
3 Materials and Methods	36
3.1 Materials	36
3.1.1 Chemicals	36
3.1.2 Data Evaluation	40
3.2 Methods	40
3.2.1 High Pressure Visual Cell.....	40
3.2.1.1 Sample preparation	43
3.2.2 Slim Tube Apparatus	46
3.2.2.1 Darcy's Law	52
3.2.3 Density Meter (Pycnometer)	53
3.2.4 Specifying the Composition and Construction of Phase Diagrams	55
4 Results and Discussion.....	59
4.1 (Pseudo-)Binary Systems.....	61
4.1.1 CO ₂ – Additive Systems	61
4.1.2 CO ₂ – (Model) Crude Oils	64
4.1.2.1 Development of Model Crude Oils	67
4.2 Comparison of CO ₂ – Additive and CO ₂ – (Model) Crude Oil Systems.....	76
4.3 Pseudoternary Systems.....	78
4.4 Pressure Profit Δp as a Measure of the Miscibility-Enhancing Effect.....	82
4.5 Search for the Best Additives	85
4.5.1 Linear and Branched Alcohols.....	85

4.5.2	Alkoxylated Alcohols as New Type of Miscibility Enhancers	90
4.5.3	Best Performing Additives: Composition Dependence of Miscibility-Enhancing Effect	95
4.6	Patent Application and Comparison to Prior Art	99
4.7	Swelling Behavior	102
4.7.1	Water-Containing Systems	107
4.7.2	Pseudoquaternary Systems: H ₂ O – CO ₂ – Aco38.0 – Additive.....	112
4.8	Simulation of Real Crude Oil Field Operations by Slim Tube Experiments.....	115
4.8.1	Slim Tube Studies	116
5	Summary and Outlook.....	128
6	Bibliography.....	132
7	Appendix.....	144
7.1	Pressure Balance	144
7.2	Safety Issues	145
7.3	Model Crude Oil 51.4	146
7.4	Viscosity of <i>n</i> -Hexadecane	147
7.5	Densities of CO ₂ and <i>n</i> -Hexadecane.....	147
7.6	CO ₂ – Aco38.0 Phase Behavior Below the Critical Point of CO ₂	149
7.7	Overview of Measured Systems.....	150
List of Figures.....		155
List of Tables.....		159
Acknowledgments.....		160
Declaration		162
Publications, Patent, Conferences and other Contributions		163

Symbols and Abbreviations

Latin

Symbol	Unit	Explanation
A	cm^2	cross sectional area
g	$\text{m}\cdot\text{s}^{-2}$	acceleration of gravity
G_m	J	free molar enthalpy
k	m^2 (darcy,d)	permeability
L	cm	length
m_0	g	mass of empty pycnometer
m_1	g	mass of pycnometer filled with water at the desired temperature until calibration mark
m_2	g	mass of the pycnometer with the quantity of the substance to investigate
m_3	g	mass of the pycnometer with the quantity of the substance to investigate and water at the desired temperature until calibration mark
m_{Additive}		mass of the additive
p	MPa	pressure
p_c	MPa	pressure of critical point
psia	Psi	pound-force per square inch absolute
psig	Psi	pound-force per square inch gauge
$p_{\text{Ø}}$	MPa	average pressure
Q	$\text{cm}^3\cdot\text{s}^{-1}$	volumetric flow rate
T	K or °C	temperature
T_c	°C	critical temperature
T_m	°C	melting temperature
V_n		valve index n (needle or ball valve)
$V_{\text{Oil phase}}$	m^3	volume of the oil phase
$V_{\text{Water phase}}$	m^3	volume of the water phase
w_{Oil}	wt%	oil mass fraction
$w_{\text{Oil,c}}$	wt%	critical oil mass fraction
	wt%	percentage by mass
w_x		mass fraction, wherein x is the given component
x		composition

Greek

Symbol	Unit	Explanation
γ_{CO_2}	wt%	additive mass fraction in CO_2
Δp	MPa	pressure profit
Δp_{max}	MPa	maximum pressure profit
μ	$\text{mPa}\cdot\text{s}$	dynamic viscosity
Θ	rad	contact angle
N	ms^{-1}	velocity
ρ	$\text{g}\cdot\text{cm}^{-3}$	density
σ_{OW}	$\text{mN}\cdot\text{m}^{-1}$	IFT between oil and water

Abbreviations

Abbreviation	Unit	Explanation
aco38.0		Asian crude oil with an API gravity of 38.0 °
API gravity	°	American Petroleum Institute gravity
CCS		carbon dioxide capture and storage
CEP		critical end point
$\text{C}_i\text{E}_j\text{P}_x$		i characterizes the number of the carbon atoms (C) in the alkyl chain, j the number of ethoxy units (E) and x the number of propoxy units (P)
Co.		Company
DDBST		Dortmund Data Bank Software & Separation Technology GmbH
DI water		deionized water
DIN		the German Institute for Standardization
EOR		enhanced oil recovery
FCM		first-contact miscible
G		Gauge
g		gaseous phase

Abbreviation	Unit	Explanation	Abbreviation	Unit	Explanation
gc		gas chromatograph	SG		specific gravity of oil relative to water at 60 °F (15.6 °C)
HP-cell		high pressure visual cell	ST		slim tube
HPLC		high performance liquid chromatography	UL		upper liquid
IFT		interfacial tension	VIT		vanishing interfacial tension
IPC		Institute of Physical Chemistry	V		vapor phase
ISO		International Organization for Standardization	Other		
I		liquid phase	Symbol	Unit	Explanation
LL		lower liquid	∅ _{out}	mm or inch	outer diameter
M		steel membrane	∅ _{in}	mm or inch	inner diameter
MCM		multiple-contact miscible			
mco38.0		model crude oil with an API gravity of 38.0 °			
mco38.8		model crude oil with an API gravity of 38.8 °			
mco47.0		model crude oil with an API gravity of 47.0 °			
MMP	MPa	minimum miscibility pressure			
MMP _p	MPa	physical minimum miscibility pressure			
MR		membrane reservoir			
N _b		bond number or Eötvös number			
NBR90		Acrylonitrile butadiene rubber 90			
N _c		capillary number			
NIST		the National Institute of Standards and Technology			
OOIP		original oil in place			
PI		piston			
POM		Polyoxymethylene			
PRV		pressure relief valves			
PT		pressure transducer			
PTFE		Poly(tetrafluoroethylene)			
PV	135 cm ³	pore volume			
S		sapphire cylinder			
SF		swelling factor			

Abstract

Despite increased environmental awareness, the demand for crude oil remains high. In order to satisfy this demand, existing production methods are being optimized with the aim of making currently inaccessible oil resources recoverable. One promising method of enhanced oil recovery (EOR) is the injection of carbon dioxide (CO₂). In the light of climate change, capture, beneficial use, and subterranean sequestration of the increasingly available CO₂ are of great interest. CO₂-EOR is thus of double benefit by improving oil recovery, while reducing CO₂ in the atmosphere. An important factor for the success of CO₂-EOR is the miscibility of the injected CO₂ and the specific crude oil. A promising approach to improve the miscibility is the addition of appropriate additives, thereby further enhancing oil recovery rates and making reservoirs accessible, which are naturally not.

The aim of this thesis, which was part of a research project with Sasol Performance Chemicals GmbH, was to systematically investigate the influence of additive type, structure and molecular mass on the miscibility-enhancing effect. As a starting point, a fast and reliable experimental procedure was developed to study the systems' phase behavior at a temperature and pressure range relevant for reservoirs, i.e. between 5 °C and 80 °C as well as 0.5 MPa and 45 MPa. Using this method, the miscibility of different types of additives and CO₂ was studied as a prerequisite for their use in CO₂-EOR. To facilitate the study of the CO₂ – crude oil miscibility behavior, four different model crude oils were designed consisting of a mixture of short- and long-chain alkanes, the Sasolwax 5805, aromatics, and naphthenes. Detailed investigations of the phase behavior showed that mixtures of CO₂ with the developed model crude oils or a real Asian crude oil exhibit a comparable asymmetric lower miscibility gap. The maximum of the miscibility gap, referred to in this work as the physical minimum miscibility pressure (MMP_p), was found at around 40 MPa for all systems, while the critical point was located at a pressure of approximately 20 MPa.

Having characterized the (pseudo-)binary side systems, the influence of 17 alcohols and 20 alkoxyated additives on the different CO₂ – (model) crude oil systems was systematically studied at an application-oriented small additive mass fraction (γ_{CO_2}) in the CO₂/additive mixture of 2 wt%. Interestingly, all investigated additives (except for one) showed a positive pressure effect ($\Delta p > 0$), i.e. they increased the miscibility of (model) crude oils with CO₂. For linear alcohols, the pressure profits were found to run through a maximum

between 1-hexanol and 1-dodecanol. The poor compatibility between short-chain 1-alcohols and long-chain alkanes on the one hand and between long-chain alcohols and CO₂ on the other hand can explain this trend. Comparing linear alcohols with branched alcohols, mostly smaller pressure profits were found for branched alcohols. Surprisingly, alkoxyated additives were able to achieve larger Δp values compared to the respective starting alcohols, which might be related to a certain compatibility of ethoxy and propoxy groups with CO₂. However, no systematic trend of the pressure profit was observed with increasing numbers of ethoxy or propoxy groups most likely due to the broad distribution of the degree of alkoxylation in the technical-grade additives. Furthermore, the pressure profits considerably increased with the API gravity of the (model) crude oils and decreasing temperature, i.e. when the miscibility gap is larger, which might indicate that the magnitude of the pressure profit scales with the MMP_p.

Besides miscibility, the swelling of crude oils by CO₂ is an important property for CO₂-EOR. Studying the swelling behavior, the best miscibility-enhancing additives also showed a considerable increase of the maximum swelling factor, thereby reducing the viscosity of the oil. This enables better flow through the reservoir resulting in higher production rates. Finally, the effect of one of the most powerful additives, i.e. threefold propoxylated 1-hexanol (C₆P₃), was studied in a slim tube experiment simulating real oil field conditions as a proof of concept. In two research visits, a slim tube apparatus was set-up at the Rice University (Houston, Texas, USA) in close collaboration with the group of Prof. Dr. George J. Hirasaki. These elaborate measurements confirmed the promising miscibility-enhancing effect of C₆P₃ via a striking lowering of the minimum miscibility pressure (MMP) and a considerably increasing oil recovery rate, especially at pressures below the MMP. Importantly, the values of the MMP, elaborately determined via slim tube measurements, correlated quantitatively with the critical (plait) point pressure p_c determined from phase behavior.

In summary, the systematic measurements of this thesis led to the identification of new, promising additives for CO₂-EOR, which were consequently filed in a patent application (EP19158014). Importantly, this thesis established phase behavior studies as a much faster and more cost-effective alternative to slim tube experiments to reliably determine technically relevant properties under reservoir conditions of interests. Since this study furthermore showed that the identification of the most effective additive for a specific oil field operation requires extensive screenings of diverse additives, this method will help to improve the efficiency of future CO₂-EOR projects.

Kurzzusammenfassung

Trotz des wachsenden Umweltbewusstseins verbleibt der Bedarf an Erdöl hoch. Um dieser Nachfrage gerecht zu werden und derzeit nicht zugängliche Ölreservoirs zu erschließen, werden bestehende Methoden zur Erdölförderung optimiert. Ein vielversprechendes Verfahren der Tertiären Erdölförderung (*Enhanced Oil Recovery*; EOR) ist die Injektion von Kohlenstoffdioxid (CO₂). Im Hinblick auf den Klimawandel ist das Einfangen, die vorteilhafte Nutzung und unterirdische Sequestrierung der stetig zunehmenden CO₂-Mengen von großem Interesse. CO₂-EOR bietet daher durch die Verbesserung der Ölförderung und die Verringerung von atmosphärischem CO₂ einen doppelten Nutzen. Ein wichtiger Faktor für den Erfolg von CO₂-EOR ist die Mischbarkeit des injizierten CO₂ mit dem jeweiligen Rohöl. Eine vielversprechende Methode die Mischbarkeit zu verbessern, ist die Verwendung von Additiven, wodurch Förderraten verbessert und nicht zugängliche Ölreservoirs erschlossen werden.

Ziel dieser Arbeit, die Teil eines Forschungsprojekts mit Sasol Performance Chemicals GmbH war, war es daher den Effekt unterschiedlicher Additive in Abhängigkeit ihres Typs sowie ihrer molekularen Struktur und Masse auf die Mischbarkeit von CO₂ und Öl systematisch zu untersuchen. Hierzu wurde zunächst eine schnelle und verlässliche, experimentelle Methode zur Messung des Phasenverhaltens in einem für Ölreservoirs relevanten Temperatur- und Druckbereich (zwischen 5 °C und 80 °C und 0.5 MPa und 45 MPa) entwickelt. Mithilfe dieser Methode wurde die Mischbarkeit verschiedener Additivtypen und CO₂ untersucht, welche eine Voraussetzung für die Verwendung in CO₂-EOR ist. Um die Messung der Mischbarkeit von CO₂ und Rohöl zu erleichtern, wurden vier Modellrohöle bestehend aus einer Mischung kurz- und langkettiger Alkane, dem Sasolwachs 5805, Aromaten und Naphthenen entwickelt. Detaillierte Untersuchungen des Phasenverhaltens zeigten, dass alle Mischungen der entwickelten Modellrohöle mit CO₂ eine asymmetrische, untere Mischungslücke aufwiesen vergleichbar zu einem asiatischen Rohöl. Das Maximum dieser Mischungslücke, welches in dieser Arbeit als physikalischer Minimum-Mischdruck (MMP_p) definiert wird, lag dabei für alle Systeme bei ca. 40 MPa, während der kritische Punkt bei einem Druck von ca. 20 MPa gefunden wurde.

Nach Analyse der (pseudo-)binären Randsysteme wurde der Einfluss von 17 Alkoholen und 20 alkoxylierten Additiven auf die Mischbarkeit von CO₂ – (Modell-)Rohölsystemen systematisch bei einem anwendungsorientierten, kleinen Massenbruch des Additivs (γ_{CO_2}) in

der CO₂/Additiv Mischung von 2 Gew.-% untersucht. Alle untersuchten Additive (mit Ausnahme eines Additivs) zeigten einen positiven Effekt ($\Delta p > 0$), d.h. sie erhöhten die Mischbarkeit der (Modell-)Rohöle mit CO₂. Lineare Alkohole zeigten ein Optimum bezüglich der Verbesserung der Mischbarkeit, das zwischen 1-Hexanol und 1-Dodecanol lag. Dieser Trend lässt sich durch die niedrige Kompatibilität von kurzkettigen 1-Alkoholen und langkettigen Alkanen einerseits und von langkettigen Alkoholen und CO₂ andererseits erklären. Der Vergleich linearer und verzweigter Alkohole ergab in den meisten Fällen geringere Verbesserungen durch die verzweigten Alkohole. Überraschenderweise erzielten alkoxylierte Additive einen höheren Δp -Wert als die entsprechenden Ausgangsalkohole. Dies kann durch eine gewisse Kompatibilität von Ethoxy- und Propoxygruppen mit CO₂ bedingt sein. Allerdings wurde kein systematischer Zusammenhang zwischen der Anzahl an Ethoxy- und Propoxyeinheiten und den Mischbarkeit verbessernden Effekten gefunden, was an der technischen Reinheit und der damit verbundenen großen Variabilität des Alkoxylierungsgrads der Additive liegen kann. Darüber hinaus wurde ein zunehmender *Pressure Profit* mit steigendem API Grad des (Modell-)Rohöls sowie mit abnehmender Temperatur festgestellt, das heißt bei größerer Mischungslücke. Dies kann darauf hindeuten, dass die Größe des erzielten *Pressure Profits* mit dem MMP_p skaliert.

Neben der Mischbarkeit ist das Schwellverhalten der Rohöle durch CO₂ eine wichtige Eigenschaft für CO₂-EOR. Die besten Mischbarkeit fördernden Additive zeigten auch eine deutliche Verbesserung des Schwellverhaltens. Die damit einhergehende, verringerte Viskosität des Öls ermöglicht einen verbesserten Fluss durch das Reservoir und damit höhere Produktionsraten. Abschließend wurde der Effekt des dreifach propoxylierten 1-Hexanols (C₆P₃), eines der besten Additive, in einem *Slim Tube* Experiment unter realen Erdöllagerstättenbedingungen untersucht. Während zweier Forschungsaufenthalte an der Rice University (Houston, Texas, USA) wurde dazu in enger Zusammenarbeit mit Prof. Dr. George J. Hirasaki eine *Slim Tube* Apparatur aufgebaut. Diese aufwendigen Messungen bestätigten die vielversprechenden, Mischbarkeit fördernden Eigenschaften von C₆P₃ durch eine erhebliche Abnahme des Minimum-Mischdrucks sowie eine deutlich erhöhte Ölförderrate, insbesondere bei Drücken unterhalb des MMP. Von großer Bedeutung ist hierbei, dass die Werte des MMP, die durch aufwendige *Slim Tube* Messungen bestimmt wurden, quantitativ mit den Drücken der kritischen Punkte (*Plait Points*) p_c aus den Phasenverhaltensstudien übereinstimmen.

Zusammenfassend konnten durch die systematischen Messungen in dieser Arbeit neue, vielversprechende Additive für CO₂-EOR identifiziert werden, was zu einer Patentanmeldung (EP19158014) führte. Darüber hinaus wurden Phasenverhaltensstudien als eine wesentlich schnellere und günstigere Alternative zu *Slim Tube* Experimenten etabliert, um eine verlässliche Bestimmung technisch relevanter Eigenschaften unter Reservoirbedingungen zu erlauben. Da diese Arbeit zudem die Notwendigkeit ausgiebiger Screenings zur Identifikation des effektivsten Additivs für ein spezifisches Ölreservoir aufgezeigt hat, wird diese Methode dazu beitragen die Effektivität zukünftiger CO₂-EOR Projekte zu verbessern.

1 Introduction

The continuously increasing world request for petroleum raises the need to both exploit reservoirs at harsher conditions (for instance larger depth) and to make unrecoverable oil in mature reservoirs accessible by enhanced oil recovery (EOR) processes [Austad, et al., 1996, Høgenesen, Standnes, Austad, 2006, Montel, et al., 2007]. The injection of carbon dioxide (CO₂) is a promising EOR technique, allowing the extraction of parts of the remaining crude oil from mature reservoirs [Kuuskraa, Wallace, 2014, Stalkup, 1978]. At the same time, one of the most important environmental issues today is the global climate change, which is caused by long-living greenhouse gases emitted by humans, among which carbon dioxide (CO₂) is a major contributor [Houghton, 2001]. Thus, CO₂-EOR provides a double benefit: carbon dioxide capture and storage (CCS) by keeping CO₂ out of the atmosphere combined with increased oil production [Metz, et al., 2005, Holm, Josendal, 1974, Holm, 1959, Yan, 2015].

The residual crude oil production from mature fields by injection of CO₂ is applied since a few decades [Manrique, et al., 2010, Lake, 1989]. Over the last two decades, more and more experience has been gained in pilot field tests to understand the CO₂-EOR process [Zhang, et al., 2015, Jia, Tsau, Barati, 2019, Tsau, Ballard, 2014]. However, the fundamental physics behind it, e.g. phase behavior, interfacial phenomena including wetting and flow, are complex making it very difficult to predict the applicability of CO₂-EOR for a given reservoir. In general, CO₂ is not fully miscible with reservoir oils under the conditions found in reservoirs. In the terminology of oil-field experts, such a behavior would be considered to be not first-contact miscible (FCM). Options to influence the interaction between crude oil and CO₂ molecules include temperature and pressure changes. Changing the temperature of a reservoir is difficult to realize, while increasing the pressure is possible, yet expensive, and might allow for a partial or even full miscibility of reservoir oil and CO₂. However, forcing the pressure above a certain threshold, the rock formation fractures, which should be avoided. Therefore, methods are required to increase the miscibility of reservoir oil and CO₂ without further increasing the pressure.

Importantly, the properties in a reservoir flowed with CO₂ or another injection fluid usually deviate considerably from the thermodynamic equilibrium. Often continuous phase separation and remixing processes occur inside the reservoirs. This type of behavior, in which the coexistence of oil- and injection fluid-rich phases of varying composition finally leads to

the miscibility of crude oil and injection fluid molecules, is named multiple-contact miscible (MCM) processes. To be more precise, in this complex process ideally, the compositions of the two phases, i.e. of the newly formed injection fluid and the crude oil phases become more and more similar approaching the critical point (cp) of their miscibility gap [Slobod, Koch, H.A., Jr., 1953, Hutchinson Jr., Braun, 1961, Stalkup, 1978]. The lowest pressure, at which miscibility is reached through this multi-contact process delivering high recovery rates at the reservoir temperature, is the so-called minimum miscibility pressure MMP [Elsharkawy, Poettmann, Christiansen, 1992].

Hence, in order to widen the application of CO₂-EOR, the MMP-determination of the respective reservoir as well as its significant lowering are crucially needed. In general, the complex processes in oil reservoirs are not easy to reproduce in laboratories. Some methods as the rising bubble method (where the point of disappearance of a gas bubble in oil is visually determined, while temperature or pressure are changed) [Christiansen, Haines, 1987], and the method of vanishing interfacial tension (where the shape of a gas bubble in oil is analyzed, while temperature or pressure are changed) [Rao, 1997] are limited to the determination of important physical and chemical properties for the process, such as phase behavior and interfacial tension between crude oil and the respective injection fluid. However, these methods do not consider factors, like diffusion, permeability, and porosity. Methods that are able to account for these complex processes and thus mimic the situation in the reservoir are core flood tests [Stalkup, 1983] and slim tube experiments [Yellig, Metcalfe, 1980]. The former uses a core sample (usually a few centimeters in size) from the reservoir, which accurately reflects the porous medium, but not the factors affecting the displacement behavior of the reservoir oil due to its significantly different diameter to length ratio. The slim tube experiment allows for the analysis of continuous phase separation and remixing processes occurring inside the reservoirs using long sand-packed tubes of small diameter and is considered as a very accurate way of measuring the MMP [Ekundayo, Ghedan, 2013].

Due to the enormous growth in computing power over the last decades, the complex fluid flows and phase equilibriums are increasingly being simulated by theoretical calculations also predicting the location of the MMP, although with lower accuracy compared to experimental determination [Teklu, et al., 2012, Johns, Dindoruk, Orr, F.M., Jr., 1993, Luks, Turek, Baker, 1987, Metcalfe, Fussell, Shelton, 1973, Monroe, et al., 1990, Orr, F.M., Jr., Johns, Dindoruk, 1993, Whitson, Michelsen, 1989, Zick, 1986]. After extensive studies both in

laboratories or on supercomputers, the designing and implementing of a field pilot test is required as final step [Al-Mjeni, et al., 2011].

Interestingly, some studies report that selected additives are capable of improving the miscibility of CO₂ and crude oils, and thus could considerably expand the range of CO₂-EOR applications [Djabbarah, N. F. U.S., 4899817, Feb 13, 1990, Fan, W.; Li, B.; Li, S.; Li, Z.; Lu, T.; Luo, H.; Nan, G.; Wang, F.; Zhang, C. CN, 104610953A, 2015, Moradi, et al., 2014, Hirasaki, Miller, Puerto, 2008]. As early as 1990, a patent reported that linear alcohols ranging from 1-methanol to 1-octanol and mixtures thereof exhibit a considerable miscibility-enhancing effect [Djabbarah, N. F. U.S., 4899817, Feb 13, 1990]. In 2014, Moradi et al. found that different linear and branched alcohols, including technical-grade, were able to reduce the interfacial tension between CO₂ and crude oil by 33% [Moradi, et al., 2014]. One year later, and thus in the year, in which the research project dealt with in this thesis was started, a patent application reported a significant reduction of the MMP using a mixture of alkoxyated additives and short-chain 1-alcohols [Fan, W.; Li, B.; Li, S.; Li, Z.; Lu, T.; Luo, H.; Nan, G.; Wang, F.; Zhang, C. CN, 104610953A, 2015]. However, besides these individual reports based mainly on interfacial tension (IFT) and phase diagram studies, there is a lack of systematic studies investigating the influence of additive type, structure and molecular mass on the miscibility-enhancing effect it produces.

1.1 Objectives

The aim of this work, which was part of a research project with Sasol Performance Chemicals GmbH, was to establish a structure-activity relationship to predict the influence of a wide variety of additives on the CO₂ – crude oil miscibility. As a starting point of this work, an experimental procedure should be developed that allows to fast and reliably investigate the influence of amphiphilic molecules on the miscibility of (model) crude oils and CO₂ in temperature and pressure ranges relevant for a variety of oil reservoirs, i.e. pressures between 0.5 MPa and 45.0 MPa and temperatures in a range of 5 °C to 80 °C.

As a prerequisite for the use of additives in the CO₂-EOR, an established measurement method should be used to investigate the miscibility of additives and CO₂. Then, model crude oils were to be designed to reflect the miscibility of a real crude oil with CO₂. To systematically investigate the miscibility-enhancing effect of various additives, the phase behavior of CO₂ – (model) crude oil systems should be characterized in detail. After this initial work, the

main objective of the thesis, namely the influence of an additive on different CO₂ – (model) crude oil systems should be studied for different classes of additives, i.e. linear, branched and alkoxyated additives with systematically varying chain lengths. If possible, the obtained results should be compared with the sparse data published mentioned above.

Besides miscibility, the swelling behavior of crude oils is an important property for oil recovery with CO₂. As soon as the injected CO₂ partially condenses in the oil phase, thereby reducing the viscosity of the oil, this enables better flow through the reservoir resulting in higher production rates. Therefore, the swelling behavior of two of the best miscibility-enhancing additives of this thesis should be studied in the CO₂ – real crude oil system.

Last but not least, the miscibility-enhancing effect of one of the most promising additives was to be investigated by means of slim tube studies. The motivation was twofold. First, the effect of one of the most powerful alkoxyated alcohols was to be studied under real oil field conditions as a proof of concept. The second aim was to demonstrate whether the MMP determined by slim tube studies was consistent with the critical (plait) point pressure p_c determined from static phase behavior measurements. To this end, research visits to set-up a slim tube apparatus at the Rice University (Houston, Texas, USA) in close collaboration with the group of Prof. Dr. George J. Hirasaki were envisaged.

2 Fundamentals

In this chapter, the basics of phase behavior and miscibility are explained. The basics of the miscible displacements including first-contact miscible, multiple-contact miscible, condensing-gas, vaporizing-gas, and CO₂-miscible processes are explained mainly based on the monograph published by Fred I. Stalkup [Stalkup, 1983]. The corresponding phase diagrams of CO₂ and/or hydrocarbon-containing systems are introduced using the parameters of interest, i.e. pressure, temperature, and composition. Additionally, the effects of additives in CO₂-EOR are presented using pseudotetrahedron phase diagrams. Finally, the methods for the determination of the miscibility conditions for EOR are briefly introduced.

2.1 Conventional Oil Recovery

From the beginning of oil production until the early 1930's, primary recovery methods were applied that use the natural energy of a reservoir for oil recovery. Due to the oil recovery, the initial pressure of the reservoir declines. In order to maintain a high pressure (which allows for recovery of more oil), fluids like water and/or natural gas were injected through one or more wells. At first, this method was consequently called "pressure maintenance". Later, it was recognized that the injected fluids, in addition to the maintenance of the reservoir pressure, also displace some original oil in place (OOIP). Since the injection of fluids follows the primary recovery process, this method was then renamed secondary recovery. However, injection fluids are immiscible with the reservoir oil and some reservoirs have rock pore formations with dead-end pores causing a high oil concentration. Therefore, these recovery methods with injection fluids are insufficient. In order to increase the overall recovery rates, further recovery methods were established, termed enhanced oil recovery (EOR) [Stalkup, 1983]. Thus, EOR processes target the remaining oil after the primary and secondary recovery. Still, only about one third of the existing oil in known reservoirs are considered to be economically recoverable with established technology [Shah, 1981, Li, et al., 2000]. Most EOR methods fall into one of the three general categories: gas flooding, chemical flooding and thermal techniques. Each of these have a variety of forms, which can also be combined [Lake, 1989]. The approach used in this thesis reflects a combination of gas and chemical flooding.

2.2 Immiscible and Miscible Displacement

Oil and water do not mix, they are immiscible. If these two fluids are filled into a vessel and allowed to reach equilibrium, two phases will be obtained, which are separated from each other by a sharp interface. The miscibility of oil and CO₂ is similar to that, depending on the pressure level. When two immiscible fluids or phases flow simultaneously through porous media, their behavior is determined by relative permeability characteristics of the porous media [Stalkup, 1983]. Thus, the overall displacement efficiency in oil recovery processes is the product of macroscopic and microscopic displacement efficiencies.

To reach high macroscopic efficiency, which is in the scale of the distances of the wells, viscous fingering has to be avoided. Viscous fingering occurs, if the displacing fluid, usually water, has a lower viscosity than the crude oil and forms fingers in the displacing front before reaching the production wells (instead of a linear or radially symmetric front). Further injection of the displacing fluid is then not able to increase the efficiency, because the fluid preferentially follows these paths in form of fingers. To avoid this viscous fingering, the viscosity of the injection fluid is increased for example by polymers or foams.

At microscopic scale, the oil can be trapped in pores, if the injection fluid flows around the oil. The reason for that is that viscous or gravitational driving forces are not high enough to overcome capillary forces [Lee, Kam, 2013]. The capillary force depends on several properties of the crude oil-brine-rock system. One property is the wettability, which is defined as the preference of a solid to be in contact with one fluid over another [Abdallah, et al., 2007]. Another property is the rock's capillary entry pressure, which has to be overcome to achieve oil migration in a small pore opening. The capillary entry pressure is the pressure difference between water and oil phases. Furthermore, the capillary pressure is influenced by the different pore sizes in the reservoir as well as different acceleration of gravity depending on the depth. These different capillary pressures influence the density of the water and oil phases resulting in different water saturations, which in turn have an impact on the wettability. As mentioned above, viscous or gravitational driving forces have to overcome the capillary force for efficient displacement. Two dimensionless numbers, the capillary number (N_c) and the bond number (N_b , or Eötvös number), are used to compare these forces. The capillary number N_c is defined as

$$N_c = \frac{v \cdot \mu}{\sigma_{OW} \cdot \cos \theta}, \quad (2.1)$$

wherein the velocity (v) and the dynamic viscosity (μ) are representing the viscous forces in the numerator, and the interfacial tension (IFT) between oil and water (σ_{OW}) and the contact angle (θ) are representing the capillary forces in the denominator [Moore, Slobod, 1955, Al-Mjeni, et al., 2011, Morrow, Songkran, 1981]. This dependency shows that a reduction of the IFT between oil and water is required to achieve a reduction in capillary forces and thus an improved oil displacement by immiscible floods [Taber, 1969, Stegemeier, 1977, Melrose, Brandner, 1974, Foster, 1973]. The interfacial tension can be lowered by three to four orders of magnitude by addition of surface-active chemicals (i.e. surfactants) [Chan, Shah, 1981, Lake, 1989, Li, et al., 2000, Kessel, 1989, Doe, Wade, Schechter, 1977, Wade, et al., 1978]. An alternative possibility is to increase the velocity of the injection fluid or to increase its viscosity by using appropriate polymers [Pye, 1964, Sandiford, 1964]. The other dimensionless number, the bond number N_b , compares the gravitational force and the capillary force and is defined as

$$N_b = \frac{\Delta \delta \cdot g \cdot L^2}{\sigma_{OW} \cdot \cos \theta}, \quad (2.2)$$

wherein the density difference of oil and water ($\Delta \delta$), the acceleration of gravity (g), and the characteristic length of oil drops (L) are representing the gravity forces in the numerator, while the capillary forces in the denominator are identical to N_c [Morrow, Songkran, 1981]. Accordingly, the production rate of oil can be improved by reducing the IFT between oil and water as described above. These numbers can also be used for other systems. For miscible displacement (most efficient displacement for components that mix with each other), no interfaces and consequently no IFT are obtained resulting in a capillary number or bond number, which become infinite. Thus, the remaining residual oil in the pores reduces to its lowest possible value [Stalkup, 1983].

2.3 Principles of Phase Behavior and Miscibility

Phase diagrams are the essential basis of every physical-chemical examination of mixing procedures. Reservoir fluids are multicomponent mixtures, which makes an exact knowledge

of the composition difficult. Even if the exact composition is known, a detailed description of its phase behavior would be complex. Therefore, an approximate method to represent the phase behavior of multicomponent mixtures utilizes triangular diagrams by grouping similar components into one pseudocomponent. In this thesis, the systems investigated contain a multicomponent mixture (the (model) crude oil), which is also represented as a pseudocomponent in the triangular diagrams of interest. Of course, a system of three pure components can be displayed more exactly with a triangular diagram. In Figure 2.1, the phase behavior of the methane – *n*-butane – decane system is shown for constant temperature and pressure of 71.1 °C and 17.2 MPa, respectively [Sage, Lacey, 1955, Hutchinson Jr., Braun, 1961]. Each apex of the triangular diagram represents 100% of a given component, while the facing side represents 0% of the same component. The system in this triangular diagram represents a two-phase mixture (2), i.e. has a miscibility gap (Figure 2.1 left). This means that mixing the three components with different relative compositions lying in the miscibility gap, e.g. represented by point S, and allowing to equilibrate, always results in two phases: a methane-rich phase (gas) equilibrium composition, represented by point Y, and a decane-rich phase (liquid) equilibrium composition, represented by point X. The equilibrated gas-rich and liquid-rich phases are connected by tie lines. The phase boundary at the gas-rich side, where the gas is saturated with condensable components, is defined as dew-point behavior. The phase boundary on the liquid-rich side, where the liquid is saturated with vaporizable components, is defined as bubble-point behavior. The dew- and bubble-point have their names due to the condensation of components from the gas-rich phase and the vaporization of components from the liquid-rich phase at these points, respectively. The point, where the dew-point curve joins the bubble-point curve (at the critical composition), is defined as plait point. At this critical point, the composition and properties of the equilibrated gas-rich and liquid-rich phases become equal. Outside of the phase boundary line or miscibility gap, any system of these components will form a single phase (1) at this temperature and pressure. Above the dew-point curve, a single phase gas region is obtained, while below the bubble-point curve, a single phase liquid region is obtained [Stalkup, 1983].

The size of the miscibility gap is influenced by pressure and temperature. By increasing the pressure from 17.2 MPa to 22.1 MPa at constant temperature, the miscibility gap of the methane – *n*-butane – decane system decreases as shown in Figure 2.1 right [Sage, Lacey, 1955, Hutchinson Jr., Braun, 1961].

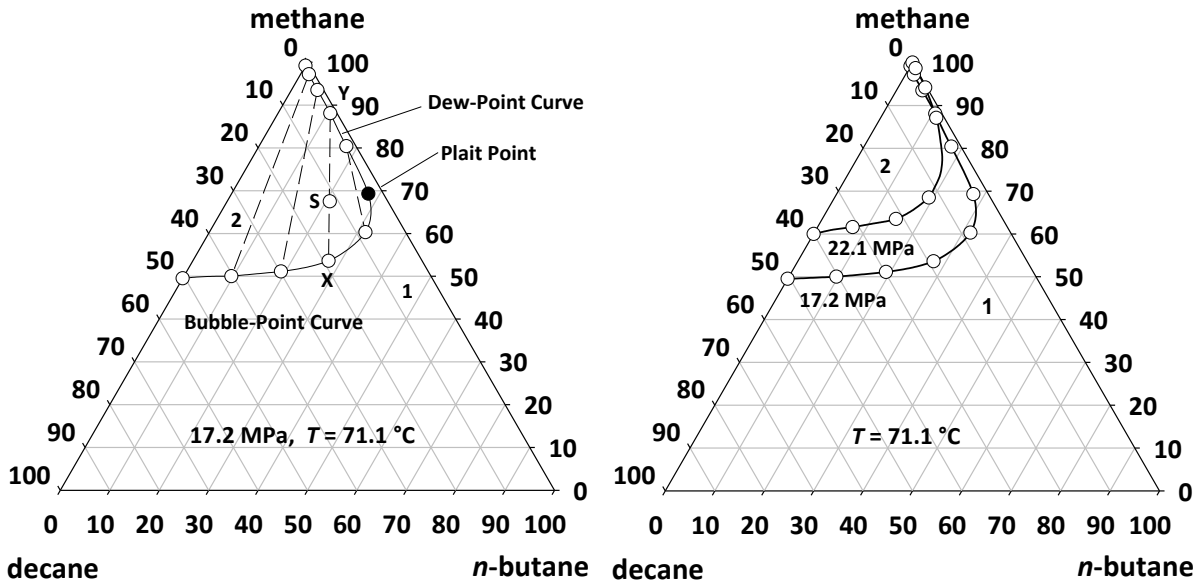


Figure 2.1: Triangular phase diagrams for the system methane – *n*-butane – decane at constant temperature and two different pressures. Source of data: [Sage, Lacey, 1955]. Redrawn from: [Hutchinson Jr., Braun, 1961].

Furthermore, by decreasing the pressure, the plait point might disappear, indicating that for lower pressures, no single phase can be obtained. Additionally, an increase in temperature increases the size of the two-phase region [Stalkup, 1983]. The pressure and temperature dependency of the solubility of a substance can be explained by the Hildebrand solubility parameter δ , which provides a quantifiable estimate of the degree of interaction between materials. The Hildebrand solubility parameter δ is defined as

$$\delta = \sqrt{\frac{\Delta H_v - RT}{V_m}}, \quad (2.3)$$

wherein ΔH_v is the enthalpy of vaporization, R the gas constant, T the temperature and V_m the molar volume. By increasing the pressure, the molar volume decreases (generally) and therewith the denominator resulting in an increased solubility and miscibility. In contrast, by increasing the temperature, the nominator decreases resulting in a decreased solubility and miscibility [Peach, Eastoe, 2014].

Furthermore, besides the coexistence of gas and liquid phases, other phase behavior has been reported, such as precipitation of solid asphaltic material [Shelton, Yarborough, 1977, Wilson, 1960], coexistence of two liquid phases [Shelton, Yarborough, 1977, Huang, Tracht, 1974, Rathmell, Stalkup, Hassinger, 1971, Gardner, Orr, Patel, 1981], coexistence of two liquid phases in addition to a gas phase [Shelton, Yarborough, 1977, Huang, Tracht, 1974, Gardner, Orr, Patel, 1981, Stalkup, 1978], and a rather complex behavior of two liquid phases,

a gas phase, and a solid phase [Shelton, Yarborough, 1977, Huang, Tracht, 1974, Stalkup, 1978], [Stalkup, 1983].

In addition to triangular diagrams, alternative methods to display phase behavior are pressure/composition- or pressure/temperature-phase diagrams ($p(x)$ - or $p(T)$ -phase diagrams). These phase behavior diagrams will be used preferentially in this thesis. In Figure 2.2, two isothermal $p(x)$ -phase diagrams for the binary $\text{CO}_2 - n$ -hexadecane system are shown schematically [Liphard, Schneider, 1975, Rathke, 2002]. The different phase behaviors at a temperature below the critical end point (CEP) of CO_2 (Figure 2.2 (a)) and a temperature above the CEP (Figure 2.2 (b)) are represented. At temperatures higher than the CEP, a liquid-gas (lg) coexistence region is found in the miscibility gap with an upper critical point. At temperatures below the CEP, two coexisting phases are obtained in the miscibility gap above the triplet line (dashed line in Figure 2.2 (a)), a liquid-liquid (l_1l_2) phase and a liquid-gas (l_2g) phase. Both miscibility gaps have an upper critical point (p_c), which is marked in the $p(x)$ -phase diagrams [Kiran, Debenedetti, Peters, 2000, Schneider, et al., 1967, Schneider, 1966].

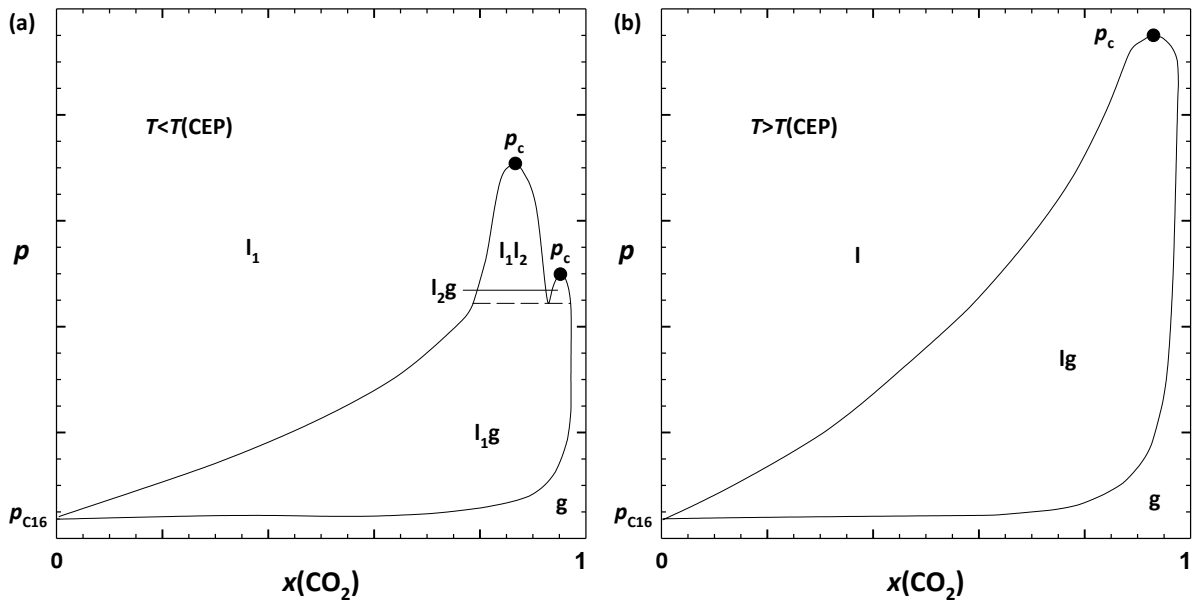


Figure 2.2: Schematical, isothermal $p(x)$ -phase diagrams of the $\text{CO}_2 - n$ -hexadecane system for different temperatures showing different coexisting phases in the miscibility gaps in (a) or a simple liquid-gas (lg) coexisting phase in (b). Diagrams based on [Liphard, Schneider, 1975, Rathke, 2002].

In Figure 2.3 left, a schematical $p(T)$ -phase diagram of a pseudo-two-component system is shown (redrawn from Lake [Lake, 1989]). The pseudo-two-component system in the $p(T)$ -phase diagram consists of a pure component A (for example CO_2) and a crude oil (M4), and is shown at three different mixtures with constant compositions (M1 to M3). The amount

of the crude oil increases from M1 to M4 with M4 being crude oil only. Of course, there are infinite mixtures of these two components A and crude oil, but for explanation just three mixtures are presented. For pure components, the bubble-point and dew-point curves coincide, which is represented by the line ending at a critical point at cp_A . For the crude oil and the three mixtures, the bubble-point and dew-point curves are shown, intersecting at their respective critical points (cp_{oil} , cp_{M1} , cp_{M2} , cp_{M3}). The dashed line connects all the critical points with each other. Beneath this dashed curve, two phases coexist for the component A, crude oil, and all possible mixtures, whereas for the components A and the crude oil, a single phase is obtained above this curve. This phase behavior is typical for CO_2 – crude oil mixtures. The highest pressure inside a miscibility gap is found at P6 for the mixture M1, which contains a high amount of A compared to the other mixtures. This maximal pressure is defined as cricondenbar. Another unique point is the cricondentherm, which represents the highest temperature inside the miscibility gap. For the presented system, the cricondentherm is found at cp_{oil} . The knowledge of these unique points (critical points, cricondenbar, and cricondentherm), representing the critical parameters in $p(T)$ -diagrams, are central to achieve efficient displacements in recovery field operations [Etter, Kay, 1961]. If these central unique parameters of the corresponding systems are known, an efficient miscible displacement can be reached by avoiding the miscibility gap or adjusting the miscibility gap by using appropriate additives (see chapter 2.6). However, to transfer the data from the $p(T)$ -diagram (Figure 2.3 left) into a $p(x)$ -diagram (Figure 2.3 right), a constant temperature must be chosen (dashed line from P1 above P6). Starting in the $p(T)$ -diagram at the selected temperature at high pressure in the single phase and decreasing the pressure to P6, a dew-point behavior for the mixture M1 occurs. Further decrease of the pressure leads to an additional dew-point behavior for M1 at P5, which furthermore corresponds to the critical point of the mixture M2. Continuing decreasing the pressure to P4, a dew-point behavior for M2 and a bubble-point behavior for M3 can be seen. At P3, a dew-point behavior is found for M3. At P2, a bubble-point behavior for the crude oil is obtained and at P1 a dew-point behavior occurs. Transferring these data (at the selected constant temperature) to a $p(x)$ -diagram, a miscibility gap as shown in Figure 2.3 right is obtained. The pressures of the dew-point behavior of the mixtures M4, M3, M2, and M1 are connected and represent the dew-point curve, while the connected bubble-point pressures of the mixtures M4 and M3 represent the bubble-point curve. The dew-point curve joins the bubble-point curve at the critical point P5 (at M2). The

green lines in the miscibility gap show the volumes of the liquid phases relative to the gaseous phases.

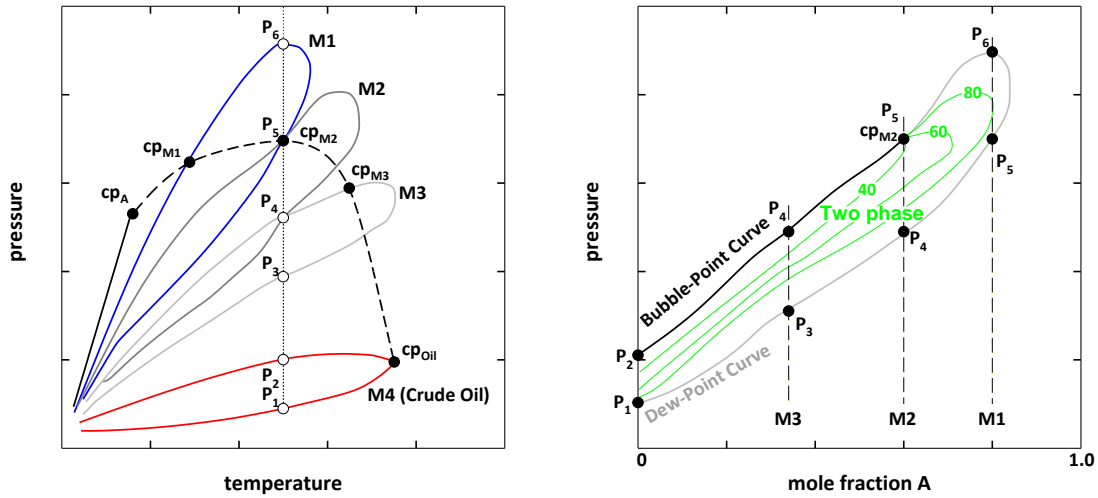


Figure 2.3: Schematical $p(T)$ - and $p(x)$ -phase diagrams consisting of a pure component A, crude oil (M4) and mixtures of both (M1, M2, and M3). All unique important points are highlighted (critical points cp_A , cp_{M1} , cp_{M2} , cp_{M3} , and cp_{Oil} ; cricondenbar represented by P_6 and cricondentherm represented by cp_{Oil}). Adopted from Lake [Lake, 1989].

2.4 The Miscible Processes

The simplest and most effective method of oil recovery (miscible displacement) is achieved by complete miscibility of the injecting fluid with the oil as mentioned already above. A first-contact miscible (FCM) process, where a complete miscibility of the injected fluid with the oil is achieved, is shown schematically in Figure 2.4 along the path of injection fluid A to the oil composition at constant pressure and temperature [Stalkup, 1983].

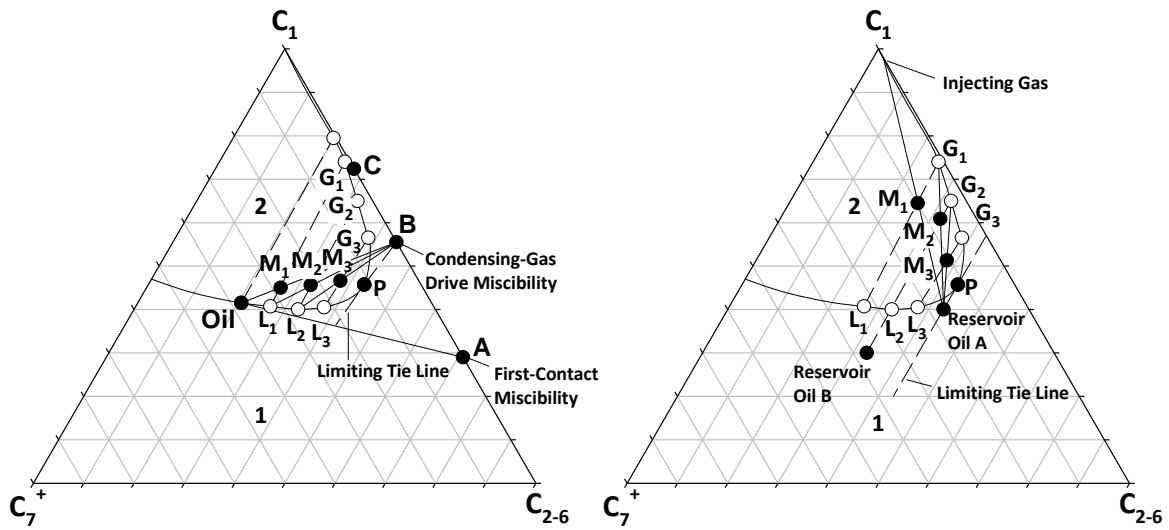


Figure 2.4: The first-contact miscibility and the condensing-gas drive miscibility (left) as well as the vaporizing-gas drive process (right) are shown schematically in pseudotriangular diagrams. Redrawn from Stalkup [Stalkup, 1983].

Here, the top apex represents methane, while the right apex represents the light molecular weight hydrocarbons from C_2 to C_6 and the left apex represents the hydrocarbon components equal to or heavier than C_7 . All mixtures on the injection path from the injection fluid A to the oil lie entirely within a single phase, i.e. first-contact miscibility conditions are sufficiently fulfilled under this pressure and temperature. However, oil fields that have already been produced by other methods usually contain more heavier components, because the light components were already recovered. When using an FCM method in such a reservoir with light injection fluids, such as ethane, propane or butane, the heavy components in the oil precipitate, i.e. do not become miscible with the injection fluids. In other words, the injection fluid starts close to or in a miscibility gap at the beginning of the injection, like the injection path from fluid B to the oil in Figure 2.4. Thus, first-contact miscible displacement cannot occur, because some compositions fall within the miscibility gap. Nevertheless, miscible displacement by injection fluids, even if they are not first-contact miscible, is possible via a dynamic miscibility by in-situ mass transfer of light-weight hydrocarbons. In Figure 2.4 left, this not first-contact miscible process is illustrated by following the injection path of the injection fluid B. The first contact of B with the oil is represented by the mixture M_1 and the corresponding tie line will separate into two phases. At the ends of this tie line, two phases occur, a B-rich (G_1) and an oil-rich phase (L_1), which are in equilibrium. Further injection of B will push the mixture into the direction of a new mixture represented by M_2 , which separates

again in two phases in equilibrium (G_2 and L_2). By continued injection of B, mixtures and phases in equilibrium are passed (G_3 and L_3), thereby gradually approaching the plait point resulting in a homogeneous phase. This multiple-contact mechanism enriches the reservoir oil with light hydrocarbons of B until it becomes miscible with B. Additionally, injection fluid mixtures between A and B can be used. This in-situ generation of miscibility is called the condensing-gas drive process or enriched-gas drive process or more commonly multiple-contact miscibility (MCM) process. In contrast to that, if a very light injection fluid is used, with a composition closer to the upper apex (C), the injection path will lie on the left of the extended tie line of the plait point. This means, the oil cannot be enriched with the light injected fluid to reach miscible conditions at the plait point, i.e. this process is immiscible. [Helfferich, 1981, Metcalfe, Fussell, Shelton, 1973, Stalkup, 1983]

Another mechanism for achieving dynamic miscible displacement is the in-situ vaporization of intermediate-molecular-weight hydrocarbons from the reservoir oil into the injected gas. This process has been called the high-pressure gas process or vaporizing-gas process. To achieve miscibility by this process, the physically attainable pressure in the reservoir has to be high. In this process, injected gases like natural gas, flue gas or nitrogen, predominantly extract the C_2 to C_5 hydrocarbons, while CO_2 can extract higher-molecular-weight hydrocarbons, which makes it more applicable for EOR [Crawford, et al., 1978, Koch, H.A., Jr., Hutchinson, C.A., Jr., 1958]. In Figure 2.4 right, the process of vaporizing-gas drive is shown schematically. Usually, the injection gas or fluid is shown on the upper corner of the pseudotriangular phase diagram. In Figure 2.4 right, it is methane. Following the path of the injection gas (methane) to the reservoir oil A, the mixture M_1 in the miscibility gap is obtained, which equilibrates into two phases at the end of the tie line, a gas-rich phase G_1 containing vaporized oil components and an oil-rich phase L_1 . Continuing to inject the gas into G_1 forms a new mixture M_2 , which also equilibrates into two phases G_2 and L_2 . Continuing these multiple-contact miscibility processes, the displacing front of the gas reaches gradually the composition of the plait point and thus miscibility with the reservoir oil A is reached. As long as the reservoir oil composition lies on or right of the extended tie line, miscibility by vaporizing-gas process is possible. If the composition of the reservoir oil lies left to the extended tie line, like reservoir oil B, miscibility cannot be reached [Stalkup, 1983]. The vaporizing-gas process with CO_2 will be explained in more detail below, since this process was studied in this thesis.

2.5 The CO₂ Miscible Process

There is interest in the CO₂ miscible process because of several advantages [Stalkup, 1983, Lake, 1989, Lee, Kam, 2013, Holm, Josendal, 1974, Yellig, Metcalfe, 1980]. The CO₂ density is similar to oils in many reservoirs, which minimizes CO₂ – oil segregation, but there is enough density difference to brine for gravity segregation. CO₂ as injection fluid has a low viscosity, which makes the injection more challenging. Since a dynamic miscibility can however be achieved in many reservoirs, a relatively low operating pressure is required. In addition, the cost and supply of CO₂ for EOR projects may be more favorable than for other hydrocarbon-miscible solvents. This is because of the availability of large quantities of CO₂ from natural deposits as well as from manufacturing and power-generating plants as by-products, which can be transported to the oil fields at acceptable costs [Stalkup, 1983].

Dynamic miscibility behavior has been shown for CO₂ as injection fluid above MMP conditions by displacement tests in long cores and slim tubes [Shelton, Yarborough, 1977, Rathmell, Stalkup, Hassinger, 1971, Holm, Josendal, 1974, Metcalfe, Yarborough, 1979, Holm, Josendal, 1982, Yellig, Metcalfe, 1980]. Additionally, extracted hydrocarbons from C₅ to C₃₀ in the CO₂-rich phase were reported by several investigators from displacement and static equilibrium cell experiments with reservoir oils [Gardner, Orr, Patel, 1981, Orr, F.M., Jr., Yu, Lien, 1981, Holm, Josendal, 1974, Holm, Josendal, 1982]. These extracted hydrocarbons may cause dynamic miscible behavior, as mentioned above.

The CO₂ miscible process and its concepts shown here are based on the behavior of CO₂ and hydrocarbons in well-characterized pseudobinary as well as pseudoternary systems [Gardner, Orr, Patel, 1981, Simon, Rosman, Zana, 1978, Graue, Zana, 1981, Holm, Josendal, 1982, Perry, 1982, Reamer, Sage, 1963, Schneider, et al., 1967, Kukarni, et al., 1974, Liphard, Schneider, 1975, Huie, Luks, Kohn, 1973, Yang, Luks, Kohn, 1976, Francis, 1954]. Metcalfe and Yarborough classified the CO₂ – reservoir oil phase behavior into two types according to the characteristics of the $p(x)$ -diagrams of different CO₂ – synthetic oil systems [Metcalfe, Yarborough, 1979]. Of note, these are hypothetical examples, which are oversimplified. For Type I, only vapor and liquid phases coexist. According to Metcalfe and Yarborough as well as Orr et al. [Orr, F.M., Jr., Yu, Lien, 1981], these conditions are mainly achieved for temperatures higher than approx. 39 °C. Type II behavior is defined by coexisting phases in the multiphase region relatively close to the critical temperature of CO₂. Possible are coexisting liquid-liquid phases, equilibrated liquid and gas phases and three phase regions coexisting of two liquids

and a gas. Moreover, for some oils, asphaltenes may precipitate [Shelton, Yarborough, 1977, Stalkup, 1978, Henry, Metcalfe, 1983, Mungan, 1981].

The temperature dependency of the transition from Type I to Type II phase behavior probably depends on the average molecular weight of the oil [Orr, F.M., Jr., Yu, Lien, 1981]. The maximum temperature for Type II behavior increases with the average molecular weight of the oil. In other words the lighter the oil, the lower the temperature of the MMP [Sebastian, Lawrence, 1992].

In Figure 2.5, a pressure composition diagram and three pseudotriangular diagrams are shown schematically for a hypothetical CO₂/reservoir oil system at constant temperature [Stalkup, 1983]. The temperature was selected high enough to achieve Type I behavior. The apexes in the pseudotriangular diagrams represent CO₂ (upper), and the pseudocomponents heavy hydrocarbons (left) and extractable hydrocarbons (right). The bubble-point curve and the dew-point curve intersect at the plait point. Additionally, the volume percent of the liquid phases are indicated as dashed lines. Their retrograde behaviors at dew-point behavior have been reported by several investigators [Simon, Rosman, Zana, 1978, Graue, Zana, 1981, Perry, 1982]. A retrograde vaporization, for example, is defined, where a gas phase disappears for increasing temperature, which is a behavior contrary to intuition [Lake, 1989].

In the triangular diagram with $p=A$ (Figure 2.5), the pressure is too low to achieve dynamic miscibility behavior. The reservoir fluid lies on the left of the extended tie line. At higher pressures, smaller miscibility gaps are obtained, which are obvious from the $p(x)$ -diagram as well as the triangular diagrams. By increasing the pressure ($p \geq B$), a corresponding decrease of the miscibility gap is seen and the composition of the reservoir fluid lies for both pressures B and C on the right of the extended tie line. Thus, dynamic miscibility behavior is possible for both pressures. The difference between both pressures is the bubble-point behavior at pressure B and the dew-point behavior at pressure C. Furthermore, suggested by this Type I phase behavior, the MMP might be in the range (at least not higher) of the pressure, at which the plait point occurs in the $p(x)$ -diagram [Stalkup, 1983].

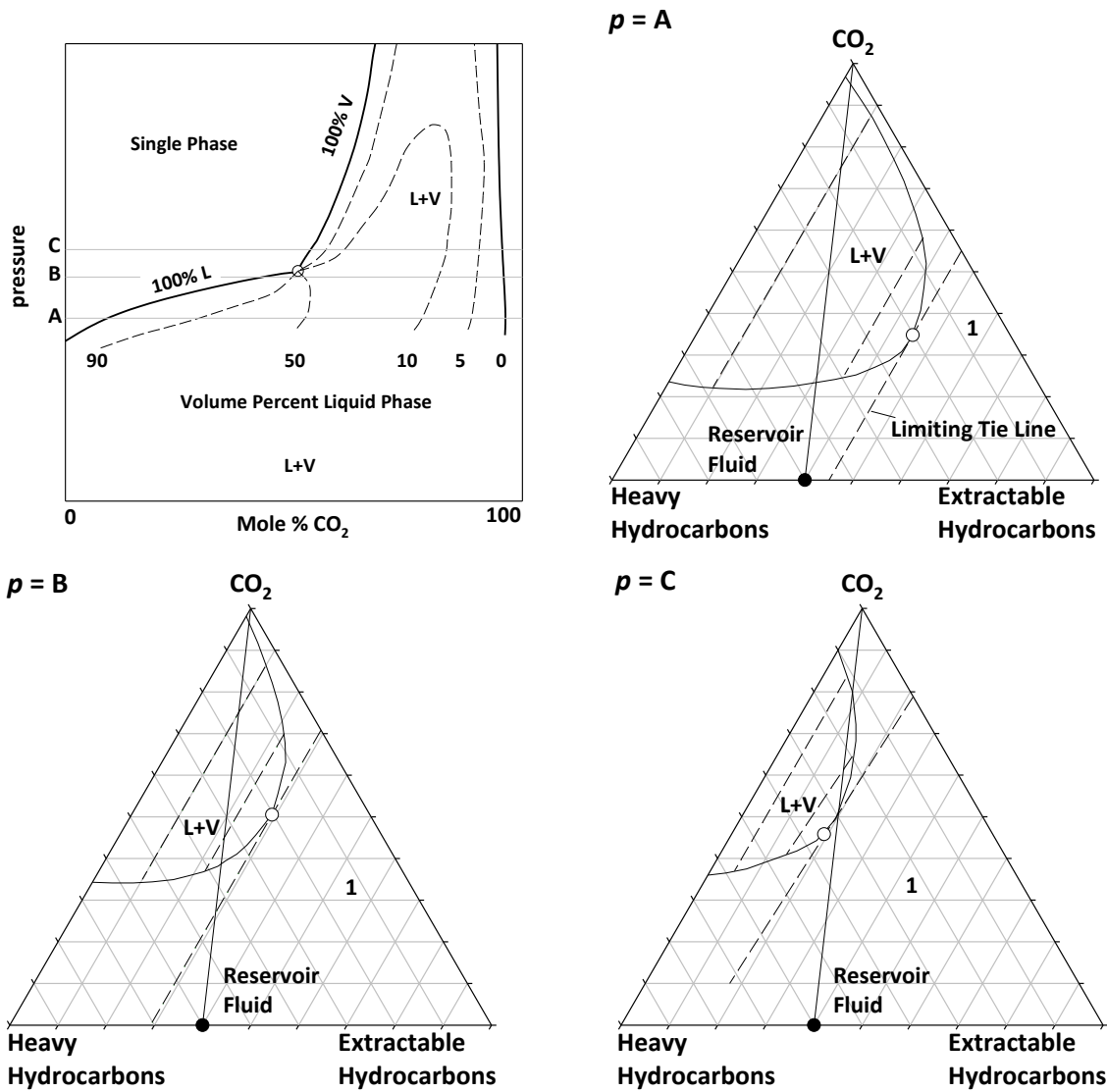


Figure 2.5: $p(x)$ -diagram and triangular diagrams are schematically shown for Type I phase behavior at constant temperature and different pressures. Redrawn from [Stalkup, 1983].

A Type II phase behavior is shown in Figure 2.6, again with a $p(x)$ -diagram and the corresponding pseudoternary plots. As mentioned before, for Type II phase behavior, several phases can coexist comprising an oil-rich phase, denoted as lower liquid (LL), because in a static view cell, it is in general the denser phase and hence the lower liquid. Additionally, a CO_2 -rich phase can coexist, denoted as upper liquid (UL), accordingly for the less dense upper phase. Furthermore, an additional two-phase region with an LL coexisting with a vapor phase (V), as well as a region, where three phases LL+UL+V can coexist, are shown. To cover several behaviors of CO_2 miscible processes, three different Type II behaviors are classified and named Type IIa, Type IIb, and Type IIc [Stalkup, 1983].

The Type IIa behavior consists of a three-phase region at lower pressures. For the exemplary system shown in Figure 2.6, the pressure of the miscibility gap decreases for

increasing CO₂ concentration. At pressure A, by increasing the amount of CO₂, a single-phase region is passed, followed by a two-phase region (LL+V) through the bubble-point curve, see the $p(x)$ -diagram as well as the triangular diagram ($p=A$). Further increase of the pressure ($p=B$) shows a similar behavior, while this time additionally, a three-phase region is passed by increasing the concentration of CO₂ before the mixture passes an additional two-phase region (LL+UL). In the three-phase region (LL+UL+V), the phase compositions are defined by the three-phase triangle. At pressure C, a similar behavior to pressure B can be seen, except for smaller two-phase regions and a smaller three-phase region, which is shifted to lower CO₂ concentrations. At pressure D, with increasing CO₂ concentration, the corresponding mixtures pass from a single phase through the plait point into a two-phase region (LL+UL). Above pressure D, at pressure E, by passing first the single-phase region, the retrograde two-phase region (LL+UL) is entered with increasing CO₂ concentration. Thus, here the volume of the LL increases first, before it decreases as the CO₂ concentration increases. This retrograde behavior is defined as swelling behavior (see chapter 4.6). Increasing the pressure from A to E leads first to an increase of the three-phase region, before it vanishes completely together with the vapor phase. The complex three-phase region can disappear before reaching the bubble-point curve as shown in this $p(x)$ -diagram in Figure 2.6, or alternatively terminate at the bubble-point curve, which probably depends on the oil composition [Orr, Heller, Taber, 1982]. If a three-phase region exists, dynamic miscibility can occur [Yellig, Metcalfe, 1980, Gardner, Orr, Patel, 1981, Stalkup, 1978, Henry, Metcalfe, 1983]. As already mentioned, to achieve dynamic miscibility here, the extended tie line of the LL+V phase (P) must lie left of the reservoir oil. This can be achieved by sufficiently high pressures. In Figure 2.6, this was achieved by pressures higher than B. Additionally, the extended tie line of the UL+V phase region have to pass to the left of the CO₂ apex of the pseudoternary plot for in-situ mass transfer. This Type IIa behavior shows that displacement miscibility will be primarily achieved by vaporizing gas mechanism, as mentioned above. But if the extractable hydrocarbons are vaporized into a vapor phase (LL+V) and extracted into the CO₂-rich liquid phase (LL+UL), a condensing gas mechanism will be present [Stalkup, 1983].

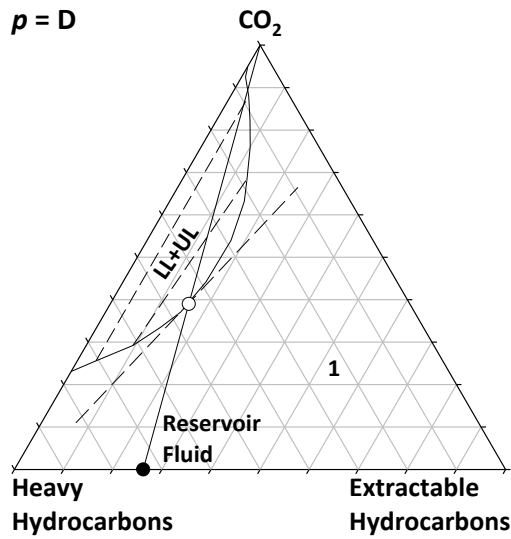
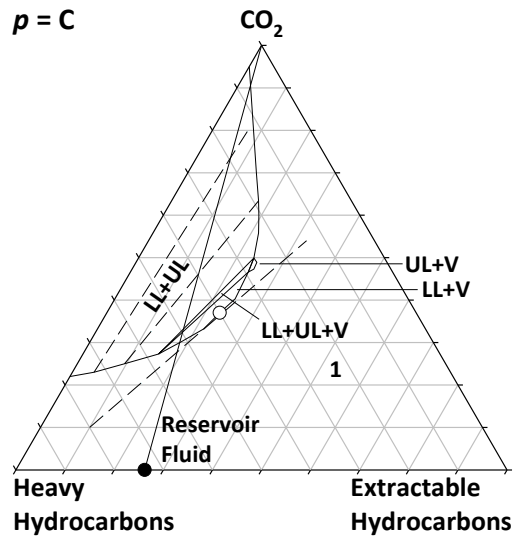
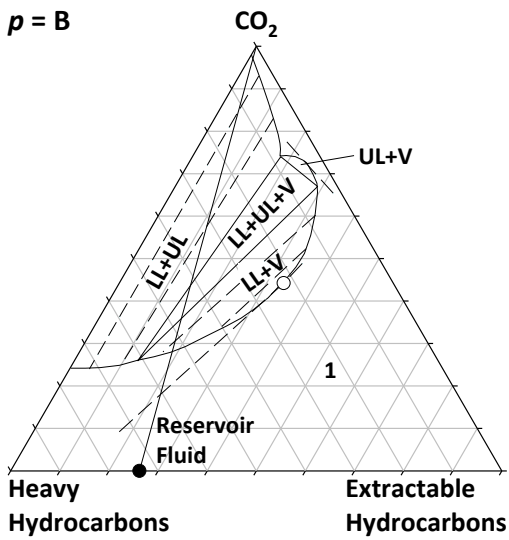
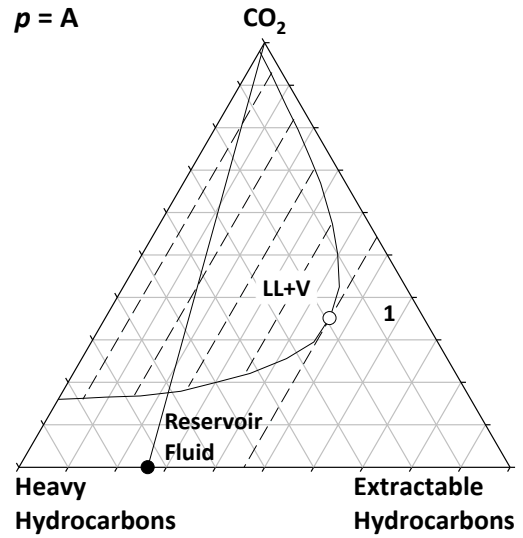
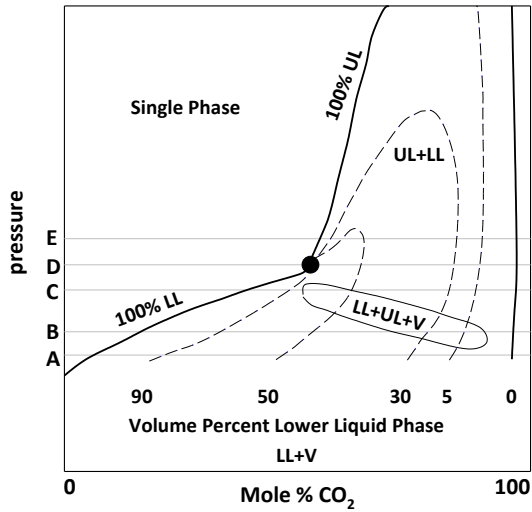


Figure 2.6: Schematic $p(x)$ -diagram and triangular diagrams for Type IIa phase behavior at constant temperature and different pressures. Redrawn from [Stalkup, 1983].

Type IIb phase behavior is shown in Figure 2.7. Again, a $p(x)$ -diagram and several pseudotriangular diagrams at constant temperature and different pressures are shown. The different characteristics for this type are a three-phase region, which is found heading to higher pressure as the CO₂ concentration increases in the $p(x)$ -diagram. Additionally, at least for pressures of interest (i.e. pressures below the formation fracture pressure), no retrograde behavior of the liquid/liquid phase is found and the critical point is shifted to high pressures (which is not shown in the $p(x)$ -diagram in Figure 2.7). Orr et al. speculated that this type of behavior is found for oils consisting of heavy hydrocarbons, which is usually the case after the first floods [Orr, F.M., Jr., Yu, Lien, 1981]. By increasing the pressure, in addition to a LL+V phase, a three-phase region in the vicinity of a critical point occurs, while the critical point moves away from the extractable hydrocarbons. An LL+UL region occurs at increased pressure ($p=B$) and grows further for further increased pressure ($p=C$), while the LL+V phase shrinks. At sufficiently high pressures ($p=E$), the V phase and two- and three-phase regions comprising the V phase disappear and just the LL+UL phase remains. To achieve dynamic miscibility, the same conditions as for Type IIa phase behavior apply, which are determined by the extended tie lines and the corresponding oil composition.

Finally, Type IIc phase behavior also has different characteristics, but it is more a combination of the other two types (therefore no extra Figure will be shown). In the $p(x)$ -diagram, no retrograde behavior is observed like in Type IIb, but the three-phase region is heading down to the right corner like in Type IIa, at least for pressures of interest. Again, for dynamic miscibility, the same conditions apply as mentioned before, the limiting tie line of the LL+V region has to lie on the left of the reservoir oil and if the UL+V region exists, its tie line has to pass to the left of the CO₂ apex in the triangular diagram, similar to Figure 2.6 ($p=B$). If these conditions are not given, the pressure must be sufficiently high for the limiting tie line of the LL+UL region to pass to the left of the reservoir oil, similar to Figure 2.7 ($p=E$). [Stalkup, 1983]

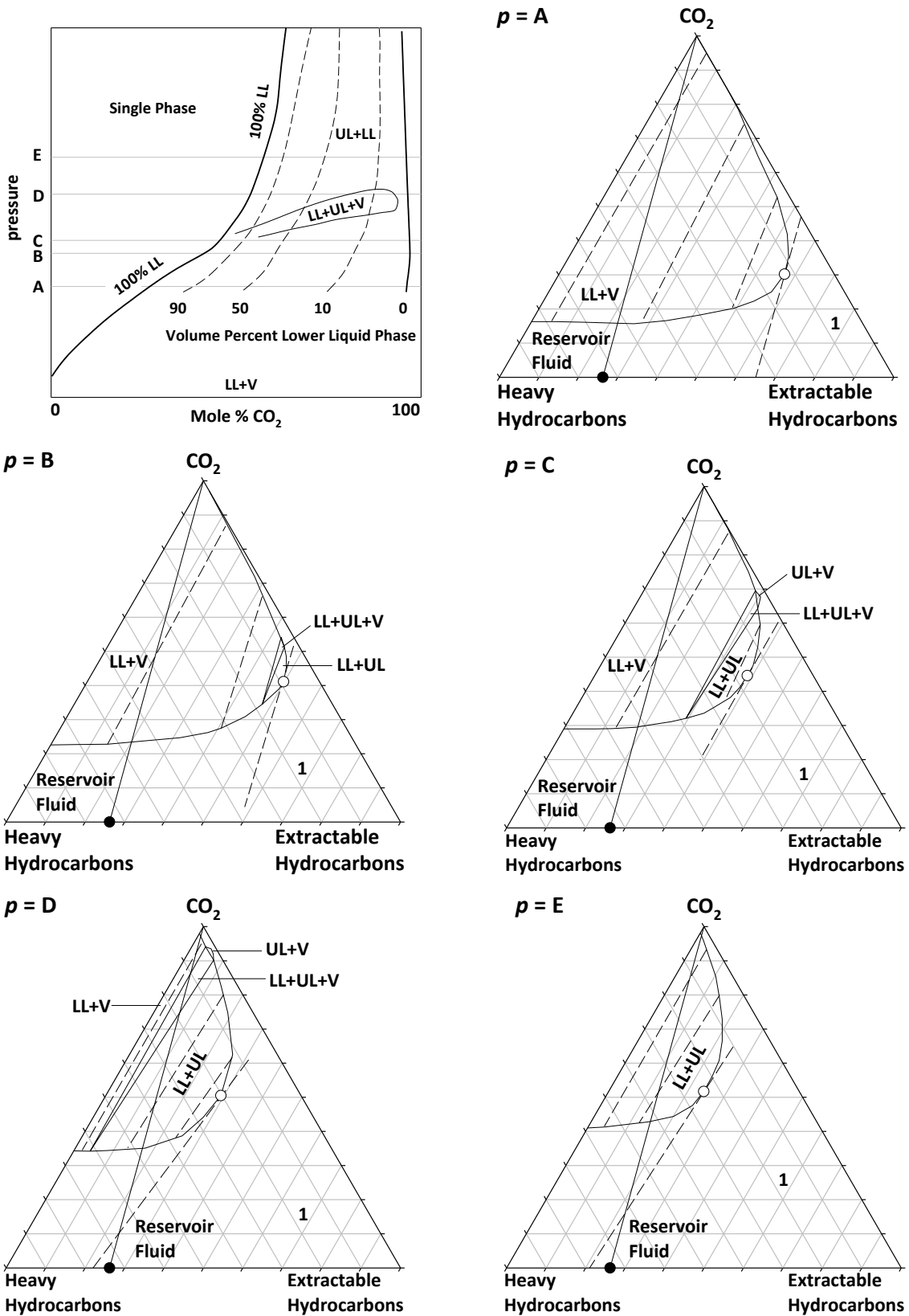


Figure 2.7: $p(x)$ -diagram and triangular diagrams are schematically shown for Type IIb phase behavior at constant temperature and different pressures. Redrawn from [Stalcup, 1983].

2.6 CO₂-EOR with Additives

The idea to reduce the interfacial tension (IFT) between water and oil by using surfactants is known almost since one century [Uren, Fahmy, 1927]. However, not only surfactants influence the IFT between injection fluid and oil, but also the injection fluid itself. Thus, a lot of activity in this area of research was done seeking solvents for miscible floods, which do not promote viscous fingering or gravity override [Gogarty, 1977, Holm, 1977]. The success of miscible flood depends on maintaining an ultralow IFT [Hirasaki, 1981]. Recent advances have been achieved especially by surfactants, which are reviewed by Hirasaki, Miller and Puerto [Hirasaki, Miller, Puerto, 2008].

The injection fluid CO₂ is, as mentioned before, an appropriate solvent to extract reservoir oil. To be able to further extract oil from already exploited reservoirs, which are no longer accessible for CO₂-EOR (usually because of remaining heavy components in the reservoir), the CO₂/oil miscibility gap has to be reduced. This can be done by increasing the reservoir pressure [Lake, 1989, Stalkup, 1983] or by reducing the IFT with miscibility-enhancing reagents, additives or surfactants. Initially, the use of surfactant to improve CO₂-EOR was patented by Bernard, Holm and Crystal in 1964 [Bernard, G. G.; Holm, L. W.; Lake, C. U.S., 3,342,256, Apr 17, 1964]. Furthermore, Wellington and Vinegar suggested, based on Computerized Tomography studies on first-contact miscible corefloods, that surfactants can provide effective mobility control for CO₂ [Wellington, Vinegar, 1985]. Mobility-controlled CO₂ floods can reduce the formation of viscous fingering as well as retard the early breakthrough of CO₂ [Heller, 1984]. Various types of alcohols have been investigated and several of them have been found to improve CO₂-EOR [Moradi, et al., 2014]. To my knowledge, however, no systematic analysis of the effect of different additives on the CO₂ – oil miscibility has been performed. The lack of such systematic analysis might be explained by the time- and cost-intensive measurements required for these studies.

Some of the data generated during this thesis have already been published [Rommerskirchen, et al., 2016a, Rommerskirchen, et al., 2016b, Rommerskirchen, et al., 2018]. The influence of additives on the CO₂-EOR flood process investigated in this thesis is shown schematically as pseudotetrahedrons in Figure 2.8 [Rommerskirchen, et al., 2018]. Three pseudotetrahedrons with increasing concentration of additive from left to right are presented for the same pressure and temperature. The upper apex indicates 100% additive, the rear right 100% CO₂, the front left 100% of the pseudocomponents with hydrocarbons

larger than C_7 and the front apex 100% of the pseudocomponents between C_1 to C_6 . The left tetrahedron shows that the oil composition with heavier hydrocarbons is on the left side of the extended tie line from the critical point, so that no dynamic miscibility is possible, as mentioned already above. By adding a small amount of additive to the CO_2 (middle tetrahedron), the miscibility gap is reduced despite the fact that the pressure and temperature remain the same. Furthermore, because of the smaller miscibility gap, the critical point shifted to a lower CO_2 concentration and consequently the extended tie line changed. Thus, the composition of the oil lies on the right side of the extended tie line, thereby enabling MCM processes through the dew-point behavior curve. By further increasing the additive concentration (right tetrahedron), the miscibility gap can be further reduced. Additionally, at this concentration of additive, the injection path changed from dew-point behavior in the middle tetrahedron, to a favorable FCM process in the right tetrahedron, which is the most effective method of oil recovery.

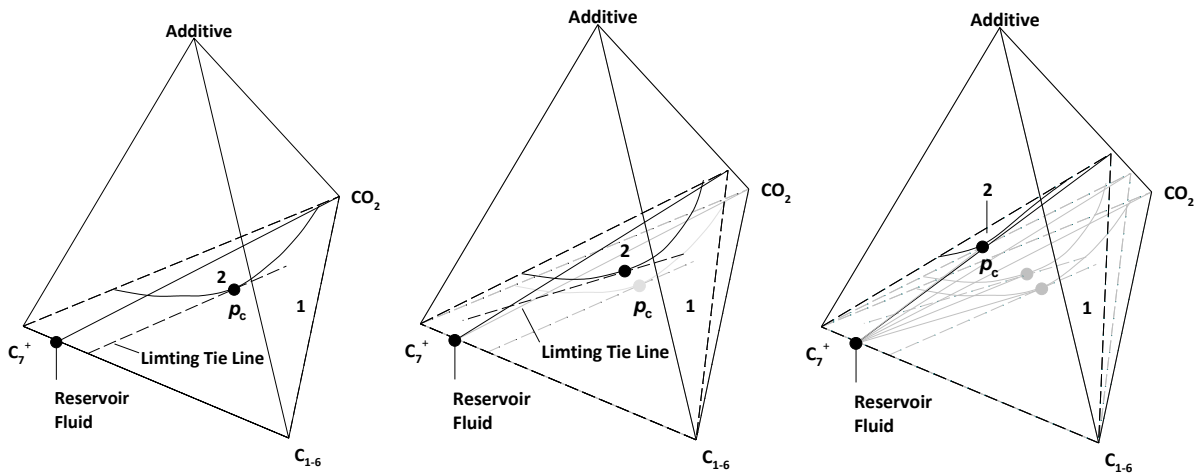


Figure 2.8: Pseudotetrahedrons showing immiscible, multiple- and first-contact miscible conditions (from left to right) depending on the increasing additive concentrations (at the same pressure and temperature). Adopted from [Rommerskirchen, et al., 2018].

2.7 Methods for Determining Miscibility Conditions

Miscible displacement tests (dynamic tests) are an appropriate method to determine the pressure to achieve dynamic miscibility with natural gas, flue gas, enriched hydrocarbons or CO_2 . The parameters that have to be measured to obtain pseudotriangular phase diagrams, such as explained before, are time-consuming and difficult. Importantly, the parameters obtained under batch and flow conditions may be different [Hutchinson Jr., Braun, 1961], or the composition of the path may influence the conditions for miscibility [Metcalf, Fussell,

Shelton, 1973]. Some methods calculate the pressure and gas composition of vapor/liquid equilibrium with appropriate equation of state or K -value correlations, with some techniques even describing the phase behavior of reservoir fluid and injection fluid CO_2 [Metcalfe, Fussell, Shelton, 1973, Fussell, 1979, Fussell, Yanosik, 1978, Rowe, Allen McGhee, Jr., 1978]. The K -value is the ratio of vapor concentration to liquid concentration at equilibrium. However, *a priori* calculation of miscibility conditions, equation of state or K -value correlations are not sufficiently accurate particularly near the critical point, which is important for achieving dynamic miscibility. Nevertheless, some relationships for estimating dynamic miscibility conditions based on experimental miscibility data with CO_2 have been proposed [Holm, Josendal, 1974, Holm, Josendal, 1982, Yellig, Metcalfe, 1980, Christian, et al., 1981, Johnson, Pollin, 1981]. Because it is not known how accurately these correlations predict the miscibility of a certain reservoir, experimental tests of the miscibility pressure should be done for a project design.

Various displacement methods have been used and conducted in horizontal or vertical consolidated porous media of various lengths and diameters and at various flow rates [Rathmell, Stalkup, Hassinger, 1971, Holm, Josendal, 1974, Holm, Josendal, 1982]. Further experiments were conducted in long, coiled sections of small diameter tubing packed with sand or glass beads. [Holm, Josendal, 1974, Yellig, Metcalfe, 1980, Johnson, Pollin, 1981]. Additional tests were performed in vertical sandpacks under gravity-stable conditions [Rutherford, 1962]. For interpreting the results obtained from these displacements, different criteria have been included, such as breakthrough and ultimate recovery at given volume of solvent injection [Holm, Josendal, 1974], visual observations of the core effluent [Rathmell, Stalkup, Hassinger, 1971, Yellig, Metcalfe, 1980], composition of produced gases [Rathmell, Stalkup, Hassinger, 1971], shape of the breakthrough and curves of ultimate recovery versus pressure or combinations of these criteria. Confusion has been caused by these different experimental methods and the interpretation criteria in trying to compare data from different investigators.

Based on these methods, according to Stalkup, the following important factors in designing displacement experiments should be considered “(1) *dynamic miscibility should be attained over a negligible fraction of displacements path length and (2) experiments should be designed to have essentially complete sweepout after injection of approximately 1.2 PV of solvent*” [Stalkup, 1983]. Furthermore, the miscible displacement tests should be designed to

prevent viscous fingering or gravity tonguing, which can occur due to the lower viscosity and gravity of the injection fluid compared to the oil they replace. A few complying methods for displacement experiments will be presented shortly with some recommendations [Stalkup, 1983]:

Gravity-stable experiments are one appropriate method. The density difference between oil and solvent, which could lead to viscous fingering or gravity tonguing, can be compensated by injecting the lighter component from the top of the test column with a sufficiently low rate.

Slim tube experiments can be used even if the density differences are small, which is usually the case for CO₂ displacements and thus impractical low rates are necessary for gravity-stable experiments. Fingering, which is initiated by flow perturbations, can be minimized by transverse dispersion and by designing the test column with small diameter and low flow velocities. For more details and recommendations for an apparatus and measuring procedure from Yellig and Metcalfe, see chapter 3.2.2.

Visual cell observations are useful for investigating in particular the transition zone, where the oil is displaced by the injection fluid, for instance CO₂. Generally, immiscible CO₂ displacement shows a sharp interface at a two-phase flow. Achieving dynamic miscibility, no sharp interface is observed, but colors at the transition zone from dark (displacing black oil) through red, orange, yellow and finally to almost clear (injection fluid) are found [Yellig, Metcalfe, 1980, Henry, Metcalfe, 1983]. A single-phase flow can be obtained by increasing the pressure above the MMP [Stalkup, 1983].

In this thesis, in addition to a dynamic miscible displacement test via a slim tube experiment, a static method with a visual cell was used. While the slim tube experiment is an approved method to reproducibly and accurately determine the MMP [Orr, Franklin M., Jr., Silva, Lien, 1983, Elsharkawy, Poettmann, Christiansen, 1996, Adel, Tovar, Schechter, 2016], the static method is demonstrated to also allow reproducible and accurate measurement of the plait point (see chapter 3.2.1). Furthermore, with this static method, it is possible to construct pseudotriangular diagrams rapidly, which are known as difficult and time-consuming [Stalkup, 1983].

3 Materials and Methods

In this chapter the materials and methods used in this thesis are described.

3.1 Materials

3.1.1 Chemicals

Most chemicals were purchased from suppliers listed below, while some have been supplied by Sasol Performance Chemicals. All chemicals were used without further purification. Deionized water, which was used for cleaning of the high pressure visual cell, the slim tube apparatus and the corresponding parts was provided by the Faculty of Chemistry of the University of Stuttgart and the Department of Chemical and Biomolecular Engineering of the Rice University.

A list of all chemicals is given in Table 3.1 including information about their chemical formula, abbreviation, supplier, molar mass, and purity, if known. The amphiphilic additives were designated by applying the nomenclature suggested by “Kahlweit and Strey” [Kahlweit, Strey, 1985]. Thus, ethoxylated alcohols are denoted as C_iE_j , while propoxylated ones are denoted as C_iP_x . Alkoxylates, which contain both ethoxy and propoxy groups, are denoted as $C_iE_jP_x$ or $C_iP_xE_j$ depending on their molecular structure, wherein i characterizes the number of the carbon atoms (C) in the alkyl chain, j the number of ethoxy units (E) and x the number of propoxy units (P).

Table 3.1: Used chemicals. Chemicals are listed alphabetically. Abbreviations of additives according to Kahlweit and Strey [Kahlweit, Strey, 1985].

Name	Chemical formula	Abbreviation	Supplier	Molar Mass in gmol ⁻¹	Purity in %
1,3-Dimethyl-cyclohexane (cis,trans)	C ₈ H ₁₆		Sigma-Aldrich	112.21	99
14-Hexyl-2,5,8,11-tetramethyl-3,6,9,12-tetraoxadocosan-1-ol	C ₂₄ H ₅₀ O ₅	ISOFOL 12P ₄	Sasol	418.65	*1
1-Butanol	C ₄ H ₉ OH	C ₄ E ₀	Fluka	74.12	98
1-Dodecanol	C ₁₂ H ₂₅ OH	C ₁₀ E ₀ P ₀	Sigma-Aldrich	186.33	≥ 98.0
1-Hexanol	C ₆ H ₁₃ OH	C ₆ E ₀ P ₀	Sasol	102.17	98.8
1-Tetradecanol	C ₁₄ H ₂₉ OH	C ₁₄ E ₀ P ₀	Acros	214.39	99
2-(2-Butoxyethoxy)-ethanol	C ₈ H ₁₈ O ₃	C ₄ E ₂	Sasol	162.23	*1
2-(2-Butyl-1-octoxy)ethan-1-ol	C ₁₄ H ₃₀ O ₂	ISOFOL 12E ₁	Sasol	230.38	*1
2-(2-Butyl-1-octoxy)propan-1-ol	C ₁₅ H ₃₂ O ₂	ISOFOL 12P ₁	Sasol	244.4	*1
2-(Hexyloxy)propan-1-ol	C ₉ H ₂₀ O ₂	C ₆ P ₁	Sasol	160.25	*1
2-[2-(1-Hexoxy)propoxy]propan-1-ol	C ₁₂ H ₂₆ O ₃	C ₆ P ₂	Sasol	218.33	*1
2-[2-(2,5,9-Trimethyl-1-decoxy)ethoxy]ethan-1-ol	C ₁₇ H ₃₆ O ₃	ITDA E ₂	Sasol	288.46	*1
[2-[2-(2,5,9-Trimethyl-1-decoxy)propoxy]propoxy]propan-1-ol	C ₂₂ H ₄₆ O ₄	ITDA P ₃	Sasol	374.58	*1
2-[2-(2-Butyl-1-octoxy)propoxy]propan-1-ol	C ₁₈ H ₃₈ O ₃	ISOFOL 12P ₂	Sasol	302.48	*1
2-[2-[2-(1-Hexoxy)ethoxy]ethoxy]ethan-1-ol	C ₁₂ H ₂₆ O ₄	C ₆ E ₃	Sasol	234.32	*1
2-[2-[2-(1-Hexoxy)propoxy]propoxy]propan-1-ol	C ₁₅ H ₃₂ O ₄	C ₆ P ₃	Sasol	276.41	*1
2-[2-[2-(2-Butoxyethoxy)propoxy]propoxy]propan-1-ol	C ₁₅ H ₃₀ O ₅	C ₄ E ₁ P ₃	Sasol	290.39	*1
2-[2-[2-(2-Butyl-1-octoxy)ethoxy]ethoxy]ethan-1-ol	C ₁₈ H ₃₈ O ₄	ISOFOL 12E ₃	Sasol	318.48	*1
2-[2-[2-(2-Butyl-1-octoxy)propoxy]propoxy]propan-1-ol	C ₂₁ H ₄₄ O ₄	ISOFOL 12P ₃	Sasol	360.56	*1
2-[2-[2-[2-(1-Butoxy)ethoxy]ethoxy]ethoxy]ethan-1-ol	C ₁₂ H ₂₆ O ₅	C ₄ E ₄	Sasol	250.32	*1
2-[2-[2-[2-(1-Hexoxy)propoxy]propoxy]propoxy]propan-1-ol	C ₁₈ H ₃₈ O ₅	C ₆ P ₄	Sasol	334.48	*1
2-[2-[2-[2-[2-(1-Hexoxy)propoxy]propoxy]propoxy]propoxy]propan-1-ol	C ₂₄ H ₅₀ O ₇	C ₆ P ₆	Sasol	450.63	*1

*1 technical-grade.

Table 3.1 continued: Used chemicals.

Name	Chemical formula	Abbreviation	Supplier	Molar Mass in g mol ⁻¹	Purity in %
2-[2-[2-[2-(1-Hexoxy)ethoxy]ethoxy]ethoxy]ethan-1-ol	C ₁₄ H ₃₀ O ₅	C ₆ E ₄	Sasol	278.38	*1
2-[2-[2-[2-(2-Hexyl-1-decoxy)propoxy]propoxy]propoxy]propan-1-ol	C ₂₈ H ₅₈ O ₅	ISOFOL 16P ₄	Sasol	474.74	*1
2-[2-[2-[2-[2-(2-Butyl-1-octoxy)propoxy]propoxy]propoxy]propoxy]propoxy]propan-1-ol	C ₃₀ H ₆₂ O ₇	ISOFOL 12P ₆	Sasol	534.79	*1
2-[2-[2-[2-[2-[2-(1-Butoxy)propoxy]propoxy]propoxy]propoxy]propoxy]propoxy]propan-1-ol	C ₂₅ H ₅₂ O ₈	C ₄ P ₇	Sasol	480.66	*1
2-[2-[2-[2-[2-[2-[2-(1-dodecoxy)ethoxy]ethoxy]propoxy]propoxy]propoxy]propoxy]propoxy]propan-1-ol	C ₃₇ H ₇₆ O ₁₀	C ₁₂ E ₂ P ₇	Sasol	680.97	*1
2-[2-[2-[2-[2-[2-[2-(2-Ethyl-1-hexoxy)ethoxy]ethoxy]propoxy]propoxy]propoxy]propoxy]propoxy]propan-1-ol	C ₃₃ H ₆₈ O ₁₀	2-EHE ₂ P ₇	Sasol	624.86	*1
2-[2-[2-[2-[2-[2-[2-(1-hexadecoxy)ethoxy]ethoxy]propoxy]propoxy]propoxy]propoxy]propoxy]propan-1-ol	C ₄₁ H ₈₄ O ₁₀	C ₁₆ E ₂ P ₇	Sasol	737.07	*1
2-[2-[2-[2-[2-[2-[2-(2-Hexyl-1-decoxy)ethoxy]ethoxy]propoxy]propoxy]propoxy]propoxy]propoxy]propan-1-ol	C ₄₁ H ₈₄ O ₁₀	ISOFOL 16E ₂ P ₇	Sasol	737.07	*1
2-[2-[2-[2-[2-[2-(2,5,9-Trimethyl-1-decoxy)propoxy]propoxy]propoxy]propoxy]propoxy]propan-1-ol	C ₂₅ H ₅₂ O ₅	ITDA P ₄	Sasol	432.69	*1
2-Butoxyethanol	C ₆ H ₁₄ O ₂	C ₄ E ₁	Acros	118.17	99
2-Butyl-1-octanol	C ₁₂ H ₂₆ O	ISOFOL 12	Sasol	186.33	*1
2-Dodecyl-1-hexadecanol	C ₂₈ H ₅₈ O	ISOFOL 28	Sasol	410.74	*1
2-Ethylhexanol	C ₈ H ₁₈ O	2-EH	Sasol	130.22	*1
2-Hexyl-1-decanol	C ₁₆ H ₃₄ O	ISOFOL 16	Sasol	242.43	*1
2-Propylheptanol	C ₁₀ H ₂₂ O	2-PH	Sasol	158.28	*1
3,6,9,12,15,18-Hexaoxatetracosan-1-ol	C ₁₈ H ₃₈ O ₇	C ₆ E ₆	Sasol	366.47	*1
Acetone	C ₃ H ₆ O		*2	58.08	*1
Asian crude oil	Crude oil	aco38.0	Sasol	n.a.	-
Benzene	C ₆ H ₆		Merck	78.11	≥ 99.0

*1 technical-grade; *2 in-house supplier; n.a., not available.

Table 3.1 continued: Used chemicals.

Name	Chemical formula	Abbreviation	Supplier	Molar Mass in g mol^{-1}	Purity in %
Carbondioxid	CO_2	CO_2	Westfalen AG	44.01	99.9
DI water	H_2O		*2	18.02	*2
Ethanol	$\text{C}_2\text{H}_5\text{OH}$		Sigma-Aldrich	46.07	≥ 99.0
Ethanol+5POC	$\text{C}_{22}\text{H}_{36}\text{O}_{16}$	Ethanol+5POC	Sasol	556.49	*1
Exxal™ 10	In average $\text{C}_{10}\text{H}_{22}\text{O}$ (C_{9-11} -iso, C_{10} -rich)	Exxal™ 10	Via Sasol	158.28	*1
Isononanol	$\text{C}_9\text{H}_{20}\text{O}$		Sasol	144.25	*1
Marlophen P4	$\text{C}_{18}\text{H}_{30}\text{O}_5$	Marlophen P4	Sasol	326.42	*1
Methanol	CH_3OH		Sigma-Aldrich	32.04	≥ 99.0
Methylcyclohexane	C_7H_{14}		Acros	98.18	99
<i>m</i> -Xylole	C_8H_{10}		Sigma-Aldrich	106.17	≥ 99.0
Naphthalene	C_{10}H_8		Merck	128.17	≥ 99.0
<i>n</i> -Cyclohexane	C_6H_{12}		Merck	84.16	≥ 99.0
<i>n</i> -Cyclohexane	C_6H_{12}		Aldrich	84.16	99.5
<i>n</i> -Cyclopentane	C_5H_{10}		Aldrich	70.13	≥ 99.0
<i>n</i> -Decane	$\text{C}_{10}\text{H}_{22}$		Aldrich	142.28	≥ 99.0
<i>n</i> -Decanol	$\text{C}_{10}\text{H}_{21}\text{OH}$		Sigma-Aldrich	158.28	≥ 98.0
<i>n</i> -Dodecane	$\text{C}_{12}\text{H}_{26}$		Aldrich	170.33	≥ 99.0
<i>n</i> -Hexadecane	$\text{C}_{16}\text{H}_{34}$		Sigma-Aldrich	226.44	99
<i>n</i> -Hexane	C_6H_{14}		Sigma-Aldrich	86.18	≥ 99.0
<i>n</i> -Octadecane	$\text{C}_{18}\text{H}_{38}$		Sigma-Aldrich	254.49	≥ 99.0
<i>n</i> -Octane	C_8H_{18}		Sigma-Aldrich	114.23	≥ 99.0
<i>n</i> -Octanol	$\text{C}_8\text{H}_{17}\text{OH}$		Sigma-Aldrich	130.23	≥ 99.0
<i>n</i> -Tetradecane	$\text{C}_{14}\text{H}_{30}$		Aldrich	198.39	≥ 99.0
Sasolwax 5805	linear and branched alkanes for chain length (<i>i</i>) = 20 to 46		Sasol		*1
TDA+5POC	$\text{C}_{33}\text{H}_{58}\text{O}_{16}$	TDA+5POC	Sasol	710.78	*1
Toluene	C_7H_8		Sigma-Aldrich	92.14	99.8
Triethanolamine	$\text{C}_6\text{H}_{15}\text{NO}_3$	TEA	Sasol	149.19	*1
Triisopropanolamine	$\text{C}_9\text{H}_{21}\text{NO}_3$	TIPA	Sasol	191.27	*1

*1 technical-grade.

The main component of the model crude oils mco47.0 and mco38.8 is the Sasolwax 5805 from Sasol Wax GmbH. The composition of the wax is shown in Figure 3.1 plotting the relative amounts (wt%) of linear and branched alkanes versus the number of C atoms. Note that the data are obtained from gas chromatography (GC) recorded and provided by the *Sasol Germany GmbH*.

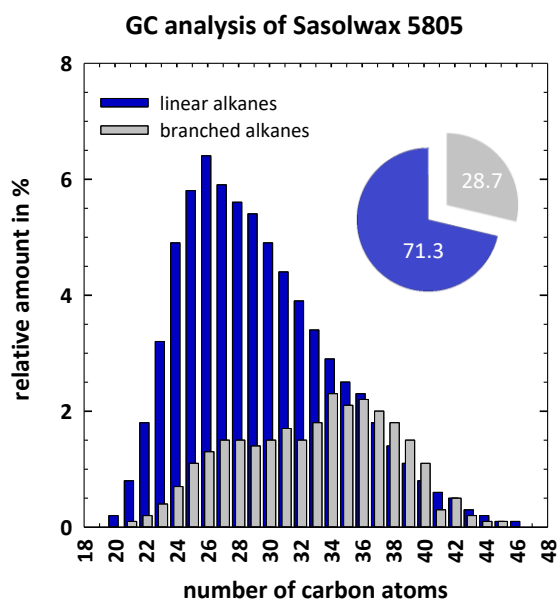


Figure 3.1: Gas chromatography analysis of Sasolwax 5805 provided by Sasol Performance Chemicals. The relative amount (wt%) of the linear (blue) and the branched (gray) alkanes is shown as a function of the number of the carbon atoms.

3.1.2 Data Evaluation

Data evaluation was done with SigmaPlot 12.5 for Windows (Systat Software Inc., San Jose, CA, USA) or Microsoft Excel 2016 (Microsoft, Redmond, WA, USA).

3.2 Methods

3.2.1 High Pressure Visual Cell

The temperature- and pressure-dependent phase behavior under reservoir conditions was determined using a high pressure visual cell (HP-cell), which was first developed at the University of Cologne, Germany and is shown as a technical sketch in Figure 3.2 [Schwan, 2006]. It allows to adjust the pressure stepless between 0.1 and 50.0 MPa (measured by a pressure transducer Type 81530 (Co. Burster, Gernsbach, Germany), which is connected to a home-built digital gauge unit). The pressure transducer (PT) was calibrated regularly using a pressure balance (Hydraulic pressure balance model CPB5800 with an accuracy of ± 0.5 MPa, Co. WIKA, Klingenberg, Germany). The calibration of the pressure sensors is explained in the appendix 7.1. The high pressure visual cell from Schwan comprises an all side polished sapphire cylinder (S, 50 mm in height, $\varnothing_{\text{out}} = 32$ mm, $\varnothing_{\text{in}} = 10$ mm, Co. Impex HighTech, Münster, Germany) allowing the visual inspection of 98% of the sample volume (when fully

filled). The sapphire cylinder is closed at the top by a screw-driven piston (PI) made of polyoxymethylene (POM) and sealed by an O-ring (6 x 2 mm, NBR 90 (acrylonitrile butadiene rubber 90), Co. hug, Ergolding, Germany) pressed against the inner surface of the sapphire. Furthermore, the sapphire cylinder is sealed at the bottom by an O-ring (14 x 3 mm, NBR 90, Co. hug, Ergolding, Germany) to a block of brass. The connection from the sapphire cylinder to the needle valve (V1) used for the injection of CO₂ was changed in this thesis. A continuous flow path without crossover drills improved the efficiency of the cleaning procedure by avoiding the retention of the high-viscous (model) crude oils or wax components in the HP-cell. To be more precise, this was achieved by connecting the sample compartment to the membrane (M, $\varnothing = 22$ mm, 0.05 mm thick, stainless austenitic steel, home-built) via a drill ($\varnothing = 0.30$ mm) through the block brass and the membrane via a thin capillary ($\varnothing_{in} = 0.8$ mm, $\varnothing_{out} = 1/16''$, stainless steel, Nr. 8020-8034, Co. LATEK, Eppelheim, Germany) to a needle valve (Nr. 8002-0120, Co. LATEK, Eppelheim, Germany).

The sample volume is separated from the pressure transducer by a membrane (stainless steel, $\varnothing = 22$ mm, 0.05 mm thick, home-built technical workshop IPC), which is sealed via two O-rings ($\varnothing = 21.8-17$ mm, 0.3 mm thick, POM, also home-built in technical workshop IPC). The transmission of the pressure to the pressure transducer is ensured by a degassed water reservoir. The pressure transducer outputs a voltage depending on the pressure, which is passed on to the digital gauge unit via a connecting cable protected against water by a hose. This converts the voltage (mV) into the corresponding pressure in bar. The digital gauge unit was calibrated after installation to the high pressure visual cell using the pressure balance CPB5800 mentioned above. The sapphire cylinder was designed to resist pressures up to 80.0 MPa. Pressure resistance of the sapphire cylinder was verified for pressures up to 50.0 MPa for different temperatures ($20\text{ }^{\circ}\text{C} < T < 90\text{ }^{\circ}\text{C}$). The temperature of the sample was adjusted by placing the HP-cell in a temperature-controlled water bath containing approx. 15 liters of DI water. The temperature was varied in a range of 5 °C to 90 °C with a precision thermostat (Model: DC30, $\Delta T = \pm 0.02$ K, Co. Thermo Haake, Karlsruhe, Germany) and determined using a thermometer (Model: GMH 3710, $\Delta T = \pm 0.01$ K, Co. Greisinger Electronic, Regenstauf, Germany).

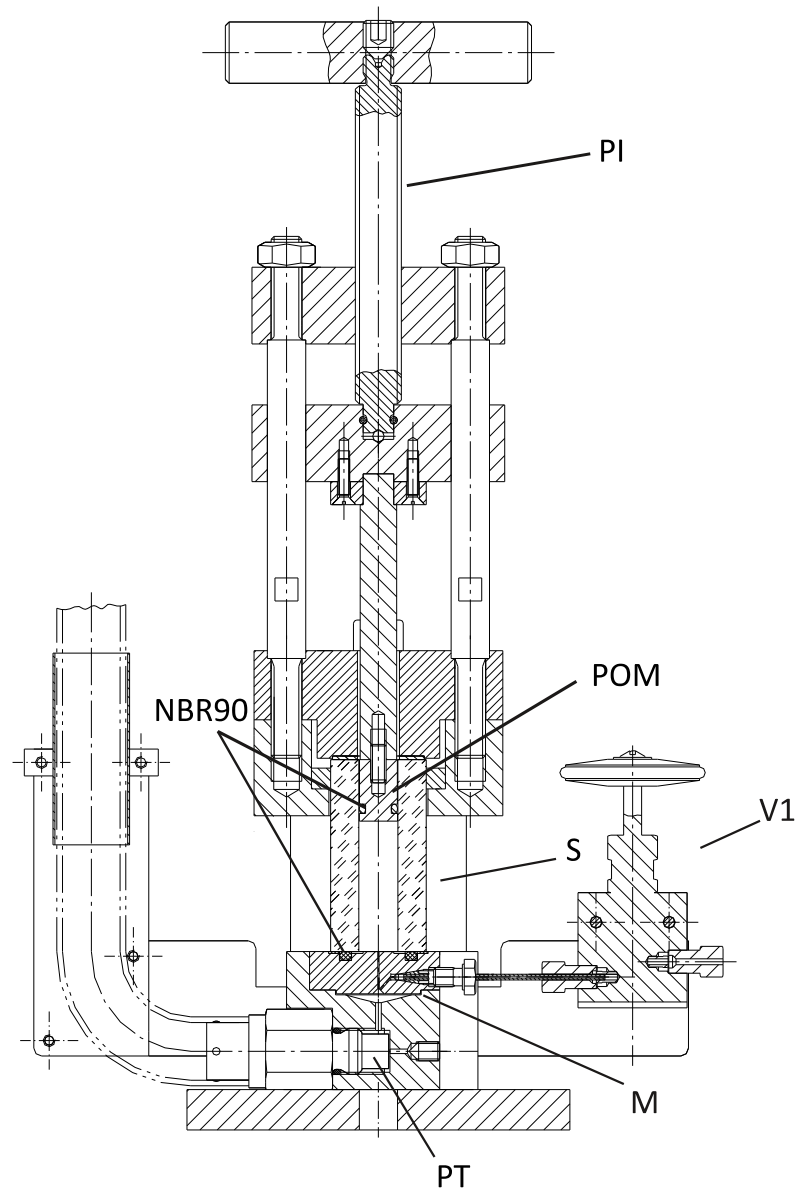


Figure 3.2: Technical sketch of the modified high pressure visual cell adapted from Schwan [Schwan, 2005]. The HP-cell was used to determine the pressure and temperature dependence of the phase behavior of CO₂-containing systems. The sample volume is enclosed by a sapphire cylinder (S), which is sealed on the top by the end part of a piston (PI), which is made of polyoxymethylene (POM) and on the bottom against a brass block by an O-ring (NBR90). Via a needle valve (V1) CO₂ can be filled in. By screwing the piston, the pressure in the sample compartment can be regulated, which is measured by a pressure transducer (PT). The pressure transducer is located inside the brass block and separated from the sample compartment by a stainless steel membrane (M).

3.2.1.1 Sample preparation

In order to prepare a sample of a given composition, the HP-cell was filled first with the desired amount of liquid or solid components at ambient conditions. The required amounts were determined by weight (used balance: Model: CP324S, error ± 0.0001 g, Co. Sartorius, Göttingen, Germany). Additionally, a magnetic stirring bar was placed in the HP-cell for homogenization. After sealing the HP-cell with the piston and weighing (see below), the HP-cell was connected to an in-house-built CO₂ filling apparatus (Department of Chemistry, University of Cologne) equipped with a membrane reservoir (MR, see Figure 3.3) to add the desired amount of liquid CO₂ (at room temperature (22 ± 0.5) °C and a pressure of (7.2 ± 0.1) MPa). Due to the small amount (approx. $1.6 \cdot 10^{-4}$ mol), the trapped air in the HP-cell was found to not affect the phase behavior of the studied systems (data not shown). So, this included air was neglected for further sample preparation. The desired volume of CO₂ filled into the sapphire cylinder was adjusted by the height of the piston according to a scale at the HP-cell. The corresponding mass can then be calculated through the density of CO₂ at the given conditions (ρ , T). Due to the large reading error of the height (± 0.5 mm), the actual mass of the added CO₂ was determined by weighing the HP-cell before and after the addition of CO₂ (used balance: Model: CPMSE4202S, maximum weight: 4.200 kg, error ± 0.007 g, Co. Sartorius, Göttingen, Germany). Prior to filling the HP-cell with CO₂, the membrane reservoir of the filling apparatus (SBO 450 – 0.6 A6 / 342 U – 250 AK, Co. HYDAC, Sulzbach, Germany), see Figure 3.3, was filled with CO₂ from a CO₂ gas bottle with a syphon tube ($p \approx 6.0$ MPa, valves V2 to V4 opened). After closing the valve V2, CO₂ is filled in the HP-cell by opening the valve V1 and slowly increasing the pressure by using N₂ from an N₂ gas bottle (pressure was reduced to 9.0 MPa with a pressure regulator, and controlled by an analog gauge G1). Having filled the volume left free in the sapphire cylinder with liquid CO₂, the valve V1 was closed and the amount of CO₂ was determined by weight. Of note, it is only possible to add additional CO₂, but not to release it without also releasing other components. Thus, the addition of too much CO₂ results in cleaning and new refilling of the HP-cell. Finally, the CO₂ and also the N₂ were released from the CO₂ filling apparatus via valve V5 and valve V6.

The HP-cell was then transferred into a water bath at the desired temperature. Here, reaching a constant pressure indicates a temperature equilibrium. Subsequently, the pressure was increased (under stirring of the mixture) until a phase transition from 2- (or multi-) phase (turbid) to 1-phase (clear) state was determined by visual inspection in both transmitted and

scattered light using an LED lamp (Model: VisiLight I-LED, Co. VWR International, Darmstadt, Germany). Afterwards, the stirring was stopped to check, whether the mixture remained in the thermodynamically stable 1-phase state. By slightly decreasing the pressure the occurrence of turbidity validated the existence of a 2- (or multi-) phase state. 2-phase and multi-phase samples are both turbid and can only be distinguished after awaiting phase separation. After recording all appearing phases and phase transition pressures, the temperature was varied (usually reduced) and the procedure was repeated to determine the pressure-dependent phase transition at different temperatures. With the method described in the previous sentences, the phase boundaries can be determined with an accuracy of ± 0.5 MPa and ± 0.1 K.

To empty and clean the HP-cell, it was reheated to at least 65 °C to ensure that all sample components (especially the wax) were in a liquid state. The sample was disposed by carefully opening the valve V1, which was connected to a capillary leading into a proper waste container. After the pressure had dropped to atmospheric pressure, the piston and stirring bar were removed to rinse the sample compartment several times with cyclohexane, acetone and DI water, until no residues were visually observed. Afterwards, the piston and the stirring bar were cleaned with cyclohexane, acetone and DI water using tissues. The O-rings of the piston and at the bottom of the sapphire cylinder were exchanged after every two measurements for safety reasons. As last step, the HP-cell was mounted without the piston in the CO₂ filling apparatus to be flushed with CO₂, thereby removing potential residues of cleaning solvents from the interior of the HP-cell.

A maintenance of all components of the HP-cell was carried out regularly every 6 to 8 weeks in order to minimize safety risks. To ensure that the HP cell measurement provides reproducible data, the phase boundaries of known systems, e.g. CO₂-*n*-alkane, were measured and compared with the existing results.

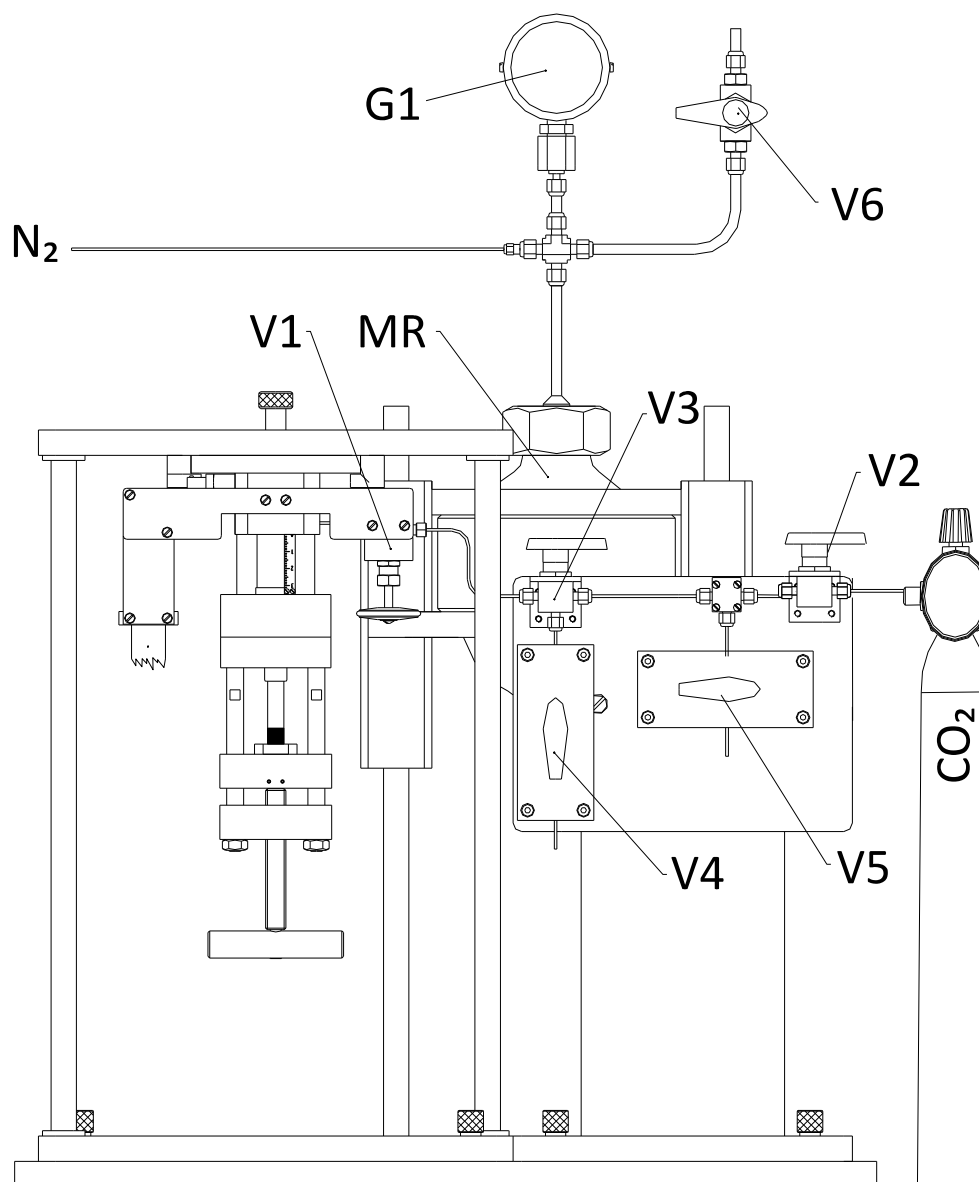


Figure 3.3: Sketch of the sealed HP-cell connected upside down to an in-house-built CO₂ filling apparatus equipped with a membrane reservoir (MR), adapted from Schwan [Schwan, 2005]. The HP-cell is connected via a needle valve (V1) and several other valves (V2 to V5) to a CO₂ gas bottle with syphon tube and the MR. The MR is also connected to a nitrogen gas bottle (N₂) via a pressure regulator, which can be used to increase the pressure up to 9.0 MPa to fill the liquefied CO₂ in the sapphire cylinder already partially filled with all liquid and solid components of the sample. The pressure can be controlled by an analog gauge (G1). The pressure in the HP-cell is displayed by a digital gauge. The pressure in the MR can be released by opening the valve V6.

3.2.2 Slim Tube Apparatus

In order to approximate the recovery process conditions of a real crude oil field operation, the dynamic behavior of a model crude oil and CO₂ without and with co-injecting of an additive was studied in a flow experiment in a home-built slim tube apparatus (ST). Such slim tube studies allow for the determination of the minimum miscibility pressure (MMP), which indicates the lowest pressure to achieve first- or multiple-contact miscibility (FCM or MCM). With the aim to study the effect of one of the most promising additives (determined from phase behavior studies) in application-oriented slim tube measurements, the MMPs of the systems CO₂ – model crude oil and CO₂ – model crude oil – C₆P₃ were determined. Therefore, in this thesis a slim tube apparatus was developed and built at the Rice University, Houston, Texas, USA in close cooperation with the group of Prof. Dr. George J. Hirasaki and the help of Dr. Maura Puerto.

The slim tube apparatus was designed according to the requirements defined by Stalkup (see Fundamentals 2.7) [Stalkup, 1983]. Thereby, the maximum pressure was estimated from phase diagram studies providing the plait point as upper limit of the MMP ($p_c = (17.2 \pm 0.5)$ MPa in the CO₂ – mco38.8 system, see Table 4.3). Concerning the dimensions of the slim tube, Holm and Josendal, as well as Yellig and Metcalfe recommend a diameter of $\varnothing_{in} \leq 6.3$ mm ($\frac{1}{4}$ inch), a length of $l > 24.4$ m (80 ft) and a pore volume (PV) larger than 85 ml [Holm, Josendal, 1974, Yellig, Metcalfe, 1980]. Thereby, the PV is the free volume left after the tube is packed with small meshed sand. Long slim tubes have been shown to minimize the transition zone length, while a smaller diameter prevents viscous fingering [Elsharkawy, Poettmann, Christiansen, 1992]. In order to fulfill all recommendations, an inner tube diameter of 3.86 mm (0.152 inch) and a tube length of 30.48 m (100 ft) was chosen yielding a total slim tube volume of 373 ml. The slim tube was packed with 623 g Ottawa sand 20/40 (high purity silica with a particle size distribution of 20 to 40 mesh (0.841 to 0.420 mm), $\rho = 2.65$ gcm⁻³) corresponding to a grain volume of 235 ml. The packing was done in 5 ml increments followed by applying 0.34 MPa (50 psi) dry air, while vibrating for 20 min with an industrial type vibrator after each sand increment. The Ottawa sand 20/40 for packing of the ST was selected based on suggestion of Prof. Dr. George J. Hirasaki to reach a permeability of approx. 120 mD (milliDarcy) close to recovery conditions. For the determination of the permeability of the sand packed slim tube, see chapter 3.2.2.1.

Based on the used parameters, a theoretical PV of 138 ml can be easily calculated. Experimentally, the PV was determined by the volume of water, with which the sand-packed slim tube could be filled at 25 °C. Prior to letting DI water flow in the slim tube by gravity, vacuum was applied. A few milliliters away from the calculated PV, the vacuum was turned off and the slim tube was filled completely with the DI water. The experimental pore volume of 135 ml determined in this way, agrees almost quantitatively with the above-mentioned theoretical PV. Note that both the packing of the slim tube and PV determination was done by Dr. Maura Puerto. A schematic drawing of the slim tube apparatus is shown in Figure 3.4. The main components are described in detail in Table 3.2.

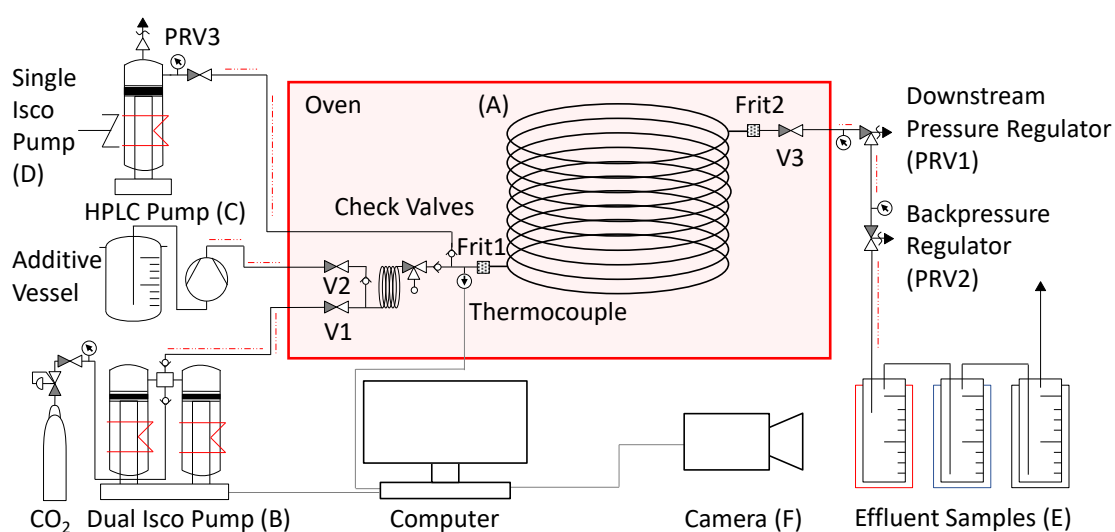


Figure 3.4: Schematic drawing of the slim tube apparatus (ST), designed by Dr. Maura Puerto. (A) Coiled tube with 30.48 m (100 ft) length, $\text{Ø}_{\text{out}} = 6.35 \text{ mm}$ ($\frac{1}{4}$ inch), $\text{Ø}_{\text{in}} = 3.86 \text{ mm}$ (0.152 inch); (B) Dual Isco pump to inject scCO_2 ; (C) HPLC pump to co-inject additive; (D) Single Isco pump to saturate the slim tube with the model crude oil; (E) from left to right: warm-trap, cool-trap, CO_2 bubbler; (F) Camera connected to a computer to monitor the effluent. Heating elements are shown in red.

Table 3.2: Main components of the slim tube apparatus.

Component	Description
Slim Tube	316 stainless steel tubing; 30.48 m (100 ft) length; \varnothing_{out} = 6.35 mm (¼ inch); \varnothing_{in} = 3.86 mm; (0.152 inch) wall thickness 1.25 mm (0.049 inch); approved for an operational pressure of up to 51.7 MPa (7,500 psi) at room temperature; coiled in 21 loops of 0.48 m (19 inch) diameter to fit the oven dimensions; by WEBCO industries, Chicago, Illinois. Dry sand packed with 20/40 Ottawa sand; 135 ml pore volume (determined as described above); 194 mD permeability (determined as described below).
Valves	Four two-way valves; one three-way/2-stem manifold valve, all rated for pressures above 51.6 MPa (7,500 psig); four Swagelok valves (Stainless Steel, Ball Valve, Part No. SS-H83PS8MM); one Parker Autoclave Engineers valve (with PTFE packing for operating up to 232 °C (450 °F), Part No. MVE2005).
Pressure relief valves (PRV)	Three pressure relief valves, two of them being used as backpressure regulators; all rated for pressures above 41.3 MPa (6,000 psig); from Swagelok (Stainless Steel, Part No. SS-4R3A-KZ), Houston, Texas. For the downstream pressure regulator, a white spring kit for R3A series proportional relief valve was used, 20.6 to 27.5 MPa (3000 to 4000 psig, Part No. 177-R3A-K1-F). For the backpressure regulator, a purple spring kit for R3A series proportional relief valve was used, 5.17 to 10.3 MPa (750 to 1500 psig, Part No. 177-R3A-K1-C). For the separate single Isco pump, which was used to inject the model crude oil, a red spring Kit for R3A series proportional relief valve was used, 27.5 to 34.4 MPa (4000 to 5000 psig, Part No. 177-R3A-K1-G).
Check valves	Three check valves were used to prevent backflow of CO ₂ , additive, and model crude oil; all rated for pressures above 41.3 MPa (6,000 psi); from Swagelok (Stainless Steel Poppet, Part No. SS-CHS2-5), Houston, Texas.
Pumps	Three pumps were used for injection; all rated for pressures above 34.5 MPa (5,000 psi): i) Dual Isco pump from Teledyne, Model 260D, for injecting supercritical CO ₂ . ii) HPLC pump from SSI, Model 12-6, to deliver additive. iii) Single Isco pump, Model 314, for injecting model crude oil. Because of 30 wt% wax content in the model crude oil, an electrical heating tape (set temperature inside the cylinder (65±7) °C) and a magnetic stirring bar with stirrer were mounted for homogenization.
Pressure Transducer	One transducer from Validyne Engineering was installed to record downstream pressure; rated for pressures up to 22.0 MPa (3,200 psig) operational pressure, Model DP15-46, Diaphragm Dash No. 64.
Sensor Interface Card	Sensor interface card UPC2100 from EasySense was used to record the up- and downstream pressure from the dual Isco pump and the pressure transducer in one second steps by a computer.
Oven	An explosion-proof oven from GS Blue M Electric Model Friction-Air HS-1202 EFG was used to temper the slim tube. It was bought refurbished from Cambridge Scientific Products, Watertown, Massachusetts. The oven was calibrated at a temperature of (65±2) °C. All lines out of the oven were heated up to (65±2) °C by heating tapes to reach thermal equilibrium during the slim tube test.

After assembling all the components of the slim tube apparatus, the dead volumes were determined from the amount of DI water displaced from different parts of the filled ST apparatus using both CO₂ and vacuum. Dead volumes of 29.3 ml from V1 to the beginning of the Frit 1, 1.6 ml from V2 to the first three-way valve and 11.3 ml from Frit 2 to the end of the line were obtained (Figure 3.4). Note that the total volume of the ST increases to 177.2 ml

when taking all dead volumes into account including the dead volume of 1.6 ml only present for measurements with additive.

Before performing slim tube experiments, the magnitude of the reasonable injection flow rates must be discussed. Adel, Tovar, and Schechter adjusted an injection flow rate of 0.06 ml/min and thus needed a very long time of 39 hours for one measurement in a 20 ft. coil and 120 hours in an 80 ft. coil resulting in similar MMP values [Adel, Tovar, Schechter, 2016]. Ekundayo and Ghedan, however, showed that for longer tubes also higher injection flow rates (corresponding to shorter measurement times) deliver similar MMP values [Ekundayo, Ghedan, 2013]. In order to verify that indeed higher injection flow rates can be used without affecting the MMP value, experiments were performed adjusting different flow rates of 0.563 ml/min and 2.000 ml/min displacing *n*-hexadecane by CO₂. Comparing the MMP value determined by static phase behavior studies with a value extrapolated from literature data published by Charoensombut-amon, Martin, and Kobayashi [Charoensombut-amon, Martin, Kobayashi, 1986] for the same *n*-hexadecane/CO₂ system showed almost perfect accordance (Figure 3.5). Since the measurements at both flow rates of 0.563 ml/min and 2.000 ml/min yielded the same MMP as the static phase behavior studies and the measurement by Charoensombut-amon, Martin, and Kobayashi, the flow rate does not influence the MMP of the *n*-hexadecane/CO₂ mixture within the studied regime. Therefore, for the experiments in this thesis, the flow rate was adjusted to 0.563 ml/min allowing to perform one experiment in one day. Note that slim tube measurements have to be done under constant observation due to the safety regulations of the Rice University.

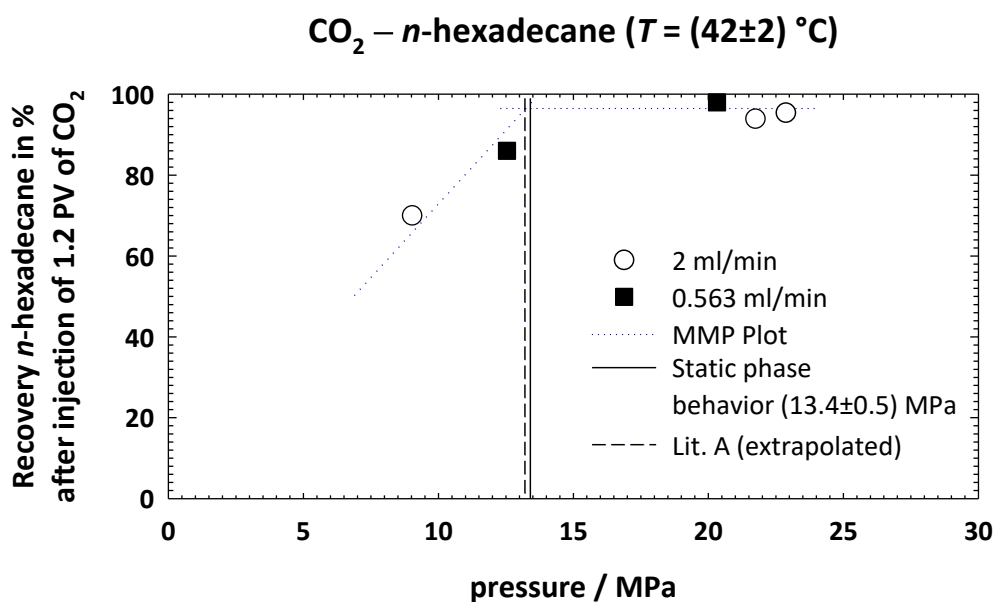


Figure 3.5: Recovered PV of *n*-hexadecane after injection of 1.2 PV of CO₂ as a function of the pressure for the CO₂ – *n*-hexadecane system at $(42 \pm 2) \text{ }^\circ\text{C}$. The two points below and above the MMP derived from measurements at flow rates of 0.563 ml/min and 2.000 ml/min can be connected by straight lines intersecting at the MMP = $(13.4 \pm 0.5) \text{ MPa}$ determined by static phase behavior studies and a value extrapolated from Charoensombut-amon, Martin, and Kobayashi (Lit. A) [Charoensombut-amon, Martin, Kobayashi, 1986].

The starting point of each slim tube measurement was to carefully clean the slim tube to remove any residual model crude oil, CO₂, or additives from the previous run. *n*-hexadecane was chosen as the cleaning agent, because it is part of the model crude oil and thus a good solvent for the components of the model crude oil and the additives. In order to be able to remove also the wax, the temperature was adjusted above its melting temperature. The following cleaning conditions were chosen: injection of 1.5 PV *n*-hexadecane with a flow rate of 2 ml/min at $(65 \pm 2) \text{ }^\circ\text{C}$ and $(22.0 \pm 2.0) \text{ MPa}$. To prove that the effluent was free of residual oil and additive, density and refractive index measurements were performed (density meter comprising a refractometer: Anton Paar model DMA-4500) and the values obtained ($\rho(65 \text{ }^\circ\text{C}) = (0.74228 \pm 0.0005) \text{ gcm}^{-3}$ and $n(65 \text{ }^\circ\text{C}) = 1.4155 \pm 0.005$) were in accordance with those of pure *n*-hexadecane [DDBSP, 2018].

Then, in order to remove any remaining CO₂, 2.2 PV of *n*-hexadecane were injected through the slim tube at $(42 \pm 2) \text{ }^\circ\text{C}$ with a pressure higher than 22.0 MPa to achieve full miscibility conditions according to Charoensombut-amon, Martin, and Kobayashi [Charoensombut-amon, Martin, Kobayashi, 1986]. Furthermore, by using a CO₂ bubbler, it was verified that the slim tube was free of CO₂ (the criterion was to be bubble-free for at least 0.5 PV injected *n*-hexadecane).

Prior to each measurement, the O-ring of the PRV for the downstream pressure regulator and, if necessary, also of the PRV for the backpressure regulator were changed according to the manuals. To start an actual slim tube measurement, the oven was heated up to the chosen measuring temperature of (65 ± 2) °C, which required 4 hours to reach thermal equilibrium (controlled by a thermocouple). After the oven and the single Isco pump (D) reached the desired temperature, 1.5 PV of the model crude oil (homogenized also at (65 ± 2) °C) were injected with a maximum injection flow rate of 2 ml/min in the ST apparatus, while the valves of the CO₂ and additive inlets were closed. Through this process and because of the full miscibility of the model crude oil with *n*-hexadecane, *n*-hexadecane can be displaced from the slim tube, leaving it saturated with the model crude oil. This process is completed when the effluent and the injected model crude oil result in the same refractive index and density. Therefore, the effluent was collected in 7 ml increments for analyses. Although saturation of the slim tube with the model crude oil was normally achieved after the injection of 1.2 PV, 1.5 PV of the model crude oil was injected (with a flow rate of 2 ml/min) to ensure that the slim tube was fully saturated. Before starting the injection of CO₂, the flow rate was adjusted to 0.563 ml/min and the respective measuring pressure was set at the downstream and backpressure relief valves. The flow rate of 0.563 ml/min was chosen to run the experiment in approx. 6 hours and to keep the differential pressure (Δp) between upstream and downstream as small as possible (differential pressure $\Delta p \approx 0.2$ MPa for the system CO₂ – *n*-hexadecane at 25 °C and with a flow rate of 0.5 ml/min, see 3.2.2.1 Darcy's Law). Note that for one measurement, including thermostating the equipment, filling the apparatus, performing the actual measurement and cleaning the slim tube apparatus, a total of $(4+2+6+3)$ h = 15 h was needed.

While for the slim tube measurements on the system containing no additive (CO₂ – model crude oil) the CO₂ was injected using only the dual Isco pump (B), for the measurements of the system containing the additive (CO₂ – (model) crude oil – C₆P₃), a co-injection was necessary. To achieve 2 wt% of additive in CO₂, flow rates of 0.563 ml/min for the CO₂ pump and of 0.008, 0.007, 0.006, and 0.005 ml/min for the additive pump were set for measurements at pressures of (17.9 ± 0.4) , (16.5 ± 0.5) , (14.3 ± 0.4) , and (13.6 ± 0.8) MPa, respectively. Of note, first the respective dead volumes of additive and CO₂ had to be injected.

The injection pressure of the system was monitored every second by an in-line pressure transducer of the dual Isco pump (D) connected via the Validyne Engineering card to

the Easy Sense 2100 software. All pressures were set and measured in psig (pressure indicated by the gauge relative to atmospheric pressure), but transferred to the SI unit MPa in this thesis. Regularly, manual notes (approximately every 10 min) from the analog gauges of the downstream and backpressure regulators were taken and added to the Easy Sense 2100 software. The produced amount of model crude oil with and without additive was monitored every 10 seconds by a camera (F) connected to a computer. Due to cooling resulting from the Joule-Thomson effect, the lines and PRVs had to be heated up to (85 ± 5) °C by heating tapes to prevent solidification of the model crude oil or *n*-hexadecane.

As described above, after each measurement, *n*-hexadecane was used to clean the slim tube displacing CO₂ and the remaining model crude oil from the tube. Adding the amount of model crude oil displaced by *n*-hexadecane to the produced amount of model crude oil should provide the injected amount of model crude oil by material balance (excluding unknown dead volumes and leakages). Indeed, the obtained results based on material balance showed good agreement with the injected values.

3.2.2.1 Darcy's Law

As mentioned above, Ottawa sand 20/40 was selected for packing the slim tube to reach a permeability of approx. 120 mD (milliDarcy = $9.869233 \cdot 10^{-16}$ m²), which reflects recovery conditions typically found in natural reservoirs (personal communication with Prof. Dr. George J. Hirasaki). Determining the volumetric flow rate Q (cm³·s⁻¹) as function of the differential pressure $\Delta p = p_1 - p_2$ (MPa) with p_1 and p_2 being the pressures of the slim tube inlet and outlet, respectively, the permeability k (in mD) of a sand packed slim tube can be calculated by using Darcy's law

$$k = Q \frac{\mu L}{A (p_1 - p_2)}, \quad (3.1)$$

wherein μ is the viscosity (mPa·s) of the driving fluid, here *n*-hexadecane at 25 °C (3.012 mPa·s, calculated by using the Vogel–Fulcher–Tammann–Hesse equation, see attachment 7.4), L the length of the slim tube (3048 cm), and A its cross sectional area ($A = \pi \cdot (0.198 \text{ cm})^2$) [Ma, et al., 2013]. By plotting the flow rate Q against the differential pressure Δp , see Figure 3.6, the permeability k can be easily obtained from the slope, via

$$k = \frac{\text{slope } \mu L}{A} \quad (3.2)$$

Based on this analysis, a value of (201 ± 7) mD was obtained, which is in the range expected for the Ottawa sand 20/40 filled slim tube. Note that the error of the HPLC pump is higher for low flow rates.

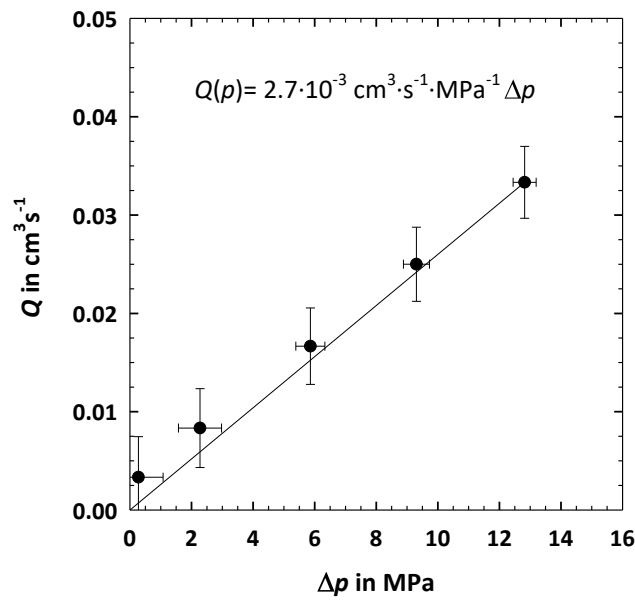


Figure 3.6: Permeability of the packed slim tube determined by plotting the flow rate Q of the injection fluid n -hexadecane as a function of the differential pressure Δp . From the slope, a permeability of $(k=201 \pm 7)$ mD is obtained at 25 °C.

3.2.3 Density Meter (Pycnometer)

Crude oils and model crude oils are often classified using the American Petroleum Institute (API) gravity. To determine the API gravity of the used oils, their densities had to be measured at 15.6 °C according to eq. (4.1). In this thesis a pycnometer with thermometer (calibrated volume of 10 cm³, DIN ISO 3507, (10 to 35) °C scale in 0.2 °C increments, Co. Glaswarenfabrik Karl Hecht GmbH & Co KG) was used for the measurement of the densities (see Figure 3.7).

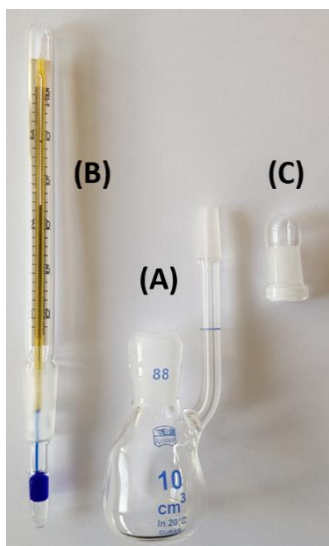


Figure 3.7: Pycnometer (A) with thermometer (B) and cap (C) to determine the densities/API gravities. (A) Pycnometer, with a calibrated volume of 10 cm³ according to DIN ISO 3507. (B) Thermometer, (10 to 35) °C scale in 0.2 °C increments. (C) Cap, to reduce vaporization.

The clean, dry, and empty pycnometer with thermometer and cap was weighed (m_0) using a balance (Model: CP324S, ± 0.0001 g, Co. Sartorius). Next, it was filled with DI water and the thermometer was set in, while ensuring that there were no air bubbles in the pycnometer. Thereafter, the pycnometer was tempered to 15.6 °C in a water bath and the DI water level was adjusted to the calibration mark with a syringe. The pycnometer was then removed from the water bath, capped, and dried outside with filtered compressed air and weighed (m_1). Afterwards, it was emptied, rinsed with acetone, and dried with filtered compressed air again. An arbitrary quantity of the substance to be investigated (usually around 2 g) was weighed in and the filled pycnometer with cap and thermometer was weighed again (m_2). Note that substances comprising solid components, like the wax, had to be melted within the pycnometer and solidified to obtain a homogeneous sample and to remove trapped air. For this purpose, the pycnometer filled with both the solid and liquid components was sealed with the thermometer and cap, heated in a water bath (usually at 50 °C) and then cooled in an ice bath. Thereafter, the remaining volume of the pycnometer was filled with DI water. Then, the pycnometer with thermometer and cap was again tempered to 15.6 °C adjusting the DI water level to the calibration mark. The pycnometer was dried again outside before weighing (m_3). Using the determined masses m_0 to m_3 in the following equation,

$$\rho_{15.6\text{ }^\circ\text{C}} = \frac{m_2 - m_0}{(m_1 - m_0) - (m_3 - m_2)} \cdot \rho_{\text{H}_2\text{O},15.6\text{ }^\circ\text{C}} \quad (3.3)$$

wherein $\rho_{\text{H}_2\text{O}}$ is the density of water at 15.6 °C (0.99001 gcm⁻³, obtained from the National Institute of Standards and Technology (NIST) REFPROP program [Lemmon, Huber, McLinden, 2013], which is based on the equation of state of Wagner and Pruß [Wagner, Pruß, 2002]), the density of the substance of interest could be calculated. Finally, the pycnometer was cleaned by heating and rinsing several times with acetone, cyclohexane and DI water, until the same value of m_0 was measured for the pycnometer.

3.2.4 Specifying the Composition and Construction of Phase Diagrams

There are several possibilities to specify the composition: mole fraction, percent by volume or mass percentage. In this thesis, mass fractions (w_X) are used for the characterization of the composition of a mixture. These can be used for a defined system A – B having the corresponding masses m_A and m_B by

$$w_A = \frac{m_A}{m_A+m_B} \text{ and } w_B = \frac{m_B}{m_A+m_B}. \quad (3.4)$$

By using

$$w_A = 1 - w_B, \quad (3.5)$$

only one of the two mass fractions is sufficient to specify the composition of a (pseudo-)binary system. Applying the nomenclature used for microemulsion systems, the mostly amphiphilic additives are defined as component C, while CO₂ is designated as component A. Following this nomenclature, the mass fraction of the additive in the CO₂/additive mixture is defined as

$$\gamma_{\text{CO}_2} = \frac{m_{\text{Additive}}}{m_{\text{Additive}}+m_{\text{CO}_2}}. \quad (3.6)$$

In order to specify the composition of (pseudo-)ternary systems made of CO₂ (A), oil (B) and additive (C) the mass fractions of the individual components are given by

$$w_X = \frac{m_X}{m_A+m_B+m_C} \text{ with } X = A, B, C. \quad (3.7)$$

Since $\sum w_x = 1$, two mass fractions are sufficient to specify the composition of the (pseudo-)ternary mixture. For the pseudoternary systems of the type CO₂ – (model) crude oil – additive studied in this thesis, besides γ_{CO_2} , the mass fraction of the model (crude) oil in the overall mixture

$$w_{\text{Oil}} = \frac{m_{\text{Oil}}}{m_{\text{Total}}} = \frac{m_{\text{Oil}}}{m_{\text{CO}_2} + m_{\text{Oil}} + m_{\text{Additive}}} \quad (3.8)$$

is used. Note that in case of the model crude oil, its composition is indicated by the mass fraction of each oil component.

As the main goal of this thesis was to elucidate the role of amphiphilic additives on the miscibility of CO₂ and crude oils, a large part of this study dealt with the determination of the phase behavior of pseudoternary CO₂ – (model) crude oil – additive systems. In order to obtain this information, $p(T)$ -phase diagrams were recorded for different relevant compositions in the Gibbs phase triangle. In the following, the general procedure for determining phase diagrams is described using the (pseudo-)binary CO₂ (A) – additive (C) system as an example. Note that the term "pseudo" is used, because in many cases the additives are technical-grade components. To determine such a phase diagram, the phase boundary between the two-phase and the one-phase state is measured as a function of pressure and temperature for samples with different additive mass fractions γ_{CO_2} .

In Figure 3.8, such $p(T)$ -diagrams are shown for the binary system CO₂ – C₄E₁P₃ at different mass fractions $\gamma_{\text{CO}_2} = 0.040$ to 0.850 . Note that the technical-grade additive C₄E₁P₃ is an alkoxyated 1-butanol (2-[2-[2-(2-Butoxyethoxy)propoxy]propoxy]propan-1-ol (for the molecular structure see Figure 3.8, right). The following general trend is found for all compositions: Increasing the temperature shifts the phase transition to a higher pressure. In order to understand the trend, the variation of the CO₂ density with temperature and pressure, which determines the interactions between CO₂ and C₄E₁P₃, has to be considered (see chapter 7.5). As an increasing density enables an improved interaction of CO₂ and C₄E₁P₃ molecules, an increasing pressure is needed to compensate for the decreasing density observed at higher temperatures. Considering the trend with increasing mass fraction of additive, at first a slight shift of the phase boundary to a higher pressure is observed when γ_{CO_2} is increased from $\gamma_{\text{CO}_2}=0.040$ to $\gamma_{\text{CO}_2}=0.075$. With further increase of the additive mass fraction, the phase boundaries shift strongly towards lower pressure.

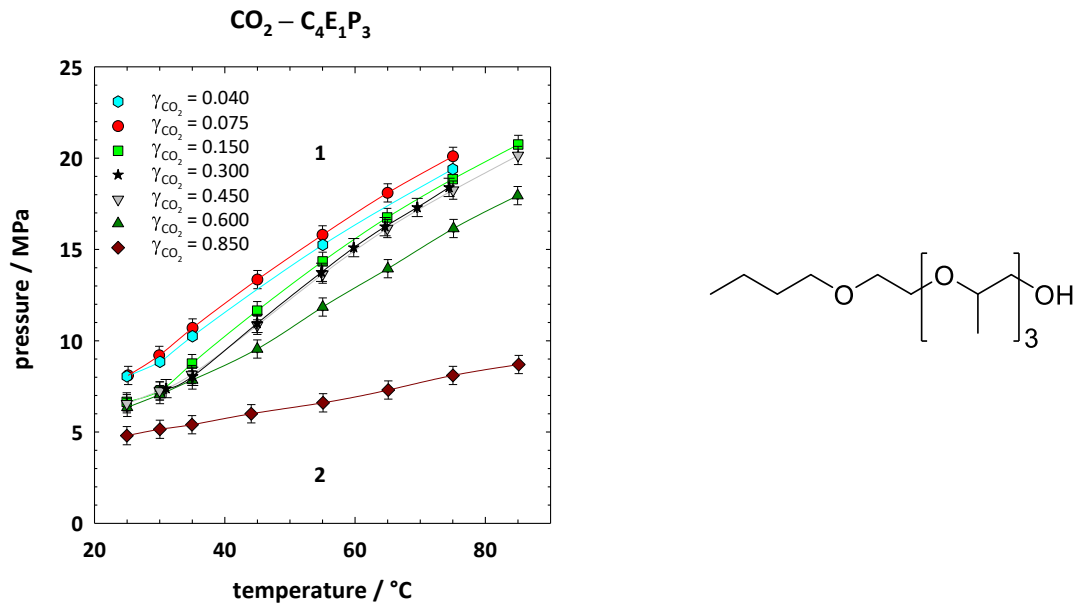


Figure 3.8: $p(T)$ -phase diagram of the binary $\text{CO}_2 - \text{C}_4\text{E}_1\text{P}_3$ system at different additive mass fractions (γ_{CO_2}). Between 25 °C and 85 °C nearly linear phase boundaries are observed. Left, $p(T)$ -phase diagram. Right, molecular structure of the short-chain amphiphilic alkoxyated 1-butanol ($\text{C}_4\text{E}_1\text{P}_3$).

For a better visualization of the influence of the additive mass fractions γ_{CO_2} on the phase behavior, $p(\gamma_{\text{CO}_2})$ - and $T(\gamma_{\text{CO}_2})$ -diagrams were constructed from the $p(T)$ -diagrams at different temperature and pressure, respectively. Figure 3.9 shows the $p(\gamma_{\text{CO}_2})$ - and $T(\gamma_{\text{CO}_2})$ -diagrams of the binary $\text{CO}_2 - \text{C}_4\text{E}_1\text{P}_3$ system.

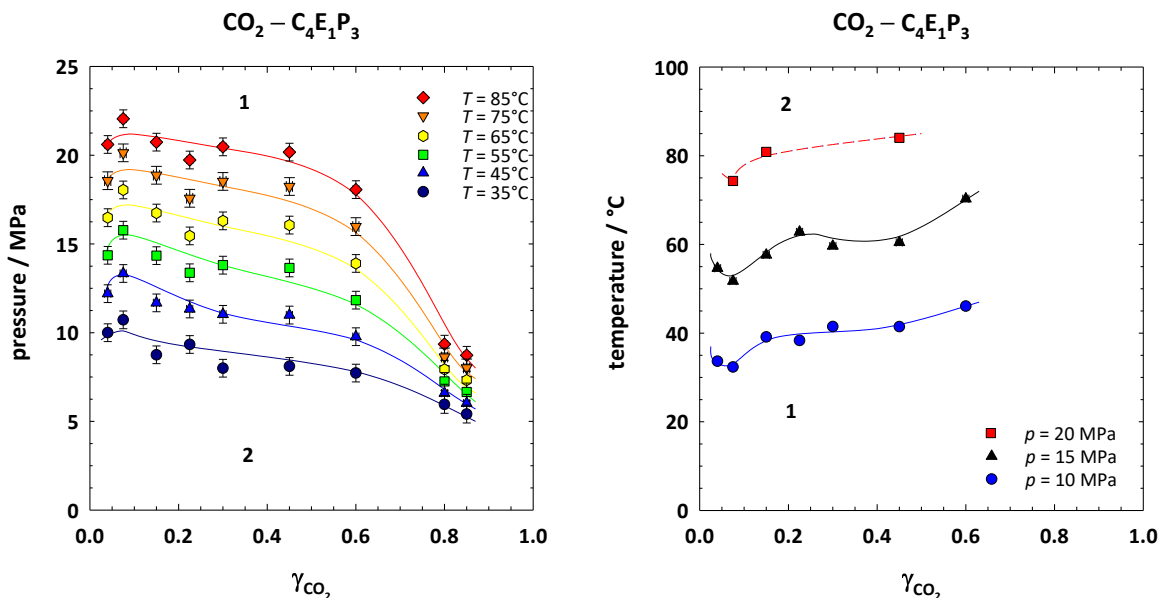


Figure 3.9: $p(\gamma_{\text{CO}_2})$ -diagram (left) and $T(\gamma_{\text{CO}_2})$ -diagram (right) of the binary $\text{CO}_2 - \text{C}_4\text{E}_1\text{P}_3$ system constructed from the corresponding $p(T)$ -diagram at different temperatures and pressures, respectively.

The $p(\gamma_{\text{CO}_2})$ -phase diagrams show lower miscibility gaps, which increase with increasing temperature, while the $T(\gamma_{\text{CO}_2})$ -phase diagrams show upper miscibility gaps, which shift to higher temperature with increasing pressure. Both trends can be explained by the variation of the CO_2 density with temperature and pressure, respectively, and its relation to interaction of CO_2 and $\text{C}_4\text{E}_1\text{P}_3$ molecules. By increasing the temperature, the density of CO_2 decreases considerably and a higher pressure is needed to compensate this decrease to improve the interaction between CO_2 and $\text{C}_4\text{E}_1\text{P}_3$ molecules.

Since we were mainly interested in the influence of additives on the pressure needed to mix CO_2 and (model) crude oil at an appropriate reservoir temperature, $p(\gamma_{\text{CO}_2})$ -phase diagrams are shown from here on.

4 Results and Discussion

Starting point of this thesis was the development of an experimental procedure, which allows to investigate the impact of amphiphilic molecules on the miscibility of (model) crude oils and CO₂. The high-pressure visual cell (HP-cell) described in section 3.2.1 allowed for the characterization of the phase behavior in temperature and pressure ranges relevant for a variety of oil reservoirs, i.e. pressures between 0.5 MPa and 45.0 MPa and temperatures in a range of 5 °C to 80 °C.

To identify promising additives, their miscibility with CO₂, which is generally in its supercritical state at reservoir conditions, was analyzed. Additionally, model crude oils were designed and compared to a dead crude oil (Asian crude oil aco38.0) with respect to their miscibility with CO₂. In that context, the pressure, where the lower miscibility gap of both CO₂ and additive as well as CO₂ and (model) crude oil is closing, was defined as physical minimum miscibility pressure (MMP_p). Setting a pressure greater than the MMP_p allows for complete miscibility of CO₂ and crude oil and is therefore of interest for oil field operations. Note, however, that the maximum usable pressure is limited by the formation fracture pressure of the particular reservoir for environmental reasons.

To achieve the main objective of the work, namely the miscibility of CO₂ and crude oils at lower pressure, the influence of a large number of additives, i.e. 17 alcohols and 20 alkoxyated alcohols, on the MMP_p of four different CO₂ – (model) crude oil systems was investigated. This was done by recording $p(T)$ -phase diagrams for at least three different oil mass fractions (w_{oil}) mostly adjusting an additive mass fraction in the CO₂/additive mixture of $y_{CO_2} = 0.020$. To compare the miscibility-enhancing effect of the different additives, the so-called **pressure profit** (Δp) given by the lowering of the MMP_p achieved by the respective additive was introduced. For selected additives, the plait point of the pseudoternary system CO₂ – (model) crude oil – additive was determined. Note that adjusting a pressure between the MMP_p and the plait point results in a multiple-contact miscible behavior, which also enables good recovery rates.

In addition to these systematic studies, additional measurements were performed to compare the best additives of this work to prior art. These data were needed to file the patent application “Injection Fluids comprising alkoxyated alcohols and the use of such fluids in oil recovery processes” [Rommerskirchen, R.; Bilgili, H.; Fischer, J.; Sottmann, T. DE, EP19158014.1, Feb 19, 2019].

Besides miscibility, the swelling behavior of the (model) crude oils is an important property for oil recovery with CO₂. As soon as the injected CO₂ partially condenses in the oil phase, thereby reducing the viscosity of the oil, this enables better flow through the reservoir resulting in higher production rates. Therefore, the swelling behavior of two of the strongest miscibility-enhancing additives of this thesis (C₆P₃ and ITDA E₂) was studied in the CO₂ – aco38.0 system.

Last but not least, in order to approximate the recovery process conditions of a real crude oil field operation, a slim tube apparatus was built-up at the Rice University (Houston, Texas, USA) in close cooperation with the group of Prof. Dr. George J. Hirasaki. The slim tube apparatus was used to study the influence of one of the most promising additives, i.e. C₆P₃, on the minimum miscibility pressure (MMP) of a CO₂ – model crude oil system. Furthermore, the data generated using the slim tube apparatus were compared to the results obtained from the phase behavior studies in the HP-cell.

Some of the results presented in this thesis have already been published:

- Rommerskirchen, R., Bilgili, H., Fischer, J. and Sottmann, T., Injection Fluids comprising alkoxyated alcohols and the use of such fluids in oil recovery processes (2019), Patent Application No. EP19158014.
- Rommerskirchen, R., Bilgili, H., Fischer, J. and Sottmann, T., Impact of Miscibility Enhancing Additives on the Flooding Scheme in CO₂ EOR Processes, SPE International, SPE Improved Oil Recovery Conference, Tulsa, SPE-190288-MS (2018).
- Rommerskirchen, R., Nijssen, P., Bilgili, H. and Sottmann, T., Reducing the Miscibility Pressure in Gas Injection Oil Recovery Processes, SPE International, Abu Dhabi International Petroleum Exhibition and Conference, Abu Dhabi, SPE-183389-MS (2016).
- Rommerskirchen, R., Nijssen, P., Bilgili, H. and Sottmann, T., Additives for CO₂ EOR Applications, SPE International, SPE Annual Technical Conference and Exhibition, Dubai, SPE-181304-MS (2016).

Starting with the experimental section, a main part of this study was focused on understanding the phase behavior of (pseudo-)binary and pseudoternary systems of the components CO₂, (model) crude oil, and additive. First, the (pseudo-)binary systems CO₂ – additive, CO₂ – (model) crude oil, and (model) crude oil – additive were investigated. Subsequently, the pseudoternary systems CO₂ – (model) crude oil – additive and thereby the pressure profiles were studied. Moreover, the influence of the hydrophilic side of the additive with regards to its alkoxylation degree and sequence (ethoxylation (EO) only, propoxylation (PO) only, EO/PO, or PO/EO) was analyzed.

4.1 (Pseudo-)Binary Systems

Many systematic studies have been conducted in the field of surfactant EOR. These studies are nicely reviewed by Hirasaki, Miller, and Puerto [Hirasaki, Miller, Puerto, 2008] and reveal that the increase of the recovery rates in water – crude oil – surfactant/alcohol systems can be related to the lowering of the interfacial tension by the surfactant/alcohol mixture. An appropriate way to study the phase behavior of these complex (pseudo-)ternary systems is, according to Kahlweit and Strey, to start with the investigation of the corresponding three (pseudo-)binary side systems of the phase prism [Kahlweit, Strey, 1985]. In this thesis, their approach was used to extensively study the phase behavior of CO₂ – (model) crude oil – additive systems. Thus, the (pseudo-)binary systems at hand are CO₂ – (model) crude oil, CO₂ – additive, and (model) crude oil – additive. The pseudobinary (model) crude oil – additive systems studied in this thesis were found to be completely miscible in the investigated temperature and pressure regime (e.g. for the systems mco47.0 – C₄E₁P₃ between 65 °C and 75 °C and a pressure range of 1.6 MPa to 35 MPa as well as mco38.0 – C₆P₃ at a temperature range of 60 °C to 80 °C between ambient pressure and 49 MPa; model crude oils mco47.0 and mco38.0 as well as additives C₄E₁P₃ and C₆P₃ are introduced in the following subchapters). Therefore, in the following, only the phase behavior of the two CO₂-containing (pseudo-)binary side systems is shown and discussed in detail.

4.1.1 CO₂ – Additive Systems

The investigations of the (pseudo-)binary side systems CO₂ – additive were started with 1-butanol (C₄E₀) as additive. C₄E₀ is a short-chain amphiphilic molecule, which has a low molecular weight and is available with high purity. One reason for this decision was the availability of comparable studies in literature [Byun, Kwak, 2002, Chen, Chang, Chen, 2002], which allow the results obtained with the HP-cell to be compared with the literature data. The temperature range investigated was limited to 60 °C to 80 °C, as this is the temperature range in certain oil reservoirs and the selected model crude oils have a high melting temperature due to the waxes they contain (see below).

In Figure 4.1, $p(\gamma_{\text{CO}_2})$ -phase diagrams of the system CO₂ – C₄E₀ at 60 °C (left) and 80 °C (right) are shown and compared with data from Byun and Kwak, and Chen et al. [Byun, Kwak, 2002, Chen, Chang, Chen, 2002]. These phase diagrams were extrapolated from the recording

of $p(T)$ -diagrams for samples with different mass fraction γ_{CO_2} of C_4E_0 in the $\text{CO}_2/\text{C}_4\text{E}_0$ mixture as described previously (3.2.4). At both temperatures, a lower miscibility gap can be observed, which is larger at the higher temperature. This behavior can easily be related to the density of CO_2 , which is in the supercritical or liquid state at the conditions at hand [Chrastil, 1982] as well as to the liquid state of the investigated additives at the analyzed conditions. The density of CO_2 decreases with increasing temperature, while it increases with increasing pressure. Thus, the observed miscibility of CO_2 and C_4E_0 at high pressure can be explained by the increased CO_2 density (at constant temperatures) leading to a better interaction of CO_2 and C_4E_0 molecules. In the same way, the shift of the phase boundary with increasing temperature to high pressures can be explained by the decreasing density as a function of temperature, which can be compensated by increasing the pressure.

Comparing the data from this work with those from the literature [Byun, Kwak, 2002, Chen, Chang, Chen, 2002], a quantitative agreement is found especially for $\gamma_{\text{CO}_2} < 0.400$. However, with increasing additive mass fractions, an increasing deviation of the measured data from the literature is observed for both temperatures. One reason for this deviation could be the design of the high-pressure visual cell used in this work. While the set-ups used in literature are characterized by relatively large sample volumes of approx. 28 cm^3 and 200 cm^3 (from Byun and Kwan and Chen et al., respectively), the cell of this work has a volume of only approx. 4 cm^3 . Remaining air in the cell during the filling process, the dead volume of approximately $5 \mu\text{l}$ between the membrane and the valve as well as a pressure sensor that has a larger deviation at lower pressures could have caused these deviations. Note that at that time, there was no in-house pressure balance. So, the pressure sensors had to be calibrated once a year at the Institute for Physical Chemistry at the University of Cologne. Additionally, leakage could have potentially impacted the data. However, when thermostating the HP-cell in a water bath, rising CO_2 bubbles would have been easy to detect.

In summary, the data obtained by the HP-cell are in good accordance with literature, especially for C_4E_0 mass fractions $\gamma_{\text{CO}_2} < 0.400$. Besides being easy to handle, the HP-cell requires smaller sample volumes compared to the other two set-ups and allows a fast screening procedure.

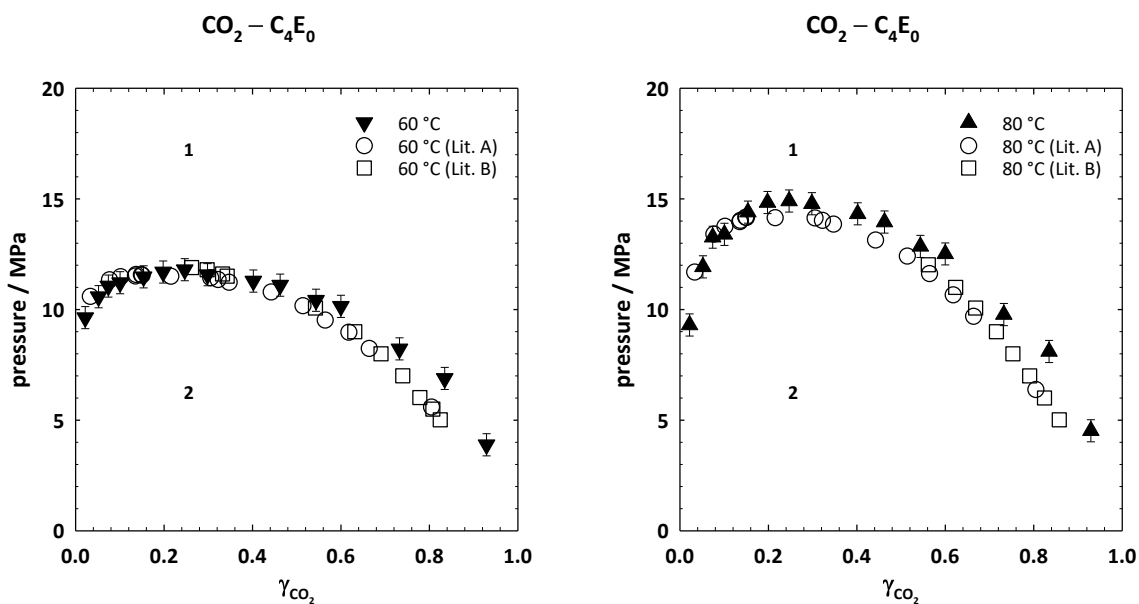


Figure 4.1: $p(\gamma_{\text{CO}_2})$ -diagrams of the system CO_2 –1-butanol at two temperatures 60 °C (left) and 80 °C (right).^{1(LW)} The lower miscibility gap shifts to higher pressure with increasing temperature. The data measured in this thesis are in quantitative agreement with literature from Byun and Kwak (Lit. A) [Byun, Kwak, 2002] and from Chen et al. (Lit. B) [Chen, Chang, Chen, 2002], especially for $\gamma_{\text{CO}_2} < 0.400$.^{1(LW)} Some measurements were carried out by Lisa Winkler (LW) during her bachelor thesis.

After it could be shown that the high-pressure visual cell used in this thesis is suitable for determining the temperature- and pressure-dependent phase behavior of mixtures with components that are gaseous at ambient pressure, the next step was to study the influence of the number of ethoxy groups j on the phase behavior of binary $\text{CO}_2 - \text{C}_4\text{E}_j$ systems. Figure 4.2 shows for comparison the $p(\gamma_{\text{CO}_2})$ -phase diagrams of the three systems $\text{CO}_2 - \text{C}_4\text{E}_0$, $\text{CO}_2 - \text{C}_4\text{E}_1$ and $\text{CO}_2 - \text{C}_4\text{E}_2$ at five different temperatures between 25 °C and 75 °C. All systems show an extended lower miscibility gap, which increases with increasing temperature. Furthermore, the $\text{CO}_2 - \text{C}_4\text{E}_2$ system shows a shoulder at low values of γ_{CO_2} , which could indicate the existence of an additional two-phase region and thus the presence of a triple line. Comparing the phase behavior of the three systems for a given temperature, an increase of the miscibility gap can be observed when the number j of ethoxy units is increased from 0 to 2. From this, one could conclude that the interaction between the CO_2 molecules and the ethoxy groups is not particularly beneficial. However, it must also be considered that the size of the molecule increases with the number of ethoxy groups, which makes it more difficult to mix.

Overall, the phase behavior study of mixtures of CO_2 and the model additives C_4E_j shows that at low temperatures, a complete miscibility of these two components can be achieved at pressures between 6 MPa and 10 MPa. At higher temperatures, higher pressures

are necessary. Considering the application of these mixtures in the CO₂-EOR, where homogeneous supercritical CO₂ enriched with additives is to be pumped into the reservoirs, the additive and supercritical CO₂ should be miscible at pressures not very far above the critical point, i.e. 7.38 MPa. While this is the case for these model additives, the miscibility of CO₂ and a series of amphiphilic additives was studied in one of the next steps. The results are summarized in section 4.2, where the miscibility of CO₂ and the respective additives is compared with the CO₂/(model) crude oil miscibility.

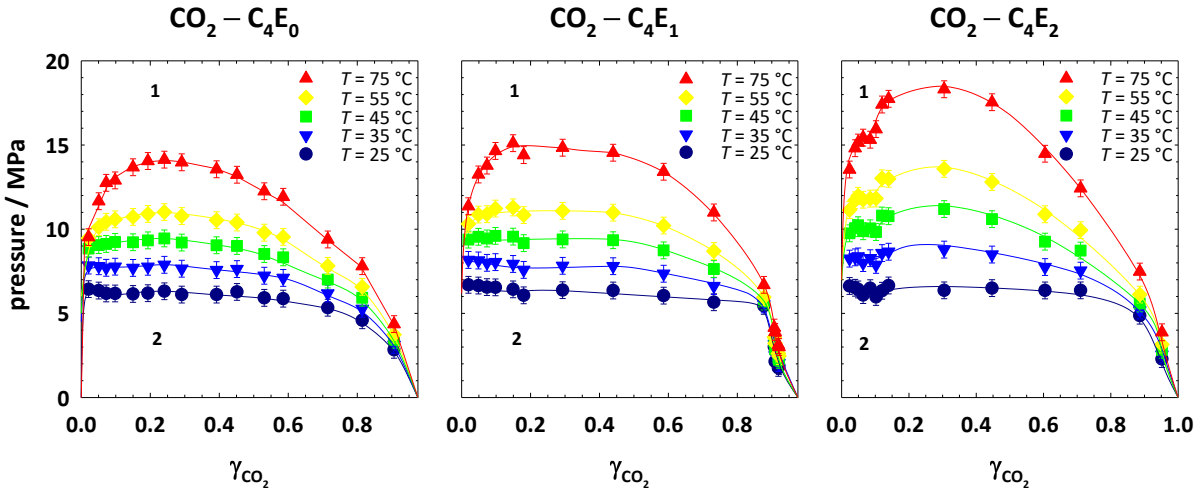


Figure 4.2: $p(\gamma_{\text{CO}_2})$ -diagrams of the systems CO₂ – C₄E_j ($j = 0$ to 2) at five different temperatures ($T = 25$ °C– 75 °C).^{(LW) 2(UF)} All three systems show a lower miscibility gap with similar shape. With increasing number of ethoxy units j , an increasing extension of the miscibility gap is observed.^{2(UF)} Some measurements were carried out by Julian Fischer for his “teaching thesis” and his internship.

4.1.2 CO₂ – (Model) Crude Oils

At the beginning of the study of the pseudobinary system CO₂ – (model) crude oil, a suitable oil had to be selected. Since crude oils are difficult to handle due to their dark color and toxicity, the investigations of this work were to be carried out primarily with model crude oils with comparable properties. For the selection of the model crude oils, a real crude oil provided by Sasol Performance Chemicals GmbH was used as a benchmark. As (model) crude oils are often classified in heavy or light crude oils using the American Petroleum Institute (API) gravity, the API gravity of this real crude oil was determined in the next step. Based on the definitions of the Baumé scales [Chandler, 1881, National Standard Petroleum Oil Tables, 1936], the API gravity is a dimensionless unit given by

$$\text{API gravity} = \frac{141.5}{\text{SG}} - 131.5, \quad (4.1)$$

wherein $SG = \rho_{oil}/\rho_{H_2O}(60\text{ }^\circ\text{F})$, i.e. the specific gravity of the oil relative to water at 60 °F (15.6 °C). The density of water at 15.6 °C and a pressure of one atmosphere is $(0.99901\pm 0.00083)\text{ gcm}^{-3}$ [Tanaka, et al., 2001]. The real crude oil sample used in this thesis showed an API gravity of 38.0 °. It thus can be classified as light crude oil referred to as Asian crude oil 38.0 (aco38.0) in this thesis.

Alkanes and mixtures of them are often used in literature to mimic the properties of crude oils, i.e. phase behavior, interfacial tension and rheology [Christov, Dohrn, 2002, Dohrn, Brunner, 1995, Dohrn, Peper, Fonseca, 2010, Fonseca, Dohrn, Peper, 2011, Fornari, Alessi, Kikic, 1990, Shariati, Peters, Moshfeghian, 1998, Al Ghafri, Maitland, Trusler, 2014]. Since some crude oils have a melting temperature close to room temperature, the longer chain *n*-alkanes *n*-octadecane, *n*-hexadecane and *n*-dodecane might be appropriate model oils to mimic the phase behavior of the pseudobinary system CO₂ – (model) crude oil [Pöhler, Scheidgen, Schneider, 1996, Kordikowski, Schneider, 1993, Zamudio, Schwarz, Knoetze, 2013]. In Figure 4.3, the phase diagrams of these CO₂ – *n*-alkane systems are shown in comparison to the phase diagram of the CO₂ – aco38.0 system at 75 °C and 80 °C. Evaluating the phase behavior of the CO₂ – *n*-alkane systems, all systems show a slightly asymmetric lower miscibility gap. As can be seen, an increasing chain length of the *n*-alkane leads to a strong increase of the miscibility gap, associated with an increasing molecular size of the oil, which makes it more difficult to mix with CO₂. Comparing the phase diagram of the CO₂ – *n*-octadecane system at 75 °C (this work) and 80 °C [Pöhler, Scheidgen, Schneider, 1996], an increasing miscibility gap is found with increasing temperature. As discussed above, the temperature trend is related to the decreasing density of CO₂ with increasing temperature, which leads to weaker interaction between *n*-alkane and CO₂ molecules. A decent overview on the phase behavior of CO₂ – *n*-alkane systems is given in the review of Fonseca, Dohrn and Peper [Fonseca, Dohrn, Peper, 2011].

In contrast to the *n*-alkane systems, the pseudobinary CO₂ – aco38.0 system shows a much more asymmetric lower miscibility gap, where the maximum of the miscibility gap is located at the CO₂-rich side around $w_{oil} \approx 0.075$. The asymmetric shape of the miscibility gap is a consequence of the complex composition of the real crude oil aco38.0 consisting of many different components. To achieve complete miscibility for the system CO₂ – aco38.0 at 75 °C, a pressure of $(36.3\pm 0.5)\text{ MPa}$ is required, while a lower pressure of $(25.1\pm 0.5)\text{ MPa}$ is sufficient for the system CO₂ – *n*-octadecane at 75 °C. Note, while the maximum of the miscibility gap in

binary systems corresponds to the critical point, this is usually not the case for pseudobinary systems. To avoid confusion, the pressure, at which the lower miscibility gap of the pseudobinary and pseudoternary systems closes, is referred to as physical minimum miscibility pressure (MMP_p). A more detailed discussion of the CO_2 – aco38.0 phase diagram will be presented below (see 4.1.2.1) in comparison with the phase diagrams of the model crude oils developed in this thesis.

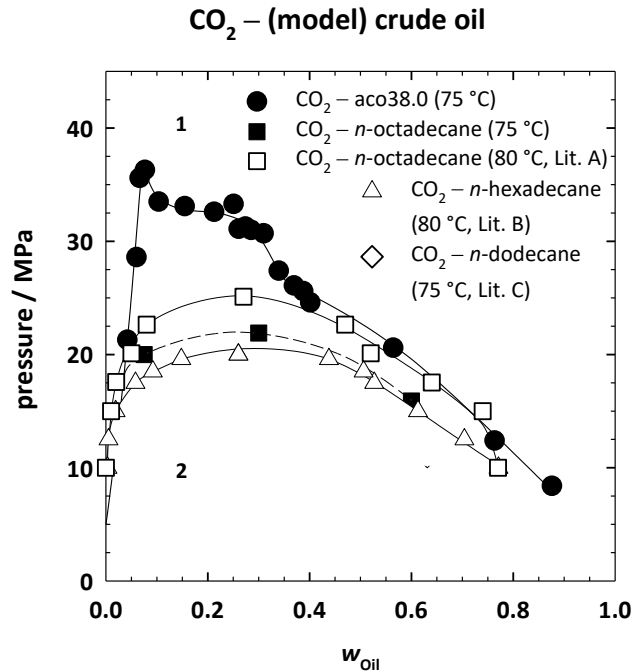


Figure 4.3: Isothermal $p(w_{oil})$ -diagram of the CO_2 – aco38.0 and the three binary CO_2 – n -alkane systems at 75 °C and 80 °C. All systems show a lower miscibility gap. The data points of the unfilled symbols are taken from Pöhler, Scheidgen and Schneider (Lit. A) [Pöhler, Scheidgen, Schneider, 1996], Kardikowski and Schneider (Lit. B) [Kardikowski, Schneider, 1993] and Zamudio, Schwarz, and Knoetze (Lit. C) [Zamudio, Schwarz, Knoetze, 2013]. The miscibility gap of the pseudobinary CO_2 – aco38.0 system is significantly more asymmetric than that of the binary model systems.

Above all, the clearly different shape of the lower miscibility gap in binary CO_2 – n -alkane systems and the pseudobinary CO_2 – aco38.0 system prove that pure n -alkanes are not suitable as model oil for crude oils. Therefore, the next step was to develop model crude oils composed of a more complex mixture of linear and branched alkanes, cycloalkanes as well as aromatics (see 4.1.2.1). Although consisting of several components, the model crude oils as well as the aco38.0 are considered as one pseudo-component in this thesis.

Based on the reservoir conditions of interest, the phase behavior studies in this thesis were usually measured above the critical point of CO_2 ($T_c = (30.978 \pm 0.015) \text{ } ^\circ\text{C}$, $p_c = (7.377 \pm 0.003) \text{ MPa}$ [Span, Wagner, 1996]). However, also oil fields with low reservoir

temperatures and pressures exist. Phase behavior studies of the CO₂ – aco38.0 system at a temperature and pressures below T_c and p_c of CO₂ are summarized in chapter 7.6.

4.1.2.1 Development of Model Crude Oils

As mentioned above crude oils, such as aco38.0, are difficult to handle due to their dark color and toxicity. Moreover, a known composition allows easier analysis of the obtained experimental data. In order to learn about the properties of an oil and its miscibility with CO₂ under reservoir pressure and temperature conditions, it is essential when selecting the composition of a model crude oil that model crude oil and crude oil have similar properties. The phase diagrams shown above clearly show that binary mixtures of CO₂ and *n*-alkanes behave differently than pseudobinary mixtures of CO₂ and the real crude oil aco38.0.

Inspired by Vitu et al. and Al Ghafri et al., who used synthetic mixtures of linear and branched alkanes (paraffins), cyclo-alkanes (naphthenes), as well as aromatics [Vitu, et al., 2007, Al Ghafri, Maitland, Trusler, 2014] as model oils to measure phase behavior, in a first attempt, a model crude oil was developed consisting of 60 wt% of short and medium-chain paraffins, 28 wt% of naphthenes and 12 wt% of aromatics. Measuring the density of this multi-component model crude oil at 15.6 °C, a density of $\rho = (0.777 \pm 0.001) \text{ g cm}^{-3}$ was obtained resulting in an API gravity of 51.4 °. It thus can be classified as very light crude oil referred to as mco51.4. As expected due to the rather low density of the oil, the CO₂ – mco51.4 system has a lower miscibility gap, which is smaller than the miscibility gap of the CO₂ – *n*-dodecane system (see 7.3) and thus compared even worse to the aco38.0 than all other model crude oils tested so far.

In order to adjust the miscibility properties of the model crude oil to those of a real crude oil, such as aco38.0, the composition of the model crude oil had to be changed to achieve a smaller value of the API gravity and a larger density, respectively. In the search for suitable components, the Sasolwax 5805 (71.3 wt% *n*-alkanes and 28.7 wt% iso-alkanes (see Figure 3.1)), characterized by an average number of carbon atoms of 30.5, was identified as an optimal candidate to adjust stepwise the API grade of a model crude oil. Using a pycnometer (for details e.g. to avoid solidification of the (model) crude oils, see 3.2.3), the density of Sasolwax 5805 was determined to be 0.918 g cm^{-3} at 15.6 °C, which corresponds to an API gravity of 22.6 ° (see Table 4.1).

For the further investigations of this thesis, a first model crude oil was successfully developed by using 30.0 wt% Sasolwax 5805 as well as 41.1 wt% paraffins, 20.7 wt% naphthenes, and 8.2 wt% aromatics. Measurements of the density resulted in an API gravity of 47.0 ° (Table 4.1). Because of this high value, the model crude oil, referred to as mco47.0, can be classified as very light crude oil. In order to develop a model crude oil with a density close to that of aco38.0, the wax content could have been further increased. Since such high fractions of *n*-alkanes are not observed in real crude oils, the fraction of aromatics was increased at the expense of the shorter-chain *n*-alkanes. The resulting second model crude oil of this work thus consisted of 30.0 wt% Sasolwax 5805, 16.1 wt% paraffins, 20.0 wt% naphthenes, and 33.9 wt% aromatics. Here, measurements of the density led to an API gravity of 38.8 ° (Table 4.1). Therefore, this model crude oil, referred to as mco38.8, which is also still a light crude oil, is similar in density to the Asian crude oil aco38.0. The detailed compositions of the model crude oils are shown as pie charts in Figure 4.4, mco47.0 at the top and mco38.8 below.

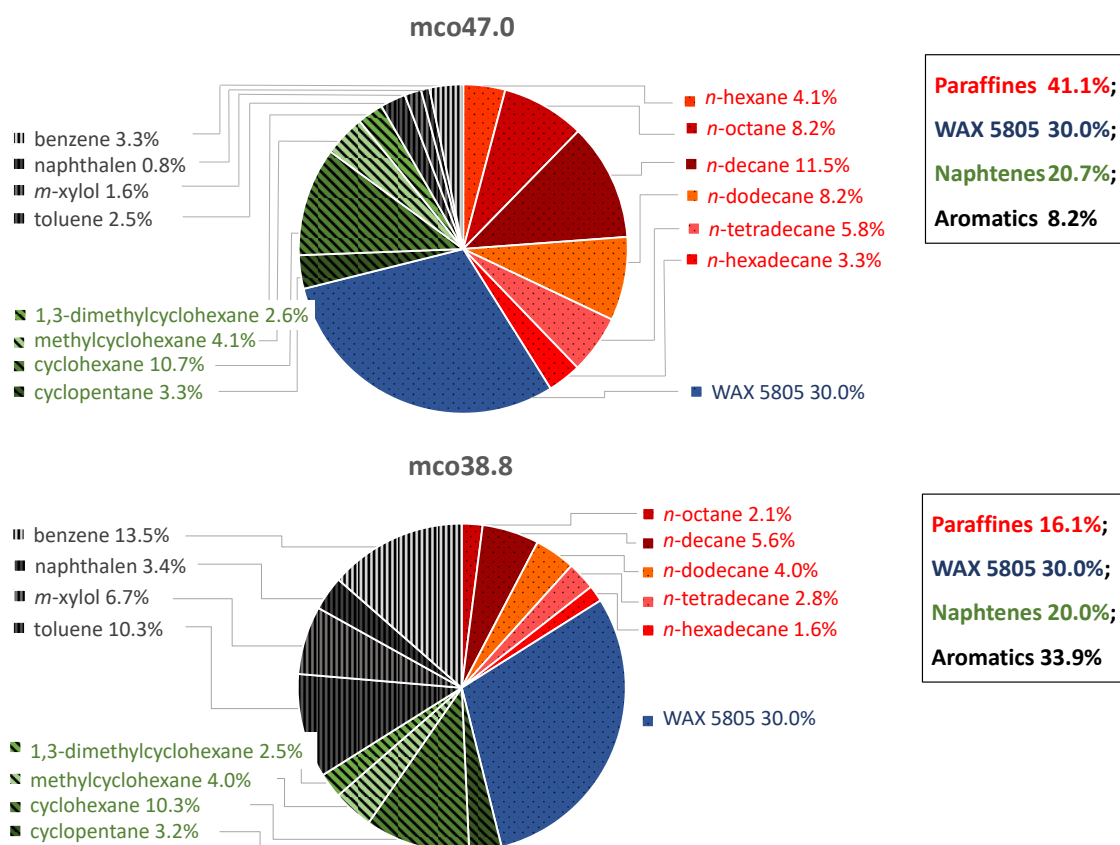


Figure 4.4: Compositions of mco47.0 (top) and mco38.8 (bottom) in wt%.

In conclusion, according to the API gravity classification, the three developed model crude oils are light crude oils (API > 31.1 °). Thereby, the model crude oil mco38.8 and the

Asian crude oil aco38.0 exhibit similar API gravities (Table 4.1). Note that due to the addition of Sasolwax 5805, which has a melting temperature of $T_m = (59.0 \pm 1.0)^\circ\text{C}$, the model crude oils mco47.0 and mco38.8 exhibit a relatively high melting point $T_m = (45.0 \pm 1.0)^\circ\text{C}$ and $T_m = (55.0 \pm 1.0)^\circ\text{C}$, respectively.

Table 4.1: Compositions, densities and API gravities of the model crude oils (mco), Asian crude oil (aco38.0) and Sasolwax 5805. Compared to mco47.0, mco38.8 contains 25.05 wt% less paraffins and 0.62 wt% less naphthenes, while the fraction of aromatics is increased by 25.67 wt%. Thus, mco38.8 exhibits an increased density and therefore a lower API gravity, which is similar to the Asian crude oil aco38.0.

(Model) Crude Oil	Paraffins / wt%	Sasolwax 5805 / wt%	Naphthenes / wt%	Aromatics / wt%	ρ (15.6 °C) / gcm ⁻³	API Gravity / °
mco51.4	60.68	0	28.06	11.26	0.777±0.001	51.4±0.2
mco47.0	41.11 ^a	30.00	20.62 ^a	8.27 ^a	0.792±0.001	47.0±0.4
mco38.8	16.06 ^b	30.00	20.00 ^b	33.94 ^b	0.830±0.001	38.8±0.4
aco38.0	†	0	†	†	0.834±0.002	38.0±0.7
Sasolwax 5805	0	100*	0	0	0.918±0.003	22.6±0.5

^aFor more details, see Figure 4.4 top. ^bFor more detail, see Figure 4.4 bottom. [†]unknown composition. *71.3 wt% of *n*-alkanes and 28.7 wt% of iso-alkanes (for details, see Figure 3.1).

After the development of model crude oils with known composition, their mixing behavior with CO₂ was investigated in the next step. For this purpose, the phase behavior of the pseudobinary systems CO₂ – mco47.0 and CO₂ – mco38.8 was measured and compared with that of the system CO₂ – aco38.0. As described in the previous chapter, the two-phase to one-phase boundary of various samples with an oil mass fraction (w_{oil}) of 0.032 to 0.876 was determined as a function of pressure and temperature between 65 °C and 80 °C. This relatively narrow temperature range results on the one hand from the high melting temperature of the model crude oils containing Sasolwax 5805 and on the other hand from the limited tightness of the HP-cell as well as safety aspects at high temperatures. Note that in the one-phase region close to the phase boundary, often a weak turbidity was observed most likely induced by poorly soluble longer chain *n*-alkanes or asphaltenes [Gonzalez, et al., 2008]. However, this weak turbidity was clearly distinguishable from the strong turbidity of the samples observed in the two-phase region.

In Figure 4.5, the phase behavior of all three systems at 65 °C and 75 °C is shown in form of $p(w_{oil})$ -diagrams. All three systems show a lower miscibility gap of comparable asymmetric shape, which runs through a maximum, referred to as physical minimum miscibility pressure (MMP_p), at low values of $w_{oil,p}$ (marked by a dashed line). Comparing the phase diagrams of the three systems in more detail, the miscibility gap of the CO₂ – aco38.0

system has a significantly wider shape than the miscibility gap of the two CO₂ – model crude oil systems, which are very similar. Here, the miscibility gap of the mco38.8 system is further extended towards high pressures and thus has a higher MMP_p at about 40 MPa. The MMP_p values of all systems are compiled in Table 4.2. The lowest value is found for the system with the highest API gravity, i.e. for the CO₂ – mco47.0 system at 75 °C. Interestingly, the MMP_p value of the CO₂ – aco38.0 system at 75 °C lies between those of the two model crude oil systems.

Furthermore, for all systems, a similar temperature dependence of the phase behavior is found. Interestingly, a smaller expansion of the miscibility gap is observed at low values of w_{oil} at 75 °C than at 65 °C. This finding is the opposite of what was expected according to the trends observed so far and might be due to the crystallization of long-chain *n*-alkanes (components of Sasolwax 5805) or asphaltenes at low temperatures and high CO₂ contents [Srivastava, Huang, 1997, Takahashi, et al., 2003, Verdier, et al., 2006, Gonzalez, et al., 2008]. However, on the oil-rich side of the phase diagram, i.e. at large values of w_{oil} , the normal temperature trend is found, i.e. the extension of the miscibility gap increases with increasing temperature. As mentioned above, this trend can be explained by the decreasing CO₂ density as a function of temperature, which has to be compensated by increasing the pressure. Furthermore, and interestingly, the two phase boundaries, recorded at different temperatures, cross similarly to an "isosbestic" point, at $w_{oil} \approx 0.300$. In summary, both model crude oils show an overall similar phase behavior as the aco38.0 with respect to the asymmetric shape and the temperature-dependence of the lower miscibility gap as well as the MMP_p.

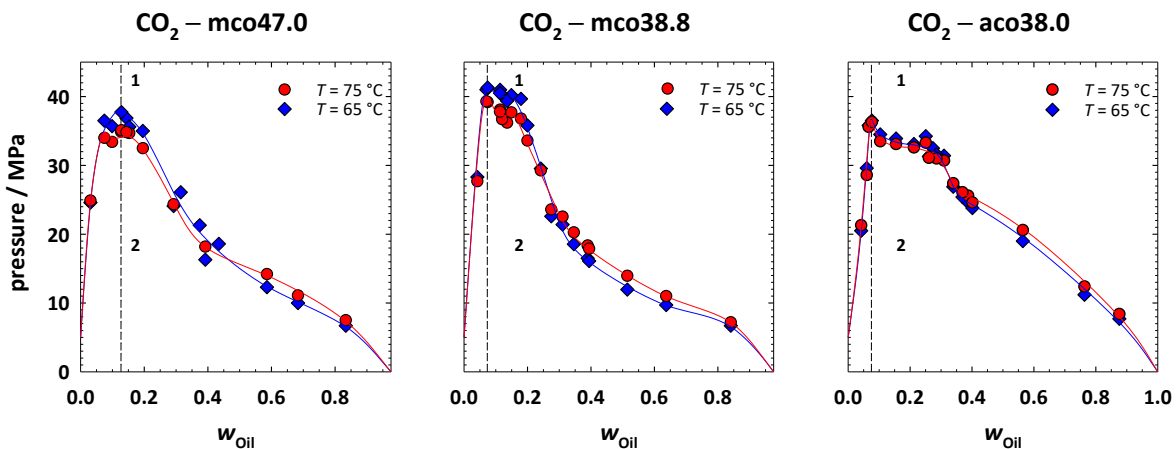


Figure 4.5: $p(w_{oil})$ -phase diagrams of the systems CO₂ – mco47.0, CO₂ – mco38.8 and CO₂ – aco38.0 at 65 °C and 75 °C.^(JF) All three systems show an asymmetric lower miscibility gap, which runs through a maximum, the physical minimum miscibility pressure (MMP_p), at low values of w_{oil} indicated by the dashed lines. Note, that the miscibility gap of the system CO₂ – aco38.0 exhibits a larger extension at high values of w_{oil} .

Table 4.2: MMP_p and $w_{oil,p}$ of the three systems CO₂ – mco47.0, CO₂ – mco38.8 and CO₂ – aco38.0 at 65 °C and 75 °C.

System	CO ₂ – mco47.0 $w_{oil,p} = 0.130 \pm 0.010$	CO ₂ – mco38.8 $w_{oil,p} = 0.075 \pm 0.010$	CO ₂ – aco38.0 $w_{oil,p} = 0.075 \pm 0.010$
Temperature / °C	MMP _p / MPa		
75	35.1±0.5	39.3±0.5	36.3±0.5
65	37.8±0.5	41.3±0.5	36.5±0.5

Besides the MMP_p, for both, fundamental research and technical application, the location of the critical point, which is often referred to as plait point in ternary or multi-component systems [Kahlweit, et al., 1987, Hand, 1930], is of great interest. From the CO₂-EOR point of view, a pressure between the pressure p_c of the plait point and the MMP_p enables a multiple-contact miscibility (MCM) process, which allows to increase the recovery rates of the oil in place (OIP).

For some of the pseudobinary and pseudoternary systems studied in this thesis, critical (plait) points were determined by setting, for a constant temperature, the composition and pressure, at which two phases of equal volume, i.e. a lower oil-rich phase and an upper CO₂-rich phase coexist. The other condition of a critical point, i.e. the same composition of the two coexisting phases, was not investigated. Instead, the critical opalescence expected near a plait point was verified.

In Figure 4.6, the plait points of the three CO₂ – (model) crude oil systems determined in this way at 65 °C are shown in the $p(w_{oil})$ -diagrams. Top right, additional photos of samples of the CO₂ – mco38.8 system and sketches of the coexisting phase volumes are shown to illustrate the determination of the plait point, which is located at a critical oil mass fraction of $w_{oil,c} = 0.38 \pm 0.02$ and a critical pressure of $p_c = (17.2 \pm 0.5)$ MPa.

Preparing a sample at the critical composition and adjusting a pressure above the critical pressure ($p > p_c$) an only weakly scattering one-phase sample is obtained (Figure 4.6 (A)). Approaching the critical pressure, the occurrence of critical opalescence was observed (Figure 4.6 (B)), which is, as mentioned above, a strong indication for the vicinity of a critical point [Kahlweit, et al., 1987]. If the pressure is reduced to or slightly below the critical value, the mixture separates into two likewise strongly scattering phases with almost the same volume (taking into account the volume of the stirring bar, Figure 4.6 (D)). When leaving the critical composition and preparing a sample $w_{oil} < w_{oil,c}$, the formation of a lower oil-rich phase is observed when passing the phase boundary coming from high pressures (Figure 4.6 (C)). In

the CO₂-EOR nomenclature, this is called condensation of oil droplets within the CO₂-rich phase and the process is referred to as “dew-point” behavior. If a sample with $w_{\text{Oil}} > w_{\text{Oil},c}$ is examined, the formation of an upper CO₂-rich phase is observed when the two-phase region is entered from high pressure (Figure 4.6 (E)). Here, bubbles of the CO₂-rich phase rise in the oil-rich phase leading to the CO₂-EOR term “bubble-point” behavior.

Interestingly, the plait point is located at similar $w_{\text{Oil},c}$ for all three CO₂ – (model) crude oil systems. However, differences in the critical pressure were determined. While the systems CO₂ – mco47.0 and CO₂ – mco38.8 show similar values of the critical pressure, i.e. $p_c = (18.5 \pm 0.5)$ MPa and $p_c = (18.8 \pm 0.5)$ MPa, respectively, a larger value of $p_c = (25.6 \pm 0.5)$ MPa is found for the CO₂ – aco38.0 system at 75 °C. The plait points determined at 65 °C, 70 °C, and 75 °C are compiled in Table 4.3.

Table 4.3: Locations of the plait (critical) points given by the values of the critical pressure (p_c) and critical oil mass fraction ($w_{\text{Oil},c}$) of the systems CO₂ – mco47.0, CO₂ – mco38.8 and CO₂ – aco38.0 at 65 °C, 70 °C and 75 °C.

System	CO ₂ – mco47.0 $w_{\text{Oil},c} = 0.39 \pm 0.02$	CO ₂ – mco38.8 $w_{\text{Oil},c} = 0.38 \pm 0.02$	CO ₂ – aco38.0 $w_{\text{Oil},c} = 0.39 \pm 0.02$
Temperature / °C	p_c / MPa		
75	18.5 ± 0.5	18.8 ± 0.5	25.6 ± 0.5
70	20.0 ± 0.5	18.2 ± 0.5	25.0 ± 0.5
65	20.0 ± 0.5	17.2 ± 0.5	24.6 ± 0.5

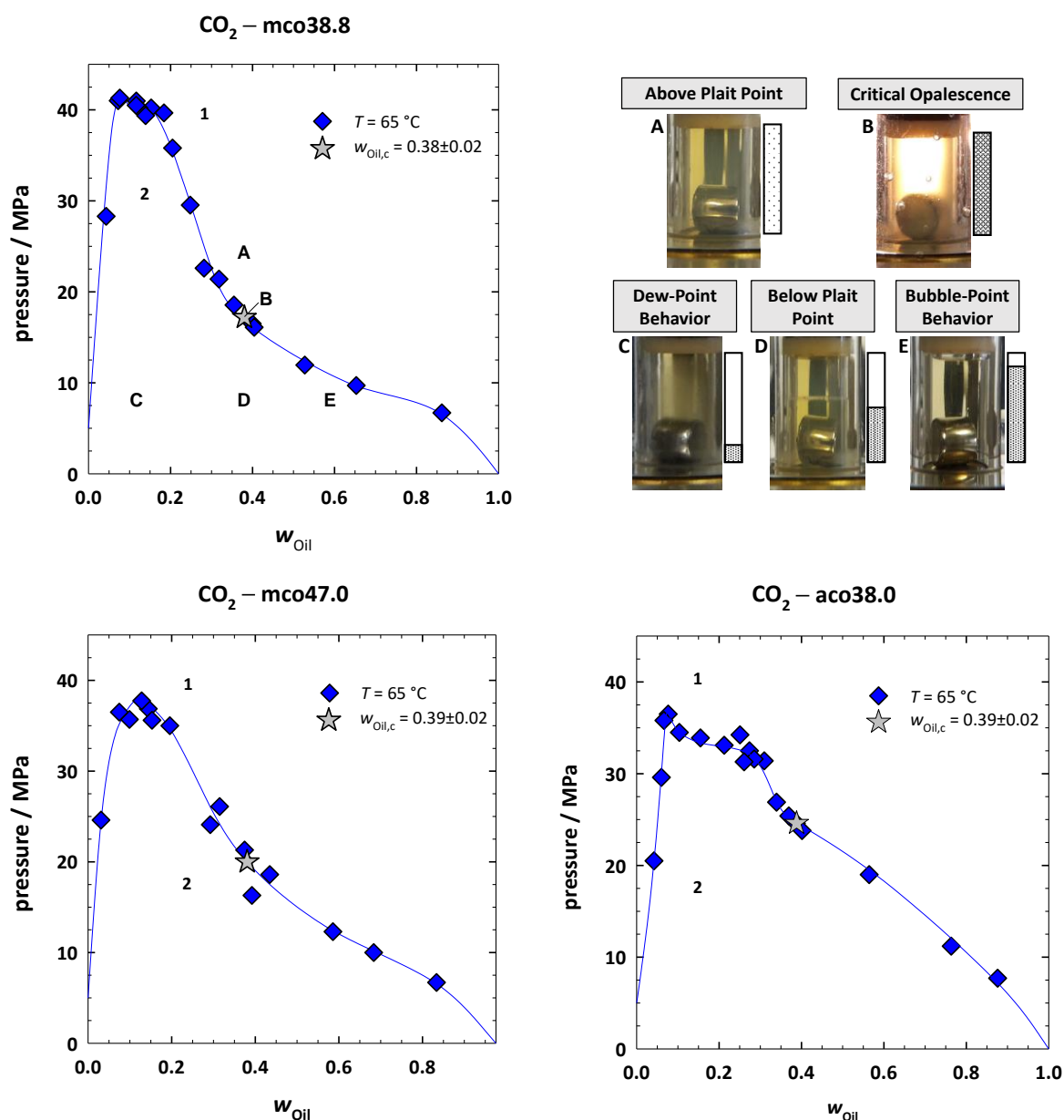


Figure 4.6: $p(w_{\text{Oil}})$ -phase diagrams of the systems $\text{CO}_2 - \text{mco47.0}$, $\text{CO}_2 - \text{mco38.8}$ and $\text{CO}_2 - \text{aco38.0}$ with plait (critical) points at 65°C .^(F) For all three systems, the plait point is located at around $w_{\text{Oil},c} = 0.39 \pm 0.02$. The $\text{CO}_2 - \text{aco38.0}$ system exhibits the highest critical pressure of $p_c = (24.6 \pm 0.5)$ MPa, see Table 4.3. The appearance of a $\text{CO}_2 - \text{mco38.8}$ sample at the critical composition is shown clearly above (A) and at (B) as well as slightly below (D) the critical pressure in the photos. Additional photos show the “dew-point” (C) and “bubble-point” (E) behavior of samples prepared at $w_{\text{Oil}} < w_{\text{Oil},c}$ and $w_{\text{Oil}} > w_{\text{Oil},c}$, respectively. Furthermore, sketches indicate the corresponding volumes of the phases.

To allow for a better comparison of the phase behavior of the three different systems and to highlight potential differences and similarities, a different representation of the miscibility gaps is additionally shown in Figure 4.7 by plotting the ratio of the pressure p to the MMP_p against the oil mass fraction w_{Oil} divided by $w_{\text{Oil},c}$. While at low $w_{\text{Oil}}/w_{\text{Oil},c}$ values the reduced miscibility gaps of the three systems lie almost on top of each other, at higher $w_{\text{Oil}}/w_{\text{Oil},c}$ values especially the reduced miscibility gap of the $\text{CO}_2 - \text{aco38.0}$ exhibits a much

larger extension. As mentioned above, this effect is possibly caused by the presence of asphaltenes in the Asian crude oil, which reduces its miscibility with CO₂. Comparing the different temperatures, smaller differences between the miscibility gaps are observed at 75 °C than at 65 °C (the area highlighted in gray in Figure 4.7 at 75 °C is smaller compared to 65 °C). In conclusion, the most important properties for the development of appropriate model crude oils for CO₂-EOR projects were reached by matching the MMP_p as well as the plait point of the aco38.0.

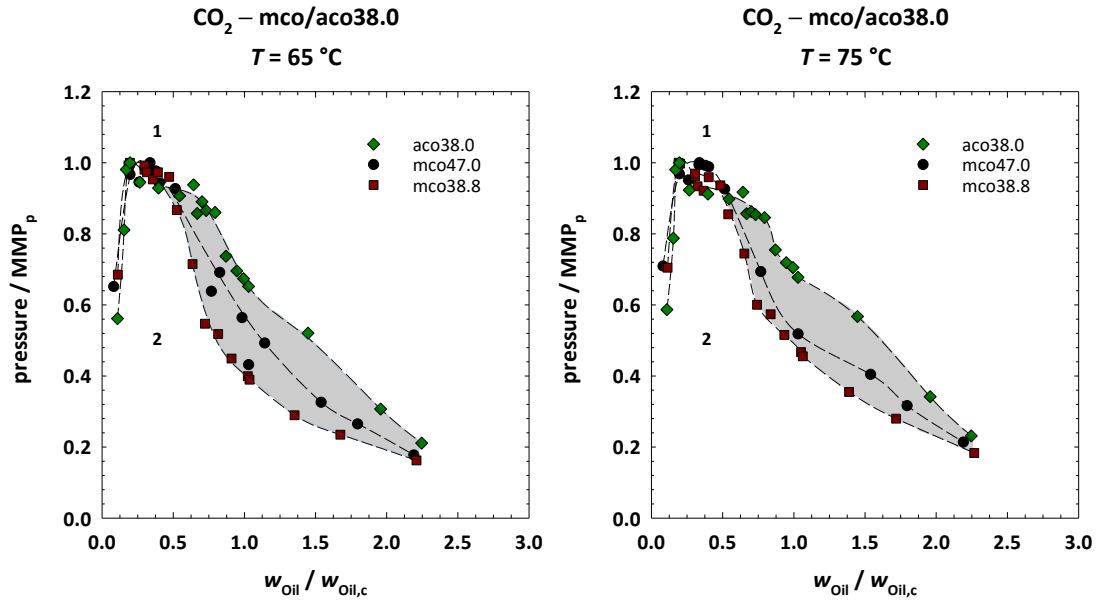


Figure 4.7: Scaled representation of the miscibility gaps of the systems CO₂ – mco47.0, CO₂ – mco38.8, and CO₂ – aco38.0 at 65 °C and 75 °C. By plotting p/MMP_p versus the mass fraction $w_{Oil}/w_{Oil,c}$, the phase boundaries lie almost on top of each other at the CO₂-rich side of the phase diagram, while larger differences (highlighted in gray) are found at intermediate values of $w_{Oil}/w_{Oil,c}$.

Because of safety regulations at the Rice University, which do not allow benzene in flow experiments, another model crude oil without benzene had to be developed for the slim tube studies performed in the group of Prof. Dr. G. Hirasaki (see chapter 4.8). Thus, the 13.5 wt% of benzene in the model crude oil mco38.8 were replaced by toluene and *m*-xylene increasing their fractions from 10.3 wt% to 18.8 wt% and 6.7 wt% to 11.8 wt%, respectively. Determining the density of the adapted model crude oil, a slightly decreased API gravity of 38.0 ° is obtained. Following the nomenclature used so far, the oil is named mco38.0. The densities, API gravities, and the changed composition of the aromatic content for the two model crude oils mco38.8 and mco38.0 are shown in Table 4.4.

Table 4.4: Densities, API gravities, MMP_p and the composition of the aromatic content of mco38.0 and mco38.8. Based on mco38.8, benzene was replaced by toluene and *m*-xylene increasing their fractions to obtain the benzene-free model crude oil mco38.0. Note that mco38.0 exhibits a slightly larger density and consequently a slightly lower API gravity.

Model crude oil	Benzene / wt%	Naphthalene / wt%	<i>m</i> -Xylene / wt%	Toluene / wt%	$\rho(15.6\text{ }^\circ\text{C})$ / gcm ⁻³	API gravity / °	MMP _p (65 °C) / MPa
mco38.8	13.5 ^a	3.4	6.7	10.3	0.830±0.001	38.8±0.4	41.3±0.5
mco38.0	0 ^b	3.4	11.8	18.8	0.834±0.001	38.0±0.3	40.4±0.5

In order to compare the miscibility-enhancing effect of amphiphilic additives studied for the three systems CO₂ – mco47.0, CO₂ – mco38.8 and CO₂ – aco38.0 with the results of the slim tube studies performed on the system CO₂ – mco38.0, it would be desirable that the systems CO₂ – mco38.8 and CO₂ – mco38.0 exhibit similar phase behavior. For verification, the phase boundary of the slim tube system CO₂ – mco38.0 was studied at three compositions, i.e. close to the composition of the MMP_p ($w_{\text{Oil},p} = 0.076 \pm 0.001$), the plait point ($w_{\text{Oil},c} = 0.397 \pm 0.001$) and at $w_{\text{Oil}} = 0.146 \pm 0.001$. In Figure 4.8, the phase diagrams of the two systems are compared at 65 °C. As can be seen, the data points of the slim tube system CO₂ – mco38.0 agree almost quantitatively with the phase boundary of the CO₂ – mco38.8 system, suggesting that both systems have a plait point that is equal within the measurement error. Therefore, the results of studies performed with the CO₂ – mco38.8 system can be directly compared with the results of the dynamic slim tube measurements performed with the CO₂ – mco38.0 system.

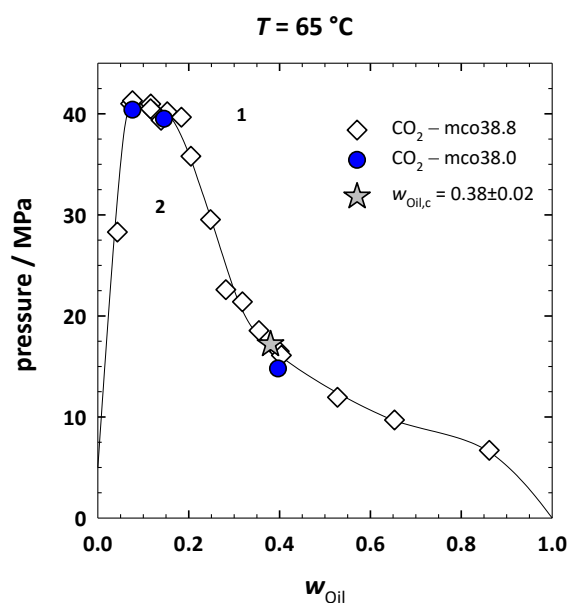


Figure 4.8: $p(w_{\text{Oil}})$ -phase diagram of the systems CO₂ – mco38.8 and CO₂ – mco38.0 at 65 °C. The changes of the composition of the aromatic content in the model crude oil have almost no effect on the phase behavior, suggesting that both systems have a plait point that is equal within the measurement error. Thus, results of studies performed on the CO₂ – mco38.8 system can be directly compared with the results from the dynamic slim tube measurements performed with the CO₂ – mco38.0 system.

4.2 Comparison of CO₂ – Additive and CO₂ – (Model) Crude Oil Systems

The aim of this thesis was to find additives that improve the miscibility of CO₂ and crude oils. To achieve this goal, the first requirement is that the additive and supercritical CO₂ must be miscible at the production pressure so that homogeneous CO₂/additive mixtures can be pumped into the reservoirs. Secondly, CO₂ and additive should be more miscible than CO₂ and crude oil, which is supposed to be improved by the additive. After the development of several (model) crude oils and the study of their phase behavior with CO₂ in the previous section, the phase behavior of 16 (pseudo-)binary CO₂ – additive systems (including the 3 systems shown in 4.1.1) was investigated to not only find additives with a reasonable CO₂ miscibility, but also to obtain a correlation between the molecular structure of the amphiphilic additives and the CO₂ miscibility. Therefore, $p(T)$ -phase diagrams were recorded for different additive mass fractions in CO₂ ranging from $\gamma_{\text{CO}_2} = 0.020$ to $\gamma_{\text{CO}_2} = 0.850$.

All phase diagram data of the CO₂ – additive systems are summarized in Table 7.2 in the appendix. At this point, a temperature of 65 °C was chosen to compare the miscibility of the different additives with CO₂ at an additive mass fraction of $\gamma_{\text{CO}_2} = 0.075 \pm 0.004$ and to relate it to the miscibility of the (model) crude oils at an oil mass fraction $w_{\text{oil}} = 0.075 \pm 0.004$. The phase transition pressures at these compositions, which correspond approximately to the MMP_p, are shown in Figure 4.9, in black for the CO₂ – additive systems and in blue for the CO₂ – (model) crude oil systems including the systems CO₂ – *n*-dodecane [Zamudio, Schwarz, Knoetze, 2013] and CO₂ – *n*-octadecane for comparison.

First, the trends found for the CO₂ – additive systems were analyzed. It can be seen that at a temperature of 65 °C especially the alkoxyated butanol derivatives (with the exception of C₄E₄) and also the propoxylated hexanol derivate C₆P₃ as well as the branched alcohols ISOFOL 12P₄ and IDTAP₄ show full miscibility with CO₂ at pressures below 22.0 MPa. Additives with a longer alcohol chain length (ISOFOL 16P₄), alkylphenol ethoxylates (MARLOPHEN P₄) and alcohol ether carboxylates (e.g. TDA+5POC) show a considerably poorer miscibility with CO₂. In addition, the amine containing triethanolamine (TEA) and triisopropanolamine (TIPA) showed no miscibility with CO₂ in the accessible pressure range. Note that the maximum adjustable pressure of the high pressure visual cell at the time these additives were studied was 35.0 MPa (marked with a * in Figure 4.9). Interestingly, although the API gravity of aco38.0 and mco38.8 are very similar, the phase transition pressure of the aco38.0 at $w_{\text{oil}} = 0.075 \pm 0.002$ is more in the range of the less dense model crude oil mco47.0.

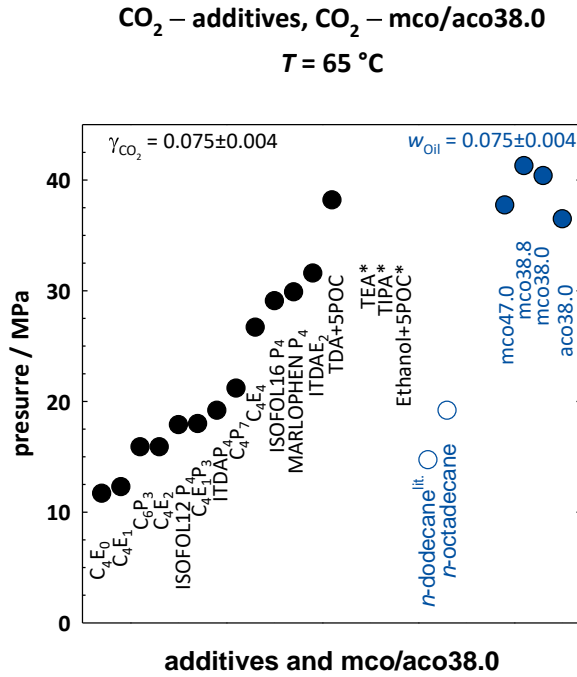


Figure 4.9: Overview of the phase transition pressures of the 16 (pseudo-)binary CO₂ – additive systems at $\gamma_{\text{CO}_2} \approx 0.075$ (black circles) and the 6 pseudobinary CO₂ – (model) crude oil systems at $w_{\text{Oil}} \approx 0.075$ (blue circles) at 65 °C. The best miscibility with CO₂ was found for the alkoxyated additives of the type C₄E_i, C₄P_x and C₄E_iP_x ($i, x < 4$), the propoxylated linear alcohol C₆P₃, as well as the propoxylated branched alcohols ISOFOL 12P₄ and ITDAP₄. Alkyl phenol ethoxylates, such as MARLOPHEN P₄ and the alcohol ether carboxylate TDA+5POC, as well as TEA and TIPA showed considerably poorer miscibility (* maximum adjustable pressure was 35.0 MPa). The miscibility behavior of the systems CO₂ – *n*-dodecane [Zamudio, Schwarz, Knoetze, 2013] and CO₂ – *n*-octadecane (unfilled circles) is shown for comparison.

The phase transition pressures of all CO₂ – (model) crude oil systems lie in a range between 38.0 MPa and 42.0 MPa. Comparing these values with the phase transition pressures of the CO₂ – additive systems, especially the alkoxyated butanol and hexanol derivatives as well as some of the longer-chain, but branched and propoxylated alcohol derivatives (ISOFOL 12P₄ and ITDAP₄) show considerably lower transition pressures.

One may assume very simplistically that the MMP_p of the pseudoternary system can be approximated similar to Dalton's law by

$$\text{MMP}_p(\text{CO}_2 - \text{Oil} - \text{Additive}) \approx x_{\text{Additive}} \text{MMP}_p(\text{CO}_2 - \text{Additive}) + x_{\text{Oil}} \text{MMP}_p(\text{CO}_2 - \text{Oil}), \quad (4.2)$$

where the x_i are the mole fractions of additive and mco in their mixture. Based on this approximation, it can be expected that most of the additives investigated should lead to a lowering of the MMP_p and thus to better miscibility of CO₂ and model crude oil. A systematical investigation of the effect of different additives in pseudoternary systems will be discussed in detail in chapter 4.5.

Furthermore, the miscibility of additives at room temperature is of great interest for the technical application. The investigations so far showed a complete miscible behavior of the investigated additives with CO₂ at room temperature for pressures above the critical pressure of CO₂. Accordingly, it should be possible to mix any amount of additive by co-injecting with CO₂ into the reservoirs. However, it is clear that both from an ecological and an economic point of view, the goal is to use the lowest possible mass fraction of the additive in the CO₂. Realistic concentrations are therefore around 1 wt%.

4.3 Pseudoternary Systems

Having determined the phase behavior of the pseudobinary side systems in the previous sections, this subchapter is focused on understanding the complex phase behavior of the pseudoternary systems CO₂ – (model) crude oil – additive. In Figure 4.10, the phase behavior of the three pseudobinary side systems is represented schematically as an unfolded phase prism at constant temperature. For the temperature range (temperatures above the high melting point of the wax component in the model crude oils ($T_m = (59.0 \pm 1.0) \text{ }^\circ\text{C}$) and pressure range investigated in this work, the two side systems containing CO₂ show a lower miscibility gap (see 4.1 and 4.2). It can be seen that the miscibility gap of the pseudobinary CO₂ – (model) crude oil system is very asymmetric due to the complex composition of the oil and has its critical point not at the maximum, but on the right side of the miscibility gap. Note that the non-ideal behavior of this system is also indicated by the inclined tie lines. The (pseudo-)binary systems CO₂ – additive show a much smaller, only slightly asymmetric miscibility gap due to the fact that pure alcohols or alkoxyated alcohols were used. Although the latter show a distribution in the degree of alkoxylation, their composition is not as complex as that of the (model) crude oils. In contrast, complete miscibility with the (model) crude oil was observed for most additives.

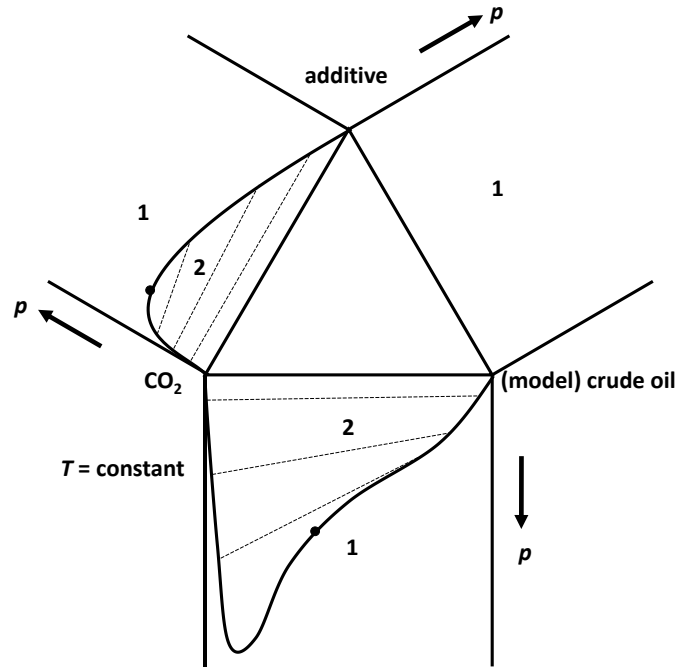


Figure 4.10: Unfolded schematic phase triangle showing the three (pseudo-)binary side systems at constant temperature. While the two (pseudo-)binary side systems CO_2 – (model) crude oil and CO_2 – additive show a lower miscibility gap, complete miscibility with the (model) crude oil is found for most additives in the temperature and pressure range studied. Note that the non-ideal behavior especially of CO_2 – (model) crude oil is reflected by the location of the critical point and the inclined tie lines.

Folding the unfolded phase prism (Figure 4.10) results in a phase prism (Figure 4.11), which shows the overall pressure-dependent phase behavior of pseudoternary systems. Each point in this phase prism is clearly defined by the pressure p and two composition variables (w_{oil} and γ_{CO_2}) for a given temperature T . Inspired by Kahlweit and Strey [Kahlweit, Strey, 1985], the phase behavior of this complex pseudoternary systems was studied by recording sections through this phase prism. For this purpose, the phase boundaries were measured as function of pressure p and oil mass fraction w_{oil} keeping the additive mass fractions γ_{CO_2} in the CO_2 /additive mixture constant. Such a $p(w_{\text{oil}})$ -section is drawn in the schematic phase prism shown in Figure 4.11 (left), which is based on the phase behavior of the systems studied in this thesis. For each composition studied, the phase boundary was determined for various temperatures between 55 °C and 75 °C. This temperature range results from typical oil reservoir conditions, the melting temperature of the developed model crude oils and the limitation of the high pressure view cell.

Note that in this thesis, such a systematic study of the phase behavior was performed only for a few pseudoternary systems. The influence of most additives on the CO_2 – (model) crude oil miscibility was determined only near the characteristic MMP_p composition (see

below). One system, for which the phase behavior was systematically investigated, was the system $\text{CO}_2 - \text{mco47.0} - \text{C}_4\text{E}_1\text{P}_3$. It was chosen because the model crude oil mco47.0 has an MMP_p similar to the Asian crude oil aco38.0, and because the alkoxyated additive $\text{C}_4\text{E}_1\text{P}_3$ shows reasonable miscibility with CO_2 (subchapter 4.2). The effect of $\text{C}_4\text{E}_1\text{P}_3$ on the miscibility gap of the $\text{CO}_2 - \text{mco47.0}$ system was investigated between 55°C and 75°C , where $p(w_{\text{oil}})$ -sections were measured at different mass fractions γ_{CO_2} of $\text{C}_4\text{E}_1\text{P}_3$ in the $\text{CO}_2/\text{C}_4\text{E}_1\text{P}_3$ mixture, i.e. at $\gamma_{\text{CO}_2} = 0.020, 0.050, 0.100, \text{ and } 0.150$. The remarkable extent of the miscibility-enhancing effect of $\text{C}_4\text{E}_1\text{P}_3$ is shown in Figure 4.11 at 65°C . It can be seen that small mass fractions of $\text{C}_4\text{E}_1\text{P}_3$ in the $\text{CO}_2/\text{C}_4\text{E}_1\text{P}_3$ mixture lead to a large reduction of the $\text{CO}_2 - \text{mco47.0}$ miscibility gap, especially on the CO_2 -rich side of the phase diagram, i.e. for oil mass fractions $w_{\text{oil}} < 0.600$. Remarkably, already at a small value of $\gamma_{\text{CO}_2} = 0.022 \pm 0.002$, the maximum of the miscibility gap, i.e. the physical minimum miscibility pressure MMP_p , is significantly lowered from (36.5 ± 0.5) MPa to (28.8 ± 0.5) MPa. By increasing γ_{CO_2} to 15 wt%, the MMP_p (located at $w_{\text{oil}} = 0.075 \pm 0.003$) is further strongly decreased to (15.2 ± 0.5) MPa.

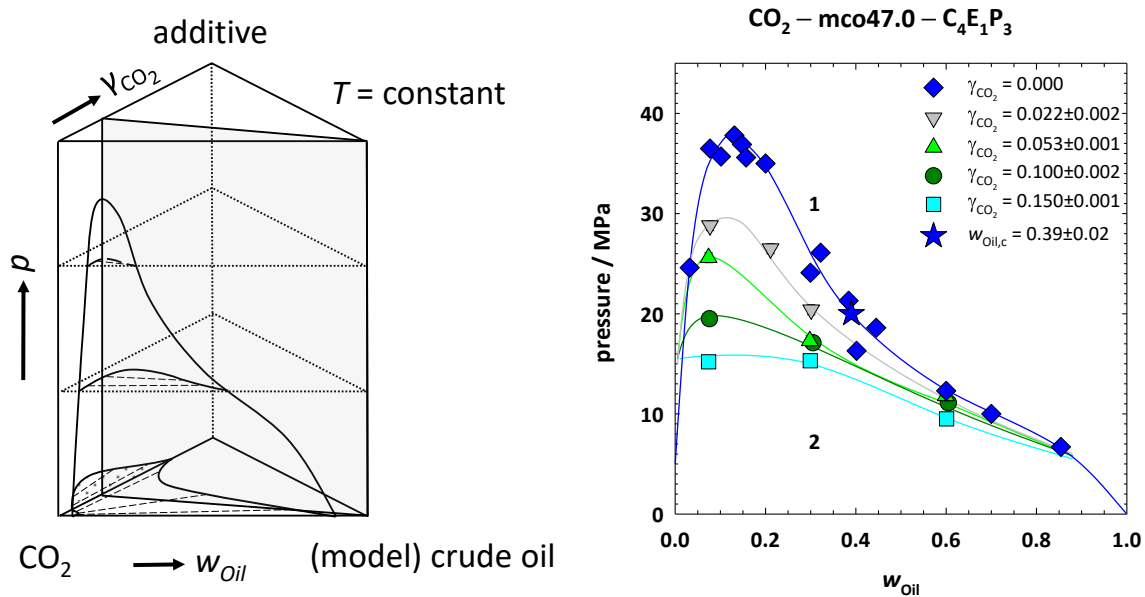
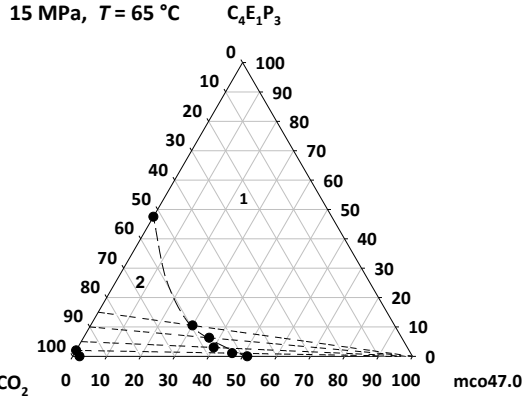


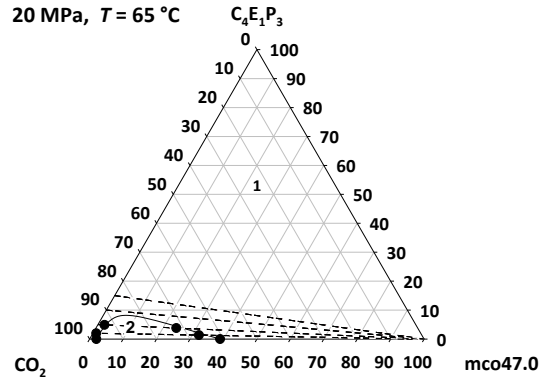
Figure 4.11: Schematic phase prism of a pseudoternary $\text{CO}_2 - (\text{model}) \text{ crude oil} - \text{additive}$ system (left) and $p(w_{\text{oil}})$ -sections through the isothermal phase prism of the system $\text{CO}_2 - \text{mco47.0} - \text{C}_4\text{E}_1\text{P}_3$ at 65°C (right). Left, phase triangles are indicated at four specific constant pressures within the phase prism. With increasing pressure, the (pseudo-)binary $\text{CO}_2 - \text{additive}$ miscibility gap disappears leading to the detachment of the miscibility gap in the Gibbs triangle from the binary $\text{CO}_2 - \text{additive}$ side. With further increasing pressure, this miscibility gap becomes smaller until it disappears at the MMP_p of the pseudobinary $\text{CO}_2 - (\text{model}) \text{ crude oil}$ system. Right, the extension of the miscibility gap decreases strongly at already small mass fractions of $\text{C}_4\text{E}_1\text{P}_3$ in CO_2 (γ_{CO_2}). Note that a $p(w_{\text{oil}})$ -section at a constant γ_{CO_2} is schematically indicated in the phase prism by a gray plane.

The $p(w_{oil})$ -sections shown in Figure 4.11 allow for the construction of isothermal and isobaric phase diagrams of the system $\text{CO}_2 - \text{mco47.0} - \text{C}_4\text{E}_1\text{P}_3$ in form of Gibbs triangles. In Figure 4.12, the obtained Gibbs triangles are shown for pressures of 15 MPa (A), 20 MPa (B), 25 MPa (C), and 30 MPa (D) and a constant temperature of 65 °C. For illustration, the $p(w_{oil})$ -sections recorded at constant γ_{CO_2} are also depicted as dashed lines in the Gibbs triangles. At 15 MPa, a large miscibility gap can be seen, which results from the miscibility gaps of the two (pseudo-)binary side systems $\text{CO}_2 - \text{mco47.0}$ and $\text{CO}_2 - \text{C}_4\text{E}_1\text{P}_3$ (Figure 4.12 (A)). By increasing the pressure to 20 MPa, the miscibility gap on the $\text{CO}_2 - \text{C}_4\text{E}_1\text{P}_3$ side closes at (17.1 ± 0.5) MPa. This leads to the detachment of the miscibility gap from the binary $\text{CO}_2 - \text{additive}$ side. Furthermore, since the miscibility gap of the pseudobinary $\text{CO}_2 - \text{mco47.0}$ system shrinks, a considerably smaller miscibility gap of the pseudoternary system is found (Figure 4.12 (B)). As the pseudobinary miscibility gap of the $\text{CO}_2 - \text{mco47.0}$ system continues to decrease as the pressure is increased to 25 MPa and 30 MPa, a further decrease of the miscibility gap of the pseudoternary system is observed until a small miscibility gap remains only for the side system $\text{CO}_2 - \text{mco47.0}$ (Figure 4.12 (C) and (D)). This evolution of Gibbs phase triangles with increasing pressure show the strong influence of the miscibility gaps of both the (pseudo-)binary $\text{CO}_2 - \text{mco47.0}$ and the $\text{CO}_2 - \text{additive}$ systems on the phase behavior of the pseudoternary system. However, a simple extrapolation from the (pseudo-)binary into the pseudoternary system is not possible for an accurate determination of the miscibility gaps, which requires measurements of the pseudoternary system. To identify the most promising additives, the respective pseudoternary systems were studied, especially $p(T)$ -phase diagrams at a constant $\gamma_{\text{CO}_2} = 0.020$ and different w_{oil} were measured, which is shown in chapter 4.5.

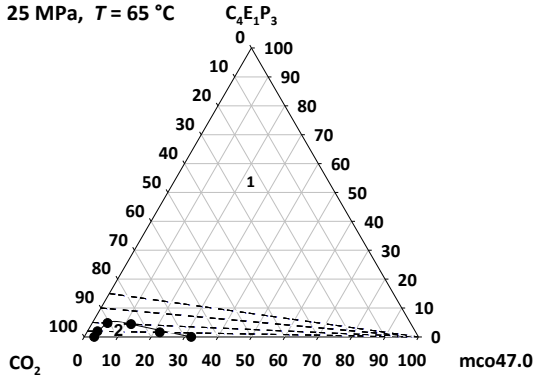
(A)



(B)



(C)



(D)

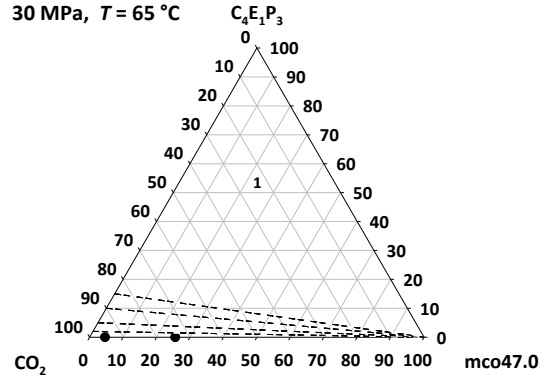


Figure 4.12: Isothermal (65°C) and isobaric Gibbs triangles of the system $\text{CO}_2 - \text{mco47.0} - \text{C}_4\text{E}_1\text{P}_3$ obtained from the $p(w_{oil})$ -sections (Figure 4.11, right) at pressures of 15 MPa (A), 20 MPa (B), 25 MPa (C), and 30 MPa (D). Axes represent wt% of the indicated component. Increasing the pressure leads to the detachment of the miscibility gap from the binary $\text{CO}_2 - \text{additive}$ side at (17.1±0.5) MPa and a further shrinking of the miscibility gap of the $\text{CO}_2 - \text{mco47.0}$ side system until it completely disappears at the MMP_p ((37.8±0.5) MPa).

4.4 Pressure Profit Δp as a Measure of the Miscibility-Enhancing Effect

At this point, a parameter is to be introduced, with which it is possible to compare the miscibility-enhancing effect of the different additive types in the four $\text{CO}_2 - (\text{model})$ crude oil systems investigated. The pressure profit

$$\Delta p = p(w_{oil}, \gamma_{\text{CO}_2} = 0) - p(w_{oil}, \gamma_{\text{CO}_2}) \quad (4.3)$$

is a simple measure for the miscibility-enhancing effect of the respective additive at a certain composition. In Figure 4.13, the pressure profit Δp induced by the additive $\text{C}_4\text{E}_1\text{P}_3$ in the system $\text{CO}_2 - \text{mco47.0}$ is illustrated by a red arrow at $\gamma_{\text{CO}_2} = 0.022 \pm 0.002$,

$w_{\text{Oil}} = 0.075 \pm 0.003$ and $65 \text{ }^\circ\text{C}$. Applying equation (4.3) to the example shown here yields a pressure profit $\Delta p = (7.7 \pm 0.5) \text{ MPa}$. Note that this composition was generally used below to characterize the miscibility-enhancing effect of the different additives in the CO_2 – (model) crude oil systems.

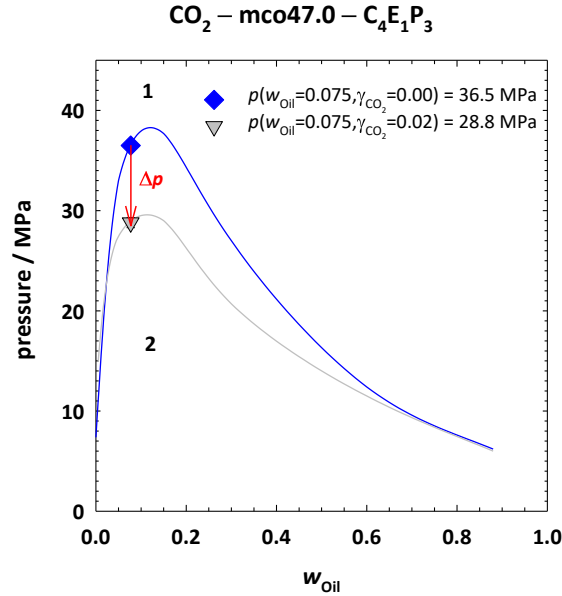


Figure 4.13: Illustration of the pressure profit Δp as a measure of the miscibility-enhancing effect of the respective additive by means of a $p(w_{\text{Oil}})$ -diagram of the system $\text{CO}_2 - \text{mco47.0} - \text{C}_4\text{E}_1\text{P}_3$ at $\gamma_{\text{CO}_2} = 0.022 \pm 0.002$ and $65 \text{ }^\circ\text{C}$. The pressure profit Δp at a composition of $w_{\text{Oil}} = 0.075 \pm 0.003$ is highlighted with a red arrow.

In the following, the pressure profit is used to discuss the influence of the composition on the miscibility-enhancing effect in the system $\text{CO}_2 - \text{mco47.0} - \text{C}_4\text{E}_1\text{P}_3$. Therefore, in Figure 4.14 (left), the observed pressure profits (Δp) are plotted as a function of the mco47.0 mass fraction w_{Oil} for different values of γ_{CO_2} . In Figure 4.14 (right), the Δp values are plotted as a function of the mass fraction γ_{CO_2} in the CO_2 /additive mixture for different values of w_{Oil} . As can be seen, the general trends are as follows: Δp decreases with increasing w_{Oil} for a given γ_{CO_2} and increases with increasing γ_{CO_2} for a given w_{Oil} .

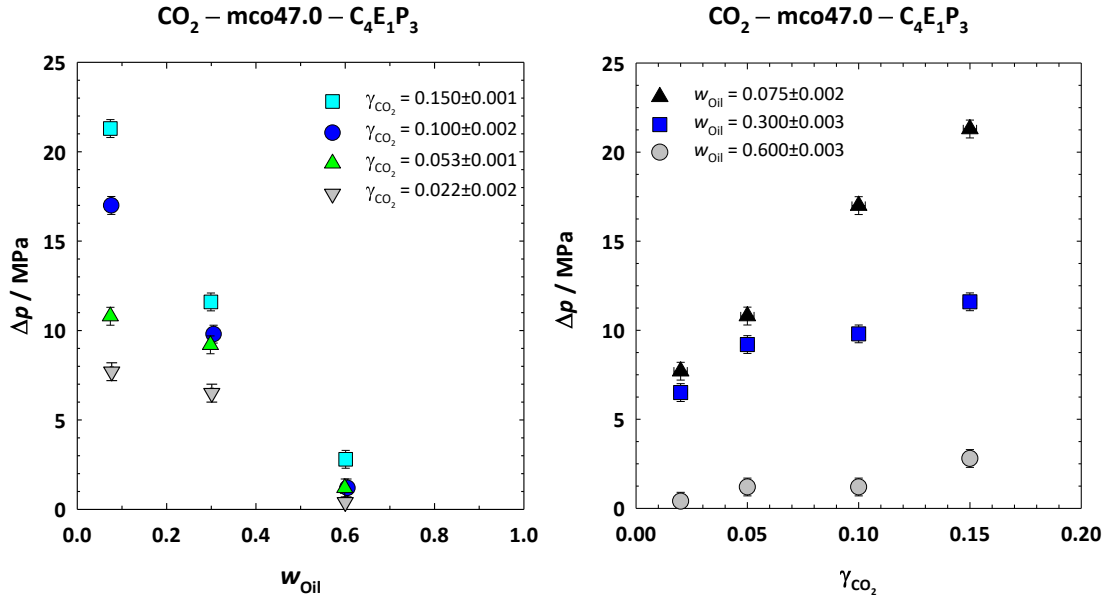


Figure 4.14: Pressure profit (Δp) as a function of the model crude oil mass fraction w_{oil} (left) and additive mass fraction γ_{CO_2} in the CO_2 /additive mixture (right) for the system $\text{CO}_2 - \text{mco47.0} - \text{C}_4\text{E}_1\text{P}_3$ at a constant temperature of 65 °C. Systematic trends were found: Δp decreases with increasing w_{oil} for a given γ_{CO_2} and increases with increasing γ_{CO_2} for a given w_{oil} .

The trend shown in Figure 4.14 (left) that the pressure profit decreases with increasing mass fraction of mco47.0 can be explained phenomenologically by the fact that more and more mco47.0 has to be made miscible with CO_2 by the same constant amount of additive. Consequently, a small but almost linear increase of Δp with increasing mass fraction γ_{CO_2} in the CO_2 /additive mixture was found at $w_{\text{oil}} = 0.600 \pm 0.003$ (Figure 4.14, right). Very interestingly, for the smaller mco47.0 mass fractions $w_{\text{oil}} = 0.075 \pm 0.002$ and $w_{\text{oil}} = 0.300 \pm 0.003$, a linear increase of the pressure profit is only found starting from $\gamma_{\text{CO}_2} = 0.022 \pm 0.002$. For these two oil mass fractions, the first small addition leads to a disproportionate increase in the pressure profit, which is reminiscent of the behavior of the partial vapor pressure of non-ideal mixtures described by Henry's law. In the pseudoternary system studied, this strongly non-ideal behavior is due to the complex composition of the model crude oil. These correlations of Δp with γ_{CO_2} and w_{oil} show clearly that the miscibility-enhancing effect is strongest at $w_{\text{oil}} = 0.075 \pm 0.002$. Therefore, the systems investigated in chapter 4.5 were measured mainly at $w_{\text{oil}} = 0.075$.

After these promising results had already been obtained with the first selected additive $\text{C}_4\text{E}_1\text{P}_3$, a systematic investigation of the miscibility-enhancing effect of 1-alcohols as a function of their chain length was performed in the following chapter, before the studies were extended to alkoxyated alcohols. Additionally, to generalize the miscibility-enhancing effect,

the influence of the different types of additives was also studied in the CO₂ – mco38.8 and the CO₂ – aco38.0 systems.

4.5 Search for the Best Additives

In the previous chapter, suitable model crude oils were developed and the miscibility of these model crude oils as well as a real crude oil and selected amphiphilic additives with CO₂ was investigated. With the aid of isothermal sections through the phase prism performed at constant additive content γ_{CO_2} in the CO₂/additive mixture as a function of pressure and oil mass fraction w_{Oil} , the interaction of the three (pseudo-)binary lower miscibility gaps CO₂ – (model) crude oil, CO₂ – additive and (model) crude oil – additive could be shown exemplarily by means of the pseudoternary system CO₂ – mco47.0 – C₄E₁P₃.

After these rather basic investigations, the actual aim of this thesis, i.e. the identification of additives enabling a better CO₂ – (model) crude oil miscibility, could be addressed. Therefore, the influence of a wide variety of additives on the miscibility of (model) crude oils and CO₂ was studied thereby attempting to find a structure-activity relationship that correlates the molecular structure of the additives with their miscibility-enhancing effect. To compare the effect of the many studied additives on the CO₂ – (model) crude oil miscibility gap, the experiments were carried out mainly at 65 °C and 75 °C at the same w_{Oil} and γ_{CO_2} . While the oil mass fraction was set to $w_{\text{Oil}} \approx 0.075$ and therewith close to the MMP_p of all investigated (model) crude oils, the additive mass fraction in the CO₂/additive mixture was set to $\gamma_{\text{CO}_2} = 0.020 \pm 0.002$, the upper limit of γ_{CO_2} in real oil field applications.

4.5.1 Linear and Branched Alcohols

Already 25 years ago, Scheidgen and Schneider found that 1-alcohols are able to enhance the miscibility between CO₂ and long-chain *n*-alkanes [Scheidgen, Schneider, 2000]. Almost at the same time, a United States patent reported that linear alcohols can be beneficially used in CO₂-EOR [Djabbarah, N. F. U.S., 4899817, Feb 13, 1990]. Inspired by these observations, the influence of linear and some branched alcohols on the miscibility of CO₂ and the two model crude oils mco47.0 and mco38.8 developed in this thesis was investigated. In the following figures, the pressure profit Δp (defined in the previous chapter by equation (4.3))

found at $w_{\text{Oil}} = 0.075 \pm 0.003$ and $\gamma_{\text{CO}_2} = 0.020 \pm 0.002$ (extracted from $p(T)$ -diagrams) was used as a measure of the miscibility-enhancing effect of the respective alcohol.

The influence of the 1-alcohol ($\text{C}_i\text{H}_{2i+1}\text{OH}$) chain length on the pressure profit (Δp) is shown in Figure 4.15 plotting Δp as a function of the number of carbon atoms i .

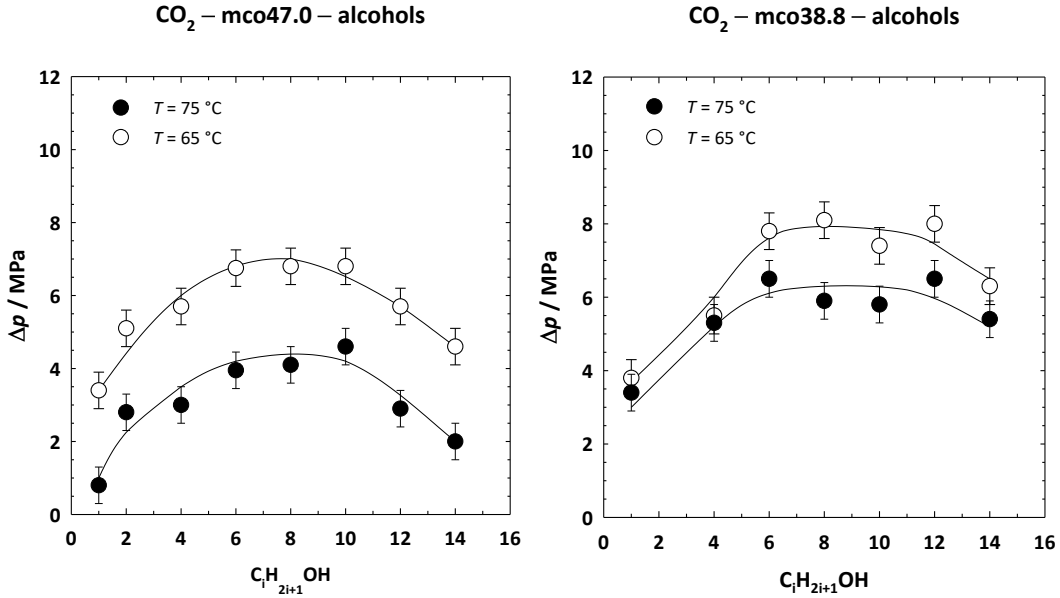


Figure 4.15: Pressure profits (Δp) at 65 °C and 75 °C obtained by the addition of 1-alcohols ($\text{C}_i\text{H}_{2i+1}\text{OH}$) to the pseudobinary systems CO_2 – mco47.0 (left) and CO_2 – mco38.8 (right) at $w_{\text{oil}} = 0.075 \pm 0.003$ and $\gamma_{\text{CO}_2} = 0.020 \pm 0.002$ (LW,JF). Similar maximum values Δp_{max} are found for the 1-alcohols with $i = 6, 8, 10$ and $i = 6, 8, 10, 12$ for the CO_2 – mco47.0 and CO_2 – mco38.8 systems, respectively. Interestingly, the observed pressure profits are larger for the model crude oil mco38.8.

Obviously, all investigated 1-alcohols increase the miscibility between CO_2 and the model crude oils mco47.0 and mco38.8, as indicated by a positive value of the pressure profit (Δp). In addition, the Δp values observed at 65 °C are generally larger than those at 75 °C, which might be related to the larger miscibility gap of the pseudobinary CO_2 – mco systems at 65 °C compared to 75 °C (see Figure 4.5).

Regarding the influence of the chain length of the 1-alcohol, for both systems, Δp depends on the number of carbon atoms i running through a maximum between 1-hexanol ($i = 6$) and 1-dodecanol ($i = 12$). An illustrative explanation for this general trend could be the poor compatibility between short-chain 1-alcohols and long-chain alkanes on the one hand and between long-chain alcohols and CO_2 on the other hand. Explicitly, for the system CO_2 – mco47.0 – 1-alcohol, a maximum pressure profit of $\Delta p_{\text{max}} = (7.1 \pm 0.5)$ MPa at 65 °C and $\Delta p_{\text{max}} = (4.5 \pm 0.5)$ MPa at 75 °C is found by the addition of 1-decanol ($\gamma_{\text{CO}_2} = 0.020 \pm 0.002$). A very similar pressure profit within the measurement error was found for 1-hexanol and 1-

octanol (especially at 65 °C). For the CO₂ – mco38.8 – 1-alcohol system, Δp values were detected, which are systematically larger than in the system containing the lighter oil mco47.0. The maximum pressure profit lies around $\Delta p_{\max} \approx 8.0$ MPa at 65 °C and $\Delta p_{\max} \approx 6.5$ MPa at 75 °C for 1-hexanol, 1-octanol, 1-decanol and 1-dodecanol.

Overall, the results obtained in this thesis indicate a tendency that the maximum pressure profit shifts to longer-chain 1-alcohols with decreasing API gravity of the oil (C₆ – C₁₀ for mco47.0, C₆ – C₁₂ for mco38.8). A similar observation was made by Scheidgen and Schneider as well as in the above-mentioned patent. For model systems containing CO₂ and long-chain *n*-alkanes, Scheidgen and Schneider [Scheidgen, Schneider, 2000] found a preliminary trend that the largest effect on miscibility is expected when the chain length of the 1-alcohol is 7 to 8 carbon atoms shorter than that of the *n*-alkane. The model crude oil mco47.0 and mco38.8 have an average number of carbon atoms of approximately 15. Thus, the ranges of 1-alcohol chain lengths with best effects fit to this trend.

Similarly, according to the U.S. patent [Djabbarah, N. F. U.S., 4899817, Feb 13, 1990], the shorter-chain alcohols methanol to butanol should be chosen for crude oils with low water saturation and an API gravity equal to or greater than 35 °, while butanol to octanol are described as a good choice for recovering crude oils with low water saturation and an API weight less than 35 °. Note that with respect to the data of this thesis and the data of Scheidgen and Schneider [Scheidgen, Schneider, 2000], longer-chain 1-alcohols are expected to have an even better miscibility-enhancing effect than the alcohols suggested in the patent. Last but not least, the observation that for a given additive larger Δp values were observed at lower temperature and lower API gravity (Figure 4.15), i.e. when the miscibility gap is larger, might indicate that the magnitude of the pressure profit scales with the MMP_p.

After investigating the influence of the chain length on the miscibility-enhancing effect of additives using 1-alcohols, the influence of branching was studied in the next step. The molecular structure of the selected branched alcohols 2-ethylhexanol, isononanol, 2-propylheptanol, Exxal™ 10, ITDA, ISOFOL 12, ISOFOL 16 and ISOFOL 28, provided by Sasol Performance Chemicals GmbH, is shown in Figure 4.16, bottom. Here, Exxal™ 10 is a mix of linear and branched C₉-C₁₁ alcohols with a maximum at C₁₀. The effect of the branched alcohols was studied by means of the CO₂ – mco47.0 system at $w_{\text{Oil}} = 0.075 \pm 0.003$ and $\gamma_{\text{CO}_2} = 0.020 \pm 0.002$. In Figure 4.16, top, the values of the pressure profit Δp obtained at 65 °C (left) and 75 °C (right) are shown together with the Δp values of the linear alcohols already

presented above. Thereby, the Δp of the branched alcohols is plotted against the number of carbon atoms in their longest chain. As can be seen, most of the branched alcohols, i.e. 2-ethylhexanol, isononanol, 2-propylheptanol, and ITDA exhibit a smaller pressure profit than the comparable linear alcohols for both temperatures. The lower hydrophobicity of the branched alcohols, which reduces the compatibility with the mostly long-chain alkane components in mco47.0 could be a reason for this trend [Márquez, et al., 1998]. The assumption that this effect could at least be compensated by the better compatibility of a branched alkyl chain with CO₂ was unfortunately not found. Only by increasing the number of carbon atoms, as in the case of ISOFOL 12, or using a mixture of linear and branched alcohols (ExxaTM 10) led to a miscibility-enhancing effect comparable to that of the linear alcohols. Further enlargement of the hydrophobic chain leads initially only to somewhat smaller Δp values due to its increasingly poorer compatibility with CO₂, as in the case of ISOFOL 16. When adding the very long-chain ISOFOL 28, even a negative value of the pressure profit gain, i.e. a poorer miscibility of CO₂ and mco47.0, was observed.

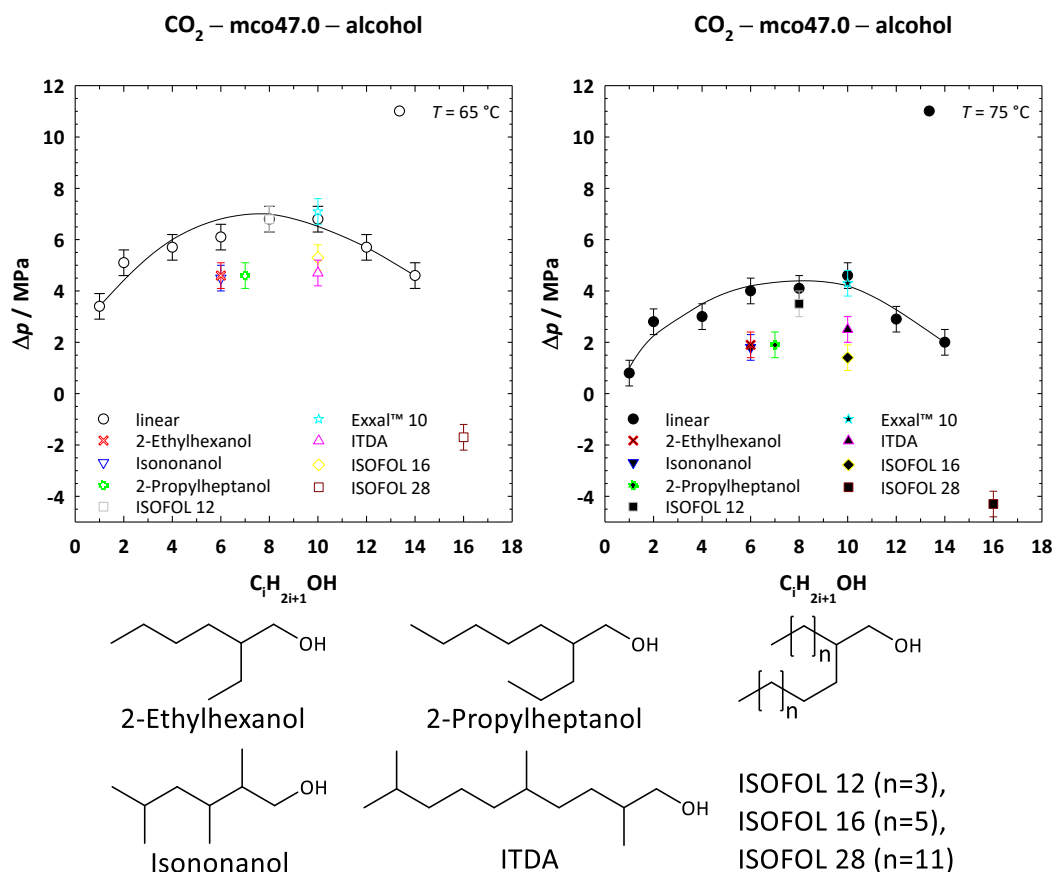


Figure 4.16: Pressure profits (Δp) at 65 °C and 75 °C obtained by the addition of linear and branched alcohols to the CO_2 – mco47.0 system at $w_{\text{oil}} = 0.075 \pm 0.003$ and $\gamma_{\text{CO}_2} = 0.020 \pm 0.002$ (top) and molecular structures of the branched alcohols (bottom). The Δp of the branched alcohols is plotted against the number of carbon atoms in their longest chain. The branched alcohols 2-ethylhexanol, isononanol, 2-propylheptanol, and ITDA exhibit smaller Δp values compared to their linear equivalents. The longer-chain branched ISOFOL 12 and the mixture of linear and branched alcohols (Exxal™ 10) provide a comparable pressure profit. A further increase of the alkyl chain leads to slightly smaller Δp values for ISOFOL 16 and to even a negative pressure profit, when the branched long-chain ISOFOL 28 is used.

Interestingly, the influence of some of the branched alcohols studied in this thesis (ISOFOL 12, ISOFOL 16, ISOFOL 28) and Lial 123A (linear and mono-branched alcohol mixture with alkyl chain lengths of 12 to 13 carbon atoms) on the interfacial tension has been investigated by Moradi et al. [Moradi, et al., 2014] a few years ago. In this publication, the interfacial tension between CO_2 and a dead crude oil as well as between CO_2 and the same crude oil mixed with *n*-heptane has been measured as a function of pressure at 102 °C and different alcohol concentrations (0, 2.5, 5.0 and 10% by volume of the final mixture). This dead crude oil, which corresponds to the crude oil without gaseous components, was taken from the Dulang oil field in Malaysia and had an API gravity of 37.8 °. Moradi et al. found that some of the alcohols, in particular Lial 123 and ISOFOL 16, enabled a reduction of the CO_2 – dead crude oil/*n*-heptane interfacial tension of up to 33%. Assuming that interfacial tension and

mixing behavior are closely correlated, the results of the interfacial tension measurements by Moradi et al. and those of the phase diagram studies in this thesis are mutually supportive.

4.5.2 Alkoxylated Alcohols as New Type of Miscibility Enhancers

So far in this thesis, the linear alcohols from 1-hexanol to 1-dodecanol and the branched alcohols Exxal™ 10 and ISOFOL 12 have been identified as the best additives for improving the miscibility of CO₂ and (model) crude oils. While the miscibility-enhancing effect of alcohols on the miscibility of CO₂ and *n*-alkanes [Scheidgen, Schneider, 2000] as well as CO₂ and crude oils [Djabbarah, N. F. U.S., 4899817, Feb 13, 1990] is partly known from the literature, the influence of alkoxylated alcohols on the above-mentioned mixtures has hardly been investigated. In particular, alkoxylated alcohols could be interesting additives, since ethoxy and propoxy groups have a certain compatibility with CO₂ [Peach, Eastoe, 2014]. However, in order to prevent the additive molecule from becoming too large and, in addition, the compatibility with the hydrophobic molecules of the model crude oil from decreasing too much, additives with a low degree of alkoxylation were selected to study their miscibility-enhancing effect on the three pseudobinary CO₂ – mco/aco38.0 systems in the next step. A series of alkoxylated alcohols (C_iE_j, C_iP_x and C_iE_jP_x) was specifically synthesized by Sasol Performance Chemicals GmbH in order to study the influence of the number of ethoxy units *j* and propoxy units *x* on the miscibility-enhancing effect.

For these studies, alkoxylated additives based on the medium-chain linear alcohols 1-butanol and 1-hexanol were mainly chosen, as well as for the branched alcohol ISOFOL 12 identified in the previous section as one of the best additives for the CO₂ – mco47.0 system (Figure 4.16), and for the less effective branched alcohol ITDA in comparison. As a measure of the miscibility-enhancing effect of the alkoxylated alcohols, the pressure profits (Δp) at 65 °C and 75 °C were again determined at $\gamma_{\text{CO}_2} = 0.020 \pm 0.002$ and $w_{\text{Oil}} = 0.075 \pm 0.003$. In Figure 4.17 to Figure 4.19, the results of these measurements are plotted by means of 20 exemplary alkoxylated additives, arranged according to the (model) crude oils in form of bar charts. To classify the miscibility-enhancing effect of the alkoxylated additives, the Δp values of the starting alcohols are plotted for comparison. All studied alkoxylated additives generate a positive pressure profit under the investigated conditions, i.e. they increase the miscibility of the (model) crude oils with CO₂.

In Figure 4.17, the pressure profits obtained by the addition of the alkoxyated additives $C_4E_jP_x$ and ISOFOL 12E_jP_x are shown for the system $CO_2 - mco47.0$ at 65 °C (blue) and 75 °C (red). At both temperatures, C_4E_4 and $C_4E_1P_3$ achieved a considerably larger Δp than 1-butanol. As expected from the previous measurements with the alcohols, an even stronger miscibility-increasing effect was observed for ISOFOL 12. Here, too, the investigated ethoxylated ISOFOL 12E₁ and the propoxylated ISOFOL 12P₄ led to larger values of the pressure profit than the starting alcohol. These results confirm the hypothesis that the introduction of ethoxy and propoxy groups, which have some compatibility with CO_2 , are able to improve the miscibility of CO_2 and (model) crude oils more than their starting alcohols. As already observed for the linear and branched alcohols, the Δp values observed at 65 °C are generally larger than those at 75 °C, which might be related to the larger miscibility gap of the pseudobinary $CO_2 - mco$ systems at 65 °C compared to 75 °C

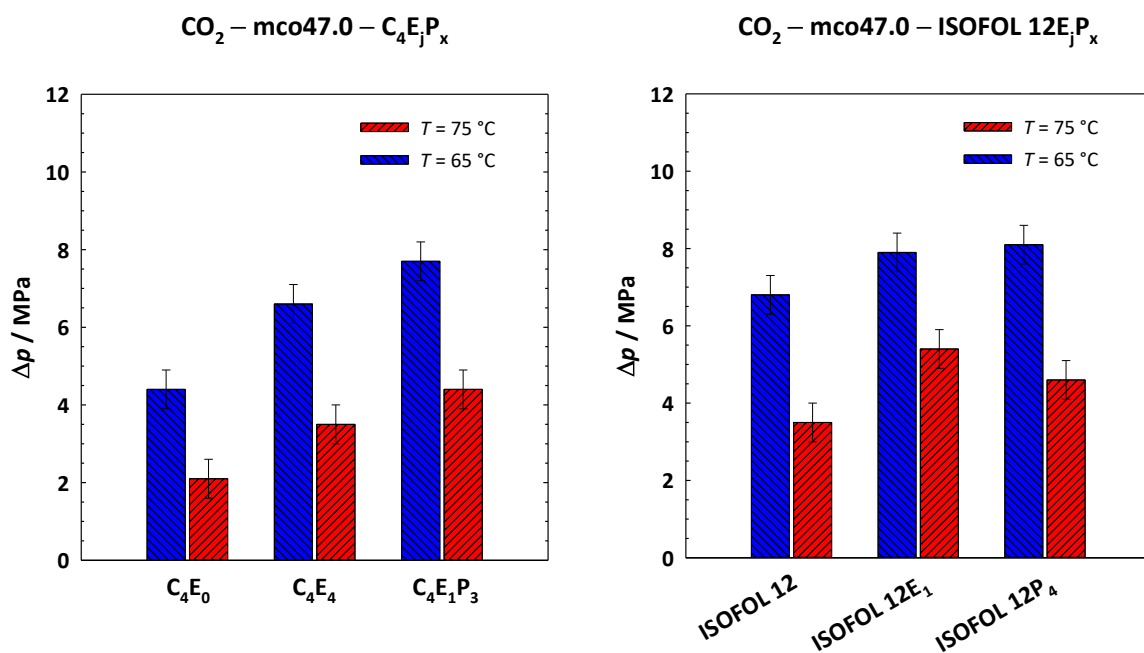


Figure 4.17: Pressure profits (Δp) at 65 °C (blue) and 75 °C (red) obtained by the addition of $C_4E_jP_x$ and ISOFOL 12E_jP_x to the pseudobinary $CO_2 - mco47.0$ system at $w_{oil} = 0.075 \pm 0.003$ and $\gamma_{CO_2} = 0.020 \pm 0.002$. The results confirm the hypothesis that the introduction of ethoxy and propoxy groups, which have some compatibility with CO_2 , are able to improve the miscibility of CO_2 and (model) crude oils more than their starting alcohols.

For the $CO_2 - mco38.8$ system, the pressure profits obtained by addition of C_4E_j , $C_6E_jP_x$ and ISOFOL 12E_jP_x are shown in Figure 4.18. All alkoxyated additives achieved improved pressure profits compared to the respective alcohol at 65 °C and 75 °C. The largest pressure profits were found for C_6P_3 ($\Delta p = (9.6 \pm 0.5)$ MPa at 65 °C, $\Delta p = (8.0 \pm 0.5)$ MPa at 75 °C) with Δp values about 2 MPa larger than those observed for the starting alcohol C_6E_0 . However, no

systematic trend of the pressure profit with increasing numbers of ethoxy or propoxy groups was observed. The broad distribution of the degree of alkoxylation in the technical-grade alkoxyated alcohols synthesized by Sasol Performance Chemicals GmbH might be the reason for this behavior.

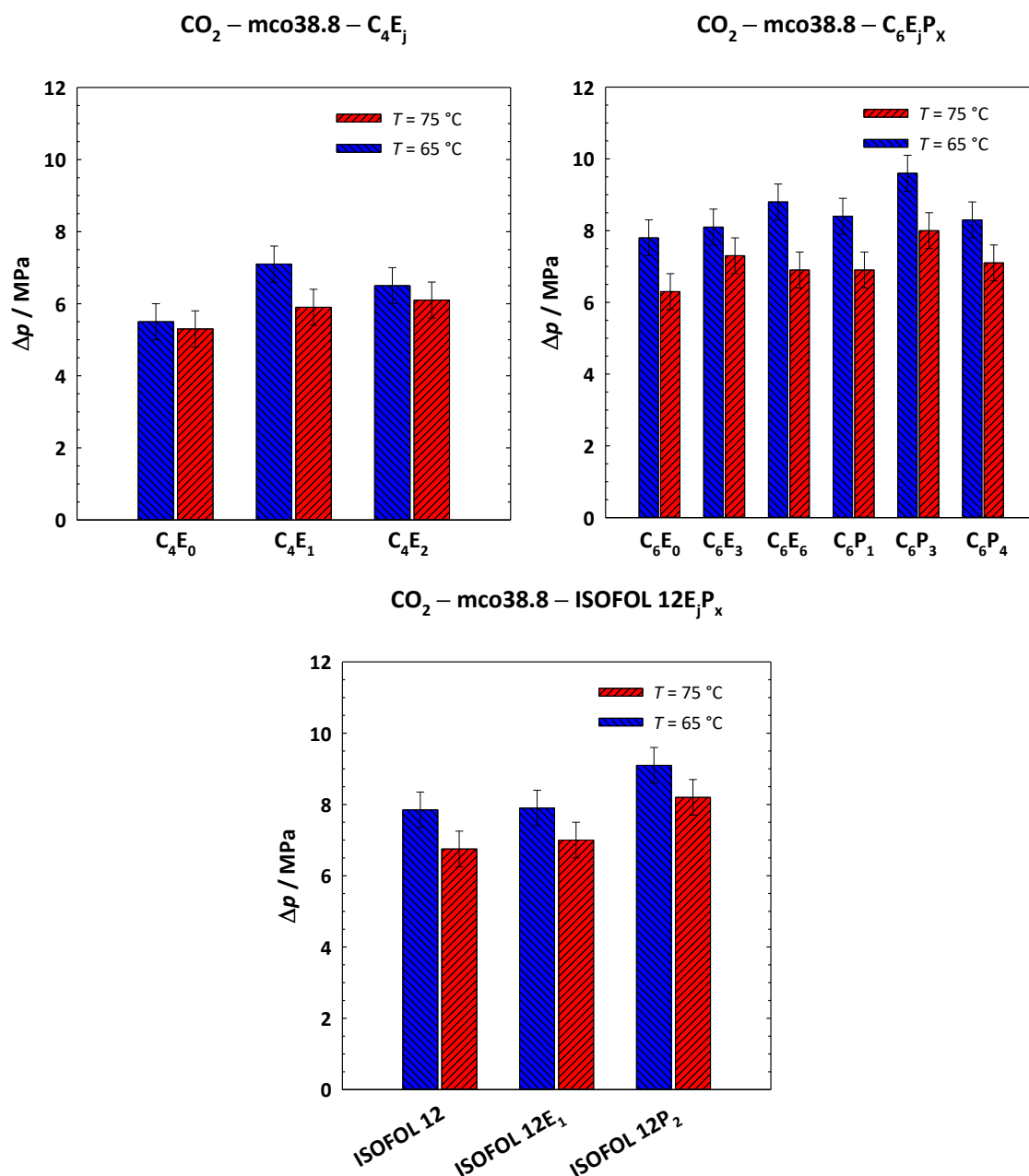


Figure 4.18: Pressure profits (Δp) obtained at 65 °C (blue) and 75 °C (red) by the addition of C₄E_j, C₆E_jP_x and ISOFOL 12E_jP_x to the pseudobinary CO₂ – mco38.8 system at $w_{oil} = 0.075 \pm 0.003$ and $\gamma_{CO_2} = 0.020 \pm 0.002$. At both temperatures, the alkoxyated additives achieved a larger Δp compared to the respective starting alcohol.

In Figure 4.19, the pressure profits obtained at 65 °C and 75 °C by addition of C₄E_j, C₆E_jP_x, ISOFOL 12E_jP_x and ITDA E_x to the pseudobinary mixture of CO₂ and the real crude oil aco38.0 are shown. As already seen for the CO₂ – model crude oil systems, a stronger

miscibility-enhancing effect is obtained by the addition of the alkoxyated additives than by the respective starting alcohol. Comparing the pressure profit obtained by C_6E_4 and C_4E_4 , a larger Δp value was found for the former additive, which is in agreement with the results obtained for the 1-alcohols, where 1-hexanol provides a larger pressure profit than 1-butanol. In line with the data of the CO_2 – mco systems, no clear trend of Δp with varying number of ethoxylated and propoxylated units was found. The best performing additive in the systems CO_2 – aco38.0 – $C_6E_jP_x$ is C_6P_1 , which induced a pressure profit of $\Delta p = (10.2 \pm 0.5)$ MPa at 65 °C and an even larger Δp of (11.0 ± 0.5) MPa at 75 °C. This inverse temperature trend is surprising, but still within the measuring error. The alkoxyated ISOFOL 12 additives generate similar pressure profits as the $C_6E_jP_x$ additives. In agreement with the miscibility-enhancing effect observed for the alcohols, the twofold ethoxylated ITDA shows a considerably lower pressure profit than the alkoxyated alcohols 1-hexanol and ISOFOL 12.

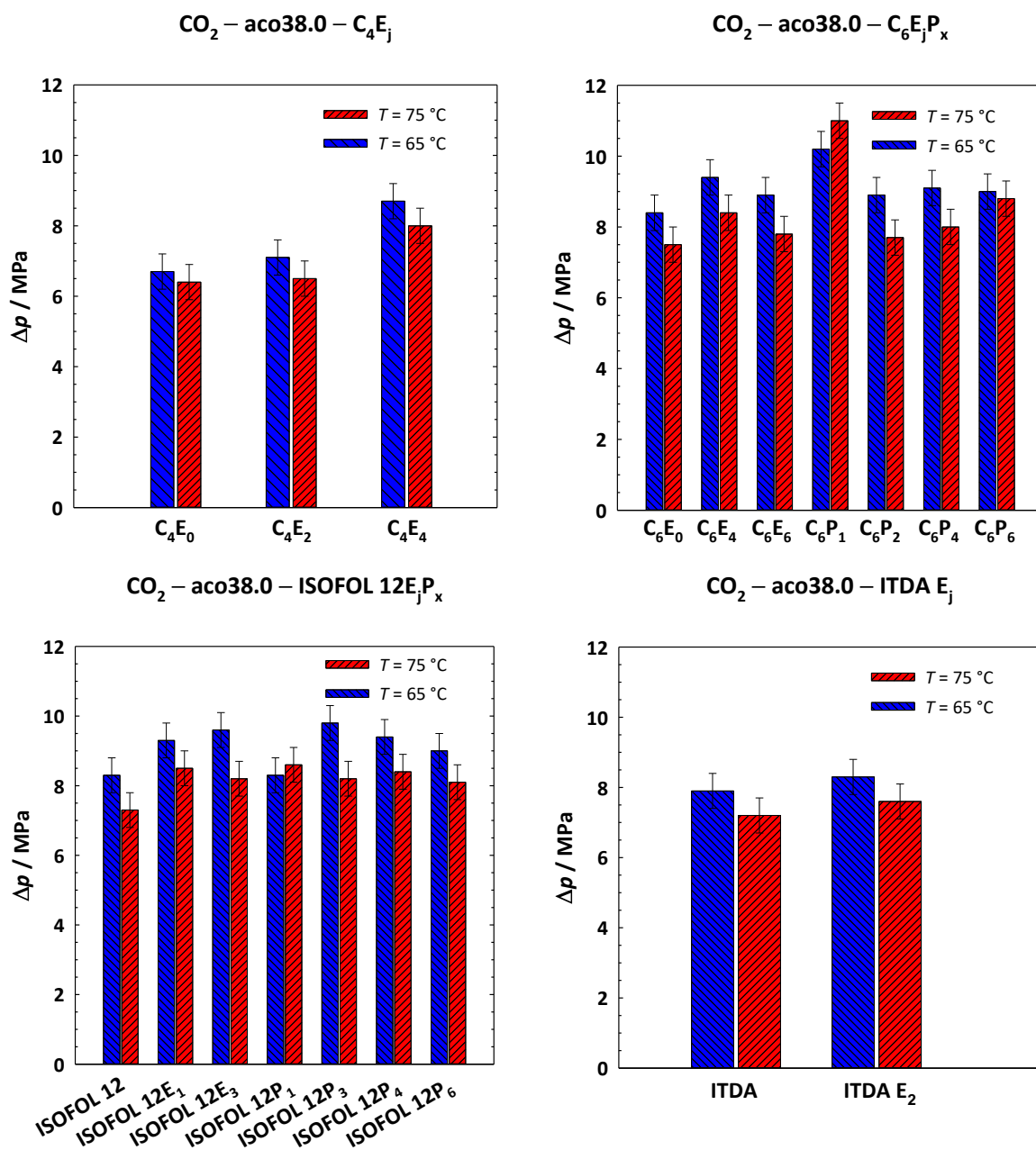


Figure 4.19: Pressure profits (Δp) obtained at 65 °C (blue) and 75 °C (red) by the addition of $\text{C}_4\text{E}_j\text{P}_x$, $\text{C}_6\text{E}_j\text{P}_x$, $\text{ISOFOL } 12\text{E}_j\text{P}_x$ and ITDA E_x to the pseudobinary $\text{CO}_2 - \text{aco38.0}$ system at $w_{\text{oil}} = 0.075 \pm 0.003$ and $\gamma_{\text{CO}_2} = 0.020 \pm 0.002$. The alkoxyated additives achieve a larger Δp compared to the respective starting alcohol. The observed trends are consistent with those found for the starting alcohols, i.e. the alkoxyated alcohols 1-hexanol and ISOFOL 12 show a considerably stronger miscibility-enhancing effect than the ethoxylated 1-butanol and ITDA.

In summary, the results obtained so far show a positive pressure profit for all amphiphilic molecules (except for ISOFOL 28), i.e. they increase the miscibility of the (model) crude oils and CO_2 . For linear alcohols, the pressure profits were found to run through a maximum between 1-hexanol ($i = 6$) and 1-dodecanol ($i = 12$). The poor compatibility between short-chain 1-alcohols and long-chain alkanes on the one hand and between long-chain

alcohols and CO₂ on the other hand can explain this trend. Furthermore, there might be the overall tendency that longer-chain alcohols show better effects in systems with lower API gravity (C₆ – C₁₀ for mco47.0, C₆ – C₁₂ for mco38.8, C₁₂ for aco38.0). Comparing linear alcohols with branched alcohols, mostly smaller pressure profits were found for branched alcohols with the exception of ISOFOL 12.

Interestingly, alkoxyated additives were able to achieve a larger Δp compared to the respective starting alcohols, which might be related to a certain compatibility of ethoxy and propoxy groups with CO₂. In agreement with the miscibility-enhancing effect observed for the alcohols before, alkoxyated 1-hexanol and ISOFOL 12 were found to exhibit the largest miscibility-enhancing effects. As outlined above, the result that no systematic trend of the pressure profit was observed with increasing numbers of ethoxy or propoxy groups could be due to the broad distribution of the degree of alkoxylation in the technical-grade alkoxyated alcohols synthesized by Sasol Performance Chemicals GmbH. Last but not least, it was found that the (model) crude oil composition and the temperature systematically influence the miscibility-enhancing effect of the additives. More precisely, the pressure profits considerably increase with the API gravity of the (model) crude oil and decreasing temperature. i.e. when the miscibility gap is larger, which might indicate that the magnitude of the pressure profit scales with the MMP_p.

Despite the systematic trends found in this thesis, no general rules for the selection of an appropriate additive can be defined. Therefore, it is necessary to perform individual screening tests of the phase behavior, in order to identify the best performing additive for a given crude oil under its reservoir conditions.

4.5.3 Best Performing Additives: Composition Dependence of Miscibility-Enhancing Effect

The systematic screening of the miscibility-enhancing effect of 17 alcohols and 20 alkoxyated alcohols on three different CO₂ – (model) crude oil systems (see Table 7.1), performed mainly at $\gamma_{\text{CO}_2} = 0.020 \pm 0.005$ and $w_{\text{oil}} = 0.075 \pm 0.006$, allowed the identification of the additives producing the largest pressure profit. Based on this screening, the propoxyated linear and branched alcohols C₆P₃ and ISOFOL 12P₄, respectively, were chosen together with the simple linear alcohol 1-butanol to investigate the composition dependence of the miscibility-enhancing effect. Similar to the comprehensive study of the pseudoternary system CO₂ – mco47.0 – C₄E₁P₃ (Figure 4.11 - Figure 4.14), the influence of these three additives on

the miscibility gap of the CO₂ – mco47.0 system was studied both as a function of the additive mass fraction γ_{CO_2} in the CO₂/additive mixture and as a function of the mco47.0 mass fraction w_{Oil} .

In Figure 4.20, the phase boundary (left) as well as the pressure profit Δp (right) are plotted as a function of γ_{CO_2} for the different additives at a temperature of 65 °C. The oil mass fraction was set to $w_{\text{Oil}} = 0.075 \pm 0.006$ and therewith close to the MMP_p composition of all investigated CO₂ – (model) crude oil systems. All three additives induce a strong decrease of the MMP_p from 36.5 MPa to less than 26 MPa by increasing γ_{CO_2} to 10 wt%. Thereby, the data seem to follow an exponential decay. Accordingly, the pressure profit Δp increases exponentially from 0 MPa to 12 MPa when γ_{CO_2} is increased.

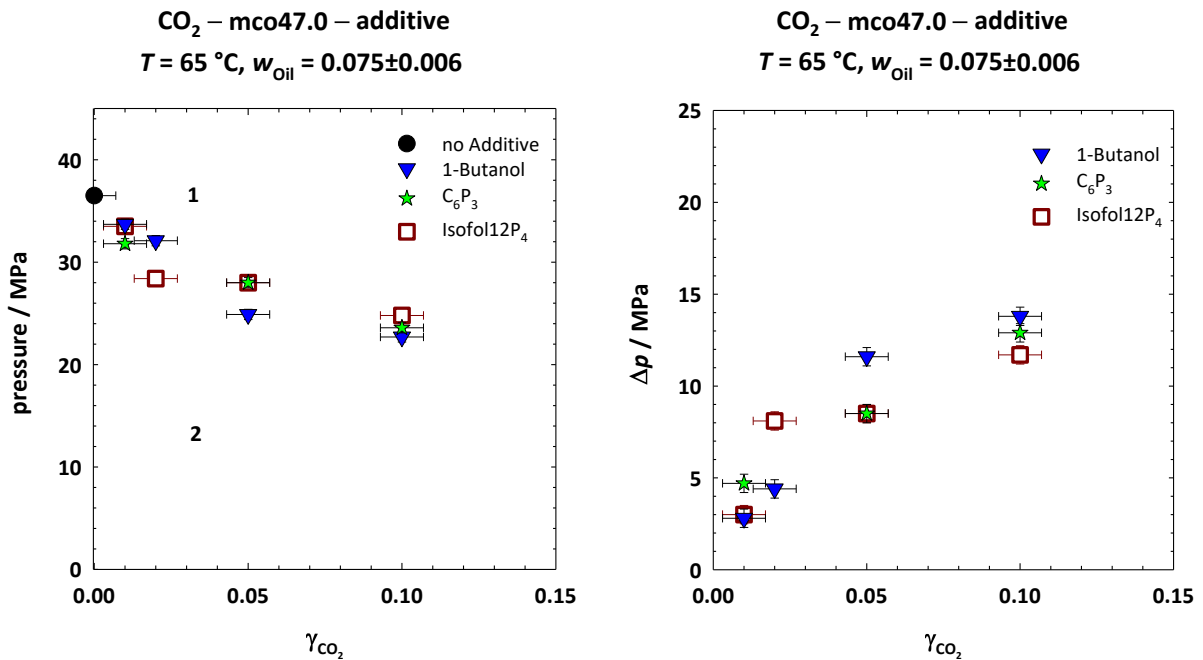


Figure 4.20: $p(\gamma_{\text{CO}_2})$ -diagram (left) and $\Delta p(\gamma_{\text{CO}_2})$ -diagram (right) of the pseudoternary CO₂ – mco47.0 – additive systems at $w_{\text{Oil}} = 0.075 \pm 0.006$ and 65 °C. For all investigated additives (1-butanol, C₆P₃ and ISOFOL 12P₄), a strong decrease near the MMP_p from approx. 36.5 MPa to less than 26 MPa is observed by increasing γ_{CO_2} to 10 wt%.

Interestingly, at low γ_{CO_2} values, the propoxylated alcohols C₆P₃ and ISOFOL 12P₄ seem to produce a stronger miscibility-enhancing effect than the shorter 1-butanol, while at higher concentrations ($\gamma_{\text{CO}_2} \geq 5$ wt%), 1-butanol shows the better performance. However, the improvement of the pressure profits for higher γ_{CO_2} has been shown above to be less prominent for higher w_{Oil} (see 4.4, Figure 4.14), i.e. the better effects of 1-butanol for high γ_{CO_2} might not be present for higher w_{Oil} , which are relevant during the injection process. Note that

the MMP_p values are very sensitive to gravimetric error because of the small amount of additive (approximately 15 mg to set $\gamma_{CO_2} = 0.010$) that was weighed into the sample due to the small total volume of the HP-cell.

Subsequently, the influence of the three additives on the miscibility of the CO_2 – mco47.0 system was investigated at a larger mass fraction of $w_{Oil} = 0.210 \pm 0.010$, while keeping the additive concentration of $\gamma_{CO_2} = 0.020 \pm 0.003$ constant. The pressure profits obtained at $w_{Oil} = 0.075 \pm 0.002$ and $w_{Oil} = 0.210 \pm 0.010$ are shown in Figure 4.21 for temperatures of 65 °C (left) and 75 °C (right). The propoxylated alcohols C_6P_3 and ISOFOI 12P₄ generate a much stronger miscibility-enhancing effect than the shorter 1-butanol. Comparing the Δp values observed at 65 °C (left) with those at 75 °C (right), the former are considerably larger. This trend was found with only one exception for all pressure profit values and could be related to the larger miscibility gap of the pseudobinary CO_2 – mco systems at 65 °C compared to 75 °C.

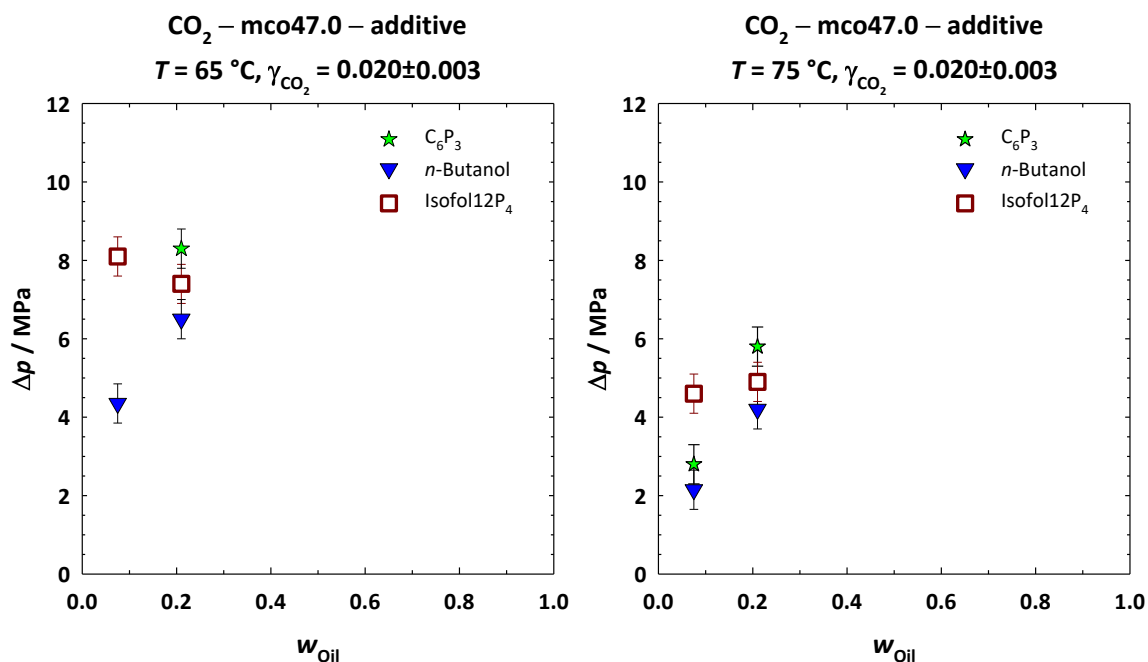


Figure 4.21: Pressure profit (Δp) of the additives 1-butanol, C_6P_3 and ISOFOI 12P₄ in the CO_2 – mco47.0 system at $\gamma_{CO_2} = 0.020 \pm 0.003$ for different w_{Oil} (0.075 ± 0.002 and 0.210 ± 0.010) and two temperatures, 65 °C (left) and 75 °C (right). The Δp values of the propoxylated alcohols C_6P_3 and ISOFOI 12P₄ are considerably larger than those of the shorter 1-butanol.

Figure 4.21 clearly shows that the threefold propoxylated 1-hexanol C_6P_3 delivered the largest pressure profit in the CO_2 – mco47.0 system at $w_{Oil} \approx 0.210 \pm 0.010$, which is closer to the critical point composition ($w_{Oil,c} = 0.390 \pm 0.020$) than the other composition analyzed ($w_{Oil} \approx 0.075 \pm 0.002$). For this reason, C_6P_3 was used for the application-oriented slim tube

studies performed at Rice University (Houston, Texas, USA) in close cooperation with the group of Prof. George J. Hirasaki. In preparation for these measurements, the influence of C_6P_3 on the miscibility gap of the CO_2 – mco38.8 was studied, as the API degree of mco38.8 agrees almost quantitatively with the API degree of the Asian crude oil aco38.0. Because of safety regulations at the Rice University, 13.5 wt% of benzene in the mco38.8 had to be replaced with toluene and *m*-xylene for the slim tube experiments. Therefore, the influence of C_6P_3 on the miscibility gap was additionally studied for the CO_2 – mco38.0 system.

In Figure 4.22, the effect of C_6P_3 on the miscibility gap of the two systems CO_2 – mco38.8 and CO_2 – mco38.0 is shown at a temperature of 65 °C. As can be seen and has already been shown above (Figure 4.8), the replacement of benzene with toluene and *m*-xylene has almost no influence on the phase behavior of the systems. Thus, the phase boundaries of the systems CO_2 – mco38.8 and CO_2 – mco38.0 lie almost on top of each other. Mco38.8 and mco38.0 will therefore be treated as the same model crude oil in this analysis. As in chapter 4.4 (Figure 4.11), the miscibility-enhancing effect of C_6P_3 was studied by means of $p(w_{oil})$ -sections through the isothermal phase prism at two different mass fractions γ_{CO_2} of C_6P_3 in the CO_2/C_6P_3 mixture, i.e. at $\gamma_{CO_2} = 0.020 \pm 0.003$ and 0.050 ± 0.003 . Again, these small γ_{CO_2} values lead to a large reduction in the miscibility gaps with, as expected, the miscibility-enhancing effect at $\gamma_{CO_2} = 0.050 \pm 0.003$ being larger than the one at $\gamma_{CO_2} = 0.020 \pm 0.003$. Although the miscibility gaps become smaller especially on the CO_2 -rich side of the phase diagram, the reduction is also observed at the composition of the critical point ($w_{oil,c} = 0.390 \pm 0.020$), which is of great interest for CO_2 -EOR projects and which will be discussed in detail in chapter 4.7.1.

In addition, due to the remarkable effect of the C_6P_3 onto the miscibility gap of the CO_2 – mco38.8/mco38.0 systems, the influence of the type of alkoxylation was studied by replacing the propoxy units with ethoxy units at $\gamma_{CO_2} = 0.050 \pm 0.003$. In Figure 4.22, both additives, i.e. C_6P_3 and C_6E_3 show a similar miscibility-enhancing effect, recognizable by the fact that the phase boundaries of the two systems CO_2 – mco38.0 – C_6P_3 and CO_2 – mco38.0 – C_6E_3 are almost quantitatively superimposed. However, as mentioned already above, the additives are technical-grade alkoxyated alcohols synthesized by Sasol Performance Chemicals GmbH with a certain distribution of the degree of alkoxylation.

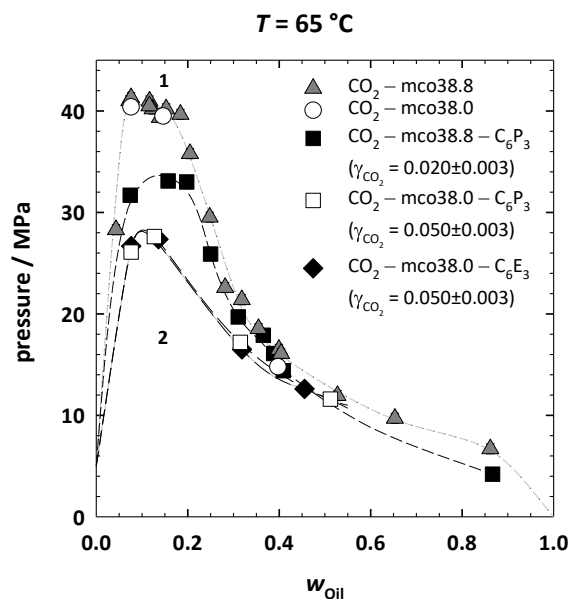


Figure 4.22: $p(w_{oil})$ -diagram of the CO_2 – mco38.8/mco38.0 and CO_2 – mco38.8/mco38.0 – $\text{C}_6\text{P}_3/\text{C}_6\text{E}_3$ systems at $65\text{ }^\circ\text{C}$ and different γ_{CO_2} . The additive-free systems CO_2 – mco38.8 and CO_2 – mco38.0 show quantitatively almost the same phase behavior. The miscibility gap decreases by addition of C_6P_3 and C_6E_3 . Furthermore, the miscibility-enhancing effects of C_6P_3 or C_6E_3 onto the phase behavior are not limited to low values of w_{oil} and consequently also shift the plait point to lower pressure.

4.6 Patent Application and Comparison to Prior Art

Triggered by the surprisingly good performance of alkoxyated additives as novel efficient miscibility enhancers in CO_2 /(model) crude oil mixtures found in this thesis, the Sasol Performance Chemicals GmbH secured the intellectual property rights by filing a patent application. However, before starting the filing process, the effect of the novel miscibility enhancers had to be compared to prior art.

As already mentioned above, one patent reported that linear alcohols ranging from 1-methanol to 1-octanol and mixtures thereof exhibit a considerable miscibility-enhancing effect [Djabbarah, N. F. U.S., 4899817, Feb 13, 1990]. Furthermore, Moradi et al. investigated the influence of different linear and branched alcohols (Alfol1214, ISOFOL 12, ISOFOL 16, and ISOFOL 28, Lial123A, Lial167, and MarlipalO13, all brand names) dissolved in *n*-heptane on the interfacial tension between CO_2 and crude oil (taken from a Dulang oil field in Malaysia, API gravity of 37.8 °) [Moradi, et al., 2014]. They found for ISOFOL 16, the best performer, a reduction of the interfacial tension of 33%. Only one patent application was found describing the miscibility-enhancing effect of alkoxyated additives related to CO_2 -EOR [Fan, W.; Li, B.; Li, S.; Li, Z.; Lu, T.; Luo, H.; Nan, G.; Wang, F.; Zhang, C. CN, 104610953A, 2015]. In this application, the authors claim a significant reduction of the minimum miscibility pressure MMP by using

linear C₁₀₋₁₈E₀₋₁₂P₂₋₁₀ or their alkoxyated alkylphenol analogues as additives. However, to ensure the solubility of these additives in CO₂, the additional use of short-chain alcohols ranging from 1-methanol to 1-pentanol (C₁₋₅) is described as mandatory. While it is shown in chapter 4.5.1, that these short-chain alcohols alone are already capable of reducing the miscibility gap, their miscibility-enhancing effect was found to be considerably smaller than the effect of the medium-chain propoxyated alcohols to be patented based on the data described in this thesis.

Thus, the next step before starting the filing process was to compare the miscibility-enhancing effect of the alkoxyated alcohols of this thesis with the mixture of rather long-chain alkoxyated alcohols and short-chain 1-alcohols used in prior art [Fan, W.; Li, B.; Li, S.; Li, Z.; Lu, T.; Luo, H.; Nan, G.; Wang, F.; Zhang, C. CN, 104610953A, 2015]. Therefore, the miscibility-enhancing effect of the additive (C₁₂E₂P₇), which is similar to the additives described in the patent (C₁₄E₂P₆ and C₁₄E₂P₈), was investigated in the CO₂ – mco47.0 system using 1-butanol (C₄E₀) as co-additive at $w_{oil} = 0.075 \pm 0.003$ and $\gamma_{CO_2} = 0.010 \pm 0.001$. Reflecting the conditions used in prior art, the mass fraction of C₄E₀ in the C₁₂E₂P₇/C₄E₀ mixture, given by

$$\delta = \frac{m_{co-additive}}{m_{co-additive} + m_{additive}}, \quad (4.4)$$

was adjusted to $\delta = 0.400$. For comparison, the influence of some alkoxyated alcohols identified in this thesis on the CO₂ – mco47.0 miscibility gap was studied with and without the co-additive 1-butanol under the same conditions.

Figure 4.23 shows the obtained pressure profits Δp at 65 °C and 75 °C for the different additives with and without 1-butanol as co-additive ($\delta = 0.400$) in form of a bar chart. Note that due to the very low additive concentrations, the pressure profits could only be determined with an accuracy of ± 1.0 MPa. The claimed C₁₂E₂P₇/1-butanol mixture exhibits only a pressure profit of $\Delta p = 0.9$ MPa (at 65 °C) and $\Delta p = 0.5$ MPa (at 75 °C), while the additive C₁₂E₂P₇ alone (not claimed in [Fan, W.; Li, B.; Li, S.; Li, Z.; Lu, T.; Luo, H.; Nan, G.; Wang, F.; Zhang, C. CN, 104610953A, 2015]) shows a pressure profit of $\Delta p = 3.4$ MPa (at 65 °C) and $\Delta p = 1.9$ MPa (at 75 °C). It is surprising that the pressure profit of the claimed mixture is even smaller than the pressure profit caused by 1-butanol alone of $\Delta p = 1.9$ MPa (at 65 °C) and $\Delta p = 1.3$ MPa (at 75 °C).

Indeed, most of the medium-chain alkoxyated additives studied in this thesis show a much larger pressure profit than the large C₁₂E₂P₇ when only one additive and no blend is

used. For example, ITDA P₃ shows larger pressure profits of $\Delta p = 4.1$ MPa (at 65 °C) and $\Delta p = 2.5$ MPa (at 75 °C) than C₁₂E₂P₇ (not claimed) and a much larger pressure profit than the claimed C₁₂E₂P₇/1-butanol mixture. The same holds true for the non-alkoxylated branched alcohol ISOFOL 12 ($\Delta p = 3.7$ MPa (at 65 °C) and $\Delta p = 2.0$ MPa (at 75 °C)). The use of the additive/1-butanol mixture also led to a decrease of the pressure profit for the additives used in this thesis compared to the additive alone.

An interesting trend emerged when the longer-chain linear and branched surfactants C₁₆E₂P₇ and ISOFOL 16E₂P₇ were used. While negative pressure profits were observed when using these long-chain additives alone, the use of mixtures of these additives with 1-butanol led to slightly positive Δp values, which is due to the miscibility-enhancing effect of 1-butanol.

Therewith, the measurements of the miscibility-enhancing effect of prior art blends of long-chain alkoxyated additives and short-chain 1-alcohols show very clearly that the use of the medium-chain alkoxyated alcohols used in this thesis represents an improvement over the already patented blends. Accordingly, a patent application with the title "Injection Fluids comprising alkoxyated alcohols and the use of such fluids in oil recovery processes" (EP19158014) was filed on February 19th, 2019 by Sasol Performance Chemicals GmbH. Note that some of the data presented in this thesis have already been published in this application.

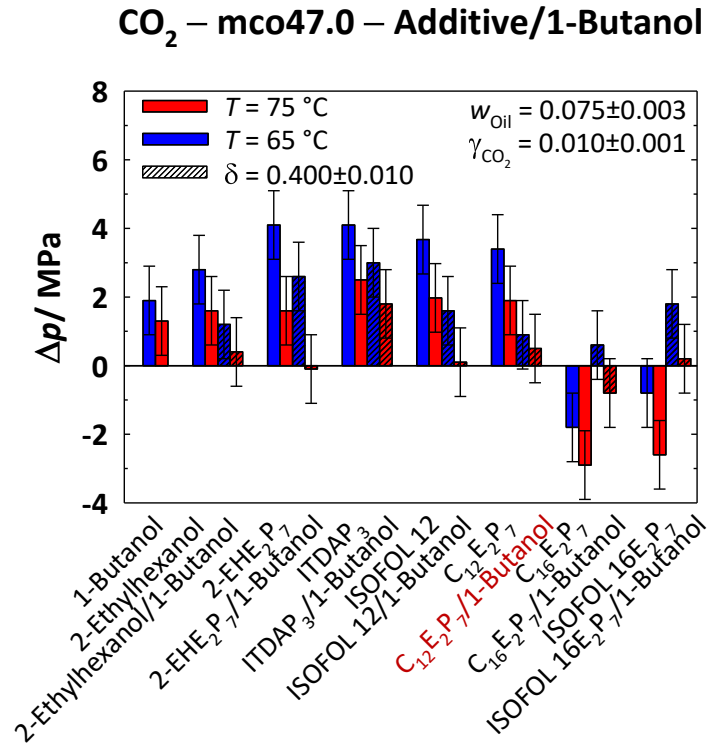


Figure 4.23: Bar chart showing the pressure profits Δp found for the different additives with and without 1-butanol as co-additive ($\delta = 0.400$) in the system CO₂ – mco47.0 at $w_{\text{Oil}} = 0.075$ and $\gamma_{\text{CO}_2} = 0.010$ at 65 °C and 75 °C. The mixture C₁₂E₂P₇/1-butanol corresponds to prior art (examples I and III of [Fan, W.; Li, B.; Li, S.; Li, Z.; Lu, T.; Luo, H.; Nan, G.; Wang, F.; Zhang, C. CN, 104610953A, 2015]). Note that the alkoxyated alcohols used in this thesis, e.g. ITDA P₃ ($\Delta p = 4.1$ MPa (65 °C) and 2.5 MPa (75 °C)), show larger pressure profits than the claimed C₁₂E₂P₇/1-butanol mixture and as the pure C₁₂E₂P₇ alone (not claimed).

4.7 Swelling Behavior

In this chapter as well as the following chapter, two technically relevant properties, the swelling behavior and the dynamically determined MMP, are analyzed. To verify the promising miscibility-enhancing effects of the additives obtained above, their influence on the swelling behavior of a crude oil-containing system was investigated. These results have already been published in “Impact of Miscibility Enhancing Additives on the Flooding Scheme in CO₂ EOR Processes” [Rommerskirchen, et al., 2018].

An important parameter, which determines the potential success of CO₂-EOR, is the ability of the injected fluid to drift into the respective crude oil causing a volume increase of the original oil in place (OOIP) and therewith a viscosity reduction [Holm, Josendal, 1982, Hand, Pinczewski, 1990]. This swelling and the associated viscosity decrease are a result of the “condensation” of CO₂ in the crude oil and make the OOIP more easily recoverable from the rock formation [Holm, Josendal, 1974]. The swelling behavior is determined via single contact phase behavior experiments measuring the solubility of CO₂ in crude oil. First studies on the

swelling behavior have been performed as early as in 1926 [Beecher, Parkhurst, 1926, Beeson, Ortloff, 1959]. Based on these studies, Welker and Dunlop developed a method to predict the swelling behavior via the solubility of CO₂ in crude oil, which was estimated on the basis of the crude oil gravity and the given pressure for systems at 80 °F and additionally verified by measurements [Welker, 1963]. These measurements, however, required a large crude oil sample volume of 50 ml to 60 ml. Based on an apparatus developed by Kohn and Kurata [Kohn, Kurata, 1958], a modified apparatus with a small sample volume of approx. 6 ml was designed by Ren and Scurto [Ren, Scurto, 2007]. Furthermore, Ren and Scurto demonstrated that just approx. 0.13% of the originally loaded *n*-decane is solubilized in the CO₂ vapor phase at initial conditions, i.e. the loss of the liquid phase into the gaseous phase can be considered negligible [Ren, Scurto, 2007]. Based on this set-up, in a recent study, Tsau, Bui, and Willhite analyzed the swelling behavior visually in a single contact apparatus with a total cell volume of 26 ml [Tsau, Bui, Willhite, 2010]. Inspired by their study, two of the best performing additives obtained so far in this thesis, the linear C₆P₃ and the branched ITDA E₂, were investigated in terms of their influence on the swelling behavior in the Asian crude oil aco38.8. To the best of my knowledge, no literature is known with regard to the effects of alkoxyated additives on swelling factor (SF) curves in CO₂-EOR. Tsau, Bui, and Willhite determined the swelling factor (SF) to

$$SF(p) = \frac{V_{\text{Oil phase}}(p)}{V_{\text{Oil phase}}(1 \text{ atm})} \quad (4.5)$$

wherein the volume of the crude oil-rich phase $V_{\text{Oil phase}}(p)$, which coexists with the CO₂-rich phase, is determined visually at the respective temperature and pressure. In this thesis, the HP-cell was used to investigate the swelling behavior. To reliably determine $V_{\text{Oil phase}}(p)$, it was crucial that the liquid components, crude oil and additive, do not vaporize into the equilibrated gaseous state of the CO₂ at the initial conditions. Thus, the initial conditions had to be chosen accordingly. After loading of the HP-cell with sample, a pressure of approx. 8.5 MPa was found at 65 °C. This pressure is below the pressures required to reach miscible conditions of the investigated additives in CO₂ at 65 °C and $\gamma_{\text{CO}_2} = 0.020 \pm 0.001$ (which would require pressures of (15.9 ± 0.5) MPa for C₆P₃ and (31.6 ± 0.5) MPa for ITDA E₂, as already shown in Figure 4.9). Therefore, the solubility of the additives in CO₂ can be considered negligible for the initial conditions. As mentioned above, Ren and Scurto demonstrated that the amount of the liquid in the gaseous CO₂ phase is negligible for *n*-decane. According to the

data presented above, that show a better miscibility for CO₂ – *n*-alkanes systems than for the CO₂ – aco38.0 system (Figure 4.3), it can be assumed that the liquid aco38.0 in the HP-cell stays in the liquid phase at initial conditions. Note that for the investigations in the high pressure visual cell also the not observable dead volume of (0.065±0.003) ml was taken into account. The initial volume $V_{\text{Oil phase}}(1 \text{ atm})$ of aco38.8 is obtained from measuring its weight and using the density at 65 °C ($\rho(\text{aco38.0}) = (0.797 \pm 0.003) \text{ g cm}^{-3}$ at 65 °C). The volumes of the phases at the different pressures analyzed were calculated based on their heights determined from photographs and the known diameter of the sample chamber. The volume of the stirring bar was also taken into account ((0.157±0.008) ml). To illustrate the influence of the two additives on the CO₂ – aco38.0 system, a set of photographs is shown in Figure 4.24 for $p \geq 12.0 \text{ MPa}$ at 65 °C. The measurements were performed at $w_{\text{Oil}} = 0.250 \pm 0.003$ and $\gamma_{\text{CO}_2} = 0.020 \pm 0.001$ starting at a pressure of 8.5 MPa (no photograph shown). By increasing the pressure, the $V_{\text{Oil phase}}$ decreases while the volume of the CO₂-rich phase increases and gets darker in color. This change in color proofs the “vaporization” of the denser lower crude oil-rich phase into the lighter upper CO₂-rich phase until just one phase remains. By addition of the additives, the transition into a one-phase occurs at lower pressures compared to the CO₂ – aco38.8 system without additive. The corresponding pressures are shown in the column on the right in Figure 4.24 for comparison.

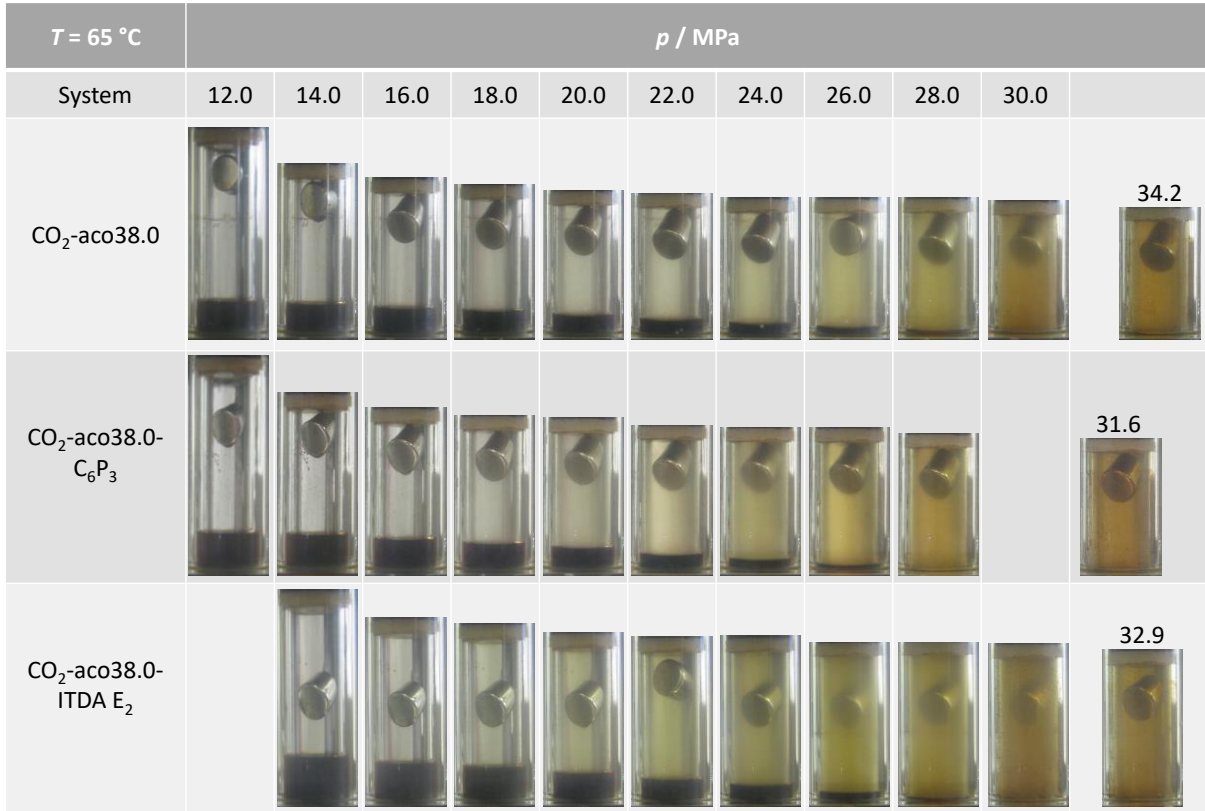


Figure 4.24: Photographs illustrating the influence of the additives C_6P_3 and ITDA E_2 on the swelling behavior of the $\text{CO}_2 - \text{aco38.0}$ system at $\gamma_{\text{CO}_2} = 0.020 \pm 0.001$, $w_{\text{oil}} = 0.250 \pm 0.003$ and $65\text{ }^{\circ}\text{C}$. The denser and darker colored oil-rich phase ($V_{\text{Oil phase}}(p)$) at the bottom and the CO_2 -rich phase on the top are shown.^(1F) The pressure for complete miscibility is lowered by the additives compared to the $\text{CO}_2 - \text{aco38.0}$ system without additive and therewith the extraction of the oil-rich excess phase is improved by the additives.

Based on the photographs in Figure 4.24, the $V_{\text{Oil phase}}(p)$ and the corresponding swelling factors (SF) at $65\text{ }^{\circ}\text{C}$ are calculated and shown in Figure 4.25 as a function of the pressure. At the first measured pressure of 8.5 MPa, the volume of the crude oil-rich phase ($V_{\text{Oil phase}}$) increases compared to the initial volume due to the “condensation” of CO_2 . As a result, an increase of the SF is obtained with the highest value found at 8.5 MPa. Because of the limited volume of the high pressure visual cell, recording of data below pressures of 8.5 MPa was not possible. In other words, it was not possible to show data for the rise of the $SF(p)$ curve from the starting point. Both investigated additives show an improved swelling behavior of the pseudoternary systems compared to the pseudobinary $\text{CO}_2 - \text{aco38.0}$ system. Thus, the maximum swelling factor increases from $SF_{\text{max}} = 1.32$ for the $\text{CO}_2 - \text{aco38.0}$ system to a value of $SF_{\text{max,additives}} = 1.39$ for both additive-containing systems indicating a higher replacement efficiency (Figure 4.25). At the maximum of the $SF(p)$ -curves, the pressure $p_{\text{max}} \approx 8.5\text{ MPa}$ is slightly larger than the critical pressure of CO_2 ($p_c = (7.3773 \pm 0.0030)\text{ MPa}$ [Span, Wagner, 1996]). It has to be mentioned that since no data below 8.5 MPa could be

recorded, p_{\max} could also be located at lower values. It is, however, assumed that the maximum SF is located above the critical pressure of CO_2 , for the analyzed temperature of $65\text{ }^\circ\text{C}$, which is above the critical temperature of CO_2 . An increased volume of the aco38.0-rich phase by C_6P_3 compared to the CO_2 – aco38.8 system is seen until the intersection of the curves at approx. 20 MPa at an SF value of 0.6. For ITDA E_2 , an increased volume compared to the CO_2 – aco38.8 system is found until the intersection at an SF value of 0.45 at 26 MPa. Thus, an improved swelling behavior is found for ITDA E_2 for a larger pressure range (increased by 6 MPa) compared to C_6P_3 . Interestingly, for both additive-containing systems, the transition to one phase is observed for similar pressures of approx. 31.6 MPa for C_6P_3 and approx. 32.9 MPa for ITDA E_2 (at SF = 0). The measurement of C_6P_3 at 30 MPa was skipped to reduce the measurement time at high temperature and pressure, thereby ensuring proper sealing of the HP-cell for the measurements at higher pressure of the phase transition (which explains the missing picture). Moreover, for C_6P_3 at 28 MPa as well as ITDA E_2 at 28 MPa and 30 MPa, the SF could not be calculated from the corresponding pictures due to large errors of the small volumes of the aco38.0-rich phases. Thus, these data points at 28 MPa and 30 MPa are missing for the two additives in the following diagram.

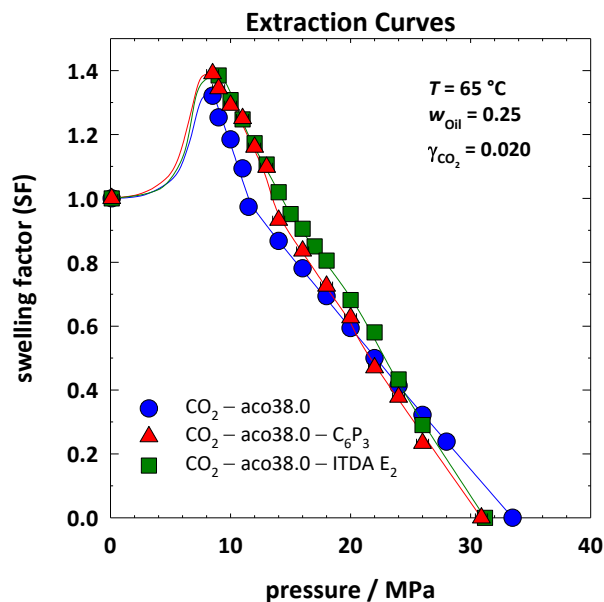


Figure 4.25: Influence of the additives C_6P_3 and ITDA E_2 on the swelling behavior of the CO_2 – aco38.0 system at $\gamma_{\text{CO}_2} = 0.020 \pm 0.001$, $w_{\text{oil}} = 0.250 \pm 0.003$ and $65\text{ }^\circ\text{C}$. ^(F)The swelling factor (SF) recorded at $65\text{ }^\circ\text{C}$ is shown as a function of pressure. Note that both investigated additives show an improved swelling behavior compared to the CO_2 – aco38.0 system indicating a higher replacement efficiency. Adopted from already published data [Rommerskirchen, et al., 2018].

Due to the improvement of the solvent properties of the CO_2 -rich phase by the additives, a faster decrease of the crude oil-rich phase volume ($V_{\text{oil phase}}(p)$) is observed in the

presence of additive. Thus, the crude oil can be produced better. Moreover, the slope of the $SF(p)$ -curve can be regarded as a measure for the efficiency of a flood, whereby a steeper slope might correspond to a faster and more efficient extraction. Comparing the slopes of the $SF(p)$ -curves, a much steeper decay is found for the two additive-containing systems at pressures above 14 MPa. As a result, the swelling factors of the additive-containing systems at 8.5 MPa are higher and one phase is already reached at lower pressures compared to the system without an additive [Rommerskirchen, et al., 2018].

The results of the influence of C_6P_3 and ITDA E_2 on the swelling behavior of the CO_2 – aco38.0 system confirm the results from the phase diagram studies showing that the additives enhance the miscibility of the CO_2 with the crude oil aco38.0.

4.7.1 Water-Containing Systems

Above the miscibility-enhancing effects of the additives were analyzed for water-free systems. Since natural systems usually comprise water, further investigations were done for water-containing systems. Before analyzing the effects of additives in the respective pseudoquaternary system H_2O – CO_2 – aco38.0 – additive, the phase behavior of the corresponding pseudoternary system H_2O – CO_2 – aco38.0 without additive was studied. The Asian crude oil was chosen because of its dark color, which allows an easier visual detection of the different phases.

In order to simplify the investigations of water in the CO_2 – aco38.0 system, the phase behavior of the system was studied at one temperature (65 °C) for one total water content of 30 wt%. Figure 4.26 shows the $p(w_{oil})$ -diagram of the pseudoternary H_2O – CO_2 – aco38.0 system (blue filled circles) in comparison to the pseudobinary CO_2 – aco38.0 system (black unfilled diamonds) already shown above (see Figure 4.5). Thereby, w_{oil} is the mass fraction of aco38.0 in the CO_2 /aco38.0 mixture. Interestingly, the addition of 30 wt% of water has almost no influence on the phase behavior of the CO_2 - and oil-rich phases at the investigated w_{oil} , i.e. complete miscibility of CO_2 and aco38.0 is observed at the same pressure independent of the presence of H_2O . Note that in the water-containing system three phases coexist. A water-, an oil- and a CO_2 -rich phase can be seen from the bottom to the top, see photograph in Figure 4.26 inside the miscibility gap. At higher pressures, a water-rich phase coexists with the CO_2 /aco38.0 mixture, which is shown by the photograph above the miscibility gap. The volumes of the existing phases are illustrated by the boxes next to the photographs for better

visibility. The volume of the H₂O-rich phase seems to be constant over the whole pressure range, whereas the other two phases form a single phase above the phase transition pressures. However, in the presence of an additional H₂O-rich phase, the determination of the phase boundary was much more difficult compared to the pseudobinary CO₂ – aco38.0 systems. While in the latter system, a fast phase transition can be easily observed by a change from a clear to a turbid phase, phase separation in the water-containing system requires a much longer time. The dark color of the water phase is due to residues of the Asian crude oil, which seem to coat the water-rich phase.

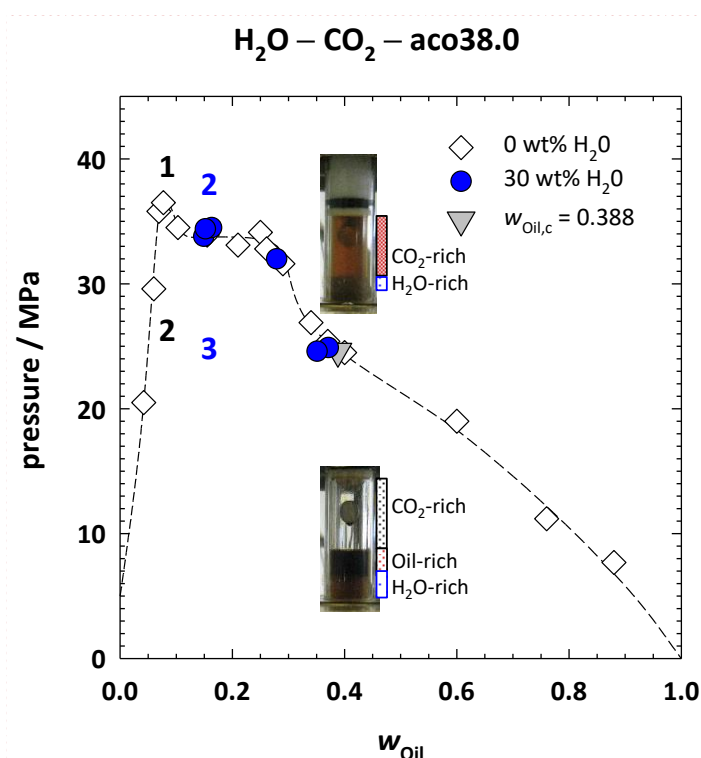


Figure 4.26: $p(w_{oil})$ -diagram of the systems CO₂ – aco38.0 (black unfilled diamonds) and H₂O – CO₂ – aco38.0 (blue filled circles) at 65 °C with photographs of the pseudoternary system. The pseudoternary system contains 30 wt% of water and w_{oil} is the mass fraction of aco38.0 in the CO₂/aco38.0 mixture. Furthermore, the plait point of the system CO₂ – aco38.0 (gray filled triangle) located at $w_{oil,c} = 0.39 \pm 0.02$ and $p_c = 24.6 \pm 0.5$ MPa is shown. Interestingly, the influence of water on the miscibility gap can be neglected. Note that in the water-containing system three phases coexist, a water-, an oil- and a CO₂-rich phase can be seen from the bottom to the top.

Furthermore, the swelling behavior of the six water-containing samples ($0.149 \leq w_{oil} \leq 0.371$, blue filled circles) shown in Figure 4.26 was investigated. As the individual determination of the oil phase volume was afflicted with a substantial error (whereas the determination of the combined oil and water phase volumes was more reliable), the swelling factor of the water-containing samples was defined according to

$$SF(p) = \frac{V_{\text{Oil phase}}(p) + V_{\text{Water phase}}(p)}{V_{\text{Oil phase}}(1 \text{ atm}) + V_{\text{Water phase}}(1 \text{ atm})} \quad (4.6)$$

Figure 4.27 shows the swelling factor (SF) as a function of the pressure together with the corresponding photographs for the sample with $w_{\text{Oil}} = 0.152$ at 65 °C. Due to the additional amount of water and the limited volume of the high pressure visual cell, no values of the SF could be recorded below 12.0 MPa. This pressure is already obtained only by loading of the sample in the HP-cell (see also chapter 4.6). Thus, a detection of the maximum in the swelling curve was not possible. The first swelling factor (at 12 MPa) shows a value of 0.89. By increasing the pressure, a decrease of the SF is found, which reflects the behavior of the already investigated water-free CO₂ – aco38.0 system (see Figure 4.25). However, due to the modified definition of the SF in equation (4.6), it levels off towards a value of $SF \approx 0.50$ for pressures above the phase transition at 34.5 MPa (black dashed line). Note that here a CO₂/aco38.0-rich phase coexists with the H₂O-rich phase. A theoretical end value of SF can be calculated for a pressure at the phase transition (34.5 MPa) based on the composition of the sample corresponding to a $w_{\text{Oil}} = 0.152 \pm 0.001$. The sample contains 30 wt% of water (0.4510 g), 11 wt% of aco38.8 (0.1583 g) and 59 wt% of CO₂ (0.88 g). The respective densities at 65 °C are 0.99488 gcm⁻³ at 34.5 MPa and 0.98054 gcm⁻³ at 1 atm for water [Lemmon, McLinden, Friend, 2013 (accessed August 7, 2019)], and 0.797 gcm⁻³ at 1 atm for aco38.0. Based on this composition, a value of $SF_{\text{theo}} \approx 0.69$ can be calculated. Thereby, the deviation between SF and SF_{theo} might be a consequence of the difficult and potentially erroneous determination of the small phase volumes at high pressures, see photos shown in Figure 4.27. Even considering a solubility of 3.5 wt% of CO₂ in water [Diamond, Akinfiev, 2003], SF and SF_{theo} deviate. In order to allow more accurate measurements at these conditions, HP-cells with a larger volume could be used.

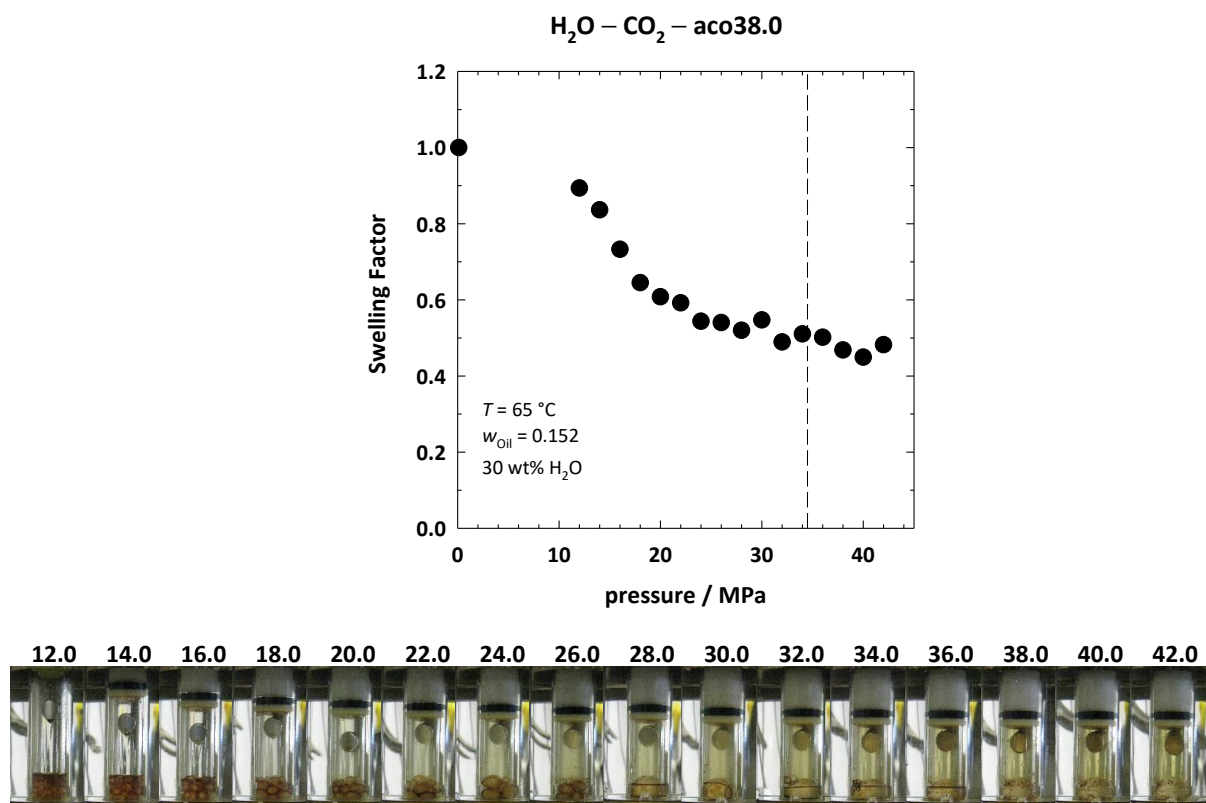


Figure 4.27: Extraction curve for modified swelling factor (SF), see equation (4.6) for the H₂O – CO₂ – aco38.0 system at 65 °C containing 30 wt% of H₂O at $w_{oil} = 0.152 \pm 0.001$ and photographs of the respective samples. Due to the additional amount of water and the limited volume of the high pressure visual cell, no values of the SF can be recorded below 12.0 MPa. Thus, only the typical decay of SF is detected. Due to the modified definition, the SF value levels off towards $SF \approx 0.50$ at large pressures. The black dashed line shows the phase transition pressure at 34.5 MPa.

In order to illustrate the behavior close to the plait point, the SF is shown as a function of the pressure at $w_{oil} = 0.371 \pm 0.001$ ($w_{oil,c}$ of the CO₂ – aco38.0 system has a value of 0.39 ± 0.02) at 65 °C including photographs of the sample (Figure 4.28). In accordance with the behavior of the water-free system, the water-containing sample shows a strong dew-point behavior at the analyzed composition near the plait point for pressures below 24.9 MPa, where the phase transition occurs. As expected, the crude oil “vaporizes” strongly into the CO₂-rich phase at this pressure leading to a strong decrease of the oil-rich phase volume or in other words to a sharp decrease in the SF. At $p = 24.9$ MPa, the full miscibility of CO₂ and aco38.0 is achieved at a swelling factor of $SF \approx 0.50$ (due to the presence of water), which stays almost constant for larger pressures. Here, the experimental value agrees almost quantitatively with the $SF_{theo} \approx 0.50$, which was also calculated based on the composition of the sample (30 wt% H₂O, 26 wt% aco38.8 and 44 wt% CO₂) taking into account the respective densities of water and aco38.0 as well as the solubility of CO₂ in water. The photographs below the diagram show the sample in the sapphire cylinder of the HP-cell at different pressures

after phase separation. Starting from lower pressures at 12.0 MPa, three coexisting phases, a water-, an aco38.0- and a CO₂-rich phase can be seen. By increasing the pressure, the volume of the oil-rich phase decreases and within a few MPa disappears, which can be seen by comparing the photographs between 24.0 MPa and 26.0 MPa. Further increase of the pressure leads to the coexistence of two phases, a CO₂/aco38.0-rich and an H₂O-rich phase, which can be seen in the photographs for pressures above 26 MPa. Furthermore, the color of the CO₂-rich phase changes with increasing pressure from clear, over yellowish, to dark red because of the miscibility of the aco38.0 in the CO₂ and vice versa.

In summary, the phase and swelling behavior of the water-containing CO₂ – aco38.0 system is in line with the behavior found for the respective water-free system. This provides a good basis to transfer the data obtained for the water-free systems to water-containing systems.

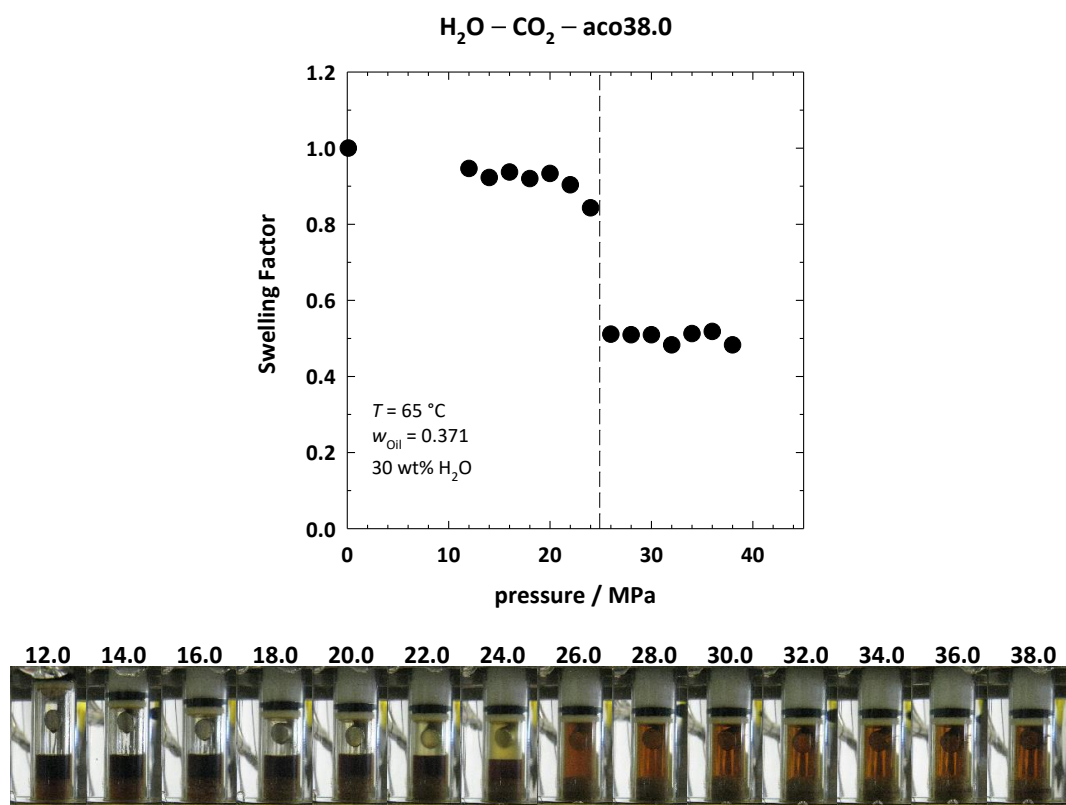


Figure 4.28: Extraction curves of the modified swelling factor SF (see eq. (4.6)) of the H₂O – CO₂ – aco38.0 system containing 30 wt% water at $w_{oil} = 0.371 \pm 0.001$ and 65 °C. **Top,** Being close to the composition of the plait point, the SF drops suddenly within a few MPa from 0.85 to 0.50 around $p = 24.9$ MPa and stays almost constant with increasing pressures. The phase transition pressure is indicated by the black dashed line. **Below,** photographs of the phase separated sample at different pressures are shown. Note, the brightness and contrast of the photographs were adjusted to see the coexisting phases more clearly. Increasing the pressure, the aco38.0-rich phase disappears between 24.0 and 26.0 MPa. The color of the CO₂-rich phase changes with increasing pressure from clear to dark red because of the vaporization of aco38.0 in CO₂ and vice versa. Note that the dark color of the water phase is due to residues of the aco38.0, which seem to coat the H₂O-rich phase.

4.7.2 Pseudoquaternary Systems: H₂O – CO₂ – Aco38.0 – Additive

Having verified the resemblance of the phase behavior of the water-containing pseudoternary H₂O – CO₂ – aco38.0 systems with the water-free systems, the effect of the additives in the respective pseudoquaternary systems were investigated. Thus, the pseudoquaternary systems H₂O – CO₂ – aco38.0 – C₆P₃ and H₂O – CO₂ – aco38.0 – ITDA E₂ were studied, both containing 30 wt% H₂O and an additive mass fraction in CO₂ of $y_{\text{CO}_2} = 0.020 \pm 0.002$. C₆P₃ and ITDA E₂ were chosen as additives, because they showed promising results so far. The phase behavior investigations of the systems containing both water and additive were extremely difficult. Besides (and due to) long separation times, experimental problems with respect to the sealing of the HP-cell occurred. Containing H₂O, CO₂, Asian crude oil and additive for long times at a high temperature of 65 °C and high pressures of up to 45.0 MPa, the sealing O-rings failed quite often. Thus, the results obtained for the phase behavior of the pseudoquaternary systems must be treated with caution.

Figure 4.29 shows the effect of the additive C₆P₃ on the phase behavior of the H₂O – CO₂ – aco38.0 system (blue filled diamonds) containing 30 wt% of H₂O in form of a $p(w_{\text{oil}})$ -diagram at 65 °C. The unfilled circles mark the phase transition from three to two phases for the pseudoternary system H₂O – CO₂ – aco38.0. Thereby, the phase boundary indicated by the dashed line corresponds to the one of the pseudobinary CO₂ – aco38.0 system. As mentioned before, the additional water seems to have no or only a marginal influence on the lower miscibility gap for systems containing no additive (see Figure 4.26). However, as can be seen in Figure 4.29, the miscibility-enhancing effect of C₆P₃ seems to be hindered by the addition of water compared to the water-free system (see Figure 4.19). Data interpretation, however, needs to consider the mentioned experimental problems.

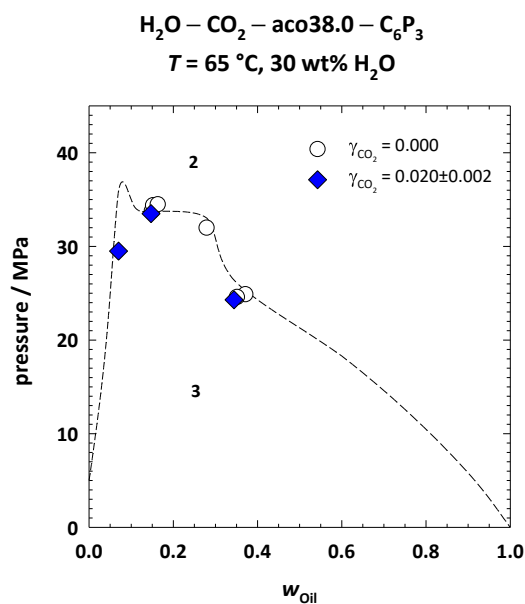


Figure 4.29: $p(w_{\text{Oil}})$ -diagram at 65 °C of the pseudoquaternary system $\text{H}_2\text{O} - \text{CO}_2 - \text{aco38.0} - \text{C}_6\text{P}_3$ with $\gamma_{\text{CO}_2} = 0.020 \pm 0.002$ (blue filled diamonds) and the pseudoternary system $\text{H}_2\text{O} - \text{CO}_2 - \text{aco38.0}$ (unfilled circles), both containing 30 wt% of H_2O . The lower miscibility gap indicated by the dashed line is based on the water-free $\text{CO}_2 - \text{aco38.0}$ system. No miscibility-enhancing effect is seen for C_6P_3 .

Furthermore, a series of swelling behavior studies was performed to understand the different effect of additive seen in the water-containing systems. However, also in these experiments, the same problems were faced. The pseudoquaternary $\text{H}_2\text{O} - \text{CO}_2 - \text{aco38.0} - \text{ITDA E}_2$ system with 30 wt% of water at a $w_{\text{Oil}} = 0.073 \pm 0.001$ (near the expected MMP_p of the water-free system), $\gamma_{\text{CO}_2} = 0.020 \pm 0.001$ and 65 °C was analyzed. While in the pseudoquaternary system containing C_6P_3 a rather clear water-rich phase was observed (data not shown), a milky water-rich phase can be seen for the system with ITDA E_2 in the photographs shown in Figure 4.30. This suggests that ITDA E_2 , as a surfactant, forms an oil-in-water emulsion, while the other – only weakly amphiphilic – additive C_6P_3 accumulates at the interfaces of the water-, oil- and CO_2 -rich phases. Note that the formation of an oil-in-water emulsion is observed for all studied pressures, i.e. between 13.0 MPa to 42.0 MPa. Additionally, the photographs show that it is really difficult to distinguish between three and two phases, i.e. to determine the phase boundary. The close inspection provided a value of (28.5 ± 0.5) MPa for the phase transition. In addition, also photographs are shown below for the water-free pseudoternary $\text{CO}_2 - \text{aco38.0} - \text{ITDA E}_2$ system at a similar oil mass fraction of $w_{\text{Oil,c}} = 0.075 \pm 0.001$ and 65 °C. The phase boundary for this system was obtained for a value of (28.4 ± 0.5) MPa, which is very close to the water-containing system. Furthermore, a change in color from clear to yellow in the CO_2 -rich phase for increasing the pressure can be seen

more clearly in the water-free system. Based on the photographs shown below, a reliable determination of the swelling factors was not possible for the pseudoquaternary system.

In conclusion, no miscibility-enhancing effects were found for the analyzed additives in the water-containing systems, although these data have to be treated with caution due to the mentioned experimental problems. Another explanation for the lacking effects by the additives is the solubility of the additives in water, thereby decreasing the amount of additive present to improve the miscibility of the oil- and CO₂-rich phases. This could be compensated by increasing γ_{CO_2} . Overall, it was not possible to reliably analyze the miscibility-enhancing effects of the additives in the water-containing systems. This would require further refinements of the HP-cell, like improved O-ring sealings and larger sample volumes.

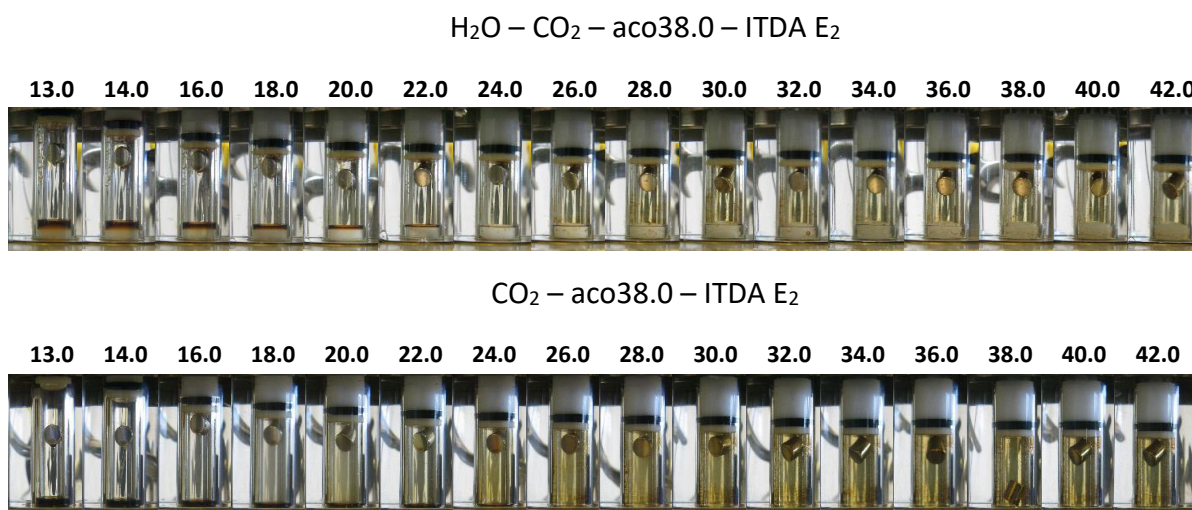


Figure 4.30: Photographs of the pseudoquaternary system H₂O – CO₂ – aco38.0 – ITDA E₂ (30 wt% of water, $w_{\text{Oil}} = 0.073 \pm 0.001$, $\gamma_{\text{CO}_2} = 0.020 \pm 0.001$) and the pseudoternary system CO₂ – aco38.0 – ITDA E₂ at 65 °C taken after phase separation at different pressures between 13.0 to 42.0 MPa. For all pressures, a milky lower phase can be seen in the water-containing system, suggesting that ITDA E₂ forms an oil-in-water emulsion. The corresponding water free system CO₂ – aco38.0 – ITDA E₂ at $w_{\text{Oil},c} = 0.073 \pm 0.001$, $\gamma_{\text{CO}_2} = 0.020 \pm 0.001$ and 65 °C provides a more clearly visible change in color from clear to yellow by increasing the pressure.

4.8 Simulation of Real Crude Oil Field Operations by Slim Tube Experiments

So far the effect of the alkoxyated alcohols was only investigated statically, i.e. by studying the phase behavior, it was found that the additives considerably reduce the miscibility gap of CO₂ – (model) crude oil systems. In order to approach the conditions of real crude oil field operations, dynamic investigations, like the MMP determination by flow experiments, more precisely by slim tube studies, were performed.

In EOR applications, simulations are an often-used method to gain information about the properties of a real crude oil field such as diffusion, permeability, porosity and pore confinement. As reviewed by Jia, Tsau, and Barati, experimental studies of these properties, which have to be performed dynamically and are much more elaborate, often provide more accurate results [Jia, Tsau, Barati, 2019]. However, to the best of my knowledge, there are no data described in literature with meaningful results on these properties for alkoxyated additives for CO₂-EOR projects. Dissolving the producer gas in crude oil and thus the swelling and extraction of the oil are the main mechanisms of oil recovery with gases, such as CO₂ [Jia, Tsau, Barati, 2019, Hawthorne, et al., 2016]. These properties can be measured by simple phase behavior experiments [Hand, Pinczewski, 1990] and respective data determined in the high pressure visual cell have been presented in chapters 4.3 – 4.7 of this thesis. However, as mentioned above, in order to take into account properties like diffusion, permeability, and porosity, dynamic slim tube measurements or core flood studies have to be performed. Both types of experiments are commonly applied procedures to evaluate the efficiency of CO₂-EOR projects and acknowledged and accepted by the industry [Elsharkawy, Poettmann, Christiansen, 1996].

The relationship between static phase behavior studies providing beside swelling/extraction properties, the critical (plait) point of the complex mixtures and the dynamically determined minimum miscibility pressure (MMP) has been discussed by some researchers. Harmon and Grigg concluded after their swelling/extraction measurements that it is hard to establish a relationship between the phase behavior and dynamic slim tube experiments [Harmon, Grigg, 1988]. They found reasonable agreement between the two methods only for low temperature (less than 43.3 °C), but not for higher temperatures (greater than 43.4 °C).

As mentioned earlier, the MMP is defined for a given reservoir and temperature as the lowest pressure to achieve first- or multiple-contact miscibility (FCM or MCM) between

reservoir oil and the injection fluid (in this thesis CO₂). It can be assumed that the MMP agrees with the pressure p_c at the critical (respectively plait) point of the mixture. This means that the interfacial tension between the oil-rich phase and the injection fluid-rich phase approaches zero [Stalkup, 1983, Hawthorne, et al., 2016, Teklu, et al., 2014]. The critical (plait) point can be determined, as performed in this thesis with the HP-cell, by static phase behavior studies. Such studies also provide the MMP_p, which was often used in this thesis to characterize the miscibility-enhancing effect of the different additives. As described earlier, the MMP_p is the pressure, where the miscibility gap of the system closes. At pressures higher than the MMP_p, always a single-phase mixture is found, independent of the composition.

Thus, the motivation to determine the MMP via slim tube studies was twofold. Firstly, to study the effect of the alkoxyated alcohols under real oil field operating conditions and to determine the influence of one of the best-acting additives on the MMP as a proof of concept. Secondly, to prove whether the MMP determined by slim tube studies is consistent with the critical (plait) point pressure p_c . For this purpose, a slim tube apparatus was set-up and validated in close collaboration with Prof. Dr. George J. Hirasaki and Dr. Maura Puerto during two research stays at Rice University (Houston, Texas, USA). The results of the slim tube studies are detailed in the following subsection.

4.8.1 Slim Tube Studies

Design and set-up of the slim tube apparatus was done in close cooperation with Prof. Dr. George J. Hirasaki and Dr. Maura Puerto. The main part of the slim tube apparatus consists of a coiled tube, which fits in an explosion-proof oven for temperature control and exhibits an inner diameter of 3.9 mm (0.152 inch) with a length of 30.48 m (100 ft). It is packed with Ottawa sand 20/40 yielding a pore volume (PV) of 135 ml. The set-up is described in detail in chapter 3.2.2.

The pseudobinary CO₂ – mco38.8 system was studied with respect to the influence of the additive C₆P₃ on the minimum miscibility pressure (MMP). The model crude oil mco38.8 was selected because of its clear phase and its API value, which covers crude oils of interest. As mentioned above, no benzene was allowed in flow experiments, due to safety regulations at the Rice University. Therefore, the composition of the benzene-containing mco38.8 had to be adapted. The benzene fraction was replaced by increasing the respective fractions of toluene and *m*-xylene leading to a model crude oil with an adapted API gravity of 38.0 (named

mco38.0). The differences of the two model crude oils mco38.8 and mco38.0 in composition, density, API gravity and MMP_p (at 65 °C) have been presented above (Table 4.4) and the differences in the phase behavior of the respective pseudobinary systems have been shown to be negligible (see chapter 4.1.2.1, Figure 4.8).

To determine the MMP, which indicates the lowest pressure to achieve first- or multiple-contact miscibility (FCM or MCM), slim tube measurements were performed at different pressures close to the MMP (two below and two above the MMP) for a given temperature. In order to allow comparison of the MMP with the pressure of the plait point (p_c) determined via statically measured phase diagrams and to avoid the crystallization of the wax component of the mco38.0, the measuring temperature was set to 65 °C. Note that due to the crystallization, the filling of the slim tube apparatus with homogenous mco38.0 was a challenge. For details, how the slim tube apparatus experiments were set-up, validated and run, see chapter 3.2.2. After filling the slim tube apparatus with mco38.0, the CO₂ was injected by a tempered dual Isco pump at the respective pressure, while measuring the volume of the recovered mco38.0. Thereby, the flow rate was adjusted to 0.563 ml/min to find a compromise between the time needed to run one experiment in a day and the correlated differential pressure (of upstream- and downstream-pressure), which should be as low as possible.

The pressures for the slim tube measurements were selected based on the results of the phase diagram studies, which provided the pressure of the plait point at $p_c = 17.2 \pm 0.5$ MPa, see Table 4.4. Accordingly, the first slim tube measurement on the CO₂ – mco38.0 system was performed at an average pressure (p_ϕ) of (15.3 ± 0.4) MPa. Due to the beneficial location of the laboratory (almost at sea level), the psig, which indicates the pressure of the gauges relative to the ambient pressure, could be expressed easily in MPa by adding the ambient pressure at sea level of 1 atm to the pressure indicated by the gauges. In Figure 4.31, the upstream pressure (before the slim tube, represented by the filled triangles) and downstream pressure (after the slim tube, represented by the unfilled triangles) as well as the recovered volume of mco38.0 (red circles) are plotted as a function of the injected volume of CO₂. The volumes of mco38.0 and CO₂ are related to the pore volume (PV = 135 ml) and are thus expressed relative to the PV. The pressure is determined by averaging the up- and downstream pressure values recorded from 0 to 1.2 PV of injected CO₂. The up- and downstream pressures are almost completely constant over the analyzed range of injected CO₂. According to literature, the oil

recoveries at different pressures should be compared at 1.2 PV of injected CO₂ to determine the MMP [Stalkup, 1978, Yellig, Metcalfe, 1980, Holm, Josendal, 1974]. At an average pressure of (15.3±0.4) MPa, the recovered PV of mco38.0 increases linearly from (0.07±0.01) PV(mco38.0) at 0.44 PV of the injected CO₂ to (0.52±0.01) PV(mco38.0) at 1.56 PV of the injected CO₂. After 1.2 PV of injected CO₂, a value of (0.38±0.01) PV(mco38.0) is obtained. A recovery of at least 0.90 PV of oil after 1.2 PV of injected fluid are considered as ultimate recovery. Thus, the oil recovery at the analyzed pressure is rather poor.

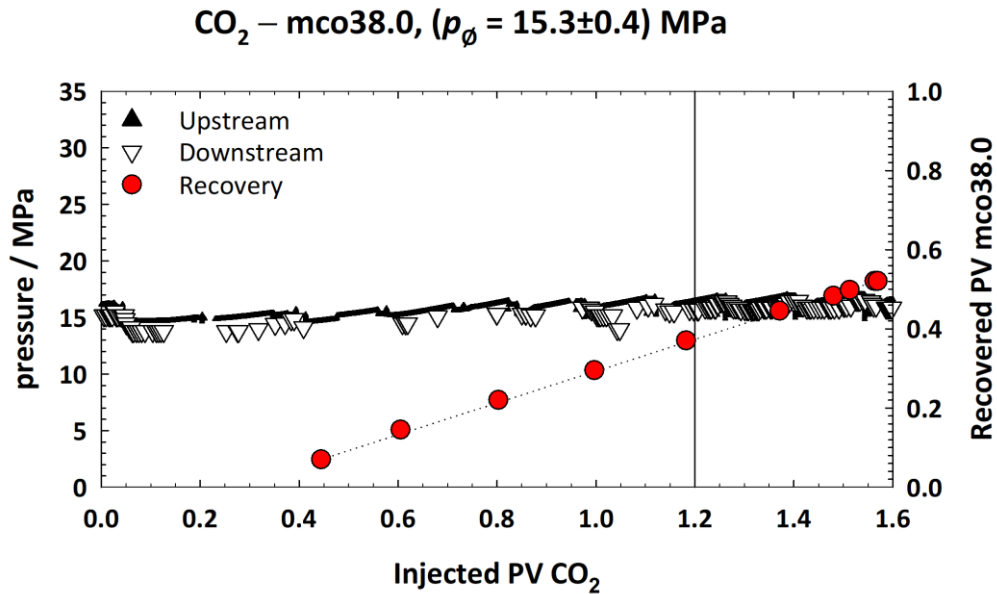


Figure 4.31: Results of slim tube measurements performed on the CO₂ – mco38.0 system at (65±2) °C with an average pressure (p_{ϕ}) of (15.3±0.4) MPa. Upstream pressure (filled triangles) and downstream pressure (unfilled triangles) as well as recovered PV of mco38.0 (red filled circles) are plotted as a function of the injected PV of CO₂. After injection of 1.2 PV of CO₂ (black line), the recovered PV of mco38.0 yields 0.38±0.01.

To determine the MMP of the CO₂ – mco38.0 system at (65±2) °C, three further slim tube runs were performed at higher pressures, i.e. at (17.0±0.3) MPa, (19.4±0.5) MPa and (19.7±0.6) MPa. The results are shown in Figure 4.32, again plotting the upstream and downstream pressure as well as the recovered PV of mco38.0 as a function of the injected volume of CO₂.

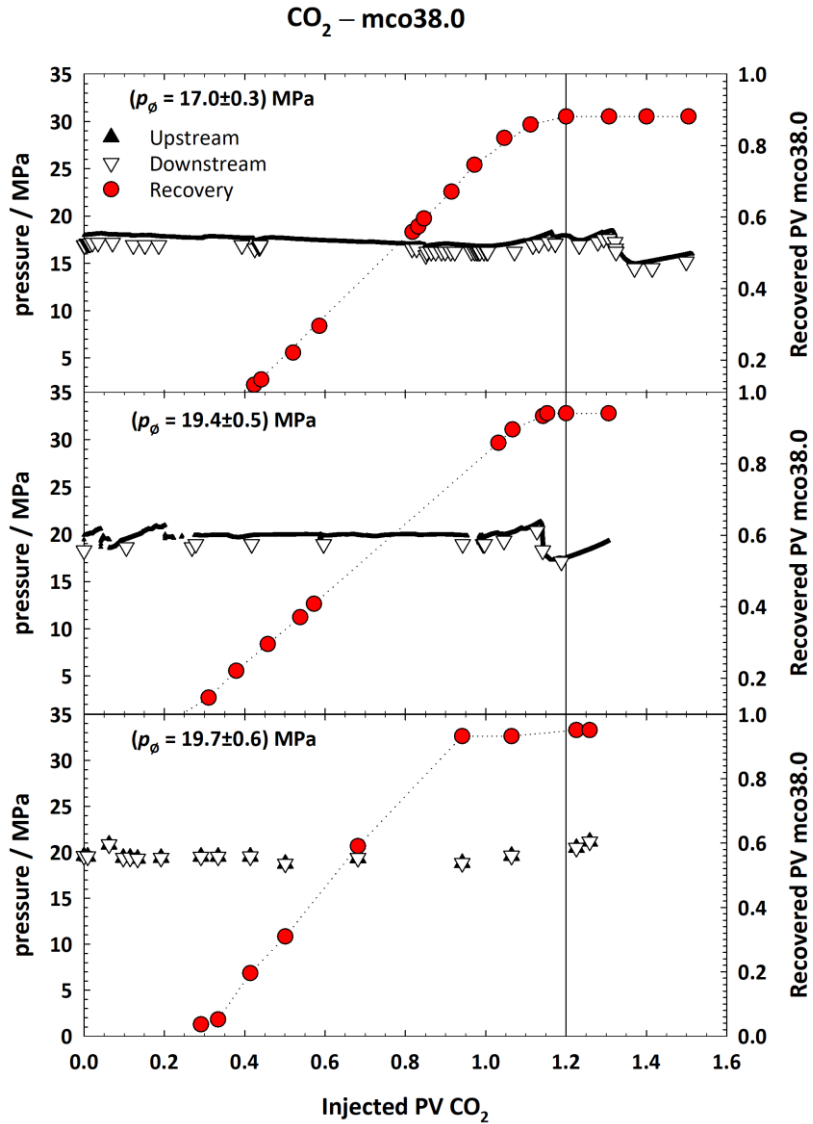


Figure 4.32: Results of slim tube measurements performed on the CO₂ – mco38.0 system at (65±2) °C and three different average pressures (p_{ϕ}) of (17.0±0.3) MPa, (19.4±0.5) MPa, and (19.7±0.6) MPa. Upstream (filled triangles) and downstream (unfilled triangles) pressures as well as recovered PV of mco38.0 (red circles) are plotted as a function of the injected PV of CO₂. The recovery of mco38.0 after the injection of 1.2 PV of CO₂ (black line) increases with increasing pressure from (0.88±0.01) over (0.94±0.01) to (0.95±0.01) of recovered PV of mco30.0.

For all investigated pressures, a similar trend with an almost linear increase of the recovered PV of mco38.0 for increasing injected PV of CO₂ is observed until the recoveries remain constant (Figure 4.32). The constant oil recovery level is already reached at lower PV of injected CO₂ for higher pressures. The recovered PV of mco38.0 at 1.2 PV of injected CO₂ (indicated by the black line) increases with increasing pressure starting at the low recovery shown above of (0.38±0.01) over (0.88±0.01) and (0.94±0.01) to (0.95±0.01) recovered PV of mco38.0. The strong increase in the recoveries seen for the three higher pressures already indicates that these measurements are performed near or above the MMP. The MMP

determination is described below in detail. Furthermore, the instant decrease of the up- and downstream pressure observed for the experiments at (17.0 ± 0.3) MPa and (19.4 ± 0.5) MPa at an injected PV of CO_2 of 1.35 and 1.15 is induced by the breakthrough of CO_2 , which was also detected via the CO_2 -bubbler. This CO_2 breakthrough occurs, when most of the oil is already recovered allowing the CO_2 to bypass the remaining oil and thus to flow through the tube with less resistance. However, at $p_{\phi} = (19.4 \pm 0.5)$ MPa, the breakthrough occurs at the PV of injected CO_2 , where the constant oil recovery level is reached, whereas at $p_{\phi} = (17.0 \pm 0.3)$ MPa, the breakthrough is observed at higher PV of injected CO_2 compared to the reaching of the constant oil recovery level. At $p_{\phi} = (19.4 \pm 0.5)$ MPa, a flood under miscible conditions (FCM flood) might be considered as a reason for the simultaneous breakthrough of the CO_2 and the almost complete recovery of mco38.0. The delay of the breakthrough of the CO_2 at $p_{\phi} = (17.0 \pm 0.3)$ MPa as well as the lower oil recovery indicate a multiple contact miscible flood (MCM flood). The reason that a CO_2 breakthrough is not observed at (19.7 ± 0.6) MPa might be related to the lower amount of data points for this experiment, which was the first run performed. In that measurement, both up- and downstream pressures had to be read out manually. Afterwards the slim tube apparatus set-up was improved by connecting the pressure transducer of the dual Isco pump to a sensor interface card, which recorded the upstream pressures automatically in a higher frequency.

In order to determine the MMP of the CO_2 – mco38.0 system at (65 ± 2) °C, the recovered PVs of the mco38.0 after the injection of 1.2 PV of CO_2 are plotted against the pressure, see Figure 4.33. Unfortunately, some of the pressure values were not selected ideally. Accordingly, the determination of the MMP turned out to be difficult. However, assuming the data point at (17.0 ± 0.3) MPa is located at or slightly below the MMP, the two points below and above the MMP (corresponding to the two lower and higher pressures, respectively) can be connected by straight lines. Their intersection defines the MMP of the CO_2 – mco38.0 system. According to this assumption, the MMP is located at (17.0 ± 0.6) MPa with a recovered PV of (0.88 ± 0.01) of mco38.0. In case that the data point at (17.0 ± 0.3) MPa would be already located above the MMP, the MMP can only be estimated somewhere in the range between 15.3 and 17.0 MPa. In any case, the MMP, which characterizes the dynamic behavior of the CO_2 – mco38.0 system, is located close to, but below the plait point pressure of $p_c = (17.2 \pm 0.5)$ MPa of the system.

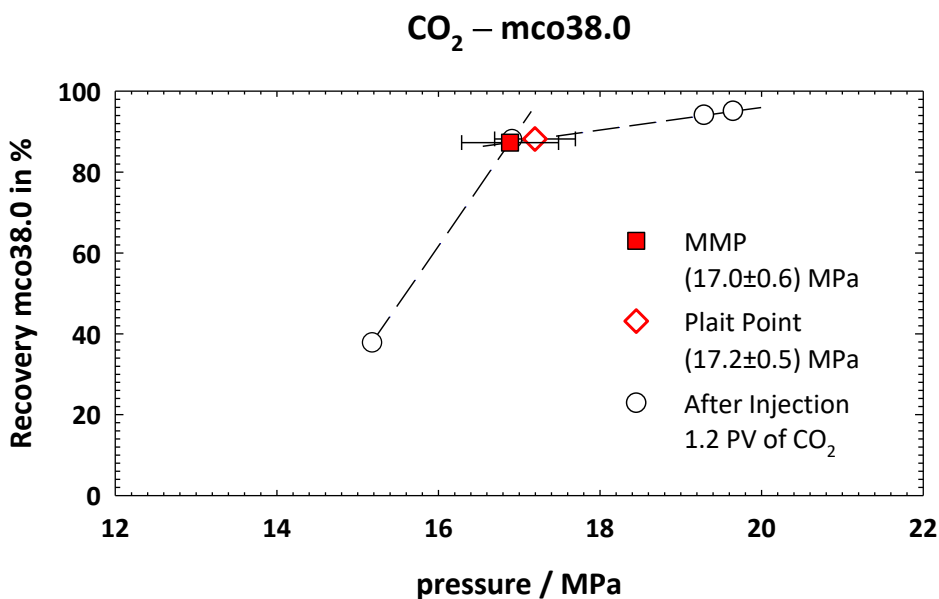


Figure 4.33: Recovered PV of mco38.0 after injection of 1.2 PV of CO₂ as a function of the pressure for the CO₂ – mco38.0 system at (65±2) °C. Assuming the data point at (17.0±0.3) MPa is slightly below the MMP, the two points below and above the MMP can be connected by straight lines intersecting at the MMP = (17.0±0.6) MPa and a recovery of (0.88±0.01) PV of mco38.0. However, if the data point at (17.0±0.3) MPa is already located above the MMP, the MMP can only be estimated in the range between 15.3 MPa and 17.0 MPa. The plait point of the system determined from phase behavior studies is located at $p_c = (17.2±0.5)$ MPa.

The effect of one of the best performing additives (C₆P₃) on the miscibility of the CO₂ – mco38.0 system was studied using the slim tube apparatus to investigate whether C₆P₃ not only decreases the pressure of the plait point (p_c), but also the MMP, which resembles more the dynamic conditions in real crude oil fields. Thus, the slim tube experiments were performed on the same systems at 65 °C by co-injecting C₆P₃ to CO₂ with a mass fraction of C₆P₃ in CO₂ of $\gamma_{CO_2} = 0.020$ at four different pressures, i.e. at (13.6±0.8) MPa, (14.3±0.4) MPa, (16.5±5) MPa and (17.9±0.4) MPa. To ensure that the measured effects are only induced by the additive and not by other factors, the same run times were used for the experiments with and without additive. Consequently, the flow rate of the pure CO₂ is lower in the experiments with C₆P₃, but with the additional flow rate of the co-injected additive, the same total flow rates and times were achieved for the runs of the experiments with C₆P₃.

In Figure 4.34, the results of the pseudoternary CO₂ – mco38.0 – C₆P₃ system for different average pressures are shown. Again, the upstream and downstream average pressures as well as the recovered pore volume of mco38.0 were plotted as a function of the injected pore volume of the mixture of CO₂ with C₆P₃. For the sake of simplicity, in the PV of injected CO₂ and the PV of recovered mco38.0, the fraction of C₆P₃ is subtracted (based on the

known volumes from the injected flow rates and the material balance) and thus no longer explicitly mentioned. As already seen for the pseudobinary system, similar trends are obtained for the three slim tube measurements at higher average pressures of (14.3 ± 0.4) MPa, (16.5 ± 0.5) MPa and (17.9 ± 0.4) MPa, i.e. the recovered PV of mco38.0 increases almost linearly with the injected PV of CO₂ with C₆P₃, while both upstream and downstream pressures remain constant. In contrast, in the slim tube run at (13.6 ± 0.8) MPa, pressure fluctuations occurred, which led to a non-linear increase of the recovered PV of mco38.0. The pressure fluctuations might be related to a leakage that was detected after the slim tube filling procedure. Due to this leakage, the O-ring in the pressure relief valve of the backpressure regulator had to be exchanged directly before the injection of CO₂. Usually, the O-ring of the pressure relief valve was exchanged already at ambient pressure before the filling of the slim tube with the mco38.0. Due to the unplanned O-ring replacement for this experiment at (13.6 ± 0.8) MPa, the pressure relief valve had to be readjusted several times during the injection process to regulate the increasing pressure of the system stepwise to reach the target average pressure. These adjustments can be seen as peaks.

The recovered PV of mco38.0 after injection of 1.2 PV of CO₂ (black vertical line) increases with increasing pressure from 0.44 ± 0.01 at (13.6 ± 0.8) MPa over 0.77 ± 0.01 at (14.3 ± 0.4) MPa and 0.83 ± 0.01 at (16.5 ± 0.5) MPa to 0.86 ± 0.01 at (17.9 ± 0.4) MPa. Thus, compared to the pseudobinary system, considerable oil recoveries are already achieved at lower pressures.

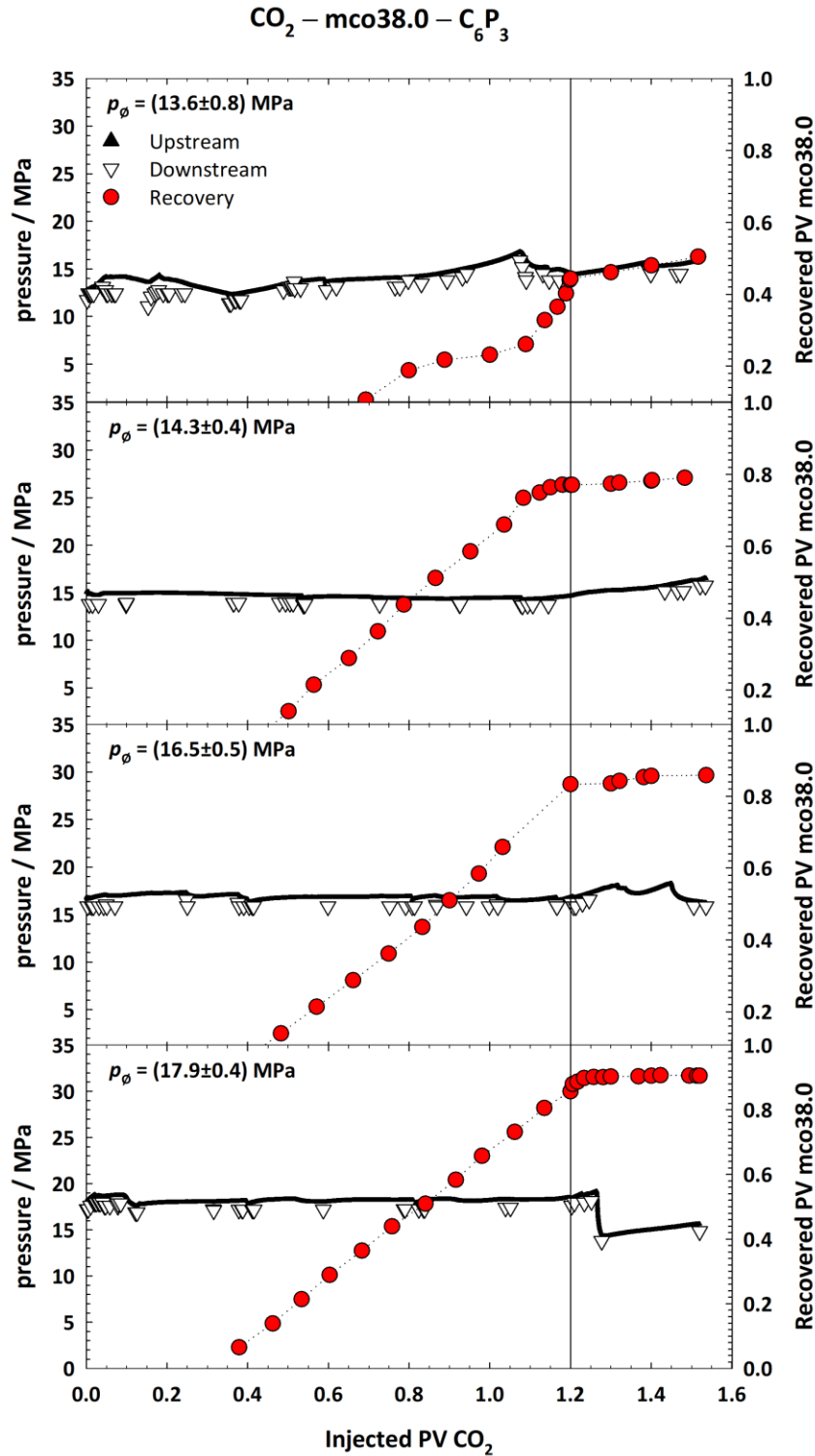


Figure 4.34: Results of slim tube measurements performed on the $\text{CO}_2 - \text{mco38.0} - \text{C}_6\text{P}_3$ system at $(65 \pm 2)^\circ\text{C}$, $y_{\text{CO}_2} = 0.020$, and four different pressures of (13.6 ± 0.8) MPa, (14.3 ± 0.4) MPa, (16.5 ± 0.5) MPa and (17.9 ± 0.4) MPa. Upstream pressure (filled triangles) and downstream pressure (unfilled triangles) as well as recovered PV of mco38.0 (red filled circles) are plotted versus the injected PV of CO_2 . The fraction of C_6P_3 is subtracted for the recovered PV of mco38.0 and the injected PV of CO_2 . The recovered PV of mco38.0 after the injection of 1.2 PV of CO_2 (black vertical line) increases with increasing pressure from 0.44 ± 0.01 , over 0.77 ± 0.01 and 0.83 ± 0.01 to 0.86 ± 0.01 .

To determine the MMP of the $\text{CO}_2 - \text{mco38.0} - \text{C}_6\text{P}_3$ system at $(65 \pm 2)^\circ\text{C}$, the recovered mco38.0 after the injection of 1.2 PV of CO_2 is plotted as a function of the pressure in Figure 4.35. Assuming that the data point at (14.3 ± 0.4) MPa is located slightly below the MMP, the two points below and above the MMP were connected by straight lines. Their intersection provides the MMP at (14.4 ± 0.8) MPa with a recovery of 0.80 ± 0.01 PV of mco38.0. As already seen for the pseudobinary system, the MMP of the pseudoternary $\text{CO}_2 - \text{mco38.0} - \text{C}_6\text{P}_3$ system is thus located close to, but below the plait point pressure of $p_c = (15.2 \pm 0.5)$ MPa obtained from the static phase behavior studies.

At pressures above the MMP and after an injection of 1.2 PV CO_2 , no further increase of the recovered mco38.0 is observed for the pseudobinary and pseudoternary systems (Figure 4.32, Figure 4.34). This indicates a properly designed slim tube apparatus meeting the conditions suggested by F. I. Stalkup Jr. (for details see chapter 3.2.2) [Stalkup, 1983].

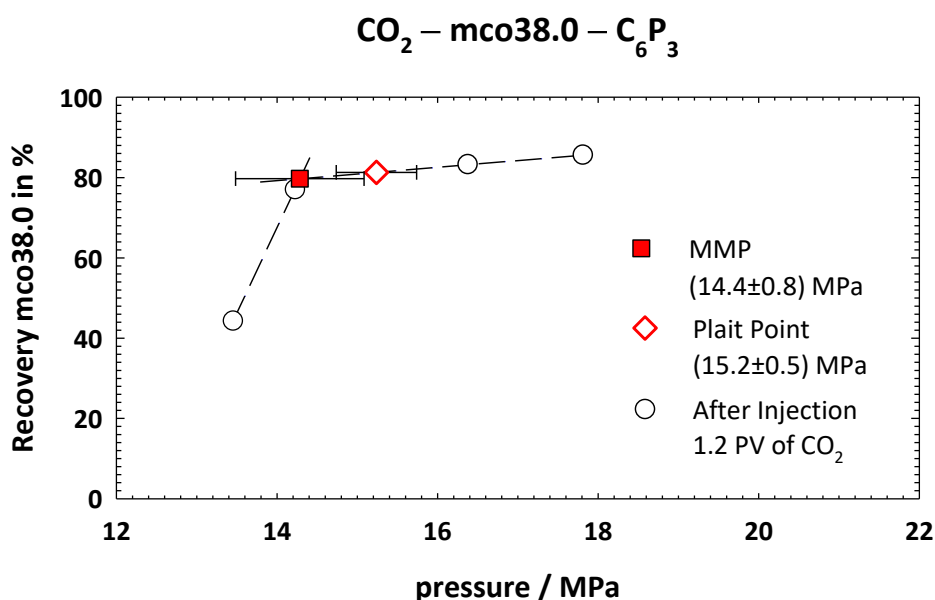


Figure 4.35: Recovered PV of mco38.0 after injection of 1.2 PV of CO_2 as a function of the pressure for the $\text{CO}_2 - \text{mco38.0} - \text{C}_6\text{P}_3$ system at $(65 \pm 2)^\circ\text{C}$ and $\gamma_{\text{CO}_2} = 0.020$. Assuming that the data point at (14.3 ± 0.4) MPa is slightly below the MMP, the two points below and above the MMP can be connected by straight lines intersecting at the MMP at (14.4 ± 0.8) MPa and a recovery of (0.80 ± 0.01) PV of mco38.0. The plait point of the system determined from phase behavior studies is located at (15.2 ± 0.5) MPa.

In Figure 4.36, the results of the slim tube measurements performed on the $\text{CO}_2 - \text{mco38.0}$ system with and without the additive C_6P_3 are compared. It impressively illustrates the effect of co-injecting 2 wt% of C_6P_3 in CO_2 on the dynamic miscibility of the mco38.0 with the injected fluid CO_2 . Interestingly, as indicated by the gray highlighted area, C_6P_3 not only lowers the MMP from (17.0 ± 0.6) MPa to (14.4 ± 0.8) MPa, but also considerably increases the oil recovery rate at pressures below the MMP of the pseudobinary

$\text{CO}_2 - \text{mco38.0}$ system. This results for example at 15.3 MPa in the increase of the recovered PV of mco38.0 from 38% to 82% by co-injecting 2 wt% of C_6P_3 . Importantly, for the studied systems, the values of the MMP elaborately determined via slim tubes measurements correlate well with the values of the plait point pressures $p_c(\text{CO}_2 - \text{mco38.0}) = (17.2 \pm 0.5)$ MPa and $p_c(\text{CO}_2 - \text{mco38.0} - \text{C}_6\text{P}_3) = (15.2 \pm 0.5)$ MPa, which were determined via much faster static phase behavior studies (for comparison see also Table 4.5).

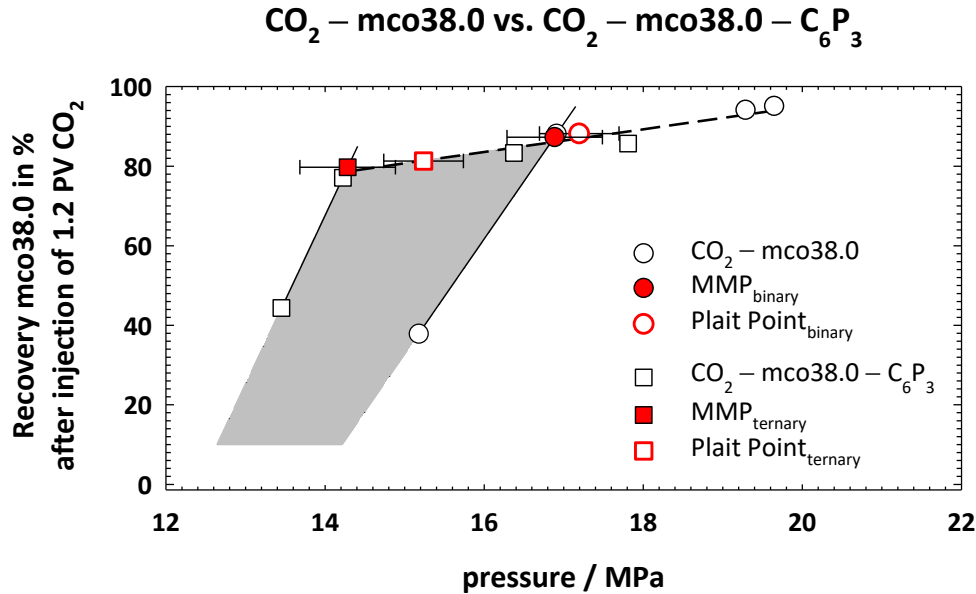


Figure 4.36: Comparison of the results of the slim tube measurements performed on the systems $\text{CO}_2 - \text{mco38.0}$ and $\text{CO}_2 - \text{mco38.0} - \text{C}_6\text{P}_3$ (2 wt% of C_6P_3 in CO_2 by co-injection) at (65 ± 2) °C. The gray highlighted area strikingly illustrates that C_6P_3 not only lowers the MMP from (17.0 ± 0.6) MPa to (14.4 ± 0.8) MPa, but also considerably increases the oil recovery rate at pressures below the MMP of the pseudobinary $\text{CO}_2 - \text{mco38.0}$ system. Importantly, the values of the MMP correlate well with the values of the plait point pressures $p_c = (17.2 \pm 0.5)$ MPa and $p_c = (15.2 \pm 0.5)$ MPa, which were determined via much simpler static phase behavior studies.

Table 4.5: Comparison of the plait point pressures determined via static phase behavior studies from the HP-cell measurements and the MMP determined via dynamic phase behavior studies from slim tube measurements. Data are compared for the systems $\text{CO}_2 - \text{mco38.0}$ and $\text{CO}_2 - \text{mco38.0} - \text{C}_6\text{P}_3$ ($\gamma_{\text{CO}_2} = 0.020 \pm 0.003$) at (65 ± 2) °C.

System at (65 ± 2) °C	$\text{CO}_2 - \text{mco38.0}$	$\text{CO}_2 - \text{mco38.0} - \text{C}_6\text{P}_3$
	p / MPa	
Plait point (statically determined via HP-cell)	17.2 ± 0.5	15.2 ± 0.5
MMP (dynamically determined via ST)	17.0 ± 0.6	14.4 ± 0.8

To the best of my knowledge, there are only published data of slim tube measurements of live and dead crude oils, but there are no measurements of a model crude oil analyzing the MMP-reducing effects of alkoxyated additives in literature. One comparison of static measurements by vanishing interfacial tension (VIT) test with dynamic slim tube

measurements for a CO₂ – Dulang crude oil system is described in literature. Voon and Awang compared the results and found a decrease of VIT and MMP by addition of different alcohols [Voon, Awang, 2015]. They concluded that the static VIT test and the dynamic slim tube measurements generate data that complement each other. However, no clear conclusion was made about the comparability of VIT and slim tube data, since no systematic analysis had been performed. Except for this publication, no further comparisons of systems with and without additives are found in literature. In line with the data of Voon and Awang, a decrease in both, the plait point and the MMP determined by static and dynamic phase behavior studies, were found by addition of the additive C₆P₃. Since in this thesis the same system was analyzed by both methods, a conclusion about the comparability of the data can be made. As mentioned above, a good correlation between the MMP from slim tube measurement and the plait point measured in the HP-cell was found.

The direct comparison of the MMP with the plait point values shows that the MMP lies slightly below the p_c (Figure 4.36, Table 4.5). This could be due to a small amount of residual air that remains in the high pressure visual cell (HP-cell) after the filling procedure. The nitrogen, which is the major component of air, is more stable compared to CO₂ and thus reduces interactions of the other components leading to higher pressures for a phase transition, as discussed by Jia, Tsau and Barati [Jia, Tsau, Barati, 2019]. The higher stability of nitrogen compare to CO₂ is based on its weaker Van der Waals attractions to the crude oil, which results in a low solubility in crude oil. Schwan removed the remaining air in the HP-cell by flushing the sample compartment in the HP-cell three times with CO₂ at low pressure between the filling steps with *n*-alkane and sample [Schwan, 2005]. In this thesis, the procedure established by Schwan was used to analyze a potential influence of residual amounts of air in the HP-cell by comparing these data with data obtained using the standard filling procedure (without an extra air replacement step). However, no differences were found in the results (results not shown). The amount of air seems to be too small to influence the interactions at the higher pressures analyzed. Therefore, the effect of air was considered negligible for all measurements in the HP-cell and is thus not considered a reason for the higher p_c values compared to the MMP. In comparison, an influence of air can be excluded for the slim tube measurements, since the slim tube was free of air due to the filling procedure. Therefore, the quadrupole-quadrupole interaction between CO₂ and oil are not negatively influenced by nitrogen [Jia, Tsau, Barati, 2019]. Other parameters considered in the slim tube

measurement, like porosity and permeability as well as the flow rate of the injected fluids, will most likely influence the MMP [Jin, et al., 2017a, Jin, et al., 2017b]. Despite all these additional factors reflected in the slim tube measurements that are not considered in the HP-cell investigations, the values of the MMP and plait point show an overall good correlation.

Furthermore, it should be mentioned that slim tube measurements are very cost intensive (the whole set-up costs approx. 75,000 \$). In comparison, the HP-cell together with the CO₂ filling apparatus cost a fraction of that, while additionally the costs for ongoing experiments, including the cleaning, are also significantly lower.

Thus, instead of performing sample- and time-consuming slim tube measurements, the plait point pressure obtained by static phase behavior measurements might be used as an estimation for the upper limit of the MMP from dynamic behavior.

5 Summary and Outlook

The main goal of this thesis was the identification of additives enabling a considerable reduction of the minimum miscibility pressure (MMP) of CO₂/(model) crude oil mixtures. With the help of these additives, already existing CO₂-EOR fields can be used more economically and reservoirs can become accessible for CO₂-EOR, which are naturally not. As a part of the investigations i) model crude oils reflecting the properties of the real crude oil were developed, ii) structure-activity relationships of the additives were found, and iii) the comparability of static and dynamic phase behavior studies was verified.

At first, using a high pressure visual cell (HP-cell), an experimental procedure was optimized to allow fast and reliable miscibility studies of the systems of interest in a temperature and pressure range relevant to reservoirs, i.e. between 5 °C and 80 °C as well as 0.5 MPa and 45 MPa. Based on this procedure, the phase behavior of (pseudo-)binary systems of the type CO₂ – additive were then investigated to determine the additives that exhibit a good miscibility with CO₂. CO₂ was found to be quite compatible with alkoxyated medium-chain linear and branched alcohols, while a very poor miscibility with alkylphenol ethoxylates and alcohol ether carboxylates was observed (Figure 4.9).

Afterwards, model crude oils were designed to facilitate the study of the CO₂ – crude oil phase behavior. Three different model crude oils mco47.0, mco38.8, and mco38.0 were designed to resemble the phase behavior of the real crude oil aco38.0. Simple alkanes of medium chain length were not able to reflect the complex phase behavior of aco38.0. However, using mixtures of short- and long-chain alkanes, the Sasolwax 5805, aromatics, and naphthenes as model crude oils (Figure 4.4, Table 4.4), asymmetric lower miscibility gaps were observed for the pseudobinary CO₂ – model crude oil systems, which have a shape similar to the CO₂ – aco38.0 system (Figure 4.6, Figure 4.8). The miscibility gaps run through a pronounced maximum, referred to as physical minimum miscibility pressure (MMP_p), which for all systems is located at about 7.5 wt% of (model) crude oil (w_{oil}) and a pressure of around 40 MPa.

On the basis of the systematic characterization of the three (pseudo-)binary side systems, the phase behavior of the pseudoternary system was exemplarily studied for the system CO₂ – mco47.0 – C₄E₁P₃. Therefore, $p(w_{oil})$ -sections were performed through the isothermal phase prism (Figure 4.11) at different mass fractions γ_{CO_2} of C₄E₁P₃ in the CO₂/C₄E₁P₃ mixture allowing for the construction of isothermal and isobaric phase diagrams

in form of Gibbs triangles (Figure 4.12). The evolution of the Gibbs phase triangles with increasing pressure illustrates the miscibility-enhancing effect of the additive $C_4E_1P_3$, which leads to a considerable shrinkage of the central miscibility gap of the pseudoternary system.

Approaching the main objective of this thesis, the influence of 17 alcohols and 20 alkoxyated additives on the miscibility behavior of CO_2 and (model) crude oil was investigated at an application-oriented small γ_{CO_2} value of 2 wt%. The pressure profit ($\Delta p = p(w_{Oil}, \gamma_{CO_2}=0) - p(w_{Oil}, \gamma_{CO_2})$) was introduced as a simple measure of the miscibility-enhancing effect of the respective additive. Interestingly, all investigated additives (apart from ISOFOL 28) showed a positive pressure profit ($\Delta p > 0$), i.e. they increased the miscibility of the (model) crude oils with CO_2 .

Some structure-activity relationships were identified for the studied additives. For linear alcohols, the pressure profits were found to run through a maximum between 1-hexanol and 1-dodecanol (Figure 4.15). Thereby, the maximum of the efficiency-enhancing effect seems to shift slightly towards longer-chain alcohols when the API gravity of the oil is decreased ($C_6 - C_{10}$ for mco47.0, $C_6 - C_{12}$ for mco38.8, C_{12} for aco38.0 (Figure 4.17 – Figure 4.19)). The maximum can be explained phenomenologically by the poor compatibility between short-chain 1-alcohols and long-chain alkanes on the one hand and between long-chain alcohols and CO_2 on the other. Comparing linear alcohols with branched alcohols, mostly smaller pressure profits were found for branched alcohols (Figure 4.16).

Surprisingly, the alkoxyated alcohols, which were systematically examined for the first time in this work with respect to their miscibility-enhancing effect, were able to achieve larger Δp values compared to the respective starting alcohols (Figure 4.17 – Figure 4.19). This positive feature could be explained by a certain compatibility of ethoxy and propoxy groups with CO_2 . However, no systematic trend of the pressure profit with respect to the ethoxylation and propoxylation degree was found, most probably due to the broad distribution of the degree of alkoxylation in the technical-grade alkoxyated alcohols synthesized by Sasol Performance Chemicals GmbH. Moreover, the pressure profits considerably increased with decreasing API gravity of the (model) crude oil and decreasing temperature, i.e. when the miscibility gap is larger, which might indicate that the magnitude of the pressure profit scales with the MMP_p .

Triggered by the surprisingly good performance of alkoxyated alcohols as novel efficient miscibility enhancers in CO_2 /(model) crude oil mixtures found in this thesis, a patent

application with the title “Injection Fluids comprising alkoxyated alcohols and the use of such fluids in oil recovery processes” (EP19158014) was filed by Sasol Performance Chemicals GmbH. Therefore, the effect of the alkoxyated alcohols was compared to blends of long-chain alkoxyated additives and short-chain 1-alcohols as prior art. These measurements showed very clearly that the use of the medium-chain alkoxyated alcohols used in this thesis represents a considerable improvement over the already patented blends.

Besides miscibility, the swelling of crude oils by CO₂ is an important property for CO₂-EOR. The additives C₆P₃ (threefold propoxyated 1-hexanol) and ITDA E₂ (twofold ethoxyated iso-tridecanol) were found to increase the maximum swelling factor (SF) from $SF_{\max} = 1.32$ to $SF_{\max, \text{additives}} = 1.39$ (Figure 4.25). Furthermore, at medium and high pressure, a much steeper slope of the $SF(p)$ -curves was found confirming the increased extraction efficiency. Due to the improved swelling behavior, the viscosity of the crude oil is further reduced facilitating the recovery of the crude oil from the tight pores in the reservoir rock, in which the crude oil is trapped. In this study, it was however not possible to determine the maximum of the swelling factor, since the lower pressure limit of the HP-cell was too high. Increasing the volume of the sample compartment of the HP-cell will allow to measure the swelling behavior at lower pressures (closer to the critical pressure of CO₂) and thus to correctly identify the maximum swelling factor. Moreover, measurements of the swelling behavior at additional temperatures would be interesting, because according to Tsau, Bui and Willhite, the swelling factor decreases with increasing temperature [Tsau, Bui, Willhite, 2010]. This is in line with the larger miscibility gap at higher temperature for high w_{oil} found in this thesis. Thus, understanding the temperature-dependent swelling behavior is important to find optimal recovery conditions.

Furthermore, the influence of water on the CO₂ – crude oil – additive systems was investigated (Figure 4.26 – Figure 4.30). The phase behavior investigations of these systems were extremely difficult. In order to reliably analyze water-comprising systems, improvements of the experimental procedure are required. These include larger sample volumes, longer separation times, and avoiding leakage.

Finally, to approach the conditions of real crude oil field operations, dynamic investigations that consider factors, like diffusion, permeability, and porosity had to be performed. Especially slim tube experiments [Yellig, Metcalfe, 1980] allow for the analysis of continuous phase separation and remixing processes occurring inside the reservoirs and are

therefore considered a very accurate way of measuring the minimum miscibility pressure (MMP). Thus, a slim tube apparatus for dynamic phase behavior studies was set-up and validated at the Rice University (Houston, Texas, USA) in close collaboration with the group of Prof. Dr. George J. Hirasaki (Figure 3.4). These elaborate measurements confirmed the promising miscibility-enhancing effect of one of the most powerful additives C_6P_3 . It was found that 2 wt% of C_6P_3 not only strikingly lower the MMP from (17.0 ± 0.6) MPa to (14.4 ± 0.6) MPa, but also considerably increase the oil recovery rate at pressures below the MMP (Figure 4.36). Importantly, the values of the MMP, elaborately determined via slim tubes measurements, correlate well with the values of the plait point pressures, which were determined via the much faster and more cost-effective static phase behavior studies using the HP-cell. Thus, instead of performing elaborate slim tube measurements, the plait point pressure can be used as an estimation for the upper limit of the MMP.

Since, according to literature, the rock formation or its salinity has an influence on the miscibility of water – crude oil – surfactant/alcohol systems [Hirasaki, Miller, Puerto, 2008], it would be interesting to investigate that influence in water/brine – CO_2 – crude oil – additive systems. To do so, static phase behavior studies with different salinities can be carried out by adding a core sample in the sample compartment of the HP-cell.

In conclusion, besides identifying promising additives to improve CO_2 -EOR, this thesis demonstrated that static phase behavior studies using the HP-cell allow for a reliable screening of additives in complex crude oil systems in short time and with low costs. Additionally, technically relevant properties like the physical minimum miscibility pressure, the minimum miscibility pressure (or plait point), and the swelling behavior can be determined easily under reservoir conditions of interests. Since this study furthermore showed that the identification of the most effective additive for a specific oil field operation requires extensive screenings of diverse additives, this method will help to improve the efficiency of future CO_2 -EOR projects.

6 Bibliography

- Abdallah, W.; Buckley, J. S.; Carnegie, A.; Edwards, J.; Herold, B.; Fordham, E.; Graue, A.; Habashy, T.; Seleznev, N.; Signer, C.; Montaron, B.; Ziauddin, M. Fundamentals of wettability. *Oilfield Review*, **2007**, *19*, 44–61.
- Adel, I. A.; Tovar, F. D.; Schechter, D. S. Fast-Slim Tube: A Reliable and Rapid Technique for the Laboratory Determination of MMP in CO₂ - Light Crude Oil Systems. In Society of Petroleum Engineers, Tulsa, Oklahoma, USA, **2016**.
- Al Ghafri, S. Z.; Maitland, G. C.; Trusler, J. P. M. Experimental and modeling study of the phase behavior of synthetic crude oil + CO₂. *Fluid Phase Equilibria*, **2014**, *365*, 20–40.
- Al-Mjeni, R.; Arora, S.; Cherukupalli, P.; van Wunnik, J.; Edwards, J.; Felber, B. J.; Gurpinar, O.; Hirasaki, G. J.; Miller, C. A.; Jackson, C.; Kristensen, M. R.; Lim, F.; Ramamoorthy, R.; Andersen, E. Has the Time Come for EOR? *Oilfield Review*, **2011**, *22* (4), 16–35.
- Austad, T.; Hodne, H.; Strand, S.; Veggeland, K. Chemical flooding of oil reservoirs 5. The multiphase behavior of oil/brine/surfactant systems in relation to changes in pressure, temperature, and oil composition. *Colloids and Surfaces A: Physicochemical and Engineering Aspects*, **1996**, *108* (2), 253–262.
- Beecher, C. E.; Parkhurst, I. P. Effect of Dissolved Gas upon the Viscosity and Surface Tension of Crude Oil. *SPE-1250-G*, **1926**, *G-26* (01), 51–69.
- Beeson, D. M.; Orloff, G. D. Laboratory Investigation of the Water-Driven Carbon Dioxide Process for Oil Recovery. *SPE-7477-PA*, **1959**, *11* (04), 63–66.
- Bernard, G. G.; Holm, L. W.; Lake, C. Methods for Recovering Oil from Subterranean Formations. U.S., 3,342,256, **1964**.
- Byun, H.-S.; Kwak, C. High pressure phase behavior for carbon dioxide-1-butanol and carbon dioxide-1-octanol systems. *Korean J. Chem. Eng.*, **2002**, *19* (6), 1007–1013.
- Chan, K. S.; Shah, D. O. The Physico-Chemical Conditions Necessary to Produce Ultralow Interfacial Tension at the Oil/Brine Interface. In *Surface Phenomena in Enhanced Oil Recovery*; Shah, D. O., Ed.; Springer US, Boston, MA, **1981**, pp 53–72.
- Chandler, C. F. The Baumé Hydrometers. *National Academy of Sciences*, **1881**, *Vol. 3*.
- Charoensombut-amon, T.; Martin, R. J.; Kobayashi, R. Application of a generalized multiproperty apparatus to measure phase equilibrium and vapor phase densities of supercritical carbon dioxide in n-hexadecane systems up to 26 MPa. *Fluid Phase Equilibria*, **1986**, *31* (1), 89–104.

- Chen, H.-I.; Chang, H.-Y.; Chen, P.-H. High-Pressure Phase Equilibria of Carbon Dioxide + 1-Butanol, and Carbon Dioxide + Water + 1-Butanol Systems. *J. Chem. Eng. Data*, **2002**, *47* (4), 776–780.
- Chrastil, J. Solubility of solids and liquids in supercritical gases. *J. Phys. Chem.*, **1982**, *86* (15), 3016–3021.
- Christian, L. D.; Shirer, J. A.; Kimbel, E. L.; Blackwell, R. J. Planning a Tertiary Oil-Recovery Project for Jay/LEC Fields Unit. *SPE-7477-PA*, **1981**, *33* (08), 1535–1544.
- Christiansen, R. L.; Haines, H. K. Rapid Measurement of Minimum Miscibility Pressure With the Rising-Bubble Apparatus. *SPE-15491-PA*, **1987**, *2* (04), 523–527.
- Christov, M.; Dohrn, R. High-pressure fluid phase equilibria: Experimental methods and systems investigated (1994–1999). *Fluid Phase Equilibria*, **2002**, *202* (1), 153–218.
- Crawford, P. B.; Reynolds, B.; Rushing, M. D.; Thomassom, B. Nitrogen May Be Used for Miscible Displacement in Oil Reservoirs. *SPE-7477-PA*, **1978**, *30* (12), 1715–1716.
- DDBSP; Dortmund Data Bank, **2018**, www.ddbst.com.
- Diamond, L. W.; Akinfiev, N. N. Solubility of CO₂ in water from -1.5 to 100 °C and from 0.1 to 100 MPa: evaluation of literature data and thermodynamic modelling. *Fluid Phase Equilibria*, **2003**, *208* (1-2), 265–290.
- Djabbarah, N. F. Miscible oil recovery process using carbon dioxide and alcohol. U.S., 4899817, **1990**.
- Doe, P. H.; Wade, W. H.; Schechter, R. S. Alkyl benzene sulfonates for producing low interfacial tensions between hydrocarbons and water. *Journal of Colloid and Interface Science*, **1977**, *59* (3), 525–531.
- Dohrn, R.; Brunner, G. High-pressure fluid-phase equilibria: Experimental methods and systems investigated (1988–1993). *Fluid Phase Equilibria*, **1995**, *106* (1), 213–282.
- Dohrn, R.; Peper, S.; Fonseca, J. M.S. High-pressure fluid-phase equilibria: Experimental methods and systems investigated (2000–2004). *Fluid Phase Equilibria*, **2010**, *288* (1), 1–54.
- Ekundayo, J. M.; Ghedan, S. G. Minimum Miscibility Pressure Measurement with Slim Tube Apparatus - How Unique is the Value? In Society of Petroleum Engineers, Abu Dhabi, UAE, **2013**.

- Elsharkawy, A. M.; Poettmann, F. H.; Christiansen, R. L. Measuring Minimum Miscibility Pressure: Slim-Tube or Rising-Bubble Method? In Society of Petroleum Engineers, Tulsa, Oklahoma, **1992**.
- Elsharkawy, A. M.; Poettmann, F. H.; Christiansen, R. L. Measuring CO₂ Minimum Miscibility Pressures: Slim-Tube or Rising-Bubble Method? *Energy Fuels*, **1996**, *10* (2), 443–449.
- Etter, D. O.; Kay, W. B. Critical Properties of Mixtures of Normal Paraffin Hydrocarbons. *J. Chem. Eng. Data*, **1961**, *6* (3), 409–414.
- Fan, W.; Li, B.; Li, S.; Li, Z.; Lu, T.; Luo, H.; Nan, G.; Wang, F.; Zhang, C. Supercritical carbon dioxide microemulsion capable of reducing minimum miscible pressure of carbon dioxide and crude oil. CN, 104610953A, **2015**.
- Fonseca, J. M.S.; Dohrn, R.; Peper, S. High-pressure fluid-phase equilibria: Experimental methods and systems investigated (2005–2008). *Fluid Phase Equilibria*, **2011**, *300* (1), 1–69.
- Fornari, R. E.; Alessi, P.; Kikic, I. High pressure fluid phase equilibria: experimental methods and systems investigated (1978–1987). *Fluid Phase Equilibria*, **1990**, *57* (1), 1–33.
- Foster, W. R. A Low-Tension Waterflooding Process. *SPE-7477-PA*, **1973**, *25* (02), 205–210.
- Francis, A. W. Ternary Systems of Liquid Carbon Dioxide. *J. Phys. Chem.*, **1954**, *58* (12), 1099–1114.
- Fulcher, G. S. Analysis of Recent Measurements of the Viscosity of Glasses. *J American Ceramic Society*, **1925**, *8* (6), 339–355.
- Fussell, D. D.; Yanosik, J. L. An Iterative Sequence for Phase-Equilibria Calculations Incorporating the Redlich-Kwong Equation of State. *SPE-6773-PA*, **1978**, *18* (03), 173–182.
- Fussell, L. T. A Technique for Calculating Multiphase Equilibria (includes associated papers 8734 and 8746). *SPE-6773-PA*, **1979**, *19* (04), 203–210.
- Gardner, J. W.; Orr, F. M.; Patel, P. D. The Effect of Phase Behavior on CO₂-Flood Displacement Efficiency. *SPE-7477-PA*, **1981**, *33* (11), 2067–2081.
- Gogarty, W. B. Oil Recovery with Surfactants: History and a Current Appraisal. In *Improved Oil Recovery by Surfactant and Polymer Flooding*; Shah, D. O., Schechter, R. S., Eds.; Academic Press, **1977**, pp 27–54.
- Gonzalez, D. L.; Vargas, F. M.; Hirasaki, G. J.; Chapman, W. G. Modeling Study of CO₂-Induced Asphaltene Precipitation†. *Energy Fuels*, **2008**, *22* (2), 757–762.

- Graue, D. J.; Zana, E. T. Study of a Possible CO₂ Flood in Rangely Field. *SPE-7477-PA*, **1981**, 33 (07), 1312–1318.
- Hand, D. B. Dimeric Distribution. *J. Phys. Chem.*, **1930**, 34 (9), 1961–2000.
- Hand, J. L.; Pinczewski, W. V. Interpretation of Swelling/Extraction Tests. *SPE-15491-PA*, **1990**, 5 (04), 595–600.
- Harmon, R. A.; Grigg, R. B. Vapor-Density Measurement for Estimating Minimum Miscibility Pressure (includes associated papers 19118 and 19500). *SPE-15491-PA*, **1988**, 3 (04), 1215–1220.
- Hawthorne, S. B.; Miller, D. J.; Jin, L.; Gorecki, C. D. Rapid and Simple Capillary-Rise/Vanishing Interfacial Tension Method To Determine Crude Oil Minimum Miscibility Pressure: Pure and Mixed CO₂, Methane, and Ethane. *Energy Fuels*, **2016**, 30 (8), 6365–6372.
- Helfferich, F. G. Theory of Multicomponent, Multiphase Displacement in Porous Media. *SPE-6773-PA*, **1981**, 21 (01), 51–62.
- Heller, J. P. Reservoir Application of Mobility Control Foams in CO₂ Floods. In Society of Petroleum Engineers, Tulsa, Oklahoma, **1984**.
- Henry, R. L.; Metcalfe, R. S. Multiple-Phase Generation During Carbon Dioxide Flooding. *SPE-6773-PA*, **1983**, 23 (04), 595–601.
- Hirasaki, G. J. Application of the Theory of Multicomponent, Multiphase Displacement to Three-Component, Two-Phase Surfactant Flooding. *SPE-6773-PA*, **1981**, 21 (02), 191–204.
- Hirasaki, G. J.; Miller, C. A.; Puerto, M. C. Recent Advances in Surfactant EOR. In Society of Petroleum Engineers, Denver, Colorado, USA, **2008**.
- Høgnesen, E. J.; Standnes, D. C.; Austad, T. Experimental and numerical investigation of high temperature imbibition into preferential oil-wet chalk. *Journal of Petroleum Science and Engineering*, **2006**, 53 (1), 100–112.
- Holm, L. W. Carbon Dioxide Solvent Flooding for Increased Oil Recovery. *SPE-1250-G*, **1959**, 216 (01), 225–231.
- Holm, L. W. Soluble Oils for Improved Oil Recovery. In *Improved Oil Recovery by Surfactant and Polymer Flooding*; Shah, D. O., Schechter, R. S., Eds.; Academic Press, **1977**, pp 453–485.
- Holm, L. W.; Josendal, V. A. Mechanisms of Oil Displacement By Carbon Dioxide. *SPE-7477-PA*, **1974**, 26 (12), 1427–1438.

- Holm, L. W.; Josendal, V. A. Effect of Oil Composition on Miscible-Type Displacement by Carbon Dioxide. *SPE-6773-PA*, **1982**, 22 (01), 87–98.
- Houghton, J. Climate change 2001. *The scientific basis ; contribution of Working Group I to the third assessment report of the Intergovernmental Panel on Climate Change*; Cambridge Univ. Press, Cambridge, **2001**.
- Huang, E. T.S.; Tracht, J. H. The Displacement of Residual Oil By Carbon Dioxide. In Society of Petroleum Engineers, Tulsa, Oklahoma, **1974**.
- Huie, N. C.; Luks, K. D.; Kohn, J. P. Phase-Equilibriums Behavior of Systems Carbon Dioxide-*n*-Eicosane and Carbon Dioxide-*n*-Decane-*n*-Eicosane. *J. Chem. Eng. Data*, **1973**, 18 (3), 311–313.
- Hutchinson Jr., C. A.; Braun, P. H. Phase Relations of Miscible Displacement in Oil Recovery. *AIChE J.*, **1961**, 7 (1), 64–72.
- Jia, B.; Tsau, J.-S.; Barati, R. A review of the current progress of CO₂ injection EOR and carbon storage in shale oil reservoirs. *Fuel*, **2019**, 236, 404–427.
- Jin, L.; Hawthorne, S.; Sorensen, J.; Pekot, L.; Kurz, B.; Smith, S.; Heebink, L.; Herdegen, V.; Bosshart, N.; Torres, J.; Dalkhaa, C.; Peterson, K.; Gorecki, C.; Steadman, E.; Harju, J. Advancing CO₂ enhanced oil recovery and storage in unconventional oil play—Experimental studies on Bakken shales. *Applied Energy*, **2017a**, 208, 171–183.
- Jin, L.; Sorensen, J. A.; Hawthorne, S. B.; Smith, S. A.; Pekot, L. J.; Bosshart, N. W.; Burton-Kelly, M. E.; Miller, D. J.; Grabanski, C. B.; Gorecki, C. D.; Steadman, E. N.; Harju, J. A. Improving Oil Recovery by Use of Carbon Dioxide in the Bakken Unconventional System: A Laboratory Investigation. *SPE-178948-PA*, **2017b**, 20 (03), 602–612.
- Johns, R. T.; Dindoruk, B.; Orr, F.M., Jr. Analytical Theory of Combined Condensing/Vaporizing Gas Drives. *SPE-20516-PA*, **1993**, 1 (02), 7–16.
- Johnson, J. P.; Pollin, J. S. Measurement and Correlation of CO₂ Miscibility Pressures. In Society of Petroleum Engineers, Tulsa, Oklahoma, **1981**.
- Kahlweit, M.; Strey, R. Phase Behavior of Ternary Systems of the Type H₂O-Oil-Nonionic Amphiphile (Microemulsions). *Angewandte Chemie International Edition in English*, **1985**, 24 (8), 654–668.
- Kahlweit, M.; Strey, R.; Haase, D.; Kunieda, H.; Schmeling, T.; Faulhaber, B.; Borkovec, M.; Eicke, H.-F.; Busse, G.; Eggers, F.; Funck, T.; Richmann, H.; Magid, L.; Söderman, O.; Stilbs,

- P.; Winkler, J.; Dittrich, A.; Jahn, W. How to study microemulsions. *Journal of Colloid and Interface Science*, **1987**, *118* (2), 436–453.
- Kessel, D. G. Chemical flooding — status report. *Journal of Petroleum Science and Engineering*, **1989**, *2* (2), 81–101.
- Kiran, E.; Debenedetti, P. G.; Peters, C. J. *Supercritical Fluids*; Springer Netherlands, Dordrecht, **2000**.
- Koch, H.A., Jr.; Hutchinson, C.A., Jr. Miscible Displacements of Reservoir Oil Using Flue Gas. *SPE-1250-G*, **1958**, *213* (01), 7–10.
- Kohn, J. P.; Kurata, F. Heterogeneous phase equilibria of the methane—hydrogen sulfide system. *AIChE J.*, **1958**, *4* (2), 211–217.
- Kordikowski, A.; Schneider, G. M. Fluid phase equilibria of binary and ternary mixtures of supercritical carbon dioxide with low-volatility organic substances up to 100 MPa and 393 K: cosolvency effects and miscibility windows. *Fluid Phase Equilibria*, **1993**, *90* (1), 149–162.
- Kukarni, A. A.; Zarah, B. Y.; Luks, K. D.; Kohn, J. P. Phase-equilibriums behavior of system carbon dioxide-*n*-decane at low temperatures. *J. Chem. Eng. Data*, **1974**, *19* (1), 92–94.
- Kuuskräa, V.; Wallace, M. CO₂-EOR set for growth as new CO₂ supplies emerge. *Oil Gas J*, **2014**, *112*.
- Lake, L. W. *Enhanced Oil Recovery*; Prentice Hall, Englewood Cliffs, NJ, **1989**.
- Lee, S.; Kam, S. I. Chapter 2 - Enhanced Oil Recovery by Using CO₂ Foams: Fundamentals and Field Applications. In *Enhanced Oil Recovery Field Case Studies*; Sheng, J. J., Ed.; Gulf Professional Publishing, Boston, **2013**, pp 23–61.
- Lemmon, E. W.; Huber, M. L.; McLinden, M. O. NIST Standard Reference Database 23: Reference Fluid Thermodynamic and Transport Properties-REFPROP, Version 9.1 | NIST. *Natl Std. Ref. Data Series (NIST NSRDS)*, **2013**.
- Lemmon, E. W.; McLinden, M. O.; Friend, D. G. Thermophysical Properties of Fluid Systems. In *NIST Chemistry WebBook, NIST Standard Reference Database 69*; P.J. Linstrom and W.G. Mallard, Ed.; National Institute of Standards and Technology, Gaithersburg MD, 20899, 2013. August 7, **2020**.
- Li, G.; Zhai, L.; Xu, G.; Shen, Q.; Mao, H.; Pei, M. Current Tertiary Oil Recovery in China. *Journal of Dispersion Science and Technology*, **2000**, *21* (4), 367–408.

- Liphard, K.G.; Schneider, G.M. Phase equilibria and critical phenomena in fluid mixtures of carbon dioxide + 2,6,10,15,19,23-hexamethyltetracosane up to 423 K and 100 MPa. *The Journal of Chemical Thermodynamics*, **1975**, 7 (9), 805–814.
- Luks, K. D.; Turek, E. A.; Baker, L. E. Calculation of Minimum Miscibility Pressure. *SPE-15491-PA*, **1987**, 2 (04), 501–506.
- Ma, K.; Lopez-Salinas, J. L.; Puerto, M. C.; Miller, C. A.; Biswal, S. L.; Hirasaki, G. J. Estimation of Parameters for the Simulation of Foam Flow through Porous Media. Part 1: The Dry-Out Effect. *Energy Fuels*, **2013**, 27 (5), 2363–2375.
- Manrique, E. J.; Thomas, C. P.; Ravikiran, R.; Izadi Kamouei, M.; Lantz, M.; Romero, J. L.; Alvarado, V. EOR: Current Status and Opportunities. In Society of Petroleum Engineers, Tulsa, Oklahoma, USA, **2010**.
- Márquez, N.; Antón, R. E.; Graciaa, A.; Lachaise, J.; Salager, J.-L. Partitioning of ethoxylated alkylphenol surfactants in microemulsion-oil-water systems. Part II: influence of hydrophobe branching. *Colloids and Surfaces A: Physicochemical and Engineering Aspects*, **1998**, 131 (1-3), 45–49.
- Melrose, J. C.; Brandner, C. F. Role of Capillary Forces In Detennining Microscopic Displacement Efficiency For Oil Recovery By Waterflooding. *PETSOC (Journal of Canadian Petroleum Technology)*, **1974**, 13 (04), 54–62.
- Metcalfe, R. S.; Fussell, D. D.; Shelton, J. L. A Multicell Equilibrium Separation Model for the Study of Multiple Contact Miscibility in Rich-Gas Drives. *SPE-6773-PA*, **1973**, 13 (03), 147–155.
- Metcalfe, R. S.; Yarborough, L. The Effect of Phase Equilibria on the CO₂ Displacement Mechanism. *SPE-6773-PA*, **1979**, 19 (04), 242–252.
- IPCC, 2005: IPCC Special Report on Carbon Dioxide Capture and Storage; Metz, B., Davidson, O., de Coninck, H. C., Loos, M., Meyer, L., Eds.; Cambridge Univ. Press, Cambridge, **2005**.
- Monroe, W. W.; Silva, M. K.; Larson, L. L.; Orr, Franklin M., Jr. Composition Paths in Four-Component Systems: Effect of Dissolved Methane on 1D CO₂ Flood Performance. *SPE-15491-PA*, **1990**, 5 (03), 423–432.
- Montel, F.; Bickert, J.; Lagisquet, A.; Galliéro, G. Initial state of petroleum reservoirs: A comprehensive approach. *Journal of Petroleum Science and Engineering*, **2007**, 58 (3), 391–402.

- Moore, T. F.; Slobod, R. L. Displacement of Oil by Water-Effect of Wettability, Rate, and Viscosity on Recovery. In Society of Petroleum Engineers, New Orleans, Louisiana, **1955**.
- Moradi, B.; Awang, M.; Bashir, A.; Sabil, K. M. Effects of alcohols on interfacial tension between carbon dioxide and crude oil at elevated pressures and temperature. *Journal of Petroleum Science and Engineering*, **2014**, *121*, 103–109.
- Morrow, N. R.; Songkran, B. Effect of Viscous and Buoyancy Forces on Nonwetting Phase Trapping in Porous Media. In *Surface Phenomena in Enhanced Oil Recovery*; Shah, D. O., Ed.; Springer US, Boston, MA, **1981**, pp 387–411.
- Mungan, N. Carbon Dioxide Flooding-fundamentals. *PETSOC-81-01-03*, **1981**, *20* (01), 7.
- National Standard Petroleum Oil Tables. *U.S. National Bureau of Standards*, **1936**, *Bureau of Standards Circular No. 59*.
- Orr, F. M.; Heller, J. P.; Taber, J. J. Carbon dioxide flooding for enhanced oil recovery: Promise and problems. *Journal of the American Oil Chemists' Society*, **1982**, *59* (10), 810A-817A.
- Orr, F.M., Jr.; Johns, R. T.; Dindoruk, B. Development of Miscibility in Four-Component CO₂ Floods. *SPE-15491-PA*, **1993**, *8* (02), 135–142.
- Orr, F.M., Jr.; Yu, A. D.; Lien, C. L. Phase Behavior of CO₂ and Crude Oil in Low-Temperature Reservoirs. *SPE-6773-PA*, **1981**, *21* (04), 480–492.
- Orr, Franklin M., Jr.; Silva, M. K.; Lien, C.-L. Equilibrium Phase Compositions of CO₂/Crude Oil Mixtures-Part 2: Comparison of Continuous Multiple-Contact and Slim-Tube Displacement Tests. *SPE-6773-PA*, **1983**, *23* (02), 281–291.
- Peach, J.; Eastoe, J. Supercritical carbon dioxide: a solvent like no other. *Beilstein Journal of Organic Chemistry*, **2014**, *10*, 1878–1895.
- Perry, G. E. Weeks Island "S" Sand Reservoir B Gravity Stable Miscible CO₂ Displacement, Iberia Parish, Louisiana. In Society of Petroleum Engineers, Tulsa, Oklahoma, **1982**.
- Pöhler, H.; Scheidgen, A. L.; Schneider, G. M. Fluid phase equilibria of binary and ternary mixtures of supercritical carbon dioxide with a 1-alkanol and an *n*-alkane up to 100 MPa and 393 K—cosolvency effect and miscibility windows (Part II). *Fluid Phase Equilibria*, **1996**, *115* (1), 165–177.
- Pye, D. J. Improved Secondary Recovery by Control of Water Mobility. *SPE-7477-PA*, **1964**, *16* (08), 911–916.
- Rathke, B. Blasenbildung in gasgesättigten Flüssigkeiten: Der Nachweis homogener Keimbildung. Dissertation; Universität zu Köln, Köln, **2002**.

- Rathmell, J. J.; Stalkup, F. I.; Hassinger, R. C. A Laboratory Investigation of Miscible Displacement by Carbon Dioxide. In Society of Petroleum Engineers, New Orleans, Louisiana, **1971**.
- Reamer, H. H.; Sage, B. H. Phase Equilibria in Hydrocarbon Systems. Volumetric and Phase Behavior of the *n*-Decane-CO₂ System. *J. Chem. Eng. Data*, **1963**, 8 (4), 508–513.
- Ren, W.; Scurto, A. M. High-pressure phase equilibria with compressed gases. *Review of Scientific Instruments*, **2007**, 78 (12).
- Rommerskirchen, R.; Bilgili, H.; Fischer, J.; Sottmann, T. Impact of Miscibility Enhancing Additives on the Flooding Scheme in CO₂ EOR Processes. In Society of Petroleum Engineers, Tulsa, Oklahoma, USA, **2018**.
- Rommerskirchen, R.; Bilgili, H.; Fischer, J.; Sottmann, T. Injection Fluids comprising alkoxyated alcohols and the use of such fluids in oil recovery processes. DE, EP19158014.1, **2019**.
- Rommerskirchen, R.; Nijssen, P.; Bilgili, H.; Sottmann, T. Additives for CO₂ EOR Applications. In Society of Petroleum Engineers, Dubai, UAE, **2016a**.
- Rommerskirchen, R.; Nijssen, P.; Bilgili, H.; Sottmann, T. Reducing the Miscibility Pressure in Gas Injection Oil Recovery Processes. In Society of Petroleum Engineers, Abu Dhabi, UAE, **2016b**.
- Rowe, Allen McGhee, Jr. Internally Consistent Correlations For Predicting Phase Compositions For Use In Reservoir Composition Simulators. In Society of Petroleum Engineers, Houston, Texas, **1978**.
- Rutherford, W. M. Miscibility Relationships in the Displacement of Oil By Light Hydrocarbons. *SPE-6773-PA*, **1962**, 2 (04), 340–346.
- Sage, B. H.; Lacey, W. N. Some properties of the lighter hydrocarbons, hydrogen sulfide, and carbon dioxide, monograph on API Research Project 37; American Petroleum Institute, New York, **1955**.
- Sandiford, B. B. Laboratory and Field Studies of Water Floods Using Polymer Solutions to Increase Oil Recoveries. *SPE-7477-PA*, **1964**, 16 (08), 917–922.
- Scheidgen, A. L.; Schneider, G. M. Fluid phase equilibria of (carbon dioxide + a 1-alkanol+ an alkane) up to 100 MPa and T=393 K: cosolvency effect, miscibility windows, and holes in the critical surface. *The Journal of Chemical Thermodynamics*, **2000**, 32 (9), 1183–1201.

- Schneider, G. Phasengleichgewichte in flüssigen Systemen bei hohen Drucken
Zusammenfassender Bericht. *Berichte der Bunsengesellschaft für physikalische Chemie*,
1966, 70 (5), 497–520.
- Schneider, G.; Alwani, Z.; Heim, W.; Horvath, E.; Franck, E. U. Phasengleichgewichte und
kritische Erscheinungen in binären Mischsystemen bis 1500 bar, CO₂ mit n-Octan, n-
Undecan, n-Tridecan und n-Hexadecan. *Chemie Ingenieur Technik*, **1967**, 39 (11), 649–656.
- Schwan, M. Überkritische Mikroemulsionen zur Herstellung nanozellulärer Schäume: Principle
of Supercritical Microemulsion Expansion; Universität zu Köln, Köln, **2005**.
- Sebastian, H. M.; Lawrence, D. D. Nitrogen Minimum Miscibility Pressures. In Society of
Petroleum Engineers, Tulsa, Oklahoma, **1992**.
- Surface Phenomena in Enhanced Oil Recovery; Shah, D. O., Ed.; Springer US, Boston, MA,
1981.
- Shariati, A.; Peters, C. J.; Moshfeghian, M. Bubble-Point Pressures of Some Selected Methane
+ Synthetic C₆₊ Mixtures. *J. Chem. Eng. Data*, **1998**, 43 (2), 280–282.
- Shelton, J. L.; Yarborough, L. Multiple Phase Behavior in Porous Media During CO₂ or Rich-Gas
Flooding. *SPE-7477-PA*, **1977**, 29 (09), 1171–1178.
- Simon, R.; Rosman, A.; Zana, E. Phase-Behavior Properties of CO₂ - Reservoir Oil Systems. *SPE-
6773-PA*, **1978**, 18 (01), 20–26.
- Slobod, R. L.; Koch, H.A., Jr. High-Pressure Gas Injection- Mechanism of recovery Increase. In
American Petroleum Institute, New York, New York, **1953**, p 15.
- Span, R.; Wagner, W. A New Equation of State for Carbon Dioxide Covering the Fluid Region
from the Triple-Point Temperature to 1100 K at Pressures up to 800 MPa. *Journal of
Physical and Chemical Reference Data*, **1996**, 25 (6), 1509–1596.
- Srivastava, R. K.; Huang, S. S. Asphaltene Deposition During CO₂ Flooding: A Laboratory
Assessment. In Society of Petroleum Engineers, **1997**, p 19.
- Stalkup, F. I. Carbon Dioxide Miscible Flooding: Past, Present, And Outlook for the Future. *SPE-
7477-PA*, **1978**, 30 (08), 1102–1112.
- Stalkup, F. I. Miscible displacement; Henry L. Doherty Memorial Fund of AIME, Society of
Petroleum Engineers of AIME, New York, **1983**.
- Stegemeier, G. L. Mechanisms of Entrapment and Mobilization of Oil in Porous Media. In
Improved Oil Recovery by Surfactant and Polymer Flooding; Shah, D. O., Schechter, R. S.,
Eds.; Academic Press, **1977**, pp 55–91.

- Taber, J. J. Dynamic and Static Forces Required To Remove a Discontinuous Oil Phase from Porous Media Containing Both Oil and Water. *SPE-6773-PA*, **1969**, 9 (01), 3–12.
- Takahashi, S.; Hayashi, Y.; Takahashi, S.; Yazawa, N.; Sarma, H. Characteristics and Impact of Asphaltene Precipitation During CO₂ Injection in Sandstone and Carbonate Cores: An Investigative Analysis Through Laboratory Tests and Compositional Simulation. In Society of Petroleum Engineers, Kuala Lumpur, Malaysia, **2003**.
- Tammann, G.; Hesse, W. Die Abhängigkeit der Viscosität von der Temperatur bei unterkühlten Flüssigkeiten. *Z. Anorg. Allg. Chem.*, **1926**, 156 (1), 245–257.
- Teklu, T. W.; Alharthy, N.; Kazemi, H.; Yin, X.; Graves, R. M. Vanishing Interfacial Tension Algorithm for MMP Determination in Unconventional Reservoirs. In Society of Petroleum Engineers, Denver, Colorado, **2014**.
- Teklu, T. W.; Ghedan, S. G.; Graves, R. M.; Yin, X. Minimum Miscibility Pressure Determination: Modified Multiple Mixing Cell Method. In Society of Petroleum Engineers, Muscat, Oman, **2012**.
- Tsau, J. S.; Ballard, M. Single Well Pilot Test of Near Miscible CO₂ Injection in a Kansas Arbuckle Reservoir. In Society of Petroleum Engineers, Tulsa, Oklahoma, USA, **2014**.
- Tsau, J.-S.; Bui, L. H.; Willhite, G. P. Swelling/Extraction Test of a Small Sample Size for Phase Behavior Study. In Society of Petroleum Engineers, **2010**.
- Uren, L. C.; Fahmy, E. H. Factors Influencing the Recovery of Petroleum from Unconsolidated Sands by Waterflooding. *SPE-1250-G*, **1927**, 77 (01), 318–335.
- Verdier, S.; Carrier, H.; Andersen, S. I.; Daridon, J.-L. Study of Pressure and Temperature Effects on Asphaltene Stability in Presence of CO₂. *Energy Fuels*, **2006**, 20 (4), 1584–1590.
- Vitu, S.; Jaubert, J.-N.; Pauly, J.; Daridon, J.-L.; Barth, D. Bubble and Dew Points of Carbon Dioxide + a Five-Component Synthetic Mixture: Experimental Data and Modeling with the PPR78 Model. *J. Chem. Eng. Data*, **2007**, 52 (5), 1851–1855.
- Vogel, H. The temperature dependence law of the viscosity of fluids. *Physikalische Zeitschrift*, **1921**, 22, 645–646.
- Voon, C. L.; Awang, M. Comparison of MMP Between Slim Tube Test and Vanishing Interfacial Tension Test. In *ICIPEG 2014*; Awang, M., Negash, B. M., Md Akhir, N. A., Lubis, L. A., Eds.; Springer Singapore, Singapore, **2015**, pp 137–144.
- Wade, W. H.; Morgan, J. C.; Schechter, R. S.; Jacobson, J. K.; Salager, J. L. Interfacial Tension and Phase Behavior of Surfactant Systems. *SPE-6773-PA*, **1978**, 18 (04), 242–252.

- Wagner, W.; Pruß, A. The IAPWS Formulation 1995 for the Thermodynamic Properties of Ordinary Water Substance for General and Scientific Use. *Journal of Physical and Chemical Reference Data*, **2002**, *31* (2), 387–535.
- Welker, J. R. Physical Properties of Carbonated Oils. *SPE-7477-PA*, **1963**, *15* (08), 873–876.
- Wellington, S. L.; Vinegar, H. J. CT Studies of Surfactant-induced CO₂ Mobility Control. In Society of Petroleum Engineers, Las Vegas, Nevada, **1985**.
- Whitson, C. H.; Michelsen, M. L. The negative flash. *Fluid Phase Equilibria*, **1989**, *53*, 51–71.
- WIKA Alexander Wiegand SE & Co. KG Operating Instructions: Hydraulic pressure balance CPB5800, de-de.wika.de/upload/OI_CPB5800_en_de_68712.pdf (accessed October 4, **2019**).
- Wilson, J. F. Miscible Displacement - Flow Behavior and Phase Relationships for a Partially Depleted Reservoir. *SPE-1250-G*, **1960**, *219* (01), 223–228.
- Yan, J. Carbon Capture and Storage (CCS). *Applied Energy*, **2015**, *148*, A1-A6.
- Yang, H.-W.; Luks, K. D.; Kohn, J. P. Phase-equilibria behavior of the system carbon dioxide-*n*-butylbenzene-2-methylnaphthalene. *J. Chem. Eng. Data*, **1976**, *21* (3), 330–335.
- Yellig, W. F.; Metcalfe, R. S. Determination and Prediction of CO₂ Minimum Miscibility Pressures (includes associated paper 8876). *SPE-7477-PA*, **1980**, *32* (01), 160–168.
- Zamudio, M.; Schwarz, C. E.; Knoetze, J. H. Experimental measurement and modelling with Aspen Plus® of the phase behaviour of supercritical CO₂ + (n-dodecane + 1-decanol + 3,7-dimethyl-1-octanol). *The Journal of Supercritical Fluids*, **2013**, *84*, 132–145.
- Zhang, K.; Perdomo, M. E. G.; Kong, B.; Sebakhy, K. O.; Wu, K.; Jing, G.; Han, J.; Lu, X.; Hong, A.; Chen, Z. CO₂ Near-Miscible Flooding for Tight Oil Exploitation. In Society of Petroleum Engineers, Brisbane, Australia, **2015**.
- Zick, A. A. A Combined Condensing/Vaporizing Mechanism in the Displacement of Oil by Enriched Gases. In Society of Petroleum Engineers, New Orleans, Louisiana, **1986**.

7 Appendix

7.1 Pressure Balance

Pressure balances are the most accurate instruments for calibration of electronic or mechanical pressure sensors. Therefore, they are used for calibration in industry, national institutes and research laboratories. The measurement of the pressure by integrated pressure generation and the pure mechanical measuring principle is ideal for maintenance of measuring instruments (e.g. high pressure visual cells). The core component of the model CPB5800 pressure balance from DH-Budenberg (a Division of WIKA Instruments Ltd.) is a very precisely manufactured piston-cylinder system, which is loaded with accurately graduated masses in order to generate individual pressure points up to 120 MPa, see Figure 7.1 (A) [WIKA Alexander Wiegand SE & Co. KG (accessed October 4, 2019)]. Additionally, a separator is connected to separate the sample compartment of the HP-cell from the oil-filled pressure balance, see Figure 7.1 (B). The separator can be used up to 70 MPa with a total measurement uncertainty of 0.006 % [WIKA Alexander Wiegand SE & Co. KG (accessed October 4, 2019)].

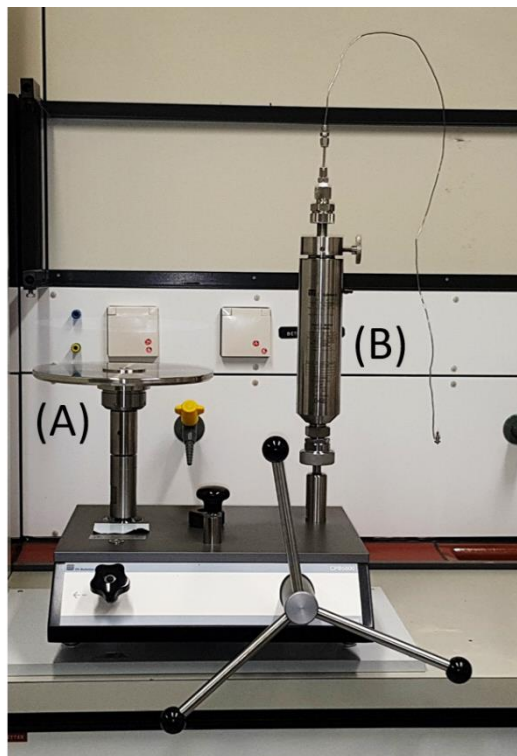


Figure 7.1: Pressure balance model CPB5800 from DH-Budenberg. (A) Piston is loaded with precisely graduated masses in order to generate a specific pressure. (B) Separator separates the special oil from the sample compartment of the HP-cell, which is filled with degassed DI water.

7.2 Safety Issues

Based on the recommendations of Schwan, who has already mentioned the general safety issues of the high pressure visual cell in his PhD thesis, the possible dangers will be described below. Additionally, safety issues for working with the slim tube apparatus will be pointed out.

There is a risk of bursting of the sapphire cylinder and the leaking of capillaries and hose connections is possible. Therefore, protective measures must be taken during all the work on the filling apparatus and the high pressure visual cell, when under pressure, to avoid injury. In particular, these protective measures are the constant wearing of a suitable protective goggles, the use of splinter guards on the filling apparatus and the use of the splinter trap net on the sapphire cylinder. As far as possible, all measurements must be carried out behind a lockable break-proof safety glass, for instance a Plexiglas®. The water bath used for tempering the high pressure visual cell offers a certain protection against splinters in the case of bursting. While measuring in a water bath, always use an intact ground fault circuit interrupter for all live devices. If the pressure in the HP-cell has risen above the critical limit of the apparatus (HP-cell $p_{\max} = 50.0$ MPa), for example due to unobserved heating, the reduction of pressure by cooling is the safest way. By switching off the heating and increasing the water cooling, pressure can be reduced without having to open the Plexiglas®. It is essential to ensure that the pressure in the measuring HP-cell is lowered as far as possible by turning the piston upwards before removing it from the water bath. When opening the HP-cell after a measurement, the internal pressure must be released via the needle valve. It may happen that the stirring bar plugs the drilled hole at the bottom of the HP-cell. In this case, the pressure gauge indicates atmospheric pressure, though there is still high pressure in the HP-cell. When loosening the screws, a sudden shooting out of the piston can then occur. This can be prevented by placing the HP-cell on the side, while the valve is being opened. If there is any remaining pressure in the HP-cell, the piston is pushed upwards as long as the two spindle-fixing nuts at the upper end of the HP-cell are not removed [Schwan, 2005].

The significantly higher volume in the ST leads to additional danger potentials. In addition to wearing personal protective equipment, such as protective goggles, some further points should be considered. When depressurizing, sudden discharge should be avoided to prevent the effluent from solidification and the valves or lines from freezing. Blocked lines or

valves can result in an increase of the pressure until a critical pressure is reached. This can lead to a dangerous uncontrolled movement of the massive oven or lines.

These safety issues are not comprehensive. In all steps, it has to be considered, which components are or will stand under what pressure, when opening valves. The display of instruments must always be treated with a healthy level of distrust.

7.3 Model Crude Oil 51.4

Figure 7.2 and Figure 7.3 show the detailed composition and phase behavior of the model crude oil 51.4 described in chapter 4.1.2.1. As expected due to the rather low density of the oil, the CO₂ – mco51.4 system has a miscibility gap, which is smaller than the miscibility gap of the CO₂ – *n*-dodecane system and thus is not able to appropriately model the properties of the aco38.0.

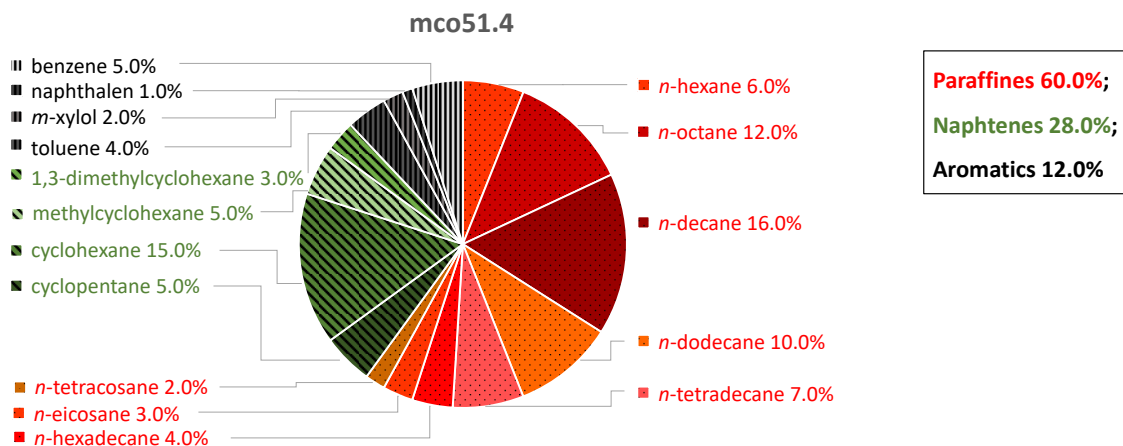


Figure 7.2: Composition of mco51.4.

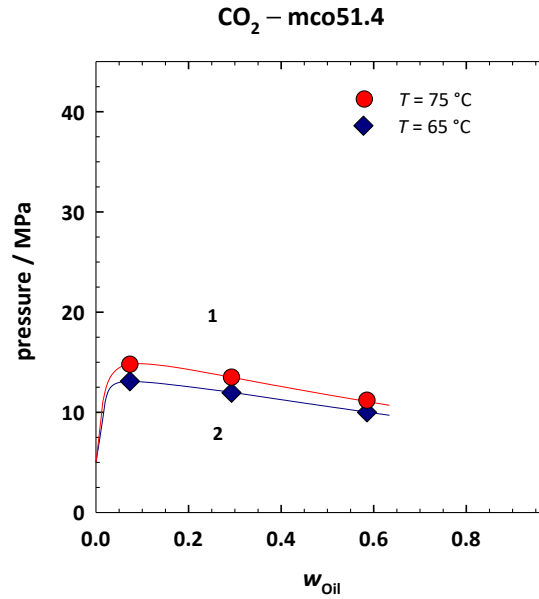


Figure 7.3: $p(w_{oil})$ -phase diagram of the system CO₂ – mco51.4 at 65 °C and 75 °C.^(1F) The system shows an asymmetric lower miscibility gap, which runs through a maximum, the physical minimum miscibility pressure (MMP_p), at low values of $w_{oil} = 0.075$. Note that the miscibility gap is smaller compared to the system CO₂ – *n*-dodecane.

7.4 Viscosity of *n*-Hexadecane

The viscosity μ (in mPa·s) of *n*-hexadecane was calculated according to the Vogel–Fulcher–Tammann–Hesse equation

$$\mu = e^{A + \frac{B}{C+T}}, \quad (7.1)$$

wherein A, B, and C are constants provided from Dortmund Data Bank Software and Separation Technology GmbH (DDBST) and T is the desired temperature (in K) [Vogel, 1921, Fulcher, 1925, Tammann, Hesse, 1926]. Using the constants $A = -4.0453$, $B = 1247.28$, and $C = 1247.28$ for $T = 298.15$ K, the viscosity of *n*-hexadecane results in 3.012 mPa·s [DDBSP, 2018].

7.5 Densities of CO₂ and *n*-Hexadecane

The densities ρ (in g·cm⁻³) of CO₂ were taken from the National Institute of Standards and Technology (NIST) [Lemmon, McLinden, Friend, 2013 (accessed August 7, 2019)].

In Figure 7.4, the temperature and pressure dependence of the density of CO₂ in form of a $\rho(p)$ -diagram is shown. At constant temperature, the CO₂ density increases with increasing pressure. At constant pressure, the density decreases with increasing temperature.

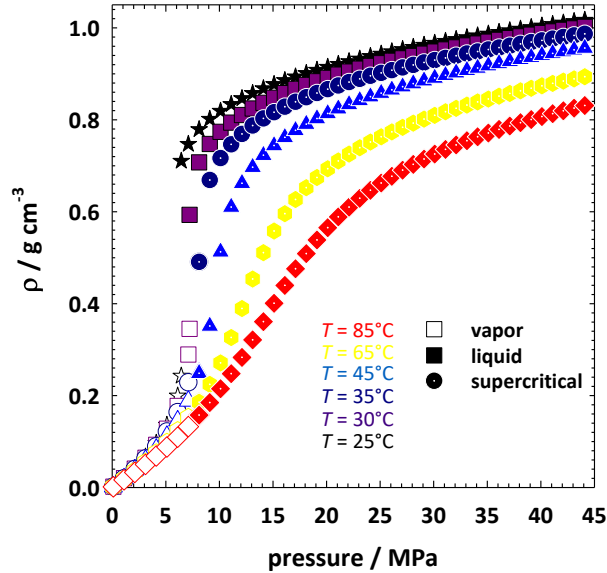


Figure 7.4: CO₂ density shown as a function of pressure for different temperatures ranging from 25 °C to 85 °C. Additionally, the different states of CO₂ are indicated by different symbols for vapor (unfilled symbols), liquid (filled symbols), and supercritical (filled and dotted symbols).

Figure 7.4 shows how significantly the densities of CO₂ differ for different pressures and temperatures. In chapter 3.2.1, it was mentioned that the high pressure visual cell was always filled at room temperature at a pressure of 7.2 MPa. The reason for that can be seen in Figure 7.4. At pressures ≥ 6.5 MPa (and 25 °C), CO₂ is in its liquid phase and shows a less strong pressure dependence of the density, which allows a more accurate filling with the desired amount of CO₂ based on density and volume.

The density ρ (in g cm^{-3}) of *n*-hexadecane was calculated according to the Dortmund Data Bank with the DIPPR105 equation:

$$\rho = \frac{A}{B^{1+(1-\frac{T}{C})^D}}, \quad (7.2)$$

wherein $A = 31.9201$, $B = 0.181893$, $C = 842.438$, and $D = 0.324527$ are constants provided from the Dortmund Data Bank Software & Separation Technology GmbH (DDBST) [DDBSP, 2018] and T is the temperature (in K). At the desired temperature of $T = 338.15$ K, the density results in a value of $\rho = 0.742822$ g cm^{-3} .

7.6 CO₂ – Aco38.0 Phase Behavior Below the Critical Point of CO₂

Based on the reservoir conditions of interest, the phase behavior studies in this thesis were usually measured above the critical point of CO₂ ($T_c = (30.9782 \pm 0.015)^\circ\text{C}$, $p_c = (7.3773 \pm 0.0030)$ MPa [Span, Wagner, 1996]). Under these conditions, CO₂ is in its supercritical state (one phase), which makes the observation of the phase transitions from a single phase to two phases easy. Since also oil fields with low reservoir temperatures and pressures exist, phase behavior studies of the CO₂ – aco38.0 system at a temperature and pressures below T_c and p_c of CO₂ were performed. Under these conditions, CO₂ can exist as liquid and gaseous state, which makes the system more complicated. In Figure 7.5, photographs of the system CO₂ – aco38.0 ($w_{oil} = 0.084$) at a temperature of 27.8 °C are shown for pressures ranging from 5 MPa to 10 MPa. At 5.0 MPa, a clear CO₂-rich upper gaseous phase and on the bottom an aco38.0-rich liquid phase, which covers half of the height of the stirring bar, can be seen. The volume of the lower aco38.0-rich phase decreases for increasing pressures up to 7.0 MPa and remains constant above. At 7 MPa, an additional liquid CO₂-rich phase starts to coexist and its volume increases with increasing pressure. At a pressure of 7.6 MPa, the gaseous CO₂-rich phase completely vanishes and only an upper liquid CO₂-rich phase remains. Due to the limited volume of the set-up and the composition of the sample, the maximum pressure, which could be achieved was 10.0 MPa. As expected for the analyzed temperature of 27.8 °C, the coexistence of liquid and gaseous CO₂ was confirmed for pressures of 7.0 MPa to 7.6 MPa.

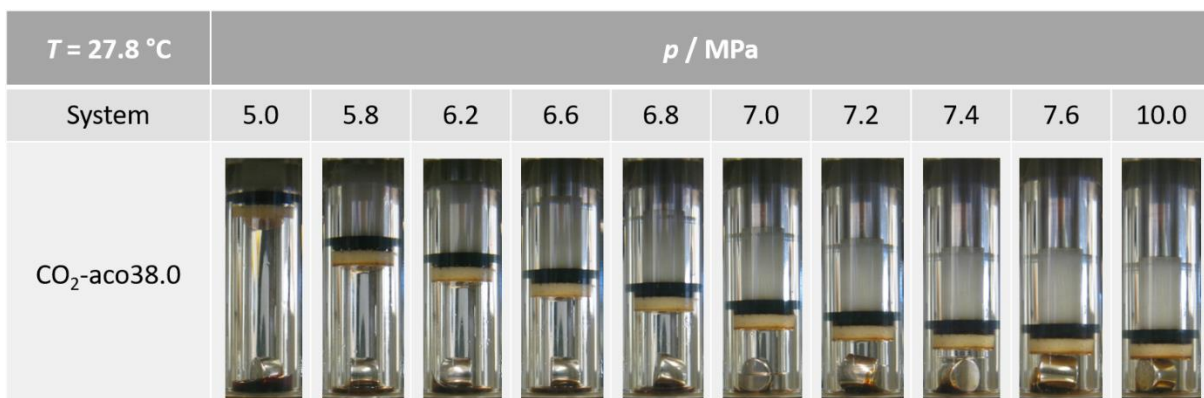


Figure 7.5: Photographs of the CO₂ – aco38.0 system ($w_{oil} = 0.084$) at a constant temperature of 27.8 °C and different pressures. At low pressures between 5 to 6.8 MPa two phases can be seen, an upper gaseous CO₂-rich phase and on the bottom an aco38.0-rich phase. By further increasing the pressure, a third phase, a liquid CO₂-rich phase, can be seen beginning at 7 MPa. By further increase of the pressure, the gaseous CO₂-rich phase transitions into the liquid CO₂-rich phase.

7.7 Overview of Measured Systems

An overview of all measured systems is given in Table 7.1. The systems are sorted by the additives (alphabetically). Additionally, all phase diagram data of the CO₂ – additive systems are shown in Table 7.2 for different additive mass fractions in CO₂ ranging from $\gamma_{\text{CO}_2} = 0.020 \pm 0.002$ to $\gamma_{\text{CO}_2} = 0.850 \pm 0.002$ and temperatures from $T = (25.0 \pm 0.1)^\circ\text{C}$ to $T = (85.0 \pm 0.1)^\circ\text{C}$.

Table 7.1: Overview of the measured systems. In the first column, the additives are shown with their abbreviation. Furthermore, the backbone alcohol is indicated as well as the corresponding number of ethoxy (EO) or propoxy (PO) units. In the last columns, it is shown for which (model) crude oils the measurements were performed, always in the presence of CO₂.

Additive	Alcohol Backbone	EO	PO	CO ₂ –				
				none	mco47.0	mco38.8	mco38.0	aco38.0
No Additive	-	-	-		x	x	x	x
C4E1	<i>n</i> -butanol	1	0	x		x		
C4E2	<i>n</i> -butanol	2	0	x		x		x
C4E1P3	<i>n</i> -butanol	1	3	x	x			
C4E4	<i>n</i> -butanol	4	0	x	x			x
C4P7	<i>n</i> -butanol	0	7	x				
C6E3	<i>n</i> -hexanol	3	0			x	x	
C6E4	<i>n</i> -hexanol	4	0					x
C6E6	<i>n</i> -hexanol	6	0			x		x
C6P1	<i>n</i> -hexanol	0	1			x		x
C6P2	<i>n</i> -hexanol	0	2					x
C6P3	<i>n</i> -hexanol	0	3	x	x	x	x	x
C6P4	<i>n</i> -hexanol	0	4			x		x
C6P6	<i>n</i> -hexanol	0	6					x
2-EH	2-hexanol	0	0		x			
2-EHE2P7	2-hexanol	2	7		x			
Lincoln8i	2-methylheptanol	0	0		x			
2-PH	2-heptanol	0	0		x			
Isononanol	1-Isononanol	0	0		x			
Exxal™ 10	C9-11iso, decanol-rich	0	0		x			

For purity see Table 3.1.

Table 7.1 continued: Overview of measured systems.

Additive	Alcohol Backbone	EO	PO	CO ₂ –				
				None	mco47.0	mco38.8	mco38.0	aco38.0
ISOFOL12	2-butyloctan-1-ol	0	0		x	x		x
ISOFOL12 E₁	2-butyloctan-1-ol	1	0		x	x		x
ISOFOL12 E₃	2-butyloctan-1-ol	3	0					x
ISOFOL12 P₁	2-butyloctan-1-ol	0	1					x
ISOFOL12 P₂	2-butyloctan-1-ol	0	2			x		
ISOFOL12 P₃	2-butyloctan-1-ol	0	3					x
ISOFOL12 P₄	2-butyloctan-1-ol	0	4	x	x			x
ISOFOL12 P₆	2-butyloctan-1-ol	0	0					x
ITDA	2,5,9-trimethyldecan-1-ol	0	0		x			x
ITDA E₂	2,5,9-trimethyldecan-1-ol	2	0	x				x
ITDA P₃	2,5,9-trimethyldecan-1-ol	0	3		x			
ITDA P₄	2,5,9-trimethyldecan-1-ol	0	4	x				
C₁₂E₂P₇	<i>n</i> -dodecanol	2	7		x			
C₁₆E₂P₇	<i>n</i> -hexadecanol	2	7		x			
ISOFOL16	2-hexyldecan-1-ol	0	0		x			
ISOFOL16 P₄	2-hexyldecan-1-ol	0	4	x				
ISOFOL16 E₂P₇	2-hexyldecan-1-ol	2	7		x			
Methanol	methanol	0	0		x	x		
Ethanol	ethanol	0	0		x	x		
<i>n</i>-butanol	<i>n</i> -butanol	0	0	x	x	x		
<i>n</i>-hexanol	<i>n</i> -hexanol	0	0		x	x		
<i>n</i>-octanol	<i>n</i> -octanol	0	0		x	x		
<i>n</i>-decanol	<i>n</i> -decanol	0	0		x	x		
<i>n</i>-dodecanol	<i>n</i> -dodecanol	0	0		x	x		
<i>n</i>-tetradecanol	<i>n</i> -tetradecanol	0	0		x	x		
<i>n</i>-hexadecane	<i>n</i> -hexadecane	0	0	x				
ISOFOL28	2-dodecylhexadecan-1-ol	0	0		x			
Ethanol+5POC	ethanol	0	[5]	x				
Marlophen P4	Phenol	0	4	x				
TDA+5POC	2,5,9-trimethyldecan-1-ol	0	[5]	x				
TEA	Triethanolamine	0	0	x				
TIPA	Triisopropanolamine	0	0	x				

[5] = 5 units of polycarbonatepropyl. For purity see Table 3.1.

Table 7.2: Phase diagram data of the CO₂ – additive systems for different additive mass fractions in CO₂ ranging from $\gamma_{\text{CO}_2} = 0.020 \pm 0.002$ to $\gamma_{\text{CO}_2} = 0.850 \pm 0.002$ and temperatures from $T = (25.0 \pm 0.1)^\circ\text{C}$ to $T = (85.0 \pm 0.1)^\circ\text{C}$. For all systems and temperatures, the phase transition pressures are given in MPa.

CO ₂ – Additive	γ_{CO_2}	25.0 °C	30.0 °C	35.0 °C	45.0 °C	55.0 °C	65.0 °C	75.0 °C	85.0 °C
<i>n</i> -butanol	0.022	6.5	7.2	7.9	8.9				
<i>n</i> -butanol	0.052	6.4	7.1	7.8	9.1	10.2	11.0		
<i>n</i> -butanol	0.074	6.3	7.0	7.7	9.1	10.6	11.7	12.7	
<i>n</i> -butanol	0.100	6.3	7.0	7.7	9.2	10.7	12.0	12.8	
<i>n</i> -butanol	0.154	6.3	6.9	7.6	9.2	10.8	12.4	13.6	
<i>n</i> -butanol	0.198	6.3	7.0	7.7	9.3	11.0	12.6	14.0	
<i>n</i> -butanol	0.247	6.4	7.1	7.8	9.4	11.1	12.7	14.1	
<i>n</i> -butanol	0.299	6.2	6.9	7.6	9.2	10.9	12.5	13.9	
<i>n</i> -butanol	0.402	6.2	6.8	7.5	9.0	10.6	12.1	13.5	
<i>n</i> -butanol	0.463	6.4	6.9	7.6	9.0	10.5	11.9	13.2	
<i>n</i> -butanol	0.544	6.0	6.6	7.2	8.5	9.9	11.1	12.2	
<i>n</i> -butanol	0.600	5.9	6.5	7.1	8.3	9.6	10.8	11.9	
<i>n</i> -butanol	0.732	5.4	5.8	6.2	7.0	7.9	8.6	9.4	
<i>n</i> -butanol	0.835	4.6	5.0	5.3	5.9	6.6	7.2	7.8	
<i>n</i> -butanol	0.929	2.8	3.0	3.2	3.5	3.7	4.0	4.4	
C ₄ E ₁	0.020	6.7	7.5	8.2	9.4	10.3	11.0		
C ₄ E ₁	0.050	6.7	7.4	8.1	9.5	10.9	12.2	13.2	
C ₄ E ₁	0.075	6.6	7.3	8.0	9.4	11.0	12.3		
C ₄ E ₁	0.100	6.6	7.3	8.0	9.5	11.3	13.0	14.6	
C ₄ E ₁	0.153	6.5	7.2	7.9	9.5	11.3	13.3	15.0	
C ₄ E ₁	0.184	6.2	6.8	7.5	9.2	10.9	12.7	14.4	
C ₄ E ₁	0.300	6.5	7.0	7.8	9.4	11.1	13.0	14.8	
C ₄ E ₁	0.451	6.4	7.1	7.8	9.3	11.0	12.8	14.5	
C ₄ E ₁	0.601	6.1	6.7	7.3	8.7	10.3	11.8	13.4	
C ₄ E ₁	0.750	5.7	6.1	6.6	7.7	8.7	9.8	11.0	
C ₄ E ₁	0.899	5.4	5.5	5.6	5.7	5.9	6.3	6.7	
C ₄ E ₁	0.930	3.0	3.1	3.2	3.3	3.6	3.9	4.2	
C ₄ E ₁	0.944	1.9	2.0	2.0	2.3	2.5	2.7	3.0	
C ₄ E ₁	0.932	2.2	2.3	2.5	2.9	3.2	3.6	3.9	
C ₄ E ₁	0.942	1.8	1.9	2.0	2.4	2.6	2.9	3.1	
C ₄ E ₁	0.151	7.7	8.0	8.5	9.5	10.7	11.1	13.1	

Table 7.2 continued: Phase diagram data of the CO₂ – additive systems.

CO ₂ – Additive	γ_{CO_2}	25.0 °C	30.0 °C	35.0 °C	45.0 °C	55.0 °C	65.0 °C	75.0 °C	85.0 °C
C ₄ E ₂	0.023	6.7	7.5	8.2	9.8	11.4	12.3		
C ₄ E ₂	0.040	6.7	7.4	8.2	10.0	11.9	13.5	14.7	
C ₄ E ₂	0.049	6.7	7.4	8.1	10.2	12.1	13.8	15.0	
C ₄ E ₂	0.064	6.3	7.0	7.7	9.8	12.0	13.8	15.3	
C ₄ E ₂	0.071	7.3	7.9	8.7	11.3	13.7	16.0	18.3	
C ₄ E ₂	0.085	6.7	7.3	8.1	10.1	12.0	13.6	15.4	
C ₄ E ₂	0.120	6.7	7.4	8.2	10.9	13.3	15.4	17.3	
C ₄ E ₂	0.140	6.8	7.7	8.5	10.6	13.2	15.5	17.6	
C ₄ E ₂	0.304	6.8	7.5	8.4	11.3	13.8	16.1	18.2	
C ₄ E ₂	0.447	6.7	7.5	8.3	10.5	13.0	15.3	17.4	
C ₄ E ₂	0.604	6.4	7.1	7.7	9.3	10.9	12.7	14.5	
C ₄ E ₂	0.952	2.3	2.4	2.6	2.8	3.2	3.6	3.9	
C ₄ E ₂	0.710	6.3	7.0	7.6	8.8	9.9	11.1	12.5	
C ₄ E ₂	0.886	4.9	5.0	5.1	5.6	6.2	6.7	7.5	
C ₄ E ₂	0.102	6.2	6.9	7.6	9.8	12.0	14.0	15.8	
C ₄ E ₂	0.151		0.8	0.9	1.0	1.1	1.1	1.3	
C ₄ E ₄	0.075	12.4	13.9	15.4	16.75	19.05	21.15	23.25	
C ₄ E ₄	0.301	12.25	14.05	15.55	18.5	21.15	23.45	25.65	27.45
C ₄ E ₄	0.500	9.2	9.5	10	11.6	13	14.4	16.1	
C ₄ E ₄	0.600	8.05	8.85	9.35	10.55	12.05	13.25	14.65	
C ₄ E ₁ P ₃	0.041	7.7	8.5	9.9	12.5	14.7	16.7	18.4	
C ₄ E ₁ P ₃	0.075	7	7.65	8.45	10.8	12.1	15.2	17.2	
C ₄ E ₁ P ₃	0.150	6.65	7.25	8.75	11.65	14.35	16.75	18.85	20.75
C ₄ E ₁ P ₃	0.225	7.5	8.4	9.1	11.4	13.4	15.6	17.5	
C ₄ E ₁ P ₃	0.300		7.3773	8.05	10.95	13.75	16.25	18.4	
C ₄ E ₁ P ₃	0.450	6.55	7.25	8.15	10.85	13.65	16.15	18.25	20.15
C ₄ E ₁ P ₃	0.600	6.35	7.05	7.85	9.55	11.85	13.95	16.15	17.95
C ₄ E ₁ P ₃	0.800	5.35	5.65	5.95	6.55	7.25	7.9	8.75	9.3
C ₄ E ₁ P ₃	0.850	4.8	5.15	5.4	6	6.6	7.3	8.1	8.7

Table 7.2 continued: Phase diagram data of the CO₂ – additive systems.

CO ₂ – Additive	γ_{CO_2}	25.0 °C	30.0 °C	35.0 °C	45.0 °C	55.0 °C	65.0 °C	75.0 °C	85.0 °C
C ₄ P ₇	0.076	8.65	10.45	12.2	15.45	18.45	21.15	23.65	
C ₄ P ₇	0.300	10.7	12.45	14.15	17.35	20.1	22.7	24.9	27.05
C ₄ P ₇	0.600	7.15	7.85	8.65	9.75	10.65	11.25	11.55	
C ₆ P ₃	0.074		6.8	8.5	10.9	13.6	16	18.2	
C ₆ P ₃	0.084						16.5	18.5	
C ₆ P ₃	0.315	5.6					17.1	19.4	
C ₆ P ₃	0.596	5.2					14.5	16.7	
MARLOPHEN P ₄	0.076	280	306		312		300		
MARLOPHEN P ₄	0.301	380	385		380		470		
ITDA E ₂	0.020	10	11.7	13	13.8	16.4			
ITDA E ₂	0.076	30	29.4	29.2	29.6	30.6	31.6	33.1	
ITDA E ₂	0.125	23.3	23.15	24.3	25.4	27.1	29.2		
ITDA E ₂	0.3	27.3	26.1	25.5	25.85	26.85	28.2	29.8	
ITDA E ₂	0.6	8.1	8.2	8.55	9.5	10.3	10.5	11.2	
ITDA P ₄	0.075	8.4	10.1	11.7	14.4	16.9	19.2	21.3	
ITDA P ₄	0.199	11.5	12.7	14	16.15	18.35	20.3	22.3	
ITDA P ₄	0.301	12.1	13.7	15.1	18.05	20.7	23.1	25.4	
ITDA P ₄	0.601	7.3	8.25	9.5	11.45	13.8	15.8	17.4	
TDA+5POC*	0.3	24.9	26.5	28.25	31.6	34.9	<35.0		
TDA+5POC*	0.600	13.7	14.45	15.9	18.8	22.2	24.7	27.1	
ISOFOL12 P ₄	0.075	8.1	9.6	11.0	14.1	15.7	17.9	19.5	
ISOFOL12 P ₄	0.199	11.5	13	14.35	17.25	19.9	22.3	24.5	
ISOFOL12 P ₄	0.301	11.05	12.55	14.2	16.7	19.4	21.9	24.1	
ISOFOL12 P ₄	0.45	10.3	0	13.1	15.7	18.3	20.7	22.8	
ISOFOL12 P ₄	0.601	7.1	8.2	9.4	11.7	14	15.8	17.7	
ISOFOL16 P ₄	0.074	16.800	15.4	17.9	19.7	23.5			
ISOFOL16 P ₄	0.300	21.2	21.3	21.2	21.9	23.2	24.45	25.9	
ISOFOL16 P ₄	0.600	10.7	11.75	12.5	14.4	16.3	18.1	19.6	

*5 units of polycarbonatepropyl. For purity see Table 3.1.

List of Figures

- Figure 2.1: Triangular phase diagrams for the system methane – *n*-butane – decane at constant temperature and two different pressures. Source of data: [Sage, Lacey, 1955]. Redrawn from: [Hutchinson Jr., Braun, 1961]..... 19
- Figure 2.2: Schematical, isothermal $p(x)$ -phase diagrams of the CO₂ – *n*-hexadecane system for different temperatures showing different coexisting phases in the miscibility gaps in (a) or a simple liquid-gas (lg) coexisting phase in (b). 20
- Figure 2.3: Schematical $p(T)$ - and $p(x)$ -phase diagrams consisting of a pure *x* component A, crude oil (M4) and mixtures of both (M1, M2, and M3). 22
- Figure 2.4: The first-contact miscibility and the condensing-gas drive miscibility (left) as well as the vaporizing-gas drive process (right) are shown schematically in pseudotriangular diagrams. 23
- Figure 2.5: $p(x)$ -diagram and triangular diagrams are schematically shown for Type I phase behavior at constant temperature and different pressures. 27
- Figure 2.6: Schematical $p(x)$ -diagram and triangular diagrams for Type IIa phase behavior at constant temperature and different pressures..... 29
- Figure 2.7: $p(x)$ -diagram and triangular diagrams are schematically shown for Type IIb phase behavior at constant temperature and different pressures. 31
- Figure 2.8: Pseudotetrahedrons showing immiscible, multiple- and first-contact miscible conditions (from left to right) depending on the increasing additive concentrations (at the same pressure and temperature)..... 33
- Figure 3.1: Gas chromatography analysis of Sasolwax 5805 provided by Sasol Performance Chemicals..... 40
- Figure 3.2: Technical sketch of the modified high pressure visual cell adapted from Schwan [Schwan, 2005]. 42
- Figure 3.3: Sketch of the sealed HP-cell connected upside down to an in-house-built CO₂ filling apparatus equipped with a membrane reservoir (MR), adapted from Schwan [Schwan, 2005]. 45
- Figure 3.4: Schematic drawing of the slim tube apparatus (ST), designed by Dr. Maura Puerto. 47
- Figure 3.5: Recovered PV of *n*-hexadecane after injection of 1.2 PV of CO₂ as a function of the pressure for the CO₂ – *n*-hexadecane system at (42±2) °C. 50
- Figure 3.6: Permeability of the packed slim tube determined by plotting the flow rate Q of the injection fluid *n*-hexadecane as a function of the differential pressure Δp 53

Figure 3.7: Pycnometer (A) with thermometer (B) and cap (C) to determine the densities/API gravities.	54
Figure 3.8: $p(T)$ -phase diagram of the binary $\text{CO}_2 - \text{C}_4\text{E}_1\text{P}_3$ system at different additive mass fractions (γ_{CO_2}).	57
Figure 3.9: $p(\gamma_{\text{CO}_2})$ -diagram (left) and $T(\gamma_{\text{CO}_2})$ -diagram (right) of the binary $\text{CO}_2 - \text{C}_4\text{E}_1\text{P}_3$ system constructed from the corresponding $p(T)$ -diagram at different temperatures and pressures, respectively.....	57
Figure 4.1: $p(\gamma_{\text{CO}_2})$ -diagrams of the system $\text{CO}_2 - 1$ -butanol at two temperatures 60 °C (left) and 80 °C (right). ^{1(LW)}	63
Figure 4.2: $p(\gamma_{\text{CO}_2})$ -diagrams of the systems $\text{CO}_2 - \text{C}_4\text{E}_j$ ($j = 0$ to 2) at five different temperatures ($T = 25$ °C-75 °C). ^{(LW) 2(JF)}	64
Figure 4.3: Isothermal $p(w_{\text{Oil}})$ -diagram of the $\text{CO}_2 - \text{aco38.0}$ and the three binary $\text{CO}_2 - n$ -alkane systems at 75 °C and 80 °C.....	66
Figure 4.4: Compositions of mco47.0 (top) and mco38.8 (bottom) in wt%.	68
Figure 4.5: $p(w_{\text{Oil}})$ -phase diagrams of the systems $\text{CO}_2 - \text{mco47.0}$, $\text{CO}_2 - \text{mco38.8}$ and $\text{CO}_2 - \text{aco38.0}$ at 65 °C and 75 °C. ^(JF)	70
Figure 4.6: $p(w_{\text{Oil}})$ -phase diagrams of the systems $\text{CO}_2 - \text{mco47.0}$, $\text{CO}_2 - \text{mco38.8}$ and $\text{CO}_2 - \text{aco38.0}$ with plait (critical) points at 65 °C. ^(JF)	73
Figure 4.7: Scaled representation of the miscibility gaps of the systems $\text{CO}_2 - \text{mco47.0}$, $\text{CO}_2 - \text{mco38.8}$, and $\text{CO}_2 - \text{aco38.0}$ at 65 °C and 75 °C.....	74
Figure 4.8: $p(w_{\text{Oil}})$ -phase diagram of the systems $\text{CO}_2 - \text{mco38.8}$ and $\text{CO}_2 - \text{mco38.0}$ at 65 °C.	75
Figure 4.9: Overview of the phase transition pressures of the 16 (pseudo-)binary $\text{CO}_2 - \text{additive}$ systems at $\gamma_{\text{CO}_2} \approx 0.075$ (black circles) and the 6 pseudobinary $\text{CO}_2 - (\text{model})$ crude oil systems at $w_{\text{Oil}} \approx 0.075$ (blue circles) at 65 °C.	77
Figure 4.10: Unfolded schematic phase triangle showing the three (pseudo-)binary side systems at constant temperature.	79
Figure 4.11: Schematic phase prism of a pseudoternary $\text{CO}_2 - (\text{model})$ crude oil – additive system (left) and $p(w_{\text{Oil}})$ -sections through the isothermal phase prism of the system $\text{CO}_2 - \text{mco47.0} - \text{C}_4\text{E}_1\text{P}_3$ at 65 °C (right).....	80
Figure 4.12: Isothermal (65°C) and isobaric Gibbs triangles of the system $\text{CO}_2 - \text{mco47.0} - \text{C}_4\text{E}_1\text{P}_3$ obtained from the $p(w_{\text{Oil}})$ -sections (Figure 4.11, right) at pressures of 15 MPa (A), 20 MPa (B), 25 MPa (C), and 30 MPa (D).	82

- Figure 4.13: Illustration of the pressure profit Δp as a measure of the miscibility-enhancing effect of the respective additive by means of a $p(w_{oil})$ -diagram of the system $CO_2 - mco47.0 - C_4E_1P_3$ at $\gamma_{CO_2} = 0.022 \pm 0.002$ and $65^\circ C$ 83
- Figure 4.14: Pressure profit (Δp) as a function of the model crude oil mass fraction w_{oil} (left) and additive mass fraction γ_{CO_2} in the CO_2 /additive mixture (right) for the system $CO_2 - mco47.0 - C_4E_1P_3$ at a constant temperature of $65^\circ C$ 84
- Figure 4.15: Pressure profits (Δp) at $65^\circ C$ and $75^\circ C$ obtained by the addition of 1-alcohols ($C_iH_{2i+1}OH$) to the pseudobinary systems $CO_2 - mco47.0$ (left) and $CO_2 - mco38.8$ (right) at $w_{oil} = 0.075 \pm 0.003$ and $\gamma_{CO_2} = 0.020 \pm 0.002$ ^(LW,JF) 86
- Figure 4.16: Pressure profits (Δp) at $65^\circ C$ and $75^\circ C$ obtained by the addition of linear and branched alcohols to the $CO_2 - mco47.0$ system at $w_{oil} = 0.075 \pm 0.003$ and $\gamma_{CO_2} = 0.020 \pm 0.002$ (top) and molecular structures of the branched alcohols (bottom). ... 89
- Figure 4.17: Pressure profits (Δp) at $65^\circ C$ (blue) and $75^\circ C$ (red) obtained by the addition of $C_4E_jP_x$ and ISO FOL $12E_jP_x$ to the pseudobinary $CO_2 - mco47.0$ system at $w_{oil} = 0.075 \pm 0.003$ and $\gamma_{CO_2} = 0.020 \pm 0.002$ 91
- Figure 4.18: Pressure profits (Δp) obtained at $65^\circ C$ (blue) and $75^\circ C$ (red) by the addition of $C_4E_jP_x$, $C_6E_jP_x$ and ISO FOL $12E_jP_x$ to the pseudobinary $CO_2 - mco38.8$ system at $w_{oil} = 0.075 \pm 0.003$ and $\gamma_{CO_2} = 0.020 \pm 0.002$ 92
- Figure 4.19: Pressure profits (Δp) obtained at $65^\circ C$ (blue) and $75^\circ C$ (red) by the addition of $C_4E_jP_x$, $C_6E_jP_x$, ISO FOL $12E_jP_x$ and ITDA E_x to the pseudobinary $CO_2 - aco38.0$ system at $w_{oil} = 0.075 \pm 0.003$ and $\gamma_{CO_2} = 0.020 \pm 0.002$ 94
- Figure 4.20: $p(\gamma_{CO_2})$ -diagram (left) and $\Delta p(\gamma_{CO_2})$ -diagram (right) of the pseudoternary $CO_2 - mco47.0 -$ additive systems at $w_{oil} = 0.075 \pm 0.006$ and $65^\circ C$ 96
- Figure 4.21: Pressure profit (Δp) of the additives 1-butanol, C_6P_3 and ISO FOL $12P_4$ in the $CO_2 - mco47.0$ system at $\gamma_{CO_2} = 0.020 \pm 0.003$ for different w_{oil} (0.075 ± 0.002 and 0.210 ± 0.010) and two temperatures, $65^\circ C$ (left) and $75^\circ C$ (right). 97
- Figure 4.22: $p(w_{oil})$ -diagram of the $CO_2 - mco38.8/mco38.0$ and $CO_2 - mco38.8/mco38.0 - C_6P_3/C_6E_3$ systems at $65^\circ C$ and different γ_{CO_2} 99
- Figure 4.23: Bar chart showing the pressure profits Δp found for the different additives with and without 1-butanol as co-additive ($\delta = 0.400$) in the system $CO_2 - mco47.0$ at $w_{oil} = 0.075$ and $\gamma_{CO_2} = 0.010$ at $65^\circ C$ and $75^\circ C$ 102
- Figure 4.24: Photographs illustrating the influence of the additives C_6P_3 and ITDA E_2 on the swelling behavior of the $CO_2 - aco38.0$ system at $\gamma_{CO_2} = 0.020 \pm 0.001$, $w_{oil} = 0.250 \pm 0.003$ and $65^\circ C$ 105
- Figure 4.25: Influence of the additives C_6P_3 and ITDA E_2 on the swelling behavior of the $CO_2 - aco38.0$ system at $\gamma_{CO_2} = 0.020 \pm 0.001$, $w_{oil} = 0.250 \pm 0.003$ and $65^\circ C$. ^(JF) 106

Figure 4.26: $p(w_{oil})$ -diagram of the systems $CO_2 - aco38.0$ (black unfilled diamonds) and $H_2O - CO_2 - aco38.0$ (blue filled circles) at 65 °C with photographs of the pseudoternary system..... 108

Figure 4.27: Extraction curve for modified swelling factor (SF), see equation (4.6) for the $H_2O - CO_2 - aco38.0$ system at 65 °C containing 30 wt% of H_2O at $w_{oil} = 0.152 \pm 0.001$ and photographs of the respective samples. 110

Figure 4.28: Extraction curves of the modified swelling factor SF (see eq. (4.6)) of the $H_2O - CO_2 - aco38.0$ system containing 30 wt% water at $w_{oil} = 0.371 \pm 0.001$ and 65 °C. 111

Figure 4.29: $p(w_{oil})$ -diagram at 65 °C of the pseudoquaternary system $H_2O - CO_2 - aco38.0 - C_6P_3$ with $\gamma_{CO_2} = 0.020 \pm 0.002$ (blue filled diamonds) and the pseudoternary system $H_2O - CO_2 - aco38.0$ (unfilled circles), both containing 30 wt% of H_2O 113

Figure 4.30: Photographs of the pseudoquaternary system $H_2O - CO_2 - aco38.0 - ITDA E_2$ (30 wt% of water, $w_{oil} = 0.073 \pm 0.001$, $\gamma_{CO_2} = 0.020 \pm 0.001$) and the pseudoternary system $CO_2 - aco38.0 - ITDA E_2$ at 65 °C taken after phase separation at different pressures between 13.0 to 42.0 MPa. 114

Figure 4.31: Results of slim tube measurements performed on the $CO_2 - mco38.0$ system at (65 ± 2) °C with an average pressure (p_{ϕ}) of (15.3 ± 0.4) MPa. 118

Figure 4.32: Results of slim tube measurements performed on the $CO_2 - mco38.0$ system at (65 ± 2) °C and three different average pressures (p_{ϕ}) of (17.0 ± 0.3) MPa, (19.4 ± 0.5) MPa, and (19.7 ± 0.6) MPa. 119

Figure 4.33: Recovered PV of $mco38.0$ after injection of 1.2 PV of CO_2 as a function of the pressure for the $CO_2 - mco38.0$ system at (65 ± 2) °C..... 121

Figure 4.34: Results of slim tube measurements performed on the $CO_2 - mco38.0 - C_6P_3$ system at (65 ± 2) °C, $\gamma_{CO_2} = 0.020$, and four different pressures of (13.6 ± 0.8) MPa, (14.3 ± 0.4) MPa, (16.5 ± 0.5) MPa and (17.9 ± 0.4) MPa..... 123

Figure 4.35: Recovered PV of $mco38.0$ after injection of 1.2 PV of CO_2 as a function of the pressure for the $CO_2 - mco38.0 - C_6P_3$ system at (65 ± 2) °C and $\gamma_{CO_2} = 0.020$ 124

Figure 4.36: Comparison of the results of the slim tube measurements performed on the systems $CO_2 - mco38.0$ and $CO_2 - mco38.0 - C_6P_3$ (2 wt% of C_6P_3 in CO_2 by co-injection) at (65 ± 2) °C. 125

Figure 7.1: Pressure balance model CPB5800 from DH-Budenberg..... 144

Figure 7.2: Composition of $mco51.4$ 146

Figure 7.3: $p(w_{oil})$ -phase diagram of the system $CO_2 - mco51.4$ at 65 °C and 75 °C.^(JF) 147

Figure 7.4: CO_2 density shown as a function of pressure for different temperatures ranging from 25 °C to 85 °C. 148

Figure 7.5: Photographs of the CO ₂ – aco38.0 system ($w_{Oil} = 0.084$) at a constant temperature of 27.8 °C and different pressures.....	149
---	-----

List of Tables

Table 3.1: Used chemicals.....	37
Table 3.2: Main components of the slim tube apparatus.....	48
Table 4.1: Compositions, densities and API gravities of the model crude oils (mco), Asian crude oil (aco38.0) and Sasolwax 5805.	69
Table 4.2: MMP _p and $w_{Oil,p}$ of the three systems CO ₂ – mco47.0, CO ₂ – mco38.8 and CO ₂ – aco38.0 at 65 °C and 75 °C.....	71
Table 4.3: Locations of the plait (critical) points given by the values of the critical pressure (p_c) and critical oil mass fraction ($w_{Oil,c}$) of the systems CO ₂ – mco47.0, CO ₂ – mco38.8 and CO ₂ – aco38.0 at 65 °C, 70 °C and 75 °C.	72
Table 4.4: Densities, API gravities, MMP _p and the composition of the aromatic content of mco38.0 and mco38.8.	75
Table 4.5: Comparison of the plait point pressures determined via static phase behavior studies from the HP-cell measurements and the MMP determined via dynamic phase behavior studies from slim tube measurements.	125
Table 7.1: Overview of the measured systems.....	150
Table 7.2: Phase diagram data of the CO ₂ – additive systems for different additive mass fractions in CO ₂ ranging from $\gamma_{CO_2} = 0.020 \pm 0.002$ to $\gamma_{CO_2} = 0.850 \pm 0.002$ and temperatures from $T = (25.0 \pm 0.1)$ °C to $T = (85.0 \pm 0.1)$ °C.....	152

Acknowledgments

Allen voran gilt mein Dank Apl. Prof. Dr. Thomas Sottmann für die großartige Betreuung, die vielen Anregungen und hilfreichen Diskussionen, die Unterstützung, besonders bei widersprüchlich erscheinenden Ergebnissen sowie das Vertrauen in meine Arbeit. Danke, dass ich in den letzten Jahren Teil deiner Gruppe am Institut für Physikalische Chemie der Universität Stuttgart sein durfte. Mein herzlicher Dank geht auch an Prof. Dr. Frank Gießelmann für die Übernahme des Zweitgutachtens dieser Arbeit. Prof. Dr. Elias Klemm möchte ich auch herzlichst danken für die Übernahme des Prüfungsvorsitzendes.

Weiterer Dank gilt unseren Kooperationspartnern von Sasol Performance Chemicals GmbH und Sasol North America für die inspirierende Zusammenarbeit und die finanzielle Unterstützung im Rahmen des Projekts. Insbesondere möchte ich mich bei Dr. Renke Rommerskirchen bedanken, aber auch bei Dr. Silke Hoppe und M.B.A. Patrick Nijssen sowie bei allen, die an diesem Projekt beteiligt waren. Darüber hinaus danke ich Sasol Performance GmbH für die Gelegenheit, diese Arbeit durchführen und veröffentlichen zu dürfen.

I am grateful to Prof. Dr. George J. Hirasaki for sharing his large experience, helpful discussions and suggestions during my time with the slim tube experiments at the Rice University. Furthermore, I would like to warmly thank Dr. Maura Puerto, who has provided valuable support on the slim tube experiments. I want to thank Ian McCarthy, who helped during the set-up of the slim tube apparatus, especially for the hours to find leakages. Furthermore, I would like to acknowledge the financial support by the Rice University Consortium on Processes in Porous Media. Additionally, I thank Mohammadreza Amirmoshiri for support in organizational and porous media questions as well as Dr. Siavash Kahrobaei for discussions on porous media questions. Thanks, my dear friends.

Ganz besonders danke ich meinen Kollegen und Freunden Kristina Schneider und Julian Fischer sowie allen „Sottmännern“ und „Stubenrauchs“, die wesentlich dazu beigetragen haben, die letzten Jahre zu einer ganz besonderen Zeit werden zu lassen. Darüber hinaus danke ich Julian Fischer für hilfreiche Anmerkungen zur schriftlichen Ausarbeitung dieser Doktorarbeit.

Bedanken möchte ich mich auch bei Lisa Winkler, Jens Pfersich, Julian Fischer und Jessica Hippele, die durch ihre Bachelor-Arbeit, Forschungspraktikum und Abschlussarbeiten zu dieser Doktorarbeit beigetragen haben.

Ein besonderer Dank gilt auch den Werkstätten des IPC. Danke an Boris Tschertsche, Daniel Relovsky, Andreas Kübler und Thomas Weigend für die Instandhaltung und die tolle Umsetzung der Messgeräte.

Zudem danke ich unseren CTAs für ihre Unterstützung, insbesondere Diana Zauser und Birgit Feucht. Vielen Dank an Frau Inge Blankenship und Frau Gisela Hoppe für die Hilfen bei den vielen und zum Teil recht langen Dienstreiseanträgen.

An dieser Stelle möchte ich mich bei den wichtigsten Menschen bedanken, bei meiner Frau Meike und unseren Familien. Anne, Baba, Abla, her şey için çok teşekkür ederim. Meike, Danke für deine permanente bedingungslose Unterstützung, dein Verständnis und deinen Glauben an mich. Ohne dich würde es diese Arbeit nicht geben. Danke für so, so vieles mehr noch, aber vor allem für dein Vertrauen in uns, HAYATIMIN AŞKI.

Declaration

I hereby declare that this thesis and the work presented in it are my own and have been prepared without any illegitimate help. All sources used have been quoted adequately.

Erklärung

Hiermit erkläre ich, dass die vorgelegte Dissertation und die darin gezeigten Daten von mir persönlich und ohne unrechtmäßige Hilfe angefertigt wurden. Alle genutzten Quellen sind entsprechend zitiert.

Harun Bilgili

Stuttgart, 10. Mai, 2021

Publications, Patent, Conferences and other Contributions

Publications

Bilgili, H., Fischer, J., Puerto, M., Hirasaki, G.J., Rommerskirchen, R., Ng, R., Hoppe, S. and Sottmann, T., Slim Tube Apparatus vs. High Pressure Visual Cell. In preparation.

Bilgili, H., Bürger M., Stubenrauch C. and Porada J.H., About the nanostructure of the ternary system Water – [BMIm]PF₆ – TX-100, *JCS*, **484**, 237-248 (2016).

Rommerskirchen, R., **Bilgili, H.**, Fischer, J. and Sottmann, T., Impact of Miscibility Enhancing Additives on the Flooding Scheme in CO₂ EOR Processes, SPE International, SPE Improved Oil Recovery Conference, Tulsa, SPE-190288-MS (2018).

Rommerskirchen, R., Nijssen, P., **Bilgili, H.** and Sottmann, T., Reducing the Miscibility Pressure in Gas Injection Oil Recovery Processes, SPE International, Abu Dhabi International Petroleum Exhibition and Conference, Abu Dhabi, SPE-183389-MS (2016).

Rommerskirchen, R., Nijssen, P., **Bilgili, H.** and Sottmann, T., Additives for CO₂ EOR Applications, SPE International, SPE Annual Technical Conference and Exhibition, Dubai, SPE-181304-MS (2016).

Patent

Sasol Performance Chemicals GmbH, Injection Fluids comprising alkoxyated alcohols and the use of such fluids in oil recovery processes (2019), Patent Application No. EP19158014.

Conference Contributions

- | | |
|---------|--|
| 06/2019 | European Committee of Organic Surfactants and their Intermediates (cesio), Munich Poster presentation |
| 04/2018 | Consortium for Processes in Porous Media, Houston Oral presentation |
| 10/2017 | Kolloid-Tagung, Munich Poster presentation |

Visiting Scientist

- | | |
|--|--|
| 02/2018 – 04/2018 and
10/2017 – 12/2017 | Rice University , Department of Chemical and Biomolecular Engineering, group of Prof. Dr. George J. Hirasaki, Houston, Texas, USA |
|--|--|

Supervised Theses of Students

Hippele, J., Einfluss von Additiven auf das Phasendiagramm des Systems Kohlenstoffdioxid – Erdöl (cco33,8), *Bachelor Thesis*, University of Stuttgart (2018).

Fischer, J., Einfluss von Additiven auf das Phasendiagramm des Systems CO₂ – Erdöl (aco38,0), *Wissenschaftliche Arbeit im Fach Chemie*, University of Stuttgart (2017).

Winkler, L., Neuartige Additive in der EOR-Anwendung: Verbesserung der Mischbarkeit von (CO₂ – Modellerdöl) – Systemen, *Bachelor Thesis*, University of Stuttgart (2016).